The Topological Susceptibility of QCD at High Temperatures

Die topologische Suszeptibilität der QCD bei hohen Temperaturen
Zur Erlangung des Grades eines Doktors der Naturwissenschaften (Dr. rer. nat.)
genehmigte Dissertation von Peter Thomas Jahn aus Gelnhausen
Tag der Einreichung: 15.10.2019, Tag der Prüfung: 27.11.2019
Darmstadt — D 17

1. Gutachten: Prof. Ph.D. Guy D. Moore
2. Gutachten: Prof. Dr. rer. nat. Jens Braun

TECHNISCHE
UNIVERSITÄT
DARMSTADT

Fachbereich Physik
Institut für Kernphysik
Theoriezentrum – AG Moore

The Topological Susceptibility of QCD at High Temperatures
Die topologische Suszeptibilität der QCD bei hohen Temperaturen

Genehmigte Dissertation von Peter Thomas Jahn aus Gelnhausen

1. Gutachten: Prof. Ph.D. Guy D. Moore
2. Gutachten: Prof. Dr. rer. nat. Jens Braun

Tag der Einreichung: 15.10.2019
Tag der Prüfung: 27.11.2019

Darmstadt — D 17

Bitte zitieren Sie dieses Dokument als:
URN: urn:nbn:de:tuda-tuprints-94854
URL: http://tuprints.ulb.tu-darmstadt.de/id/eprint/9485

Dieses Dokument wird bereitgestellt von tuprints,
E-Publishing-Service der TU Darmstadt
http://tuprints.ulb.tu-darmstadt.de
tuprints@ulb.tu-darmstadt.de

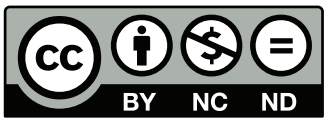

Die Veröffentlichung steht unter folgender Creative Commons Lizenz:
Namensnennung – Nicht kommerziell – Keine Bearbeitungen 4.0 International
https://creativecommons.org/licenses/by-nc-nd/4.0/

To Klary who passed away way too early.
I've never met a cat as good-hearted and lively as you.

Erklärung zur Dissertation

Hiermit versichere ich, dass ich die vorliegende Dissertation selbstständig angefertigt und keine anderen als die angegebenen Quellen und Hilfsmittel verwendet habe. Alle wörtlichen und paraphrasierten Zitate wurden angemessen kenntlich gemacht. Die Arbeit hat bisher noch nicht zu Prüfungszwecken gedient.

Darmstadt, den 06. Dezember 2019

(Peter Thomas Jahn)

Abstract

Two of the most challenging problems in modern physics are the origin of dark matter and the strong *CP* problem. The latter means the non-observation of the violation of the combined particle-antiparticle and parity (*CP*) symmetries by the strong interaction which is conceptually allowed. Both problems – although *prima facie* disparate – could be simultaneously solved by the Peccei-Quinn mechanism. This results in a new particle, the axion. Despite strong experimental efforts, the discovery of the axion is yet to come, making precise theoretical predictions of its properties, especially its mass, highly valuable. The axion's properties are closely related to the topological structure of the vacuum of quantum chromodynamics (QCD). The QCD vacuum exhibits topologically non-trivial fluctuations of the gauge fields with the most important fluctuations being instantons. These topological fluctuations are quantified by the topological susceptibility χ_{top} that controls the axion mass and therefore is – especially at high temperatures – an important input for axion cosmology. Since topological effects are inherently non-perturbative, lattice QCD is particularly suitable for precisely determining χ_{top}. However, lattice simulations become extremely challenging at high temperatures because χ_{top} is very suppressed. In this work, we develop and establish a novel method based on a combination of gradient flow and reweighting that artificially enhances the number of instantons and therefore allows to determine χ_{top} at high temperatures. For computational simplicity, we content ourselves to pure SU(3) Yang-Mills theory for developing the method, but it is explicitly designed to be applicable also in full QCD. In particular, we provide a discretization of the instanton that allows for an analysis of the lattice-spacing effects on a lattice study of χ_{top}. We then present the reweighting method that is eventually used to determine χ_{top} up to 2 GeV in pure SU(3) Yang-Mills theory which constitutes the first direct determination of χ_{top} at such high temperatures.

Zusammenfassung

Zwei der spannendsten Probleme der modernen Physik sind der Ursprung der dunklen Materie und das starke *CP*-Problem. Letzteres beschreibt die Nichtbeobachtung einer Verletzung der kombinierten Teilchen-Antiteilchen- und Parität (*CP*)-Symmetrien durch die starke Wechselwirkung, die grundsätzlich erlaubt ist. Beide Probleme – obwohl a priori unterschiedlich – könnten gleichzeitig durch den Peccei-Quinn-Mechanismus gelöst werden. Dieser postuliert das Axion als neues Elementarteilchen. Trotz starker experimenteller Bemühungen steht die Entdeckung des Axions noch aus, sodass präzise theoretische Vorhersagen über dessen Eigenschaften, insbesondere dessen Masse, sehr wertvoll sind. Die Axioneigenschaften sind eng mit der topologischen Struktur des Vakuums der Quantenchromodynamik (QCD) verknüpft. Das QCD-Vakuum weist topologisch nichttriviale Fluktuationen der Eichfelder auf, quantifiziert durch die topologische Suszeptibilität χ_{top}, welche die Axionenmasse kontrolliert und daher – insbesondere bei hohen Temperaturen – ein wichtiger Parameter für die Axionkosmologie ist. Die wichtigsten Fluktuationen sind dabei Instantone. Da topologische Effekte intrinsisch nichtperturbativ sind, eignen sich Gittersimulationen besonders gut zur präzisen Bestimmung von χ_{top}. Diese werden jedoch bei hohen Temperaturen sehr anspruchsvoll, da χ_{top} stark unterdrückt ist. In dieser Arbeit stellen wir eine neue Methode vor, basierend auf einer Kombination aus Gradientenfluss und Regewichtung, die die Anzahl der Instantone künstlich erhöht und es daher ermöglicht, χ_{top} bei hohen Temperaturen zu bestimmen. Zur Entwicklung der Methode beschränken wir uns auf SU(3) Yang-Mills-Theorie, was numerisch deutlich günstiger ist. Die Methode ist jedoch so konzipiert, dass sie auch auf volle QCD angewandt werden kann. Insbesondere entwickeln wir eine Diskretisierung des Instantons, was eine Analyse der Diskretisierungseffekte bei eine Gitterberechnung von χ_{top} ermöglicht. Weitherin stellen wir die Regewichtungs-Methode vor, die schließlich verwendet wird, um χ_{top} bis zu Temperaturen von 2 GeV in reiner SU(3) Yang-Mills-Theorie zu bestimmen, was die erste direkte Bestimmung von χ_{top} bei solch hohen Temperaturen darstellt.

Contents

Chapter 1

Introduction

Everything that surrounds us, including ourselves, is obviously made up of *matter*, i.e., of atoms that bind together to form solid states, organic tissues, etcetera. Surprisingly, from cosmological observations, there is strong experimental evidence that a vast majority of our Universe actually does not comprise ordinary hadronic matter but rather the more exotic and not yet directly observed *dark matter* and *dark energy*. In fact, only about five percent of the Universe is made up of atoms as indicated in Fig. 1.1. Dark energy is made necessary to explain the observation that the expansion of the Universe is accelerating [1,2]. Of particular interest in this work is dark matter. Its existence is necessary to explain a plethora of different experimental observations like galaxy rotation curves [3], the Bullet Cluster [4], gravitational lensing [5], or the cosmic microwave background [6]. Although dark matter seems to gravitationally make up a dominant part of galaxies, it has not been directly detected. We therefore know that it has to be *dark*, i.e., it only very weakly (if at all) interacts via the electromagnetic interaction. In particular, it cannot have any electrical charge and is therefore invisible to standard detection techniques. We also know that dark matter needs to be *cold*, i.e., it propagates with highly non-relativistic velocities [7], and that it is *matter*, i.e., it clumps gravitationally. The origin of dark matter is one of the greatest mysteries of modern physics.

An at first glance unrelated unsolved problem in modern physics is the so-called *strong* CP *problem*. *CP* symmetry is the product of charge conjugation (*C*), i.e., replacing a particle with its anti particle, and parity (*P*), i.e., creating a "mirror image" of the Universe by inverting all spatial coordinates. In a *CP*-symmetric theory it should therefore be indistinguishable if a particle moves in the "real world" or its anti particle moves in a "mirror world." There is no reason for the fundamental theory of the strong interaction between quarks and gluons, quantum chromodynamics (QCD), to be *CP* symmetric. However, in nature there is no evidence for *CP* violation of the strong interaction at all.

In this work, we delve into the connection of both problems via the so-called *axion* and provide a step towards the theoretical understanding of its properties. This chapter serves to embed this work into its physical context. We briefly introduce the reader to the Standard Model of particle physics and the theory of general relativity that are needed to understand dark matter and the strong *CP* problem. We then present the Peccei-Quinn mechanism that may solve both problems at once by introducing the axion as a new particle. The connection of the axion's properties with the topology of the QCD vacuum is discussed subsequently. We conclude this chapter by giving an overview of the remainder of this thesis.

The Standard Model of Particle Physics

At the beginning of the 20th century, atoms were believed to be the most fundamental particles matter is made of. Nowadays, however, we know that atoms are not fundamental but consist of electrons and nucleons, and the latter further feature a substructure of quarks and gluons which are now believed to be the most fundamental objects. Besides quarks, gluons, and electrons, a whole "zoo" of further particles was found, including neutrinos, muons, the W and Z bosons, and bound states of quarks and gluons called hadrons. Our current knowledge of elementary particles is described by the *Standard Model of particle physics* (SM). This theory encompasses three of the four fundamental interactions, namely the

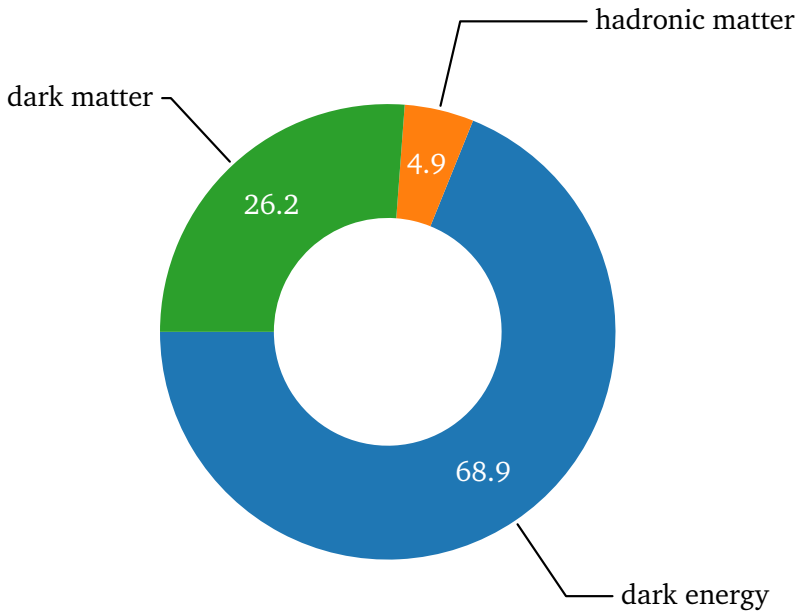

Figure 1.1.: Energy content (in percent) of our Universe based on the experimental results of the 2018 Planck mission [8, 9].

strong, the weak, and the electromagnetic interactions,[1] in terms of relativistic quantum field theories and classifies all known elementary particles.

The SM is experimentally extremely well confirmed. In the electroweak sector, the discovery of the Higgs boson at the large hadron collider at CERN, Geneva, in 2012 [11, 12] almost 50 years after its prediction [13–15] belongs to the greatest successes of the SM. Also the theoretical calculation of the electron g factor agrees to over ten significant digits with the experimental result, making it one of the predictions that are verified with the highest accuracy in the history of physics [16]. In the strong sector, the Nobel-prize awarded development of deep inelastic scattering that led to the experimental discovery of the quarks as well as the discovery of gluons and all predicted hadrons belong to the greatest successes of the SM. However, the SM cannot be the end of the story since it does not include gravity and does not explain some phenomena like neutrino oscillations, baryon asymmetry, the existence of dark matter, or the strong *CP* problem. For a detailed introduction to the SM, we refer to Ref. [17].

General Relativity and Dark Matter

The fourth fundamental interaction that is not part of the SM is gravity. Its state-of-the-art description is the theory of general relativity (GR), introduced by Einstein in 1915 as a geometrical theory of gravity where the spacetime is curved by matter and other forms of energy [18]. The curvature and dynamics of spacetime are described by the Einstein field equations. GR is extremely successful in, e.g., describing the behavior of massive astrophysical objects and is experimentally very well confirmed. The classical tests of GR, proposed by Einstein, are the perihelion precession of planet orbits, the curvature of light rays, and the gravitational redshift and time dilatation. One of the greatest successes of GR was the Nobel prize-awarded recent discovery of gravitational waves more than 100 years after their prediction by the LIGO and VIRGO collaborations [19]. This started a whole new era of multi-messenger astronomy, i.e., the observation of different astronomical signals from the same event. Those signals encompass gravitational waves, electromagnetic radiation, cosmic rays, and neutrinos. Since the different signals are created in disparate processes, they reveal different aspects of the source. It is expected that this will also deliver heavy impact on non-cosmological observables and, e.g., yield strong constraints of the

[1] Note that the weak and the electromagnetic interactions are unified at the electroweak scale $v \approx 246\,\text{GeV}$ [10] and emerge from the *electroweak interaction*.

equation of state of strongly interacting matter [20]. GR further lays the basis of modern cosmology. Such being the case, the experimental evidence for dark matter mentioned above is based on GR. As a consequence, the necessity of dark matter could be surrogated by assuming that GR is not the correct description of gravity. However, due to the overwhelming confirmations of GR, we see no reason to doubt the existence of dark matter and shall now discuss possible candidates. For a more detailed introduction into GR, cosmology, and dark matter, we refer to the review in Ref. [21] and standard textbooks [22–25].

In recent years, many candidates for dark matter have been proposed. One suggestion was to consider large astrophysical objects that consist of baryonic matter such as primordial black holes or dark neutron stars to account for dark matter. These objects are called *massive compact halo objects* (MACHOs). However, MACHOs seem to be experimentally ruled out to account for dark matter as the number of these objects is significantly too small [26, 27]. This also indicates that dark matter needs to be non-baryonic because other forms of baryonic matter are expected to be too bright. The evident SM candidate for dark matter is then the neutrino. However, because of their extremely small mass, neutrinos are highly relativistic and could hence only contribute to hot dark matter. This suggests that particles beyond the SM are needed to explain dark matter. There are two particularly promising beyond-SM candidates for dark matter. The first family of candidates are *weakly interacting massive particles* (WIMPs).[2] WIMPs are hypothetical particles with masses in the range from 10 GeV to a few TeV. One of the most promising WIMPs is the neutralino. For a review, we refer to Ref. [28]. The second beyond-SM candidate for dark matter is the *QCD axion*. This particle is a particularly promising dark matter candidate because it could not only explain the observed dark matter in our Universe but also solve the strong *CP* problem and therefore is a nice interplay between particle physics and cosmology. The role of the axion is discussed in detail subsequently, starting with the strong *CP* problem.

The Strong *CP* Problem

The strong interaction is in the SM described by a relativistic quantum field theory called quantum chromodynamics (QCD). The action of this theory contains all renormalizable, Poincaré invariant, and gauge invariant dimension-four operators that can be built out of quark and gluon fields. This being the case, it also contains the so-called *theta term*

$$S_\theta = \theta Q\,, \tag{1.1}$$

where the integer Q is the so-called *topological charge* and θ is a constant parameter. This term is a result of the complex topological structure of the QCD vacuum. The vacuum of QCD comprises infinitely many topologically distinct classical vacua that are connected via quantum tunneling described by so-called *instantons*, i.e., fields with non-zero topological charge. For an extensive introduction to QCD and its topological properties, we refer to Chap. 2. Since the theta term can be rewritten in terms of the chromo-electric and chromo-magnetic fields via $S_\theta \propto \vec{E}\cdot\vec{B}$, it breaks the combined charge-conjugation C (i.e., replacing a particle with its antiparticle) and parity P (i.e., reversing all spatial coordinates) symmetry.[3] In nature, however, the strong interaction was never observed to break *CP* symmetry. This would manifest in, e.g., a non-vanishing dipole moment of the neutron [29]

$$d_\mathrm{n} = -1.52(71)\times 10^{-16}\,\mathrm{e\,cm}\cdot\theta \tag{1.2}$$

if θ were non-zero (e is the electrical charge of the electron). In fact, experimental measurements of the neutron's dipole moment [30, 31] give an upper bound of

$$|d_\mathrm{n}| < 3.0\times 10^{-26}\,\mathrm{e\,cm} \tag{1.3}$$

[2] Note that the term "weakly" in this context refers to the strength of the interactions and not to the weak interaction.
[3] Note that the electric field is a vector while the magnetic field is an axial vector.

and therefore constrain θ to be

$$|\theta| \lesssim 1.97 \times 10^{-10} \tag{1.4}$$

which is consistent with zero and shows that no *CP* violation has yet been observed. The question of why θ is so small and no *CP* violation was ever observed in QCD is called the *strong* CP *problem* and is still an unsolved problem in physics. Note that this small value of θ is perfectly allowed. However, there is no reason for θ to be small because *CP* does not seem to be a fundamental symmetry as it is broken by the weak interaction. This is a so-called *fine-tuning problem*. In general, fine tuning means that a free parameter of a physics model needs to obtain a very precise value to describe certain observations. This is considered to be conceptually problematic if there is no mechanism that explains the precise value of the parameter.[4] We now discuss a possible mechanism that explains that the theta parameter of QCD vanishes.

The Peccei-Quinn Mechanism and the Axion

In 1977, Roberto Peccei and Helen Quinn proposed a solution to the strong *CP* problem by introducing an additional global $\mathrm{U}(1)_{\mathrm{PQ}}$ symmetry that is spontaneously broken by a scalar field [33, 34]. Weinberg and Wilczek soon realized that this requires the existence of a new light pseudo-scalar particle that was called *axion*[5] [36, 37]. In 1983, it was then realized that this particle could play the role of dark matter in the Universe [38–40]. For detailed reviews on axions and their cosmological role, we refer to Refs. [41–45]. Despite strong experimental efforts, however, axions have not yet been detected. For a review on the experimental status of axion searches, we refer to Ref. [46]. Theoretical investigations of the axion's properties are therefore highly valuable and could help the experimentalists.

The Peccei-Quinn mechanism for solving the strong *CP* problem works by proposing an additional global symmetry $\mathrm{U}(1)_{\mathrm{PQ}}$ that is spontaneously broken by a complex scalar field ϕ. The effective potential of this field may be written as [43]

$$V = \frac{\lambda}{2}\left(|\phi|^2 - \frac{f_{\mathrm{a}}^2}{2}\right)^2 + \frac{\lambda}{3}T^2|\phi|^2, \tag{1.5}$$

where f_{a} denotes the scale at which the symmetry is spontaneously broken and λ is a coupling. The form of the minimum of this potential depends on the temperature. In the following, we describe how the form of this minimum may have evolved during the cosmic evolution, where the Universe started out very hot and then cooled down due to its expansion. At high temperatures $T \gg T_{\mathrm{c}}^{\mathrm{PQ}} \equiv \sqrt{3} f_{\mathrm{a}}$, the effective potential has a unique minimum at $\phi = 0$ (cf. left panel of Fig. 1.2). In this case, both the Lagrangian and the ground state obey the $\mathrm{U}(1)_{\mathrm{PQ}}$ symmetry. As the temperature decreases, the minimum at $\phi = 0$ becomes unstable as soon as $T < T_{\mathrm{c}}^{\mathrm{PQ}}$. The potential then is of the "Mexican-hat" form and the minimum builds a circle with radius $|\phi| = f_{\mathrm{a}}/\sqrt{2}$ (cf. middle panel of Fig. 1.2). Since the true vacuum is now realized by a specific choice on this circle, the ground state is no longer $\mathrm{U}(1)_{\mathrm{PQ}}$ invariant. The symmetry is said to be spontaneously broken. The consequence of the spontaneous breakdown of a symmetry is the existence of a massless mode, a so-called Nambu-Goldstone boson [47–49]. In the case of the spontaneous breakdown of $\mathrm{U}(1)_{\mathrm{PQ}}$, this massless boson is the axion a which is the azimuthal excitation and may be written as

$$\phi = \frac{1}{\sqrt{2}}|\phi| \mathrm{e}^{\mathrm{i}a/f_{\mathrm{a}}}. \tag{1.6}$$

[4] The (heuristic) principle that fundamental theories should not be fine-tuned is called *naturalness*, see, e.g., Ref. [32].

[5] Actually, Wilczek "called this particle the *axion*, after the laundry detergent, because that was a nice catchy name that sounded like a particle and because this particular particle solved a problem involving *axial* currents." [35]

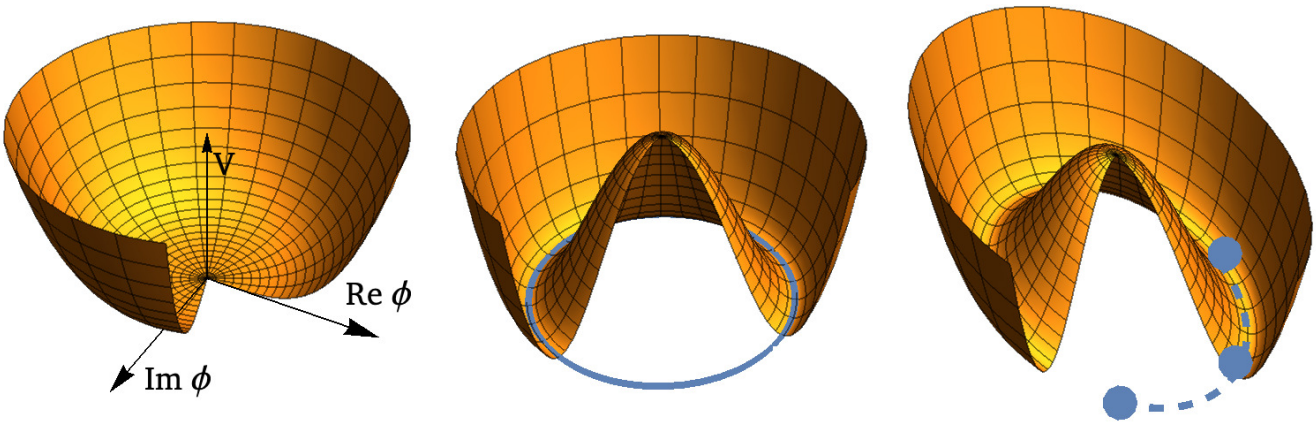

Figure 1.2.: Sketch of the axion potential for different temperatures during the cosmic evolution of the Universe. Left: $T \gg T_c^{PQ}$. The potential has a unique minimum and $U(1)_{PQ}$ symmetry is exact. Middle: $T < T_c^{PQ}$. The potential is of the "Mexican-hat" form. Its minimum is an infinitely degenerate ring and choosing a specific value on this ring spontaneously breaks $U(1)_{PQ}$. Right: $T \lesssim \Lambda_{QCD}$. Non-perturbative topological effects of QCD explicitly break $U(1)_{PQ}$ what causes a tilt of the Mexican-hat potential. The axion field starts oscillating around the unique minimum.

As an azimuthal excitation, the massless axion has a shift symmetry $a \to a + \xi$. When the temperature further decreases, at the order of the QCD scale $T \sim \Lambda_{QCD} = 341(12)\,\text{MeV}$ [50], non-perturbative topological effects of QCD explicitly break the $U(1)_{PQ}$ symmetry. This "tilts" the Mexican-hat potential and thus breaks the continuous shift symmetry of the axion down to a discrete shift symmetry $a \to a + 2\pi n f_a$, $n \in \mathbb{Z}$. The potential therefore now has a unique minimum, cf. right panel of Fig. 1.2.

To ensure the invariance of the QCD action under the $U(1)_{PQ}$ and hence the shift symmetry of the axion field, the QCD action needs to be modified to be

$$S = S_{QCD} + \theta Q - \frac{1}{2}\int \mathrm{d}^4x\,(\partial^\mu a)\big(\partial_\mu a\big) + S_{int}(\partial_\mu a, \Psi) + \frac{a}{f_a}Q\,, \tag{1.7}$$

where S_{QCD} is the "standard" QCD action without theta term, S_{int} denotes all derivatively coupled axion interactions with other fields Ψ, and $\frac{1}{2}\int \mathrm{d}^4x\,(\partial^\mu a)\big(\partial_\mu a\big)$ is the axion kinetic energy. The axion's coupling to gluons $\frac{a}{f_a}Q$ is not invariant under the shift symmetry and causes the explicit breaking of $U(1)_{PQ}$ due to non-perturbative topological QCD effects. Note that as a consequence the theta term is effectively replaced by $(\theta + a/f_a)Q$. This coupling term also induces an effective potential for the axion with minimum [41]

$$\left\langle \frac{\partial V_{eff}}{\partial a} \right\rangle = -\frac{1}{f_a}\langle Q\rangle = 0 \qquad \text{for} \qquad \langle a\rangle = -\theta f_a\,. \tag{1.8}$$

Consequently, as soon as the axion field reaches its vacuum expectation value, the theta term and thus the *CP* violation is canceled out and the strong *CP* problem is dynamically solved without the necessity of fine-tuning. In the following, we rewrite the scalar field $a \to a - \langle a\rangle = a - \theta f_a$ with the deviation of its vacuum expectation value.

We now consider the effective potential of the axion in more detail. Due to the remaining discrete shift symmetry, the axion potential needs to be $2\pi f_a$ periodic. At high temperatures, conventional perturba-

tion theory works. In this framework, a calculation in the so-called *dilute instanton gas approximation* (DIGA) predicts the axion potential (cf. Sec. 2.4.4 for more details)

$$V_\mathrm{a} = m_\mathrm{a}^2 f_\mathrm{a}^2 \left(1 - \cos\left(\frac{a}{f_\mathrm{a}}\right)\right). \tag{1.9}$$

Note that a consequence of the explicit symmetry breaking is that the axion is not massless any more, but becomes a massive pseudo-Nambu-Goldstone boson with a mass

$$m_\mathrm{a}^2 \equiv \left\langle \frac{\partial^2 V_\mathrm{a}}{\partial a^2} \right\rangle. \tag{1.10}$$

The Topological Susceptibility

In QCD, the axion mass is highly temperature-sensitive, depending on how strongly the potential is tilted by non-perturbative topological effects at a given temperature. The temperature dependence is hence given by the *topological susceptibility*

$$m_\mathrm{a}^2(T) f_\mathrm{a}^2 \equiv \chi_\mathrm{top}(T), \qquad \chi_\mathrm{top}(T) \equiv \lim_{V\to\infty} \frac{\langle Q^2 \rangle}{V} \tag{1.11}$$

that describes the fluctuations of the topological charge. For a detailed discussion on the role of topology in QCD, we refer to Sec. 2.4. A theoretical prediction of the axion mass and also its thermal production in the early Universe, therefore, requires the calculation of the topological susceptibility in a temperature range between 550 MeV and 1150 MeV as investigated in Ref. [51]. The upper bound corresponds to roughly $7\,T_\mathrm{c}$, where $T_\mathrm{c} = 156.5(15)\,\mathrm{MeV}$ [52] is the confinement-deconfinement crossover temperature of QCD. Our current knowledge of the temperature dependence of the topological susceptibility is sketched in Fig. 1.3. At zero temperature, effective field theories for describing the low-energy part of QCD like chiral perturbation theory work and the susceptibility is known to high precision [53, 54]:

$$\chi_\mathrm{top}^{1/4}(0) = 75.44(34)\,\mathrm{MeV}, \qquad m_\mathrm{a}(0) = 5.691(51)\,\mu\mathrm{eV}\,\frac{10^{12}\,\mathrm{GeV}}{f_\mathrm{a}}. \tag{1.12}$$

Cosmological observations bound the PQ symmetry breaking scale to $10^9\,\mathrm{GeV} \lesssim f_\mathrm{a} \lesssim 10^{17}\,\mathrm{GeV}$ [42] which in turn bounds the axion mass to $6\times10^{-11}\,\mathrm{eV} \lesssim m_\mathrm{a} \lesssim 6\times10^{-3}\,\mathrm{eV}$. In fact, in a recent study, the axion mass was predicted to be $m_\mathrm{a} = 26.2(34)\,\mu\mathrm{eV}$ [55] using the high-temperature lattice determination of the topological susceptibility from Ref. [56]. The aim of this work is to develop a novel method for determining the topological susceptibility that is capable to confront these results.

At very high temperatures, conventional perturbation theory works. A DIGA calculation predicts the temperature dependence of the susceptibility at leading order to be (cf. Sec. 2.4.4 for more details)

$$\chi_\mathrm{top}(T) \propto T^b, \qquad b = -7 - N_\mathrm{f}/3, \tag{1.13}$$

where N_f is the number of quark flavors that are active at the corresponding temperature. Consequently, for pure SU(3) Yang-Mills theory we expect $b = -7$ and for full QCD in the interesting temperature regime $b = -8$. However, the exponent is known only approximately since the DIGA calculations are only valid at extremely high temperatures, much higher than the temperatures relevant for axion cosmology. Also, quantum fluctuations and electrical screening may change this result [51, 53].

To see how sensitive the axion's properties are to a precise determination of the topological susceptibility, we consider the thermal production of axions in the early Universe via the *misalignment mechanism* [38–40]. As soon as the temperature reaches the QCD scale, PQ symmetry is explicitly broken

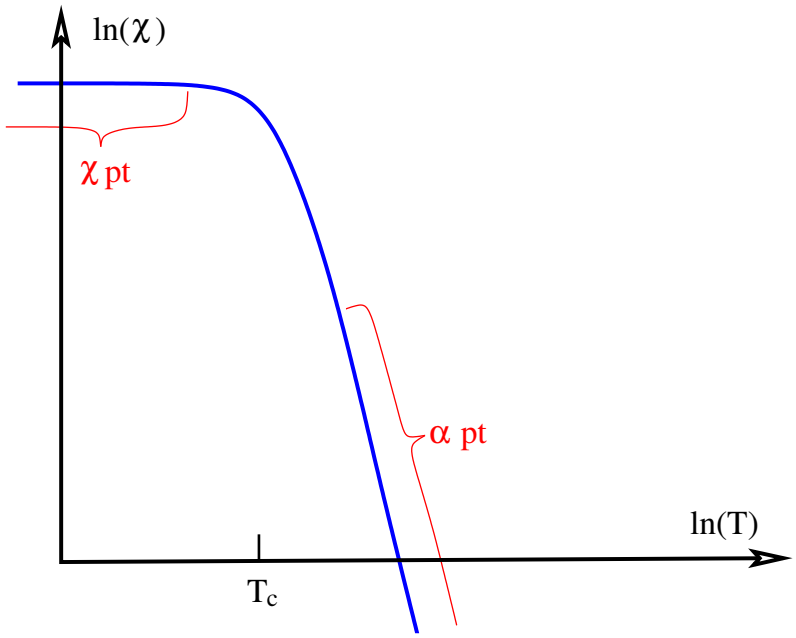

Figure 1.3.: Sketch of our current knowledge of the temperature dependence of the QCD topological susceptibility. At small temperatures, chiral perturbation theory works and the susceptibility is known to high accuracy. While at small temperatures the susceptibility is rather constant, at high temperatures it rapidly decreases. At very high temperatures, ordinary perturbation theory works and predicts a power-law behavior $\chi_{\text{top}} \propto T^{-7-N_f/3}$, but in the temperature range relevant for axion cosmology the susceptibility is known only approximately. Image taken from Ref. [51].

and the axion potential gets tilted. Consequently, the axion field that initially had an arbitrary value on the vacuum manifold starts oscillating around the true minimum of the potential. This evolution of the axion field is described by the equation of motion

$$\ddot{a}(t) + 3H(t)\,\dot{a}(t) + m_a^2(t)\sin(a(t)) = 0\,, \tag{1.14}$$

where $H(t)$ is the Hubble parameter that describes the rate of the expansion of the Universe and $m_a^2(t) = \chi_{\text{top}}(t)/f_a^2$. This equation can be numerically solved as a function of temperature, starting at $T = 3\,\text{GeV}$ for decreasing temperatures. Since we expect the axion to be massless at high temperatures, we have the initial conditions $\dot{a}(3\,\text{GeV}) = 0$ and a random initial value $a(3\,\text{GeV}) \equiv a_0 \in [-\pi\,, \pi]$. For more details on the calculation and how to rewrite the equation of motion in terms of temperature, we refer to Ref. [44] and the supplementary information of Ref. [56]. The result of the axion field as a function of temperature is shown in Fig. 1.4 for different values of the exponent b. It shows that the temperature at which the axion starts oscillating and therefore gets massive crucially depends on the temperature dependence of the topological susceptibility. Also the mass, i.e., the frequency of the oscillations, strongly depends on a precise determination of the temperature dependence of the topological susceptibility.

A precise determination of the topological susceptibility from first principles at high temperatures would, therefore, be very valuable. In the last years, there was a lot of progress in determining the susceptibility from lattice QCD [56–63]. However, most of those studies are in the pure-glue approximation or do not reach the required high temperatures. In fact, the smallness of the topological susceptibility makes it very difficult to determine it on the lattice since virtually no configuration will have a non-zero topological charge. Only the study of Ref. [56] reached temperatures of 1.5 GeV; however, they did not

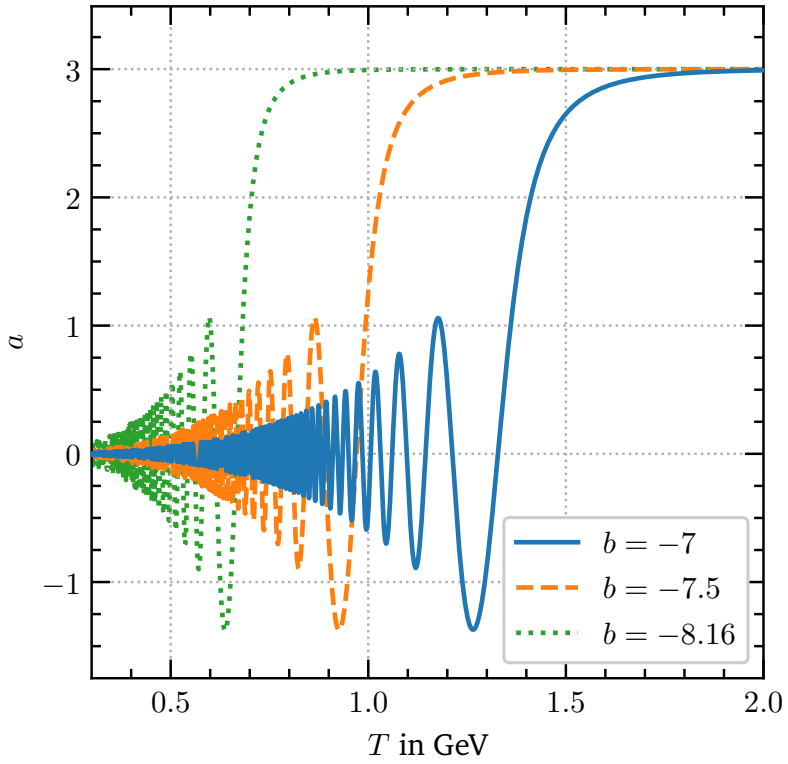

Figure 1.4.: Axion field as a function of temperature from solving the equation of motion (1.14) of the misalignment mechanism for $a_0 = 3$ and different temperature dependences of the topological susceptibility. The value $b = -8.16$ is the result of a lattice determination in Ref. [56].

determine the susceptibility directly at a given high temperature, but started at a low temperature and differentially worked up to high temperatures.

Aim of this Work

This work aims to develop and establish a new method based on lattice QCD that allows a direct determination of the topological susceptibility up to temperatures of 1.15 GeV. The main purpose of this work is in this respect not to give a final answer to the temperature dependence of the susceptibility in full QCD, but rather to develop and test the method. The basic idea of our method is to artificially enhance the number of instantons that are very rare at high temperatures. This method is called *reweighting* and allows for a statistically powerful sampling of topological effects. For simplicity, we constrain ourselves to the case of pure Yang-Mills theory which is computationally less involved. However, we design our method such that it can then be extended to a full QCD setup. But this will be the subject of future work.

Using this method, we precisely determined the topological susceptibility of pure SU(3) Yang-Mills theory up to $7\,T_c$. This is the first direct determination of the susceptibility at such high temperatures. This temperature is sufficiently high to determine the axion mass. A study of the topological susceptibility in full QCD based on the method presented in this work will therefore be a very promising approach to precisely determine the axion mass and ideally to help experimentalists to eventually detect the axion.

This thesis is organized as follows: Chap. 2 contains an introduction into the theory of the strong interaction, namely quantum chromodynamics, with a focus on its topological properties. We discuss in detail the complex vacuum structure of QCD and introduce instantons and calorons that play an important role in the remainder of this work. We also define the topological susceptibility which is the central quantity in this work. In Chap. 3, we then present the lattice approach to QCD and introduce all quantities and concepts that are needed in the remainder of this work. In particular, we introduce the

concept of gradient flow which is an important tool to define the lattice discretization of the topological charge. In Chap. 4, we present a lattice discretization of topological fields, namely of instantons and calorons. These are then used to determine systematic errors in the determination of the topological susceptibility on the lattice. This chapter is based on work published in Ref. [64]. The lattice method to determine the topological susceptibility based on a reweighting approach is then developed in Chap. 5. Using this method, the topological susceptibility is determined up to $4.1\,T_c$ in pure SU(3) Yang-Mills theory. This chapter is based on work published in Refs. [65, 66]. In Chap. 6, an improvement of the reweighting technique is presented and the topological susceptibility is calculated up to $7\,T_c$ in pure SU(3) Yang-Mills theory. This chapter is based on not yet published work [67]. Chap. 7 contains a concluding discussion of the main results of this thesis and addresses possible further investigations. The units and conventions used in this work are summarized in App. A.

Some parts of this thesis are adopted from the original publications [64–67] without explicit citation. The author of this thesis was involved in all steps of those projects and in writing the final papers.

Chapter 2

Quantum Chromodynamics

Every interaction in nature can be traced back to four fundamental interactions: Gravity, the electromagnetic interaction, the weak interaction, and the strong interaction. The latter three forces can be successfully quantized in form of a relativistic quantum field theory (QFT) and build the basis of the Standard Model (SM) of particle physics. In this work, quantum chromodynamics (QCD), the QFT describing the strong interaction, is of special interest. This chapter serves as a wrap-up of the most important issues and properties of QCD that are relevant for this work. We start with a detailed description of the QCD Lagrangian and then address its path integral formulation within thermal field theory. Chiral symmetry and the chiral anomaly are discussed subsequently. This leads to a conclusive roundup of the role of topology in the QCD vacuum, which builds the basis of the remainder of this work. In particular, the central quantity of this work, namely the topological susceptibility, is introduced in Sec. 2.4.3. For a more thorough and complete introduction to QCD, we refer to the literature [68, 69].

For the units and conventions regarding, e.g., Euclidean and Minkowski spacetime and the γ matrices used in this work, we refer to App. A.

2.1 The QCD Lagrangian

QCD is the relativistic quantum field theory describing the strong interaction between quarks and gluons. In this section, we define the basic ingredients of this theory and then introduce its Lagrangian. The issue of the QCD running coupling that leads to the necessity of non-perturbative approaches for studying low-energy aspects of QCD is discussed subsequently.

Quarks are fundamental massive spin-$1/2$ fermions represented by Dirac fields

$$q_f^{\alpha,c}(x) \qquad \text{and} \qquad \bar{q}_f^{\alpha,c}(x) \equiv \left(q_f^{\alpha,c}(x)\right)^\dagger \gamma_0 \,, \tag{2.1}$$

where $f = 1, \ldots, N_\mathrm{f}$ denotes the (known) quark flavors called *up*, *down*, *strange*, *charm*, *bottom*, and *top*; α is a Dirac index, and c is a color index. The quark flavors differ in their mass (and their electrical charge) as shown in Tab. 2.1. Color is the charge of the strong interaction and therefore the analog to the electrical charge known from the electromagnetic interaction. The $N_\mathrm{c} = 3$ color charges are commonly called *red*, *green*, and *blue*.

A fundamental principle in QCD that is found in nature is that it must be invariant under local rotations in color space, i.e., loosely speaking, under exchanging the color charges. This property is called *gauge invariance* and the corresponding symmetry group SU(N_c) is called the *gauge group* of QCD. The quarks transform under the fundamental representation of SU(3) while the antiquarks transform under the anti-fundamental representation of SU(3). In contrast to quantum electrodynamics (QED), the QFT of the electromagnetic interaction, with its abelian gauge group U(1), SU(3) is non-abelian. This has profound consequences, making QCD a very complicated theory where calculations become much more challenging than, e.g., in QED as discussed below.[1]

Gluons are the massless spin-1 gauge bosons of QCD mediating the strong interaction. They transform under the adjoint representation of SU(3) and are represented by a Lorentz vector $A_\mu^a(x)$, where μ is a

[1] Note that QED is very well accessible via perturbation theory.

Table 2.1.: Masses m of the different quark flavors [10].

	flavor					
	up (u)	down (d)	strange (s)	charm (c)	bottom (b)	top (t)
m	2.2 MeV	4.7 MeV	95 MeV	1.275 GeV	4.18 GeV	173 GeV

Lorentz index and $a = 1, \ldots, N_c^2 - 1 = 8$. Consequently, the gauge field $A_\mu(x)$ can be represented by a 3×3 matrix that is expressed using the generators T_a of SU(3)

$$A_\mu(x) = A_\mu^a(x) T_a \,. \tag{2.2}$$

Note that we work with antihermitian generators that fulfill $[T_a, T_b] = f_{abc} T^c$ with the structure constants f_{abc} throughout this thesis. For more details on our conventions regarding the Lie groups SU(N), we refer to App. A.1. As opposed to the uncharged photons in QED, gluons carry color charges themselves and hence interact with each other.

The QCD Lagrangian comprises all renormalizable, Poincaré invariant, and gauge invariant dimension-four operators that can be built out of quark and gluon fields. Without theta term, it reads[2]

$$\mathcal{L}_{\text{QCD}} = -\frac{1}{4g_s^2} F^a_{\mu\nu} F_a^{\mu\nu} + \bar{q}_f \left(\mathrm{i} \not{D} - m_f \right) q_f \,, \tag{2.3}$$

where g_s is the strong coupling constant, and consists of basically two parts. The first term is the kinetic energy of the gluons, expressed by the *field-strength tensor*

$$F^a_{\mu\nu}(x) = \partial_\mu A^a_\nu(x) - \partial_\nu A^a_\mu(x) + f^a{}_{bc} A^b_\mu(x) A^c_\nu(x) \,. \tag{2.4}$$

Hereby, the third term of the field-strength tensor results from the commutator of gauge fields and is therefore a consequence of the non-commutativity of SU(3). The second term of the QCD Lagrangian (2.3) contains the interactions of quarks and gluons. This is introduced via the gauge principle as the minimal coupling term

$$D_\mu \equiv \partial_\mu + \mathrm{i} A_\mu \tag{2.5}$$

and we used the Feynman slash notation $\not{D} \equiv D_\mu \gamma^\mu$.

One central issue of QCD is its so-called *running coupling*, i.e., the energy dependence of the coupling constant. While the running of the coupling of QED is rather mild at typical energy scales, the QCD coupling strongly depends on the energy scale as depicted in Fig. 2.1. To one-loop order, the energy dependence of the coupling is given by (up to two-loop order this result is independent of the renormalization scheme) [70, 71]

$$\alpha_s(Q^2) \equiv \frac{g_s^2(Q^2)}{4\pi} = \frac{4\pi}{\left(11 - \frac{2}{3} N_f\right) \ln\left(Q^2 / \Lambda^2_{\text{QCD}}\right)} \,. \tag{2.6}$$

It is very peculiar that, for $N_f = 6$ which is realized in nature, α_s decreases with increasing energy, giving rise to two interesting limits. At very high energies or equivalently small distances, the coupling constant is small and asymptotically vanishes at vanishing distances. This phenomenon is called *asymptotic freedom* because two quarks behave asymptotically as free particles. The discovery of this

[2] The theta term is discussed in detail in Sec. 2.4.2.

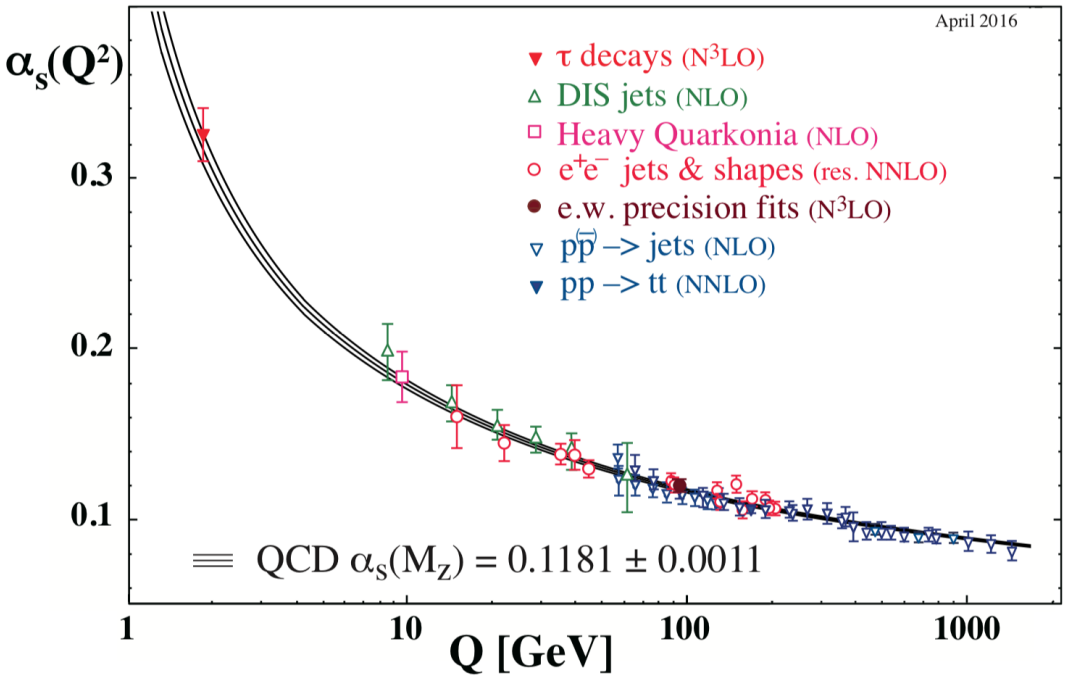

Figure 2.1.: Comparison of experimental values and theoretical predictions of the QCD coupling constant α_s as a function of momentum transfer Q. The coupling is small at high energies (asymptotic freedom) and diverges for small energies (confinement). Image taken from Ref. [10].

phenomenon [70, 71] was awarded the 2004 Nobel prize to Gross, Wilczek, and Politzer. Since in this regime the coupling constant is small, perturbation theory can be applied.

At low energies, i.e., large distances, on the other hand, the coupling constant becomes very large and eventually diverges at the scale $\Lambda_{\mathrm{QCD}} = 341(12)\,\mathrm{MeV}$ [50]. As a consequence, the separation of two quarks yields an increase in energy that is sufficient to create new quark-antiquark pairs. This is a consequence of *confinement* which is the phenomenon that at low energies only color-neutral objects are observed. Those color-neutral objects are called *hadrons* and are divided into the bosonic *mesons* that – in the simplest case – consist of a quark and an antiquark (where color and anticolor form a color-neutral state) and the fermionic *baryons* that – in the simplest case – consist of three quarks with all different colors.[3] The mechanism of confinement is yet not fully understood theoretically and the subject of current research (see, e.g., Ref. [72] for a review).

As a consequence, non-perturbative approaches are needed to study low-energy QCD. Examples of non-perturbative approaches are *effective field theories*, the *anti-de Sitter/conformal field theory (AdS/CFT) correspondence*, the *functional renormalization group (FRG)*, and *lattice QCD*. The idea of effective field theories like, e.g., *chiral perturbation theory* (χPT) is that at low energies, quarks and gluons are not resolved as the fundamental degrees of freedom but rather hadrons are the effective degrees of freedom. The quarks and gluons are hence integrated out, while the symmetries of the theory like chiral symmetry are taken into account. χPT is nowadays a standard approach to nuclear forces at low energies [73, 74]. The AdS/CFT correspondence allows the formulation of a strongly-coupled conformal field theory in terms of a weakly-coupled theory of gravity in an anti-de Sitter spacetime [75]. Due to the weak coupling, the problem may be solved there perturbatively and can then be translated back to the conformal field theory. This method was successful in, for instance, predicting a lower bound of the QCD shear viscosity [76, 77]. The FRG is an implementation of Wilson's renormalization group approach that interpolates between the full quantized microscopic theory, expressed by the effective average action, and

[3] The fact that the combination of red, green, and blue gives a color-neutral ("white") state refers to additive color mixing and is actually the reason why the strong charges are named after colors and also explains the name quantum *chromo*dynamics.

the classical macroscopic theory, described by the classical action. This is done by solving a set of exact differential equations. In solving those equations, however, truncations need to be introduced. The FRG approach is particularly successful in studying critical phenomena and phase transitions by investigating simpler effective models that belong to the same universality class as the actual system of interest. This led, e.g., to some qualitative insight to the phase diagram of QCD, cf. Sec. 2.3. In lattice QCD, the theory is discretized on a spacetime grid and the QCD path integral is evaluated numerically. This approach is very successful at vanishing chemical potential and leads to precise theoretical determinations of, e.g., hadron masses. Unlike FRG and AdS/CFT, lattice QCD is a systematically improvable approach that is grounded on the fundamental theory; unlike χPT, it is applicable at all temperatures and energy scales. Therefore, we use this approach in the remainder of this work and describe the method in detail in Chap. 3.

2.2 Path Integral Formalism and Thermal Field Theory

At his point, we have introduced QCD as a field theory describing quarks and gluons. Since in the remainder of this work we shall mostly consider QCD at high temperatures, we now shortly introduce the basics of thermal field theory and the path-integral formalism. For a more detailed introduction to thermal field theory, we refer to the standard introductory textbooks [78–80]; for an in-depth discussion of the path-integral formalism, we refer to standard QFT textbooks [69, 81].

The basic quantity in quantum statistical mechanics is the *partition function*[4]

$$\mathcal{Z}(T) \equiv \operatorname{tr} \mathrm{e}^{-\beta H}, \qquad \beta \equiv \frac{1}{T}, \tag{2.7}$$

where T is the temperature and β is the standard notation for the inverse temperature. All thermodynamic quantities like entropy, pressure, or susceptibilities are then obtained as derivatives of the free energy

$$\mathcal{F} = -T \ln \mathcal{Z}. \tag{2.8}$$

The thermodynamic partition function (2.7) can also be expressed as a path integral. To derive this expression, we follow Ref. [79] and for simplicity constrain ourselves to standard quantum mechanics. However, the result can directly be extended to quantum field theory. We start with the probability amplitude of a particle to be found at position q' at time t when it was located at position q at time 0

$$P(t, q', q) \equiv \langle q' | \, \mathrm{e}^{-\mathrm{i}t\hat{H}} \, | q \rangle, \qquad \hat{H} \equiv \hat{H}_0(\hat{p}) + \hat{V}(\hat{q}) \equiv \frac{\hat{p}^2}{2m} + \hat{V}(\hat{q}), \tag{2.9}$$

where $\hat{H}$ is the Hamiltonian of the system that is split up into a kinetic term $\hat{H}_0$ and a potential $\hat{V}$. We rewrite this expression by using *Trotter's Lie product formula*

$$\exp(A+B) = \lim_{n\to\infty} \left[\exp(A/n) \exp(B/n) \right]^n \tag{2.10}$$

for two matrices A and B. With this, the transition amplitude can be rewritten as

$$P(t, q', q) = \lim_{n\to\infty} \langle q' | \left(\mathrm{e}^{-\mathrm{i}(t/n)\hat{H}_0} \mathrm{e}^{-\mathrm{i}(t/n)\hat{V}} \right)^n | q \rangle \, . \tag{2.11}$$

[4] For the derivation of the path-integral formulation of the partition function, we constrain ourselves to the canonical ensemble.

Note that this corresponds to discretizing the time dimension to infinitesimally small time slices. We now rename $q' \equiv q_n$ and $q \equiv q_0$ and insert $(n-1)$ completeness relations $\mathbb{1} \equiv \int \mathrm{d}q_i \, |q_i\rangle \langle q_i|$:

$$P(t, q_n, q_0) = \lim_{n\to\infty} \left(\prod_{j=1}^{n-1} \int \mathrm{d}q_j \right) \left(\prod_{i=0}^{n-1} \langle q_{i+1}| \, \mathrm{e}^{-\mathrm{i}(t/n)\hat{H}_0} \mathrm{e}^{-\mathrm{i}(t/n)\hat{V}} \, |q_i\rangle \right). \tag{2.12}$$

Since the potential is diagonal in position space, these matrix elements can easily be evaluated to be

$$\langle q_{i+1}| \, \mathrm{e}^{-\mathrm{i}\epsilon\hat{H}_0} \mathrm{e}^{-\mathrm{i}\epsilon\hat{V}} \, |q_i\rangle = \mathrm{e}^{-\mathrm{i}\epsilon V(q_i)} \langle q_{i+1}| \, \mathrm{e}^{-\mathrm{i}\epsilon\hat{H}_0} \, |q_i\rangle = \sqrt{\frac{m}{2\pi\mathrm{i}\epsilon}} \exp\left[\mathrm{i}\, m \frac{(q_{i+1}-q_i)^2}{2\epsilon} - \mathrm{i}\epsilon V(q_i) \right], \tag{2.13}$$

where we defined $\epsilon \equiv t/n$. With this, the transition amplitude reads

$$P(t, q_n, q_0) = \lim_{n\to\infty} \left(\prod_{i=1}^{n-1} \int \mathrm{d}q_i \right) \left(\frac{mn}{2\pi\mathrm{i}t} \right)^{n/2} \exp\left[\mathrm{i} \left(\frac{m}{2} \sum_{j=0}^{n-1} \epsilon \left(\frac{q_{j+1}-q_j}{\epsilon} \right)^2 - \sum_{j=0}^{n-1} \epsilon V(q_j) \right) \right] \tag{2.14}$$

and if the limit is taken[5]

$$P(t, q', q) \equiv \int_{x(0)=q}^{x(t)=q'} \mathcal{D}x \exp\left[\mathrm{i} \int_0^t \mathrm{d}s \left(\frac{1}{2} m\dot{x}^2(s) - V(x(s)) \right) \right] \equiv \int_{x(0)=q}^{x(t)=q'} \mathcal{D}x \exp\left[\mathrm{i} \int_0^t \mathrm{d}s \, L(x(s)) \right], \tag{2.15}$$

where L is the classical Lagrangian of the system and the path integral integrates over all possible paths starting at q and ending at q'. The integration measure is to be understood as the infinite-dimensional measure

$$\mathcal{D}x \equiv \prod_{x\in\mathbb{R}} \mathrm{d}q(x). \tag{2.16}$$

We now turn to the path integral expression of the thermodynamic partition function (2.7). In position space, the trace is evaluated to be

$$\mathcal{Z}(T) = \int \mathrm{d}q \, \langle q| \, \mathrm{e}^{-\beta H} \, |q\rangle \equiv \int \mathrm{d}q \, P(-\mathrm{i}\beta, q, q) \equiv \int_{x(0)=x(\beta)} \mathcal{D}x \exp\left[-\int_0^\beta \mathrm{d}\tau \, L_\mathrm{E}(x(\tau)) \right], \tag{2.17}$$

where

$$L_\mathrm{E} \equiv -L_\mathrm{M}(\tau = \mathrm{i}t) = \frac{1}{2} m \left(\frac{\mathrm{d}x}{\mathrm{d}\tau} \right)^2 + V(x) \tag{2.18}$$

is the so-called *Euclidean Lagrangian* that is obtained from the usual Lagrangian in Minkowski space by a Wick rotation, i.e., by introducing an imaginary time $\tau = \mathrm{i}t$. Moreover, we see from the finite-temperature partition function (2.17) that the imaginary time is compactified on the interval $[0, \beta]$ and periodicity in $x(\tau)$ is required, i.e., $x(0) = x(\beta)$. Note that this result can be directly transferred to quantum field theory, where bosons obey periodic boundary conditions, while fermions obey antiperiodic

[5] Note that we omitted the normalization constant because it has no physics relevance.

boundary conditions. This path integral contains a summation over all possible "paths" (field configurations) weighted by the classical Euclidean action. In the classical theory, only the path of minimal action is realized. The path-integral formulation, on the other hand, creates quantum fluctuations around this classical path and therefore provides a quantum formulation of the theory.

Let us finally discuss the QCD partition function in the grand-canonical ensemble with finite baryon chemical potential μ in some detail. It is given by[6] [80]

$$\mathcal{Z}_{\mathrm{QCD}} \sim \int \mathcal{D}A\,\mathcal{D}q\,\mathcal{D}\bar{q}\,\exp\left[-\int_0^\beta \mathrm{d}\tau \int \mathrm{d}^3x \left(\mathcal{L}^{\mathrm{E}}_{\mathrm{QCD}}[A,q,\bar{q}] + \bar{q}\big(\mu\gamma^0\big)q\right)\right], \tag{2.19}$$

where the integration measures are to be understood as the infinite-dimensional measures

$$\mathcal{D}A \equiv \prod_{\mu,a}\prod_{x\in\mathbb{R}^4} \mathrm{d}A^a_\mu(x), \qquad \mathcal{D}q \equiv \prod_{f,\alpha,c}\prod_{x\in\mathbb{R}^4} \mathrm{d}q_f^{\alpha,c}(x), \qquad \mathcal{D}\bar{q} \equiv \prod_{f,\alpha,c}\prod_{x\in\mathbb{R}^4} \mathrm{d}\bar{q}_f^{\alpha,c}(x) \tag{2.20}$$

and the Euclidean QCD Lagrangian reads

$$\mathcal{L}^{\mathrm{E}}_{\mathrm{QCD}} = \frac{1}{4g_{\mathrm{s}}^2}F^a_{\mu\nu}F^a_{\mu\nu} + \bar{q}(\not{D}+m)q\,, \qquad \not{D} \equiv \gamma_\mu\big(\partial_\mu + \mathrm{i}A_\mu\big). \tag{2.21}$$

Since the fermionic fields in the path integral are described via anti-commuting Graßmann variables to ensure Fermi statistics, it is convenient to explicitly integrate out the fermionic degrees of freedom:

$$\begin{aligned}
\mathcal{Z}_{\mathrm{QCD}} &\sim \int \mathcal{D}A\,\mathcal{D}q\,\mathcal{D}\bar{q}\,\exp\left[-\int_0^\beta \mathrm{d}\tau \int \mathrm{d}^3x \left(\mathcal{L}^{\mathrm{E}}_{\mathrm{G}}[A] + \bar{q}\big(\not{D}+m+\mu\gamma^0\big)\bar{q}\right)\right] \\
&= \int \mathcal{D}A\,\det\big(\not{D}+m+\mu\gamma^0\big)\exp\big[-S^{\mathrm{E}}_{\mathrm{G}}[A]\big] \\
&= \int \mathcal{D}A\,\exp\big[-S^{\mathrm{E}}_{\mathrm{G}}[A] + \mathrm{tr}\ln\big(\not{D}+m+\mu\gamma^0\big)\big],
\end{aligned} \tag{2.22}$$

where $\mathcal{L}^{\mathrm{E}}_{\mathrm{G}}$ and $S^{\mathrm{E}}_{\mathrm{G}}$ are the gauge parts of the Euclidean Lagrangian and action, respectively. This result has profound consequences. The Dirac operator fulfills γ_5 hermiticity, i.e., $\gamma_5\not{D}\gamma_5 \equiv \not{D}^\dagger$. Consequently,

$$\begin{aligned}
\det\big(\not{D}+m+\mu\gamma^0\big) &= \det\big[\big(\not{D}+m+\mu\gamma^0\big)\gamma_5^2\big] = \det\big[\gamma_5\big(\not{D}+m+\mu\gamma^0\big)\gamma_5\big] = \det\big(\not{D}^\dagger+m-\mu\gamma^0\big) \\
&= \det\big(\not{D}+m-\mu^*\gamma^0\big)^\dagger = \det{}^*\big(\not{D}+m-\mu^*\gamma^0\big).
\end{aligned} \tag{2.23}$$

This shows that the determinant is only real for vanishing or purely imaginary baryon chemical potential [82]. As a consequence, the exponential in the QCD path integral (2.22) is only positive definite for vanishing or purely imaginary baryon chemical potential. This is the infamous sign problem of lattice QCD, cf. Chap. 3.

[6] Note that for the sake of simplicity we explicitly ignored the issues of ghost fields and gauge fixing since these only become important when applying perturbation theory.

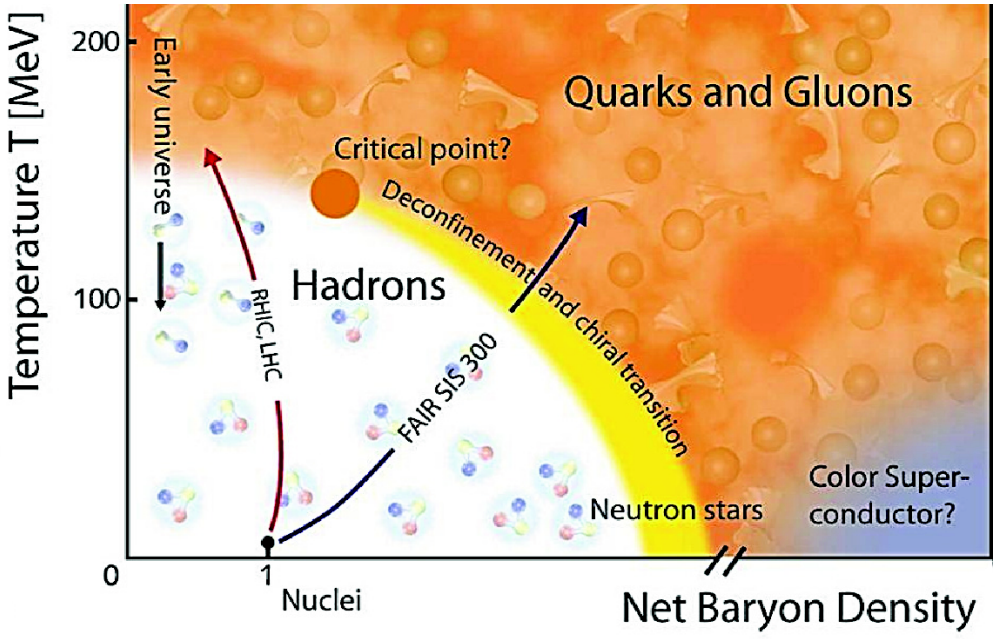

Figure 2.2.: Conjectured phase diagram of strongly interacting matter. At small temperatures and densities, ordinary hadronic matter exists. In this hadronic phase, chiral symmetry is spontaneously broken and confinement prevails. At high temperatures and densities, the strong coupling constant becomes very small and quasi-free quarks and gluons are expected to from a quark-gluon plasma. This phase is characterized by deconfinement and restored, i.e., not spontaneously broken, chiral symmetry. The hadronic and quark-gluon plasma phases are separated by two phase transitions, namely the confinement-deconfinement and the chiral phase transitions. At high densities and low temperatures, more exotic phases like color-superconducting phases may exist. Figure taken from Ref. [83].

2.3 Chiral Symmetry and the Chiral Anomaly

A very natural question to ask is how matter ultimately behaves under extreme conditions, i.e., when it is intensively heated or compressed. At low temperatures and densities, quarks and gluons are confined into hadrons and form the "standard" matter that surrounds us. The behavior of this quark matter at high temperatures and/or densities is the subject of intensive current research. This question is not only academic but is also relevant for understanding, e.g., the early Universe (high temperatures) or the core of neutron stars (high densities). A sketch of the conjectured phase diagram of QCD that shows the different states of strongly interacting matter in a temperature-baryon density diagram is shown in Fig. 2.2. Due to asymptotic freedom, it is expected that at very high temperatures and densities quarks and gluons are deconfined and quasi-free and form a so-called *quark-gluon plasma* (QGP). The hadronic and the QGP phase are separated by a deconfinement phase transition; lattice simulations suggest that this transition is a smooth crossover [84]. Another phase transition that appears in the QCD phase diagram is the *chiral phase transition* that is accompanied by the spontaneous breakdown of *chiral symmetry*. This has profound consequences on the hadron spectrum as discussed in the remainder of this section. It is remarkable that both the deconfinement and the chiral phase transition seem to appear at the same temperature [85]. Experimentally, the QCD phase diagram is probed via heavy-ion collisions at the *Large Hadron Collider* (LHC) at CERN, the *Relativistic Heavy Ion Collider* (RHIC) at Brookhaven National Laboratory, and the prospective *Facility for Antiproton and Ion Research* (FAIR) in Darmstadt. For more details regarding the experimental and theoretical investigations of the QCD phase diagram, we refer to Refs. [86–89].

Let us now address the consequences of chiral symmetry in more detail. Chirality is a Lorentz-invariant notion that is based on the eigenvalues of γ_5 acting on a Dirac field

$$\gamma_5 q = \pm q\,. \tag{2.24}$$

Fields with eigenvalue $+1$ are called *right-handed* and those with eigenvalue -1 are called *left-handed*. In the case of massless fields, chirality coincides with *helicity*, the projection of the spin vector on the momentum vector. A general Dirac field q can be decomposed into a left-handed and a right-handed component

$$q_{\mathrm{L/R}} \equiv \frac{1 \mp \gamma_5}{2} q\,. \tag{2.25}$$

It turns out that in the case of massless quarks,[7] the so-called *chiral limit*, the QCD Lagrangian is invariant under separate local U(3) rotations of the left- and right-handed fields. This so-called chiral symmetry group is denoted as

$$\mathrm{U(3)_L} \times \mathrm{U(3)_R} \simeq \mathrm{SU(3)_L} \times \mathrm{SU(3)_R} \times \mathrm{U(1)_L} \times \mathrm{U(1)_R}\,. \tag{2.26}$$

This group isomorphic to the $\mathrm{SU(3)_V} \times \mathrm{U(1)_V}$ vector symmetry group and the $\mathrm{SU(3)_A} \times \mathrm{U(1)_A}$ axial symmetry transformations.[8]

The QCD ground state spontaneously breaks chiral symmetry down to the vector subgroup $\mathrm{SU(3)_V} \times \mathrm{U(1)_V}$. The symmetry $\mathrm{SU(3)_V}$ is sometimes called the *flavor symmetry* $\mathrm{SU(3)_f}$ and builds the basis of the *eightfold way*, the predecessor of the quark model. Since the broken group $\mathrm{SU(3)_A}$ has eight generators and $\mathrm{U(1)_A}$ has one generator, we expect according to the Goldstone theorem [47–49] the existence of nine massless Nambu-Goldstone bosons in QCD. However, we do not observe any massless states in QCD in vacuum. The solution is that the quarks are actually not massless and the mass term of the Lagrangian explicitly breaks chiral symmetry. But since the light quark masses are very small, chiral symmetry can still be considered as an approximate symmetry and the effects of its explicit breakdown are expected to be small. Instead of massless Nambu-Goldstone bosons, we therefore expect the existence of very light pseudo-Nambu-Goldstone bosons. Indeed, the mesons of the pseudoscalar octet, namely the pions, the kaons, and the η meson, are significantly lighter than the other hadronic states and play the role of the pseudo-Nambu-Goldstone bosons of the spontaneous breakdown of the chiral symmetry of QCD.

However, these are only eight pseudo-Nambu-Goldstone bosons and not the expected nine. The ninth one would be the η' meson whose mass is, though, too large to be explained from chiral symmetry. The reason for this is that the axial symmetry $\mathrm{U(1)_A}$ is admittedly a symmetry of the QCD Lagrangian in the chiral limit; however, it is not a symmetry of the partition function as the measure explicitly breaks it [90] and the correct chiral symmetry is actually $\mathrm{SU(3)_V} \times \mathrm{SU(3)_A} \times \mathrm{U(1)_V}$. A symmetry of the action of a theory that is broken in the full quantum theory, i.e., in the path-integral formulation, is called an *anomaly*; in the case of $\mathrm{U(1)_A}$ it is called *chiral anomaly* (or *axial anomaly*).

The Noether theorem states that every continuous symmetry is accompanied by a conserved current and a conserved charge [91]. In the case of the axial symmetry, the current in the chiral limit reads

$$j^5_\mu = \bar{q}\gamma_\mu\gamma_5 q\,. \tag{2.27}$$

[7] Since the up, down, and strange quarks are significantly lighter than the heavy quarks (cf. Tab. 2.1), we consider only three-flavor QCD in the remainder of this discussion. This is justified because $m_{\mathrm{c,b,t}} \gg \Lambda_{\mathrm{QCD}}$.

[8] Note that, strictly speaking, $\mathrm{SU(3)_A}$ is not a group as it is not closed. The combination $\mathrm{SU(3)_V} \times \mathrm{SU(3)_A}$, however, is a group.

As first shown by Adler, Bell, and Jackiw in QED, the chiral anomaly can be computed perturbatively [92, 93]. In the case of QCD, the chiral anomaly is given by the non-vanishing divergence

$$\partial_\mu j^5_\mu = \frac{N_\mathrm{f}}{16\pi^2} F^a_{\mu\nu}\tilde{F}^a_{\mu\nu}, \qquad \tilde{F}_{\mu\nu} \equiv \frac{1}{2}\epsilon_{\mu\nu\rho\sigma}F_{\rho\sigma}\,, \tag{2.28}$$

where $\tilde{F}_{\mu\nu}$ is the *dual field-strength tensor*. To study the implications of the chiral anomaly in some detail, we consider the spectrum of the Dirac operator $\mathcal{D} \equiv \not{D}$:

$$\mathcal{D}\psi_n = \lambda_n \psi_n\,, \tag{2.29}$$

where ψ_n are the eigenfunctions of the Dirac operator with eigenvalues λ_n. The fact that the Dirac operator anticommutes with γ_5, i.e., $\gamma_5\mathcal{D} = -\mathcal{D}\gamma_5$, implies that non-vanishing eigenvalues appear in pairs with opposite signs:

$$\mathcal{D}\psi_n = \lambda_n\psi_n \quad\Leftrightarrow\quad \gamma_5\mathcal{D}\psi_n = \gamma_5\lambda_n\psi_n \quad\Leftrightarrow\quad -\mathcal{D}\gamma_5\psi_n = \lambda_n\gamma_5\psi_n \quad\Leftrightarrow\quad \mathcal{D}\psi_{-n} = -\lambda_n\psi_{-n}\,, \tag{2.30}$$

i.e., $\psi_{-n} \equiv \gamma_5\psi_n$ is an eigenfunction of $\mathcal{D}$ with eigenvalue $-\lambda_n$. However, the Dirac operator can still have unpaired *zero modes*, i.e., eigenfunctions $\psi_{0,k}$ with vanishing eigenvalues $\lambda_k = 0$. In analogy to the quark fields, also the zero modes can be left- or right-handed:

$$\psi^{\mathrm{L/R}}_{0,k} = \frac{1 \mp \gamma_5}{2}\psi_{0,k}\,. \tag{2.31}$$

Note that the Dirac operator is flavor-independent and hence each eigenvalue appears N_f times.

Integrating both sides of the axial anomaly equation (2.28) (and dividing by $2N_\mathrm{f}$), we obtain (see, e.g., Ref. [94])

$$Q \equiv \frac{1}{32\pi^2}\int \mathrm{d}^4x\, F^a_{\mu\nu}\tilde{F}^a_{\mu\nu} = n_\mathrm{L} - n_\mathrm{R} \equiv \mathrm{index}(\mathcal{D})\,, \tag{2.32}$$

where we defined the *topological charge* Q and $n_{\mathrm{L/R}}$ are the numbers of left- and right-handed zero modes per flavor of the Dirac operator. The difference of those numbers is the so-called *analytical index* of the Dirac operator. Eq. (2.32) is a result of the renowned *Atiyah-Singer index theorem* [95, 96] and relates a property of the gauge field to the fermionic chiral zero modes of the theory. It also shows that each gauge configuration can be classified by the topological charge that has to be an integer and thus cannot be changed by smooth variations of the gauge fields which is characteristic for topological properties. We elaborate more on the role of topology in QCD in the next section.

2.4 Topology and the QCD Vacuum

Topology is a branch of mathematics that plays an important role in modern physics. It studies the general properties of spaces and objects under continuous deformations. In this respect, the notion of *topological equivalence* is essential. Loosely speaking, two objects are called topologically equivalent if they can be continuously deformed into each other. Mathematically, this is described by a *homeomorphism*, i.e., a continuous map that has a continuous inverse. In this sense, e.g., the letters "A" and "R" are topologically equivalent, while the numbers "0" and "8" are not; 0 can be continuously deformed into 8, but not vice versa.

Another important notion is that of *homotopy* which classifies maps between topological spaces. For the only spaces we consider, namely hyperspheres S^n, two maps $f, g : S^n \to S^m$ are homotopic if their images $f(S^n), g(S^n) \in S^m$ are homeomorphic. Homotopy builds an equivalence class and the different

equivalence classes form the so-called *homotopy group* $\pi_n(S^m)$. In the following, we shall address the homotopy groups of hyperspheres in some detail.

- The homotopy group $\pi_1(S^1)$ classifies maps from a circle to another circle. Intuitively this can be described by how a rubber band can be wrapped around a ring. The topologically different kinds of "wrapping" can be characterized by an integer, the so-called *winding number* n: The rubber band can only touch the ring and not wrap around it ($n = 0$), it can wrap around the ring counter-clockwise ($n = +1$) or clockwise ($n = -1$), it can wrap around the ring twice counter-clockwise ($n = +2$) or clockwise ($n = -2$) and so on. We have therefore established that $\pi_1(S^1) = \mathbb{Z}$.
- The homotopy group $\pi_2(S^2)$ classifies maps from a sphere to another sphere. Intuitively this can be described by how a bag can be wrapped around a ball and then sealed. This can again be described by an integer n: The bag can touch the ball without wrapping around it ($n = 0$), it can be wrapped around the ball once ($n = \pm 1$), it can be wrapped around the ball once, then twisted and wrapped around the ball again ($n = \pm 2$) and so on. Note that twisting counter-clockwise corresponds to $+1$ and clockwise to -1; counter-clockwise and clockwise twists cancel each other. We therefore established that $\pi_2(S^2) = \mathbb{Z}$.

This also generalizes to higher-dimensional hyperspheres:

$$\pi_d(S^d) = \mathbb{Z}\,, \qquad d \in \mathbb{N}\,. \tag{2.33}$$

It turns out that these topological concepts are relevant for the vacuum of QCD that we shall address in the remainder of this chapter. For a more detailed and mathematically more rigorous introduction into topological concepts and their application in physics, we recommend Ref. [97].

2.4.1 Instantons and the Vacuum Structure of QCD

In this section, we explore the classical vacuum structure of QCD and its connection to topology that plays a fundamental role in the remainder of this work. We start by showing that the QCD vacuum comprises infinitely many classical vacua that differ by a topological invariant. Instantons are then introduced as tunneling events between those vacua and explicit expressions for the simplest instanton gauge fields are derived.

We consider pure SU(3) Yang-Mills theory with the Euclidean action

$$S = \frac{1}{4g_s^2} \int \mathrm{d}^4x\, F^a_{\mu\nu}(x) F^a_{\mu\nu}(x)\,. \tag{2.34}$$

Since the action is quadratic in the field-strength tensor, its minimum is given by gluon fields with vanishing field-strength tensor. These are the so-called *pure gauges*

$$A^{\mathrm{pg}}_\mu(x) = \mathrm{i}\, g^\dagger(x) \partial_\mu g(x)\,, \qquad g : \mathbb{R}^4 \to \mathrm{SU}(3)\,, \tag{2.35}$$

i.e., gauge transformations of the "trivial" vacuum $A_\mu \equiv 0$. However, this does not describe a unique classical vacuum state. In fact, we need to classify all maps $\mathbb{R}^4 \to \mathrm{SU}(3)$ to investigate the structure of the classical vacuum of QCD. For this, it is convenient to restrict ourselves to maps that approach a constant at spatial infinity, i.e., $\lim_{|\vec{x}|\to\infty} g(x) = \mathbb{1}$. This identifies spatial infinity effectively as a single point but does not affect the local physics inside the infinitely large box. As a consequence, the whole space $\mathbb{R}^4$ is compactified to the three-sphere S^3 and we are left to classify all maps $S^3 \to \mathrm{SU}(3)$. However, according to a theorem by Bott [98] it is sufficient to only consider SU(2) subgroups of any simple Lie group G for studying mappings $S^3 \to G$. Consequently, we are left with classifying the maps

$S^3 \to \mathrm{SU}(2)$. As SU(2) is diffeomorphic to a three-sphere,[9] this problem reduces to classifying all maps $S^3_{\text{space}} \to S^3_{\text{group}}$. Above we have elaborated that $\pi_3(S^3) = \mathbb{Z}$. Consequently, the classical vacuum of QCD consists of infinitely many topologically distinct vacua, where each can be classified by an integer winding number ν [99]. This winding number of the homotopy class the map g belongs to, in mathematics also known as *Pontryagin index* or *Chern-Simons characteristic*, is given as the so-called *Cartan-Maurer integral invariant* [68, 100]

$$\nu[g] = \frac{1}{24\pi^2}\int_{S^3} \mathrm{d}^3\theta\, \epsilon_{abc}\,\mathrm{tr}\left[\left(g^\dagger(\theta)\frac{\partial g(\theta)}{\partial\theta_a}\right)\left(g^\dagger(\theta)\frac{\partial g(\theta)}{\partial\theta_b}\right)\left(g^\dagger(\theta)\frac{\partial g(\theta)}{\partial\theta_c}\right)\right], \tag{2.36}$$

where the θ_i are angular coordinates describing the surface of a three-sphere. An example of a map in the homotopy class with unit winding number, i.e., an SU(2) element $g_{(1)}$ with $\nu[g_{(1)}] = 1$, is

$$g_{(1)} = \frac{\mathrm{i}\,\sigma_\mu x_\mu}{\sqrt{x^2}}\,, \qquad \sigma_\mu \equiv (\mathrm{i}\cdot\mathbb{1}, \vec{\sigma}) \tag{2.37}$$

with $\vec{\sigma}$ the vector of Pauli matrices, and a general map with winding number $n \in \mathbb{Z}$ is obtained by

$$g_{(n)} = g^n_{(1)}\,, \qquad \nu\big[g_{(n)}\big] = n\,. \tag{2.38}$$

Note that maps that belong to the same homotopy class are gauge equivalent and connected via a "small" gauge transformation in the sense that the gauge transformation can be built up from a series of infinitesimal gauge transformations that vanish at spatial infinity. Maps that belong to different homotopy classes are also gauge equivalent; however, the gauge transformations that connect them cannot be built from a series of infinitesimal gauge transformations and are therefore "large" [101]. Also note that if the map g can be written as the product $g = g_1 g_2$, then the winding number of g adds up from the winding numbers of g_1 and g_2:

$$\nu[g_1 g_2] = \nu[g_1] + \nu[g_2]\,. \tag{2.39}$$

We have so far elaborated that the classical QCD vacuum is not unique but actually comprises infinitely many topologically distinct vacua that can be labeled by an integer topological invariant (2.36). As known from quantum mechanics, quantum tunneling connects the different vacua by allowing the system to tunnel through finite potential barriers. The true QCD vacuum is thus "lifted" due to quantum tunneling, described by so-called *instantons*. Instantons are field configurations that – in Minkowski spacetime – describe tunneling between topologically inequivalent vacua and are defined as solutions of the classical Euclidean equations of motion $D_\mu F_{\mu\nu} \equiv 0$ with finite action. Also at finite temperatures, tunneling solutions exist and are called *calorons*. For extensive reviews on instantons, there is a plethora of literature to which we refer the interested reader [94, 100, 102–108].

The importance of solutions of the classical Euclidean field equations with finite energy was first pointed out in 1975 by Polyakov in Ref. [109] and at about the same time the instanton solution was found [110]. These works appeared shortly after the discovery of asymptotic freedom and before lattice QCD was well established, so neither perturbative nor numerical approaches to the low-energy regime of QCD were available at that time. They therefore opened a new era of analytic low-energy QCD research that turned out to have profound consequences:

The complex vacuum structure of QCD was first described in Refs. [99, 111]. This led to the insight that QCD is *a priori* not *CP* invariant and the QCD Lagrangian should contain the theta term (cf.

[9] Note that any $g \in \mathrm{SU}(2)$ can be written as $g = \mathrm{i}\,\vec{a}\cdot\vec{\sigma} + a_0\mathbb{1}$ with the Pauli matrices $\vec{\sigma} = (\sigma_1, \sigma_2, \sigma_3)$ and a unit vector $a \equiv (a_0, \vec{a}) = (a_0, a_1, a_2, a_3)$, i.e., $|a| = 1$. This follows from the fact that every $g \in \mathrm{SU}(2)$ has unit determinant and identifies the manifold of the group parameters of SU(2) with the sphere S^3 embedded in $\mathbb{R}^4$.

Sec. 2.4.2). A possible solution of the strong *CP* problem, i.e., the experimental non-observation of a *CP* violation in QCD, via the Peccei-Quinn mechanism led to the prediction of the axion that is also a dark matter candidate as described in detail in Chap. 1. Another consequence is the explicit breakdown of the $U(1)_A$ symmetry by instantons, cf. Sec. 2.3. Although Polyakov proved that in 2+1-dimensional compact QED confinement is explained by instantons [112], the confident hope that also the confinement of QCD may be explained using instantons was dashed. However, instantons revolutionized the qualitative understanding of the vacuum structure of non-abelian gauge theories and were the first explicit non-perturbative effects that distinguished non-abelian gauge theories from the perturbatively well understood abelian theories like QED [104].

Before we address the instantons of Yang-Mills theory in detail, we start our discussion with a toy model, namely a 1+1-dimensional field theory in a double-well potential, that reveals the most important notions in a vivid manner. In particular, all quantities have simple analytic expressions and can be easily visualized.

A Toy Model for Instantons

We now discuss instantons (in this context really solitons) in a 1+1-dimensional double-well potential. We start by discussing the minima of this potential and then explicitly find solutions of the equations of motion. Besides the trivial solutions, there exist non-trivial solutions that describe tunneling between the different minima, the solitons. Our discussion of this toy model follows Refs. [100, 101]. In Minkowski space, this theory is described by the Lagrangian

$$\mathcal{L} = \frac{1}{2}\big(\partial_\mu \phi\big)\big(\partial^\mu \phi\big) - U(\phi), \qquad U(\phi) \equiv \frac{1}{4}\big(\phi^2 - 1\big)^2, \tag{2.40}$$

where $\mu = t, x$. The theory has the symmetry $\phi \to -\phi$ and the potential has two degenerate minima $U(\pm 1) = 0$ (cf. top left panel of Fig. 2.3). The Euler-Lagrange equation reads

$$\frac{\mathrm{d}^2\phi}{\mathrm{d}t^2} - \frac{\mathrm{d}^2\phi}{\mathrm{d}x^2} = -\big(\phi^2 - 1\big)\phi \tag{2.41}$$

and we are interested in time-independent solutions with finite energy that therefore satisfy

$$\frac{\mathrm{d}^2\phi}{\mathrm{d}x^2} = \big(\phi^2 - 1\big)\phi\,. \tag{2.42}$$

It is not obvious if there are non-trivial solutions other than the two constant minima $\phi(x) = \pm 1$. To solve this equation, we first recognize that it is equivalent to finding minima of the potential energy

$$V[\phi] = \int \mathrm{d}x \left[\frac{1}{2}\left(\frac{\mathrm{d}\phi}{\mathrm{d}x}\right)^2 + U(\phi)\right]. \tag{2.43}$$

Note that this expression corresponds to the Euclidean Lagrangian of a particle moving in the potential $\tilde{U} \equiv -U$ (cf. top right panel of Fig. 2.3):

$$L[x] = \int \mathrm{d}\tau \left[\frac{1}{2}\left(\frac{\mathrm{d}x}{\mathrm{d}\tau}\right)^2 - \tilde{U}(x)\right]. \tag{2.44}$$

For the energy to be finite, we require the field to approach one of the two minima of the potential at spatial infinity, i.e., $\phi(\pm\infty) = \pm 1$. In the particle picture, this means that the particle has to be on one of the "hills" of the inverse potential for $\tau \to \pm\infty$. This defines a map $\phi : \{-\infty, \infty\} \to \{-1, 1\}$ and classifying those maps is equivalent to classifying the maps $S^0 \to S^0$. The corresponding homotopy

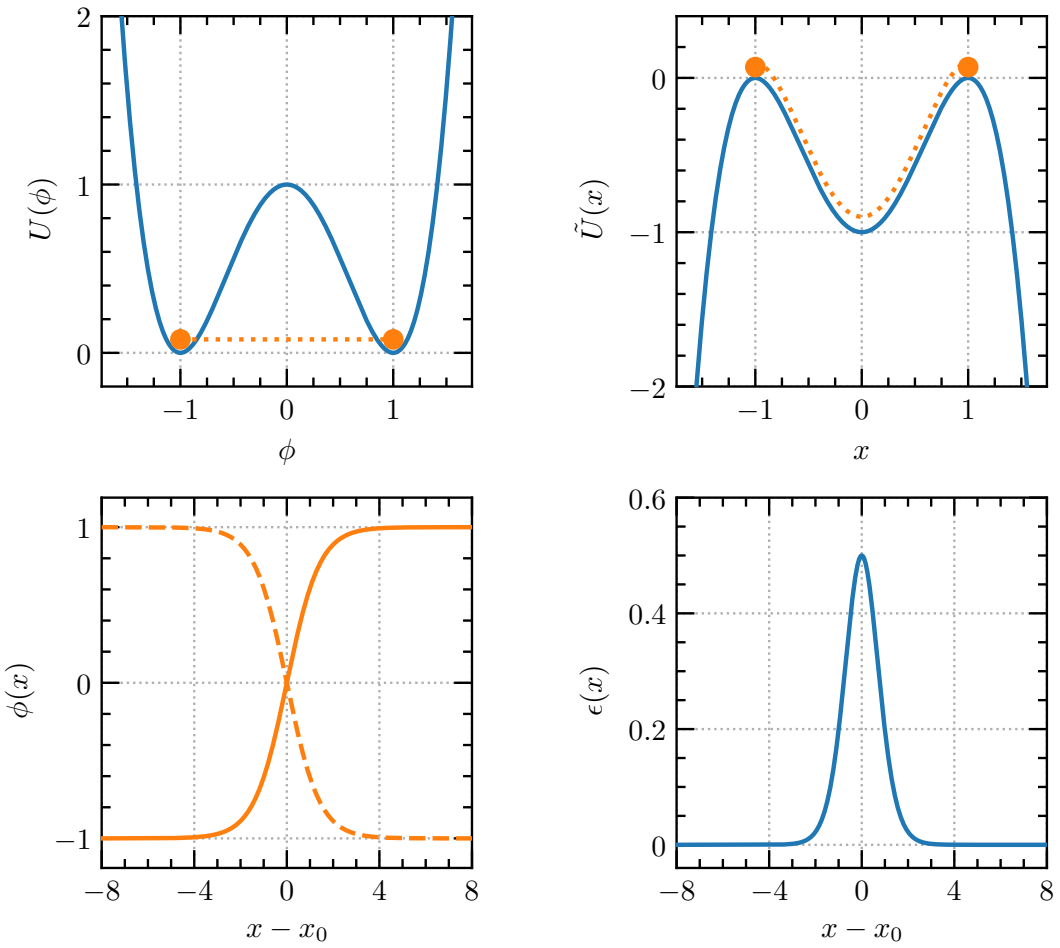

Figure 2.3.: Upper left: Double-well potential in Minkowski space. The tunneling through kinks is indicated with the dotted line. Upper right: Inverse potential in Euclidean space. The kink corresponds to "rolling" from one hill to another as indicated by the dotted line. Lower left: Kink (solid line) and anti-kink (dashed line) solutions that describe quantum tunneling between the classical minima. Lower right: Energy density of the kink solution. The fact that the energy density is spatially well concentrated gives the kink its interpretation as a pseudoparticle.

group $\pi_0(S^0) = \mathbb{Z}_2$ is given by the cyclic group of order 2 which only consists of two elements $\{0, 1\}$. 0 corresponds to the trivial case where the system stays in one of the minima, 1 corresponds to the case where the system tunnels from one minimum to the other one. Still, it is not clear if these tunneling solutions exist, if they are stable, and if there is an analytically closed form.

Let us now try to find the non-trivial solutions of the equation of motion. Since the particle motion has zero energy, the equation of motion corresponds to

$$\frac{1}{2}\left(\frac{\mathrm{d}x}{\mathrm{d}\tau}\right)^2 = \tilde{U}(x) \qquad \longrightarrow \qquad \frac{1}{2}\left(\frac{\mathrm{d}\phi}{\mathrm{d}x}\right)^2 = U(\phi)\,, \tag{2.45}$$

where we translated the equation of motion back to the language of field theory. A straightforward integration of this equation for the double-well potential (2.40) yields the solution

$$\phi(x) = \pm \tanh\left[\frac{1}{\sqrt{2}}(x - x_0)\right], \tag{2.46}$$

where x_0 is a constant of integration. Both solutions are depicted in the bottom left panel of Fig. 2.3. The solution with the positive sign corresponds to moving from the minimum at $\phi = -1$ to the minimum at $\phi = +1$ and is called *kink*, in the literature also known as *soliton* [101] or *lump* [100]. The solution with the negative sign accordingly corresponds to moving in the opposite direction and is called *anti-kink*. The parameter x_0 corresponds to the "position" of the kink and reflects the translational invariance of the theory. Since the energy density of the kink is very localized around its position, cf. bottom right panel of Fig. 2.3, it may be interpreted as a particle; it is therefore sometimes also called a *pseudoparticle*.

The topological nature of the kink suggests that we can define a conserved topological current, also known as *Chern-Simons current*

$$K^\mu = \frac{1}{2}\epsilon^{\mu\nu}\partial_\nu\phi\,, \qquad \partial_\mu K^\mu = 0\,. \tag{2.47}$$

The corresponding charge is called the topological charge and is given as

$$Q = \int_{-\infty}^{\infty} \mathrm{d}x\, K^0 = \frac{1}{2}\int_{-\infty}^{\infty} \mathrm{d}x\, \partial_x\phi = \frac{1}{2}[\phi(\infty) - \phi(-\infty)] = \begin{cases} 0\,, & \text{trivial solution} \\ 1\,, & \text{kink} \\ -1\,, & \text{anti-kink} \end{cases}. \tag{2.48}$$

It is hence an integer that characterizes the topology of the vacuum and describes if a given field stays in one vacuum or tunnels between different vacua.

By studying the topological structure of the minima of this simple toy model, we introduced important quantities like the Chern-Simons current or the topological charge in a vivid manner. Those quantities are also important in the context of the QCD vacuum as discussed next.

Instantons in SU(3) Yang-Mills Theory

We now return to the case of SU(3) Yang-Mills theory by generalizing the ideas presented in the discussion of the toy model. The requirement of finite action demands the field-strength tensor to vanish at spacetime infinity, i.e., the gauge field needs to approach a pure gauge at infinity,

$$\lim_{r\to\infty} A_a(x) \equiv \bar{A}_a(\theta) = \mathrm{i}\, g^\dagger(\theta)\partial_a g(\theta)\,. \tag{2.49}$$

In the analogy of the toy model, this corresponds to demanding that the field needs to be in one of the two minima at spatial infinity. Inserting this form in the winding number (2.36) yields

$$\nu = \frac{1}{8\pi^2}\int_{S^3} \mathrm{d}^3\theta\, \epsilon_{abc}\,\mathrm{tr}\left[\bar{A}_a(\theta)\partial_b\bar{A}_c(\theta) - \frac{2\mathrm{i}}{3}\bar{A}_a(\theta)\bar{A}_b(\theta)\bar{A}_c(\theta)\right]. \tag{2.50}$$

This can be rewritten in terms of a surface integral of a four-dimensional current as

$$\nu = \frac{1}{8\pi^2}\int_{S^3} \mathrm{d}^3\theta\, n_\mu\epsilon_{\mu\nu\rho\sigma}\,\mathrm{tr}\left[\bar{A}_\nu(\theta)\partial_\rho\bar{A}_\sigma(\theta) - \frac{2\mathrm{i}}{3}\bar{A}_\nu(\theta)\bar{A}_\rho(\theta)\bar{A}_\sigma(\theta)\right] \equiv \frac{1}{8\pi^2}\int_{S^3} \mathrm{d}^3\theta\, n_\mu K_\mu\big[\bar{A}\big], \tag{2.51}$$

where n_μ is the normal vector on the surface of the sphere and

$$\begin{aligned} K_\mu\big[\bar{A}\big] &\equiv \epsilon_{\mu\nu\rho\sigma}\,\mathrm{tr}\left[\bar{A}_\nu(\theta)\partial_\rho\bar{A}_\sigma(\theta) - \frac{2\mathrm{i}}{3}\bar{A}_\nu(\theta)\bar{A}_\rho(\theta)\bar{A}_\sigma(\theta)\right] \\ &= \frac{1}{2}\epsilon_{\mu\nu\rho\sigma}\,\mathrm{tr}\left[\bar{A}_\nu(\theta)F_{\rho\sigma}\big[\bar{A}\big] + \frac{2\mathrm{i}}{3}\bar{A}_\nu(\theta)\bar{A}_\rho(\theta)\bar{A}_\sigma(\theta)\right] \end{aligned} \tag{2.52}$$

is the the Chern-Simons current in analogy to the Chern-Simons current (2.47) of the toy model. Using the Gauß-Ostrogradsky integral theorem, we can transform the surface integral into a volume integral:

$$\nu = \frac{1}{8\pi^2} \int \mathrm{d}^4x \, \partial_\mu K_\mu[A], \tag{2.53}$$

where the Chern-Simons current now contains the full gauge fields and not their asymptotic form any more. The divergence of the Chern-Simons current reads

$$\partial_\mu K_\mu = \frac{1}{4} F^a_{\mu\nu} \tilde{F}^a_{\mu\nu} \tag{2.54}$$

and the winding number is eventually determined via

$$\nu = \frac{1}{32\pi^2} \int \mathrm{d}^4x \, F^a_{\mu\nu} \tilde{F}^a_{\mu\nu} \equiv Q, \tag{2.55}$$

where we defined the topological charge Q.

This calculation shows that the topological charge is completely determined by the asymptotic behavior of the gauge fields on the large three-sphere. It furthermore does not depend on the local behavior of the gauge fields, i.e, it is invariant under small variations δA_μ of the gauge fields [104]:

$$\delta Q = \frac{1}{32\pi^2} \int_{S^3} \mathrm{d}\sigma_\mu \, \delta K_\mu = \frac{1}{8\pi^2} \int_{S^3} \mathrm{d}\sigma_\mu \, \tilde{F}^a_{\mu\nu} \delta A^a_\nu = 0 \tag{2.56}$$

because the field-strength tensor vanishes at spatial infinity. This shows that the topologically different sectors are truly disparate.

Let us now consider the charge associated with the Chern-Simons current, called *Chern-Simons number*:

$$N_{\mathrm{CS}} = \int \mathrm{d}^3x \, K_0 = \frac{1}{2} \int \mathrm{d}^3x \, \epsilon_{ijk} \, \mathrm{tr}\left[A_i F_{jk} + \frac{2\mathrm{i}}{3} A_i A_j A_k \right]. \tag{2.57}$$

Note that this charge is not conserved because the Chern-Simons current is also not conserved. For a vacuum state, the gauge field is a pure gauge $A_k = \mathrm{i}\, g^\dagger \partial_k g$ and the field-strength tensor vanishes. The Chern-Simons number therefore equals the winding number of the classical vacuum:

$$N_{\mathrm{CS}} = \nu[g]. \tag{2.58}$$

With this, the topological charge may be rewritten as

$$Q = \int \mathrm{d}^4x \, \partial_\mu K_\mu = \int \mathrm{d}^4x \, (\partial_0 K_0 + \partial_i K_i) = \int \mathrm{d}^3x \mathrm{d}\tau \, \partial_0 K_0 = \int \mathrm{d}^3x \, K_0 \Big|_{\tau=-\infty}^{\infty} = N_{\mathrm{CS}}(\infty) - N_{\mathrm{CS}}(-\infty), \tag{2.59}$$

where the integral over the spatial part of the Chern-Simons current vanishes in the temporal gauge $A_0 \equiv 0$. This shows that a gauge configuration with a non-zero topological charge Q indeed describes the tunneling between topologically distinct vacua whose difference in winding number is Q [111, 113].

In the remainder of this section, we explicitly derive the instanton solutions with unit topological charge. These are the most important topologically non-trivial gauge fields and in Chap. 4 we provide a lattice discretization of these objects that allows to study "clean" topological objects on the lattice. We start our discussion by noting that the Yang-Mills action (2.34) can be rewritten in terms of the dual field-strength tensor (2.28) and satisfies the so-called *Bogomol'nyi inequality* [114]

$$S = \frac{1}{4g_s^2}\int \mathrm{d}^4x \left[\pm F^a_{\mu\nu}\tilde{F}^a_{\mu\nu} + \frac{1}{2}\left(F^a_{\mu\nu} \mp \tilde{F}^a_{\mu\nu}\right)^2\right] \geq \frac{1}{4g_s^2}\left|\int \mathrm{d}^4x\, F^a_{\mu\nu}\tilde{F}^a_{\mu\nu}\right| = \frac{8\pi^2|Q|}{g_s^2} \tag{2.60}$$

with the topological charge Q (2.32). The lower bound of the action, i.e., the equality in Eq. (2.60), is satisfied if and only if the field configuration is (anti-)self-dual, i.e.,

$$F^a_{\mu\nu} = \pm\tilde{F}^a_{\mu\nu}\,. \tag{2.61}$$

It can be shown that if a self-dual solution exists, it automatically fulfills the equation of motion since $D_\mu\tilde{F}_{\mu\nu} \equiv 0$ is identically fulfilled. Self-dual fields are called instantons, anti-self-dual fields are called anti-instantons. The action of instantons is therefore determined by the topological charge Q:

$$S_\mathrm{I} = \frac{8\pi^2|Q|}{g_s^2}\,. \tag{2.62}$$

In each topological sector with topological charge Q, Eq. (2.62) is the absolute minimum of the action. The instanton solutions therefore dominate the path integral in this sector and other contributions become negligible at weak coupling. Instantons, accordingly, build the basis of semiclassical approximations of the QCD vacuum like, e.g., the dilute instanton gas approximation that we discuss in Sec. 2.4.4. This form of the instanton action also reflects that instantons are inherently non-perturbative as the Taylor expansion of the Boltzmann weight $\exp(-S_\mathrm{I})$ around $g_s = 0$ vanishes identically.

To explicitly obtain expressions of $Q = 1$ instanton and caloron fields, we now solve the self-duality condition (2.61) following Refs. [115–117]. For this, we consider the gauge group SU(2) and embed our solutions in SU(3). This can be done via

$$A^{\mathrm{SU(3)}}_\mu = \left(\begin{array}{cc|c} & & 0 \\ & A^{\mathrm{SU(2)}}_\mu & 0 \\ \hline 0 & 0 & 0 \end{array}\right) \tag{2.63}$$

using that SU(2) is a subgroup of SU(3), see also App. A. For solving the self-duality condition, we start with the *Ansatz*

$$A_\mu(x) = f\left(x^2\right)\cdot \mathrm{i}\, g^\dagger_{(1)}(x)\partial_\mu g_{(1)}(x)\,, \tag{2.64}$$

where $g_{(1)}$ is an element of SU(2) that belongs to the homotopy class with unit winding number as defined in Eq. (2.37). This *Ansatz* for the instanton gauge field has the same angular dependence at every point and hence approaches the pure gauge at spatial infinity uniformly in all directions if $\lim_{x\to\infty} f = 1$. Plugging this *Ansatz* into the self-duality equation, one finds after a tedious but straightforward calculation (see, e.g., Ref. [103]) the result

$$f(x^2) = \frac{x^2}{x^2+\rho^2}\,, \tag{2.65}$$

where ρ is a constant of integration that is called *scale*, *size*, or *radius* of the instanton. The corresponding instanton gauge field was first found by Belavin, Polyakov, Schwartz, and Tyupkin (BPST) [110] and reads

$$A_\mu(x) = \frac{x^2}{x^2+\rho^2} \cdot \mathrm{i}\, g_{(1)}^\dagger(x)\partial_\mu g_{(1)}(x)\,. \tag{2.66}$$

Inserting the explicit form of $g_{(1)}$, we arrive at the more convenient form

$$A_\mu(x) = \eta_{a\mu\nu}\frac{(x-z)_\nu \sigma^a}{(x-z)^2+\rho^2}\,, \tag{2.67}$$

where we explicitly incorporated the translational invariance of the instanton solution by including four new parameters z_μ that describe the *position* or *center* of the instanton, in analogy to the position x_0 of the kink in the toy model. ρ and z are called *collective coordinates* of the instanton. Note that the action does not depend on those coordinates.[10] We also introduced the *'t Hooft symbol*

$$\eta_{a\mu\nu} \equiv \epsilon_{0a\mu\nu} + \delta_{a\mu}\delta_{\nu 0} - \delta_{a\nu}\delta_{\mu 0}\,, \tag{2.68}$$
$$\bar\eta_{a\mu\nu} \equiv \epsilon_{0a\mu\nu} - \delta_{a\mu}\delta_{\nu 0} + \delta_{a\nu}\delta_{\mu 0}\,. \tag{2.69}$$

The 't Hooft symbols map the generators of SU(2), namely the Pauli matrices σ_i, to the generators of Euclidean Lorentz transformations, i.e., SO(4):

$$\bar\sigma_{\mu\nu} = -\mathrm{i}\eta_{a\mu\nu}\sigma^a\,, \qquad \sigma_{\mu\nu} = -\mathrm{i}\bar\eta_{a\mu\nu}\sigma^a\,, \tag{2.70}$$

where

$$\sigma_{\mu\nu} \equiv \frac{1}{2}\left(\bar\sigma_\mu\sigma_\nu - \bar\sigma_\nu\sigma_\mu\right) \quad \text{and} \quad \bar\sigma_{\mu\nu} \equiv \frac{1}{2}\left(\sigma_\mu\bar\sigma_\nu - \sigma_\nu\bar\sigma_\mu\right) \qquad \left(\bar\sigma_\mu \equiv (-\mathrm{i}\cdot\mathbb{1}\,,\vec\sigma)\right)$$

are two inequivalent sets of generators of SO(4) that are anti-self-dual and self-dual, respectively. Note that these properties correspond to the group isomorphism $\mathrm{SO}(4) \simeq \mathrm{SU}(2)\times\mathrm{SU}(2)$ and instantons and anti-instantons transform under disparate SU(2) groups, respectively. Important properties of the 't Hooft symbols are summarized in App. A.3.

The action of the BPST instanton is obtained by integrating the action density

$$F^a_{\mu\nu}F^a_{\mu\nu} = \frac{192\rho^4}{\left((x-z)^2+\rho^2\right)^2} \tag{2.71}$$

over the whole spacetime:

$$S = \frac{1}{4g_s^2}\int \mathrm{d}^4x F^a_{\mu\nu}F^a_{\mu\nu} = \frac{8\pi^2}{g_s^2}\,. \tag{2.72}$$

The BPST instanton therefore has topological charge $Q=1$. This was expected, because in the *Ansatz* we explicitly chose, the group element $g_{(1)}$ belongs to the homotopy class of unit winding number. The corresponding anti-self-dual BPST anti-instanton solution with $Q=-1$ is obtained by replacing the anti-'t Hooft symbol with the 't Hooft symbol, i.e., $\bar\eta_{a\mu\nu} \to \eta_{a\mu\nu}$. The energy density (2.71) is very localized

[10] Note that in principle also SU(N_c) rotations of the instanton field in color space do not affect the action. This adds $4N_c-5$ collective coordinates [107].

around the center of the instanton and falls off with $|x|^4$. This gives the instanton a particle character. In their original publication, Belavin *et al.* called their solution pseudoparticles because of the above-mentioned particle-like character. The name instanton was later introduced by 't Hooft in Ref. [118], indicating that these solutions are localized in time and hence appear almost instantaneously.

The BPST instanton (2.67) is given in the so-called *regular gauge* where all the contribution to the topological charge comes from infinity where the pure-gauge form is approached. However, in practice it is often more convenient to "move" the topological information to the position of the instanton. This is achieved by a singular gauge transformation and the BPST instanton in the *singular gauge* reads

$$\begin{aligned} A_\mu^{a,\,\text{sing}} &= g\Big(A_\mu^a + \mathrm{i}\,\partial_\mu\Big)g^\dagger\,, & g &= \frac{\mathrm{i}\sigma_\mu(x-z)_\mu}{\sqrt{(x-z)^2}} \\ &= 2\bar{\eta}_{a\mu\nu}\frac{\rho^2(x-z)_\nu}{(x-z)^2\big((x-z)^2+\rho^2\big)}\,. \end{aligned} \tag{2.73}$$

Note that the apparent singularity at the center of the instanton, i.e., at $x = z$, is not "physical" but merely a gauge artifact as all gauge invariant quantities like the action density are smooth at this point. Also note that the 't Hooft symbol is replaced by the anti-'t Hooft symbol in the singular gauge.

This expression can be rewritten in the form[11]

$$A_\mu^a = -\bar{\eta}_{a\mu\sigma}\partial_\sigma \ln\left[1+\frac{\rho^2}{(x-z)^2}\right] \equiv -\bar{\eta}_{a\mu\sigma}\partial_\sigma \ln\phi_{\mathrm{I}}(x) \tag{2.74}$$

and allows for the construction of multi-instanton solutions, as was first suggested by 't Hooft in an unpublished work, cf. Refs. [116, 117]. The general idea is to start from the *Ansatz*

$$A_\mu^a(x) = \bar{\eta}_{a\mu\sigma}a_\sigma(x)\,, \qquad a_\sigma \equiv -\partial_\sigma \ln\phi\,. \tag{2.75}$$

Plugging this *Ansatz* into the definition of the field-strength tensor (2.4), we find

$$F_{\mu\nu}^a = \bar{\eta}_{a\mu\nu}a_\sigma a_\sigma + \bar{\eta}_{a\nu\sigma}\big(a_{\sigma\mu}+a_\sigma a_\mu\big) - \bar{\eta}_{a\mu\sigma}(a_{\sigma\nu}+a_\sigma a_\nu)\,, \tag{2.76}$$

where we used the property (A.25) and introduced the notation $a_{\rho\sigma} \equiv \partial_\rho a_\sigma$. The dual field-strength tensor then reads

$$\tilde{F}_{\mu\nu}^a = \frac{1}{2}\epsilon_{\mu\nu\alpha\beta}F_{\alpha\beta}^a = \bar{\eta}_{a\mu\nu}a_{\sigma\sigma} + \bar{\eta}_{a\nu\sigma}\big(a_{\sigma\mu}+a_\sigma a_\mu\big) - \bar{\eta}_{a\mu\sigma}(a_{\sigma\nu}+a_\sigma a_\nu) \tag{2.77}$$

and the self-duality condition reduces to

$$a_{\sigma\sigma} = a_\sigma a_\sigma \tag{2.78}$$

and hence [116]

$$\frac{\Box\phi}{\phi} = 0\,. \tag{2.79}$$

[11] From now on, we shall always work in the singular gauge and for convenience drop the superscript "sing."

A solution to this equation found by 't Hooft is given by [116, 117]

$$\phi(x) = 1 + \sum_{k=1}^{n} \frac{\rho_k^2}{(x - z_k)^2} \tag{2.80}$$

and describes a configuration consisting of n instantons with sizes ρ_k and centers z_k. In fact, this configuration has $Q = n$, where a unit contribution to the topological charge is obtained from each pole at the center of each instanton and no contribution is obtained from spatial infinity. This results from the fact that this multi-instanton solution is given in the singular gauge. Note that for $n = 0$ the solution reduces to $A_\mu \equiv 0$ which is the trivial solution that belongs to the $Q = 0$ sector. Moreover, for $n = 1$ the BPST instanton (2.73) is recovered.

Up to now, we have studied solutions of the classical equations of motion by solving the self-duality condition. We showed that field configurations with non-vanishing topological charge Q describe quantum tunneling between topologically distinct classical vacua whose difference in winding number is Q. Moreover, we constructed explicit $Q = 1$ BPST instanton solutions and $Q = n$ solutions by superposing n BPST instantons. As a next step, we discuss the finite-temperature generalization of instantons.

Calorons

Also at finite temperatures, tunneling solutions exist and the form (2.80) of ϕ serves as a convenient starting point for a generalization of the instanton to finite temperatures. As we saw in Sec. 2.2, in thermal field theory time is compactified to $[0, \beta]$ and periodic boundary conditions apply. An instanton at finite temperatures should therefore fulfill

$$\phi(\tau, \vec{x}) = \phi(\tau + \beta, \vec{x}) . \tag{2.81}$$

This is achieved by considering an instanton with radius ρ at position z with an infinite number of (time-)copies by setting $z_k = (z_0 + k\beta, \vec{z})$ and $\rho_k \equiv \rho$. We therefore have

$$\phi = 1 + \sum_{k=-\infty}^{\infty} \frac{\rho^2}{(\vec{x} - \vec{z})^2 + (x_0 - z_0 - k\beta)^2} . \tag{2.82}$$

The sum can be evaluated analytically and yields [117]

$$\phi_{\mathrm{HS}}(x) = 1 + \frac{\pi\rho^2 \sinh \frac{2\pi|\vec{x}-\vec{z}|}{\beta}}{\beta|\vec{x} - \vec{z}|\left(\cosh \frac{2\pi|\vec{x}-\vec{z}|}{\beta} - \cos \frac{2\pi(x_0 - z_0)}{\beta}\right)} . \tag{2.83}$$

This expression was first found by Harrington and Shepard in 1978 [117] and the corresponding gauge field

$$A_\mu^a(x) = -\bar{\eta}_{a\mu\sigma} \partial_\sigma \ln \phi_{\mathrm{HS}}(x) \tag{2.84}$$

is therefore called *Harrington-Shepard (HS) caloron*.[12] The HS caloron has – as the BPST instanton – topological charge $Q = 1$ and action $S = 8\pi^2/g_s^2$. In the zero-temperature limit $\beta \to \infty$, the HS caloron approaches – as expected – the BPST instanton, i.e.,

$$\lim_{\beta \to \infty} \phi_{\mathrm{HS}}(x) = 1 + \frac{\rho^2}{(x - z)^2} = \phi_{\mathrm{I}}(x) . \tag{2.85}$$

[12] The name "caloron" is suggested by the Latin "calor" – heat.

The HS anti-caloron is then – in analogy to the BPST anti-instanton – obtained by replacing the anti-'t Hooft symbol by the 't Hooft symbol, i.e., $\overline{\eta}_{a\mu\sigma} \to \eta_{a\mu\sigma}$.

This concludes our discussion of instantons, calorons, and the classical QCD vacua. We saw that the QCD vacuum comprises infinitely many topologically distinct classical vacua that are connected via instantons that describe quantum tunneling events. Calorons are then the finite-temperature generalization of instantons. We also explicitly derived solutions for the simplest instanton and caloron gauge fields. In Chap. 4, we develop a lattice discretization of both the BPST instanton and the HS caloron. These "clean" topological configurations with $Q = 1$ allow us to study the behavior of topological lattice operators. In the next section, we address how the "true" QCD vacuum is described.

2.4.2 The Theta Vacua

In the previous section, we showed that the classical structure of the QCD vacuum is very complex and comprises infinitely many topologically different vacua $|n\rangle$ labeled by an integer winding number n. If there were no quantum tunneling between vacua with different winding numbers, the classical vacua $|n\rangle$ would be eigenstates of the Hamiltonian. However, due to tunneling, the true vacuum that is an eigenstate of the Hamiltonian has to be a superposition of the classical topological vacua.

We start our discussion by considering an operator T that changes the vacuum topology, i.e., $T|n\rangle = |n+1\rangle$ [111]. We elaborated above (cf. the discussion below Eq. (2.38)) that the topological vacua are connected via "large" gauge transformations, and T hence also describes a gauge transformation. Such being the case, the Hamiltonian commutes with T and energy eigenstates, i.e., eigenstates of the Hamiltonian, have to be also eigenstates of T. Because T is a gauge transformation, it has to be unitary and hence its eigenvalues need to have modulus one, i.e., are given as $\mathrm{e}^{\mathrm{i}\theta}$, where $\theta \in [0, 2\pi]$. The corresponding eigenstates are given as the Fourier transform

$$|\theta\rangle \equiv \sum_{n=-\infty}^{\infty} \mathrm{e}^{-\mathrm{i}n\theta}\,|n\rangle\,, \qquad\qquad T\,|\theta\rangle = \mathrm{e}^{\mathrm{i}\theta}\,|\theta\rangle\,. \tag{2.86}$$

We now show following Ref. [101] that these so-called *theta vacua* are true eigenstates of the Hamiltonian. The transition probability of two theta vacua is given by

$$\langle\theta'|\mathrm{e}^{-HT}|\theta\rangle = \sum_{n,m} \mathrm{e}^{\mathrm{i}n\theta'}\mathrm{e}^{-\mathrm{i}m\theta}\langle n|\mathrm{e}^{-HT}|m\rangle = \sum_{n,m} \mathrm{e}^{\mathrm{i}n\left(\theta'-\theta\right)}\mathrm{e}^{\mathrm{i}(n-m)\theta}\langle n|\mathrm{e}^{-HT}|m\rangle\,. \tag{2.87}$$

The remaining matrix element describes the transition probability from the vacuum with winding number n to the vacuum with winding number m. But this transition is induced by instantons with winding number $Q = n - m$; as a path integral, it is therefore given as

$$\langle n|\mathrm{e}^{-HT}|m\rangle = \int \mathcal{D}A_\mu\,\mathrm{e}^{-S}\delta_{Q,n-m}\,. \tag{2.88}$$

The transition probability of two theta vacua thus reads

$$\begin{aligned}\langle\theta'|\mathrm{e}^{-HT}|\theta\rangle &= \sum_{n,m} \mathrm{e}^{\mathrm{i}n\left(\theta'-\theta\right)}\mathrm{e}^{\mathrm{i}(n-m)\theta}\int \mathcal{D}A_\mu\,\mathrm{e}^{-S}\delta_{Q,n-m} \\ &= \left(\sum_n \mathrm{e}^{\mathrm{i}n\left(\theta'-\theta\right)}\right)\left(\sum_k \mathrm{e}^{\mathrm{i}k\theta}\int \mathcal{D}A_\mu\,\mathrm{e}^{-S}\delta_{Q,k}\right) \\ &= 2\pi\delta\left(\theta-\theta'\right)\int \mathcal{D}A_\mu \mathrm{e}^{-S+\mathrm{i}Q\theta}\,,\end{aligned} \tag{2.89}$$

showing that the theta vacua are completely disparate and the system cannot evolve from one to another. Each theta vacuum hence describes a physically different world [119]. Eq. (2.89) suggests that the value of θ is fixed by adding the so-called *theta term*

$$\mathcal{L}_\theta = -\mathrm{i}\theta q = -\mathrm{i}\frac{\theta}{32\pi^2} F^a_{\mu\nu}\tilde{F}^a_{\mu\nu} \tag{2.90}$$

to the (Euclidean) QCD Lagrangian, where

$$q(x) \equiv \frac{1}{32\pi^2} F^a_{\mu\nu}(x)\tilde{F}^a_{\mu\nu}(x) \tag{2.91}$$

is the topological charge density whose spacetime integral is the topological charge. Note that this term is a renormalizable, Poincaré invariant, and gauge invariant dimension-four operator and therefore has every right to be included in the QCD Lagrangian.

At this point, a natural question is why the theta term is often omitted in the QCD Lagrangian even though it fulfills all criteria that are required to appear in the Lagrangian. In fact, we saw in the discussion above that the topological charge density can be written as a total divergence and hence has no effect on the equations of motion. However, the theta term still has physical consequences as it explicitly breaks *CP* symmetry. Since this is not observed in nature, θ is required to be very small, although it could *a priori* take on any value between 0 and 2π. To explain this small value of θ is the strong *CP* problem that may be dynamically solved via the Peccei-Quinn mechanism as discussed in detail in Chap. 1.

As can be seen from the calculation in Eqs. (2.87)–(2.89), in terms of the partition function, a single topological sector with winding number ν is determined by

$$\mathcal{Z}_\nu = \int \mathcal{D}A_\mu \, \mathrm{e}^{-S} \delta_{Q\nu} \tag{2.92}$$

and the full partition function of a theta vacuum is given by the Fourier transform

$$\mathcal{Z}(\theta) = \sum_\nu \mathrm{e}^{\mathrm{i}\theta\nu} Z_\nu = \int \mathcal{D}A_\mu \, \mathrm{e}^{-S+\mathrm{i}\theta Q}\,, \tag{2.93}$$

with θ being an angular variable that is constrained to $\theta \in [0, 2\pi]$. The free energy of the theta vacuum is then defined as

$$\mathcal{F}(\theta) = -\ln \mathcal{Z}(\theta) = -\ln\left[\int \mathcal{D}A_\mu \, \mathrm{e}^{-S+\mathrm{i}\theta Q}\right] \tag{2.94}$$

and is a good starting point for studying the distribution of the topological charge and the basis for the definition of the topological susceptibility that we introduce in the next section.

2.4.3 The Topological Susceptibility

In this section, we define the central quantity of this work, namely the topological susceptibility. In general, a susceptibility is a measure for the response of a system to some perturbation. One well-known example of a susceptibility is the magnetic susceptibility that determines the magnetization M that a material experiences under exposure to an external magnetic field H:

$$M = \chi_\mathrm{m} H\,, \tag{2.95}$$

where χ_m is the magnetic susceptibility. In the path-integral formulation, the susceptibility is determined via the second derivative of the free energy [69]:

$$\chi_\mathrm{m} \sim \frac{\partial^2 \mathcal{F}}{\partial H^2}\,. \tag{2.96}$$

In complete analogy, we define the topological susceptibility as the response to a non-zero value of θ:

$$\chi_\mathrm{top} \equiv \frac{1}{\beta V}\frac{\partial^2 \mathcal{F}(\theta)}{\partial \theta^2}\bigg|_{\theta=0} \equiv \frac{\langle Q^2\rangle}{\beta V} \equiv \int \mathrm{d}^4x\, \langle q(0)q(x)\rangle\,. \tag{2.97}$$

The topological susceptibility measures fluctuations of the topological charge in the QCD vacuum and has many implications. Since topological effects are inherently non-perturbative, lattice QCD is a perfectly suitable method to precisely determine the susceptibility. While it is very precisely known at zero temperature via χPT [53], χPT fails above T_c, leaving lattice QCD as our only first-principles, systematically improvable method. However, lattice calculations at high temperatures become extremely challenging because the susceptibility is strongly suppressed. Nevertheless, the knowledge of the topological susceptibility at high temperatures is relevant for axion cosmology as elaborated in detail in Chap. 1. In particular, the axion mass is determined by the temperature dependence of the susceptibility:

$$m_\mathrm{a}^2(T) f_\mathrm{a}^2 = \chi_\mathrm{top}(T)\,. \tag{2.98}$$

This led to a lot of recent progress in determining this quantity at high temperatures [56–63]. In Chaps. 5 and 6, we also develop a novel method for determining the topological susceptibility at very high temperatures on the lattice.

The topological susceptibility is also closely related to the chiral anomaly and the explicit breaking of $\mathrm{U}(1)_\mathrm{A}$. As discussed in Sec. 2.3, the $\mathrm{U}(1)_\mathrm{A}$ symmetry of QCD is anomalous and explicitly broken by an instanton background field. As a consequence, the η' meson is not a Nambu-Goldstone boson, not even for vanishing quark masses, i.e., in the chiral limit. In 1979, Witten [120] and Veneziano [121] proposed a mechanism that explains the mass of the η' via the topological nature of the chiral anomaly. They found the result

$$\chi_\mathrm{top}^\mathrm{quenched} = \frac{f_\pi^2}{2N_\mathrm{f}}\left(m_\eta^2 + m_{\eta'}^2 - 2m_\mathrm{K}^2\right), \tag{2.99}$$

where f_π is the pion decay constant and m_η, $m_{\eta'}$, and m_K are the η, η', and kaon masses, respectively. In the chiral limit, both the kaon and the η meson are massless Nambu-Goldstone bosons and the mass of the η' meson therefore reads

$$m_{\eta'}^2 = \frac{2N_\mathrm{f}}{f_\pi^2}\chi_\mathrm{top}^\mathrm{quenched} \tag{2.100}$$

and is determined by the topological susceptibility calculated in zero-temperature pure SU(3) Yang-Mills theory.

The main aim of this work is to develop a method for determining the topological susceptibility at high temperatures on the lattice. In the next section, we present a semiclassical model of the QCD ground state that predicts for high temperatures the temperature dependence of the topological susceptibility. This result shows that the number of calorons becomes extremely small at high temperatures, which makes a statistically powerful lattice determination very challenging.

2.4.4 The Dilute Instanton Gas

In this section, we conclude our discussion on the role of topology in QCD by introducing a semiclassical model of the QCD vacuum that is based on the perturbative computation of fluctuations around the minimum of the partition function. We saw above that the QCD partition function is dominated by classical local minima – the instantons. An approximate ground state is therefore described, in the simplest case, by gas of non-interacting, well separated instantons. This so-called *dilute instanton gas approximation* (DIGA) was pioneered at zero temperature by 't Hooft [122] and further elaborated by Callan, Dashen, and Gross [119, 123]. Gross, Pisarski, and Yaffe eventually found the finite-temperature extension of the DIGA [124]. This model is powerful enough to determine the θ-depending free energy of QCD and hence also to derive the axion potential (1.9). It also predicts the temperature dependence of the topological susceptibility. In Chap. 4, we shall combine the DIGA with lattice discretization effects to study systematics of the lattice determination of the topological susceptibility.

The partition function of a one-BPST instanton (or one-anti-instanton) background field reads [123]

$$\mathcal{Z}_{\mathrm{I}} = \mathcal{Z}_{\bar{\mathrm{I}}} = \beta V \cdot \int_0^\infty \mathrm{d}\rho\, D(\rho, T) \equiv \beta V D\,, \tag{2.101}$$

where βV is the spacetime volume, $D(\rho, T)$ is the density of instantons of size ρ at temperature T, and

$$D(T) \equiv \int_0^\infty \mathrm{d}\rho\, D(\rho, T) \tag{2.102}$$

is the integrated instanton density. Note that in his initial calculation of the instanton density at zero temperature, 't Hooft found that the integral has an infrared divergence, meaning that very large instantons populate the vacuum, which contradicts the diluteness assumption. This "infrared disaster" [122] is fixed in a thermal medium as quantum fluctuations induce a Debye screening of the instanton electrical field and hence suppress their contribution [124].

In the following discussion, we shall often omit the explicit temperature dependence of D to simplify notation. A general instanton background with topological charge Q can be generated by the superposition of n BPST instantons and $\bar{n}$ BPST anti-instantons with $Q = n - \bar{n}$. By assuming a dilute gas of non-interacting, well-separated instantons, the corresponding partition function reads

$$\mathcal{Z}_Q \simeq \sum_{n,\bar{n}} \frac{\mathcal{Z}_{\mathrm{I}}^n \mathcal{Z}_{\bar{\mathrm{I}}}^{\bar{n}}}{n!\bar{n}!}\, \delta_{Q,n-\bar{n}} = \sum_{n,\bar{n}} \frac{(\beta V D)^{n+\bar{n}}}{n!\bar{n}!}\, \delta_{Q,n-\bar{n}}\,, \tag{2.103}$$

where the factorials take into account the possible permutations of instantons and anti-instantons. In analogy to Eq. (2.93), the theta vacuum is then described via the Fourier transform

$$\begin{aligned}\mathcal{Z}(\theta) = \sum_Q \mathrm{e}^{\mathrm{i}\theta Q}\, \mathcal{Z}_Q = \sum_{n,\bar{n}} \frac{(\beta V D)^{n+\bar{n}}}{n!\bar{n}!}\, \mathrm{e}^{\mathrm{i}\theta(n-\bar{n})} = \left(\sum_n \frac{\left(\beta V D\, \mathrm{e}^{\mathrm{i}\theta}\right)^n}{n!}\right)\left(\sum_{\bar{n}} \frac{\left(\beta V D\, \mathrm{e}^{-\mathrm{i}\theta}\right)^{\bar{n}}}{\bar{n}!}\right) \\ = \exp\left(\beta V D\, \mathrm{e}^{\mathrm{i}\theta}\right) \cdot \exp\left(\beta V D \mathrm{e}^{-\mathrm{i}\theta}\right) = \exp(2\beta V D \cos\theta)\,.\end{aligned} \tag{2.104}$$

The corresponding free energy reads

$$\mathcal{F}(\theta) = -\ln \mathcal{Z} = -2\beta V D \cos\theta\,. \tag{2.105}$$

Note that this results in an effective potential

$$V(\theta,T)\equiv\frac{1}{\beta V}(\mathcal{F}(\theta)-\mathcal{F}(0))=2D(T)(1-\cos\theta)\equiv\chi_{\text{top}}(T)(1-\cos\theta) \tag{2.106}$$

which is precisely the axion potential that we introduced in Eq. (1.9). The topological susceptibility in the DIGA is given as

$$\chi_{\text{top}}(T)\equiv\frac{1}{\beta V}\frac{\partial^2}{\partial\theta^2}\mathcal{F}(\theta)\bigg|_{\theta=0}=2D(T)\,. \tag{2.107}$$

The topological susceptibility is therefore proportional to the instanton density. This is in analogy to the magnetic susceptibility which is proportional to the magnetization that is defined as the density of magnetic dipoles in the material.

We now give the explicit expressions for the instanton density which is given as

$$D(T)=\int_0^\infty \mathrm{d}\rho\, D_0(\rho)G(\pi\rho T)\,, \tag{2.108}$$

where $D_0(\rho)$ is the instanton density at zero temperature, first calculated by 't Hooft in his seminal paper [122], and $G(\pi\rho T)$ are thermal corrections first determined by Gross, Pisarski, and Yaffe [124, 125]. We do not address the very involved calculation of these quantities but only give their results here. The zero-temperature instanton density to one-loop renormalization group invariant form in the $\overline{\text{MS}}$ scheme reads [124, 126]

$$D_0(\rho)=\frac{d_{\overline{\text{MS}}}}{\rho^5}\left(\frac{8\pi^2}{g_{\text{s}}^2(\mu_{\text{r}}=\rho^{-1})}\right)^6\left(\prod_{i=1}^{N_{\text{f}}}\rho m_i\right)\exp\left(-\frac{8\pi^2}{g_{\text{s}}^2(\mu_{\text{r}}=\rho^{-1})}\right), \tag{2.109}$$

where m_i is the mass of the quark with flavor i,

$$d_{\overline{\text{MS}}}=\frac{\exp\left(\frac{5}{6}-4.534122+0.291746\,N_{\text{f}}\right)}{\pi^2}\,, \tag{2.110}$$

and

$$\frac{4\pi^2}{g_{\text{s}}^2(\rho^{-1})}=\frac{33-2N_{\text{f}}}{6}\ln\left(\frac{1}{\rho\Lambda_{\text{QCD}}}\right)+\frac{153-19N_{\text{f}}}{66-4N_{\text{f}}}\ln\left(\ln\left(\frac{1}{\rho\Lambda_{\text{QCD}}}\right)\right)+\mathcal{O}\left(\frac{1}{\ln\left(\rho\Lambda_{\text{QCD}}\right)}\right) \tag{2.111}$$

is the renormalization-group improved running coupling of QCD. Note that replacing the strong coupling constant by the renormalization-group running coupling takes into account the quantum fluctuations.

The thermal corrections read [124, 125]

$$G(\lambda)=\exp\left\{-\frac{1}{3}\lambda^2(6+N_{\text{f}})-6A(\lambda)\left(3+\frac{N_{\text{f}}}{3}\right)\right\} \tag{2.112}$$

with the function

$$A(\lambda)=-\frac{1}{12}\ln\left(1+\frac{1}{3}\lambda^2\right)+\alpha\left(1+\gamma\lambda^{-3/2}\right)^{-8}, \tag{2.113}$$

where the parameters read $\alpha = 0.01289764$ and $\gamma = 0.15858$. Note that this thermal correction factor cuts off the ρ integral at $\pi\rho T \sim 1$ and therefore avoids the infrared disaster [124].

Putting everything together, we see that the topological susceptibility, to leading order perturbation theory, at high temperatures approximately scales as

$$\chi_{\text{top}}(T) \propto T^{-7-N_f/3}. \tag{2.114}$$

As this result reflects only the leading-order approximation of the temperature dependence of the topological susceptibility, and is expected to only be valid at very high temperatures, it is not sufficient for a precise determination of the topological susceptibility that can be used for axion cosmology. It is also expected that taking into account Debye screening may change this result. In particular, the DIGA predicts for pure SU(3) Yang-Mills theory the exponent to be -7, while in full QCD in the energy regime relevant for axion cosmology, i.e., for $N_f = 3$, the exponent is predicted to be -8. This result shows that the topological susceptibility is expected to fall off very quickly at high temperatures, making a statistically powerful lattice study challenging. One aim of this work is to determine the exponent for pure SU(3) Yang-Mills theory in a lattice study by measuring the topological susceptibility at three high temperatures. For this, we develop a new method that artificially enhances the number of the at high temperatures very rare calorons. This is explicitly done in Chaps. 5 and 6.

Chapter 3

Lattice Gauge Theory

As discussed in the previous chapter, perturbative approaches to QCD fail at low energies due to the large coupling constant. Lattice gauge theory is an alternative approach that is based on the numerical evaluation of the path integral of a QFT on a discretized spacetime grid. The foundations of lattice gauge theories were laid in 1974 by Kenneth G. Wilson in his seminal paper *Confinement of Quarks* [127]. In this chapter, we discuss the lattice formulation of QCD and elaborate all concepts that are relevant for this work. Because the remainder of this work will only consider the *quenched approximation*, i.e., pure SU(3) Yang-Mills theory without dynamical quarks, we shall only discuss the discretization of the gauge fields in this chapter. Moreover, we address the lattice discretization of the topological charge, which is the central quantity for a lattice determination of the topological susceptibility. We conclude this chapter with a discussion of the basic idea of lattice simulations including the statistical analysis. For detailed reviews on lattice gauge theory, we refer to the standard textbooks [128–131]. For our actual lattice simulations, we use the publicly available lattice code *openQCD-1.6* by Martin Lüscher [132]. We again want to stress that we work with antihermitian generators of SU(3) throughout this work, cf. App. A.1.

3.1 Basic Concepts of Lattice Gauge Theory

The basic idea of lattice gauge theories is discretizing four-dimensional spacetime on a four-dimensional hypercubic grid

$$\Lambda = \left\{ x = (x_0, x_1, x_2, x_3) \mid x_1, x_2, x_3 = 1, 2, \ldots, N_\mathrm{L};\ x_0 = 1, 2, \ldots, N_\tau \right\}, \tag{3.1}$$

where the lattice points are separated by the *lattice spacing* a, N_L is the number of lattice points in the spatial directions, and N_τ denotes the number of lattice points in the temporal direction. *A priori*, the lattice spacing has no physical meaning. On the lattice, all discretized operators need to be dimensionless and are rescaled by powers of a, i.e., $\mathcal{O} = a^{-d}\mathcal{O}_\mathrm{lat}$, where d is the dimension of the operator $\mathcal{O}$ in the continuum. However, *a posteriori*, a physical value is assigned to a in a process called *scale setting* by calculating a physically well-known quantity on the lattice, cf. Sec. 3.6. The coupling constant g_s as a physical input parameter is then connected to the lattice spacing.[1] Note that the discretization naturally introduces a momentum cutoff a^{-1} that regularizes the theory and removes ultraviolet divergences. This regularization scheme has the great advantage that gauge symmetry is manifestly conserved, although at the cost of the breaking of continuous Poincaré symmetry down to discrete translations and hypercubic rotations. In this work, we only consider *isotropic* lattices where the lattice spacing in the temporal and spatial directions is the same. However, in some applications, anisotropic lattices may be favorable, for instance when a very fine temporal resolution is required. To obtain continuum results from lattice QCD calculations, the continuum limit needs to be taken. However, lattice simulations are in general computationally very expensive and it is not feasible to simulate arbitrarily small lattice spacings. In practice, one therefore simulates only three or four different lattice spacings and then extrapolates to the continuum.

Following the statistical interpretation of the path integral given in Sec. 2.2, we work in the Euclidean (imaginary time) formulation of the theory. The action is then positive definite and hence the Boltz-

[1] Note that the only physical input parameters are the gauge couplings and the quark masses.

mann weight $\exp(-S)$ is positive and can be interpreted as a probability measure. Note, however, that extensions such as the inclusion of baryon chemical potential [133] or non-zero values of θ, or a lattice formulation in real time, lead to a complex action, cf. Eqs. (2.22) and (2.23). The Boltzmann weight then becomes highly oscillatory and cannot be interpreted as a probability measure any more. This issue is the infamous *sign problem* and as a consequence the applicability of lattice QCD is restricted to zero chemical potential. For a discussion of different approaches around the sign problem, we refer to Ref. [82].

As elaborated in Sec. 2.2, at finite temperature imaginary time is compactified to the interval $[0, \beta]$ with the inverse temperature β and (anti-)periodic boundary conditions are employed for bosons (fermions). Consequently, the physical extent of the temporal direction of our lattice is connected with the temperature of the system:

$$T = \frac{1}{aN_\tau}. \tag{3.2}$$

3.2 Pure Gauge Theory on the Lattice

In order to put pure SU(3) Yang-Mills theory on the lattice, we need to find a discretization of the gauge action

$$S_\mathrm{G} = -\frac{1}{2g_\mathrm{s}^2}\int \mathrm{d}^4x\, \mathrm{tr}\big[F_{\mu\nu}(x)F_{\mu\nu}(x)\big]. \tag{3.3}$$

A basic property that the lattice discretization of a gauge theory has to fulfill is gauge invariance. To obtain a discretization of the gauge action, we first need to note that in a naïve discretization of the fermion action, where a quark field $q(x)$ is placed on each lattice site x, terms of the form $\bar{q}(x)q(x+\hat{\mu})$ arise due to the discretized derivative that are clearly not gauge invariant.[2] To obtain a gauge-invariant expression, we therefore need *gauge transporters*. In the continuum, gauge transporters are defined as the path-ordered exponential integral of the gauge field A_μ

$$G(x,y) \equiv \mathcal{P}\exp\left(\int_{\mathcal{C}_{xy}} A\cdot \mathrm{d}s\right), \tag{3.4}$$

where $\mathcal{C}_{xy}$ is a path connecting the points x and y. Under SU(3) gauge transformations, the gauge transporter transforms as

$$G(x,y) \;\to\; \Omega(x)G(x,y)\Omega^\dagger(y), \qquad\qquad \Omega\colon \mathbb{R}^4 \to \mathrm{SU}(3). \tag{3.5}$$

A lattice discretization of the gauge transporter that connects two neighboring lattice sites x and $x+\hat{\mu}$ is given by the so-called *link variable*[3]

$$U_\mu(x) = \exp\big(aA_\mu(x)\big) = G(x, x+\hat{\mu}) + \mathcal{O}(a) \tag{3.6}$$

[2] We denote with $\hat{\mu}$ a vector with length a pointing in μ direction.

[3] We again want to stress that we work with antihermitian generators of SU(N) throughout this work such that there is no factor of i in the exponential.

that transforms via

$$U_\mu(x) \;\to\; \Omega(x) U_\mu(x) \Omega^\dagger(x+\hat{\mu})\,. \tag{3.7}$$

The link variables are oriented elements of the gauge group SU(3) that live on the links between two neighboring lattice sites, i.e., $U_\mu(x)$ lives on the link between x and $x+\hat{\mu}$. Note that the link variable pointing in the negative direction from x to $x-\hat{\mu}$ is given as

$$U_{-\mu}(x) = U_\mu^\dagger(x-\hat{\mu})\,. \tag{3.8}$$

Using the link variables, the combination $\bar{q}(x)U_\mu(x)q(x+\hat{\mu})$ is now gauge invariant.

The link variables are also the basic ingredient for discretizing the gauge action. For this, we first note that the trace of a closed loop $\mathcal{L}$ of link variables is gauge invariant:

$$\begin{aligned} L[U] \equiv \operatorname{tr}\left[\prod_{(x,\mu)\in\mathcal{L}} U_\mu(x)\right] &= \operatorname{tr}\big[U_{\mu_1}(x_1)U_{\mu_2}(x_2)\cdots U_{\mu_n}(x_n)\big] \\ &\to \operatorname{tr}\big[\Omega(x_1)U_{\mu_1}(x_1)\Omega^\dagger(x_2)\Omega(x_2)U_{\mu_2}(x_2)\Omega^\dagger(x_3)\cdots U_{\mu_n}\Omega^\dagger(x_1)\big] = L[U]\,, \end{aligned}$$

where we used the invariance of the trace under cyclic permutations and the unitarity of SU(3). The simplest possible closed loop consists of only four link variables that build a square and is the so-called *plaquette*[4]

$$\square_{\mu\nu}(x) \equiv U_\mu(x)U_\nu(x+\hat{\mu})U_\mu^\dagger(x+\hat{\nu})U_\nu^\dagger(x) \equiv$$  . (3.9)

Using the representation (3.6) of the link variables and Taylor-expanding it in the lattice spacing using the Baker-Campbell-Hausdorff formula, it is straightforward to show that

$$\square_{\mu\nu}(x) = \exp\big(a^2 F_{\mu\nu}(x) + \mathcal{O}(a^3)\big) = \mathbb{1} + a^2 F_{\mu\nu}(x) + \frac{a^4}{2} F_{\mu\nu}(x)F_{\mu\nu}(x) + \mathcal{O}(a^6)\,. \tag{3.10}$$

A simple discretization of the gauge action using plaquettes found by Wilson is the *Wilson gauge action*

$$S_{\mathrm{W}} = \frac{\beta_{\mathrm{lat}}}{3} \sum_{x\in\Lambda} \sum_{\mu<\nu} \operatorname{Re}\operatorname{tr}\big[\mathbb{1} - \square_{\mu\nu}(x)\big]\,, \tag{3.11}$$

where we use the common *inverse coupling* $\beta_{\mathrm{lat}} = 6/g_s^2$.[5] The Wilson action consists essentially of the sum over the trace of all possible plaquettes where the real part ensures that both orientations of each plaquette are taken into account. This can easily be seen by noting that

$$\operatorname{Re}\square_{\mu\nu}(x) = \frac{1}{2}\big(\square_{\mu\nu}(x) + \square_{\mu\nu}^\dagger(x)\big) = \frac{1}{2}\big(\square_{\mu\nu}(x) + \square_{\nu\mu}(x)\big)\,. \tag{3.12}$$

[4] In the following, we shall often visualize closed loops of link variables. These visualizations show the μ-ν plane, where μ points to the right and ν points to the top, and the lattice site x is denoted with a blue dot that is also the starting and end point of the loop. Note that in those closed loops *no* summation over μ and ν is implied as both indices are fixed.

[5] To avoid confusion between the inverse coupling and the inverse temperature that are usually both named β in the literature, we shall denote the inverse coupling β_{lat}.

By expanding the link variables and using the Baker-Campbell-Hausdorff formula, it follows that

$$S_{\mathrm{W}} = \frac{\beta_{\mathrm{lat}}}{3} \sum_{x\in\Lambda} \sum_{\mu<\nu} \mathrm{Re}\,\mathrm{tr}\big[\mathbb{1} - \square_{\mu\nu}(x)\big] = -\frac{a^4}{2g_{\mathrm{s}}^2} \sum_{x\in\Lambda} \sum_{\mu,\,\nu} \mathrm{tr}\big[F_{\mu\nu}(x) F_{\mu\nu}(x)\big] + \mathcal{O}\big(a^2\big), \tag{3.13}$$

showing that the Wilson action approaches the continuum action up to $\mathcal{O}\big(a^2\big)$ corrections.

3.3 Symanzik Improvement Program

When discretizing a theory on the lattice, we always have to work with finite differences and operators approach their continuum expressions only in the continuum limit where the lattice spacing is sent to zero, $a \to 0$. However, the continuum limit is usually an involved task since the computational resources limit the number of lattice points that can be achieved. Thus, in practice, one works with, e.g., three different lattice spacings and extrapolates the results to $a = 0$. One way to improve the stability of those extrapolations is the reduction of discretization effects. A systematic way for reducing discretization effects is the *Symanzik improvement program* [134, 135] that we shall discuss here for the gauge action. In the previous section, we saw that the simple Wilson gauge action reproduces the continuum Yang-Mills action up to errors of $\mathcal{O}\big(a^2\big)$. The central idea of Symanzik was to add higher-order terms to the action that vanish in the continuum limit. By tuning the coefficients appropriately, we can cancel the discretization effects order by order.

For the Wilson action, the simplest higher-order terms have dimension six; those are closed loops of six link variables. The general form of the improved action is then given as the so-called *Lüscher-Weisz action* [136–138]

$$S_{\mathrm{imp}} = \frac{\beta_{\mathrm{lat}}}{3} \sum_{i=0}^{3} c_i\big(g_{\mathrm{s}}^2\big) \sum_{x} \sum_{U\in\mathcal{P}_i(x)} \mathrm{Re}\,\mathrm{tr}[\mathbb{1} - U], \tag{3.14}$$

where the c_i are coefficients of the different sets of closed loops

$\mathcal{P}_0(x) \equiv$  (6 different *plaquettes* per site),

$\mathcal{P}_1(x) \equiv$ 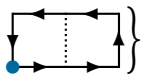 (12 different *rectangles* per site),

$\mathcal{P}_2(x) \equiv$ 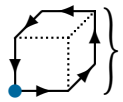 (16 different *parallelograms* per site),

$\mathcal{P}_3(x) \equiv$ 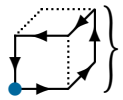 (48 different *bent rectangles* per site).

Choosing the coefficients appropriately allows to cancel discretization errors order by order. In this work, we only want to remove the discretization effects of $\mathcal{O}\big(a^2\big)$. It is therefore sufficient to only consider one type of dimension-six operators, namely the simple 1×2 rectangles in $\mathcal{P}_1$ [139]. In the following, we hence set $c_2 = c_3 \equiv 0$ and consider actions of the form

$$S_{\mathrm{imp}} = \frac{\beta_{\mathrm{lat}}}{3} \sum_{x} \sum_{\mu<\nu} \Big\{ c_0\,\mathrm{Re}\,\mathrm{tr}\Big(\mathbb{1} - \square_{\mu\nu}(x)\Big) + c_1\Big[\mathrm{Re}\,\mathrm{tr}\Big(\mathbb{1} - P_{\mu\nu}^{(1\times 2)}(x)\Big) + \mathrm{Re}\,\mathrm{tr}\Big(\mathbb{1} - P_{\mu\nu}^{(2\times 1)}(x)\Big)\Big] \Big\}, \tag{3.15}$$

where we introduced the rectangles

$$P_{\mu\nu}^{(1\times2)}(x) \equiv U_\mu(x)U_\nu(x+\hat{\mu})U_\nu(x+\hat{\mu}+\hat{\nu})U_\mu^\dagger(x+2\hat{\nu})U_\nu^\dagger(x+\hat{\nu})U_\nu^\dagger(x) \equiv \quad , \tag{3.16}$$

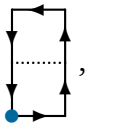

$$P_{\mu\nu}^{(2\times1)}(x) \equiv U_\mu(x)U_\mu(x+\hat{\mu})U_\nu(x+2\hat{\mu})U_\mu^\dagger(x+\hat{\mu}+\hat{\nu})U_\mu^\dagger(x+\hat{\nu})U_\nu^\dagger(x) \equiv \quad . \tag{3.17}$$

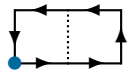

The coefficients c_0 and c_1 can be calculated perturbatively and are conventionally normalized such that

$$c_0\big(g_s^2\big) + 8c_1\big(g_s^2\big) = 1\,. \tag{3.18}$$

This condition can always be enforced by an appropriate renormalization of the coupling [138]. At tree level, the coefficients are constant; two popular choices lead to the *Symanzik action* [136, 137], where $c_0 = {}^5/_3$ and $c_1 = {}^{-1}/_{12}$, and to the *Iwasaki action* [140, 141], where $c_0 = 3.648$ and $c_1 = -0.331$.

Via Eq. (3.14) we can also introduce an *overimproved* action by demanding that the $\mathcal{O}\big(a^2\big)$ errors do not cancel, but instead appear with the opposite sign. This is achieved by the choice of parameters $c_0 = {}^7/_3$, $c_1 = {}^{-1}/_6$. We shall use the overimproved action in the context of gradient flow in Chap. 4.

3.4 The Lattice Field-Strength Tensor

In this section, we address the lattice discretization of the field-strength tensor. This is a particularly important quantity as it is the main building block for the discretization of the topological charge which is the central observable needed for the lattice determination of the topological susceptibility. We therefore discuss different discretizations of the field-strength tensor and then address the definition of the topological charge on the lattice.

In Eq. (3.10), we saw by expanding the plaquette that

$$\square_{\mu\nu}(x) = \mathbb{1} + a^2 F_{\mu\nu}(x) + \mathcal{O}\big(a^4\big). \tag{3.19}$$

A simple lattice representation of the field-strength tensor is therefore given as

$$F_{\mu\nu}^{\text{lat}}(x) = \frac{1}{2a^2}\left[\Big(\square_{\mu\nu}(x) - \square_{\mu\nu}^\dagger(x)\Big) - \frac{1}{3}\,\text{tr}\Big(\square_{\mu\nu}(x) - \square_{\mu\nu}^\dagger(x)\Big)\mathbb{1}\right] + \mathcal{O}\big(a^2\big)\,, \tag{3.20}$$

where we subtracted the trace to ensure that the field-strength tensor as an element of the Lie algebra $\mathfrak{su}(3)$ is traceless. The disadvantage of this discretization is that it is "centered" not on the lattice site x but in the middle of the μ-ν plaquette of x. This leads to $\mathcal{O}(a)$ errors in the expression $\epsilon_{\mu\nu\rho\sigma}F_{\mu\nu}F_{\rho\sigma}$ that is needed in the discretization of the topological charge.

In the remainder of this section, we discuss more sophisticated discretizations of the field-strength tensor that turn out to be useful in the lattice definition of the topological charge. We start with the standard clover definition and then present the Symanzik improvement procedure that is used to obtain an $\mathcal{O}\big(a^2\big)$ improved version of the field-strength tensor. We finally present the lattice discretization of the topological charge.

3.4.1 Clover Field-Strength Tensor

A more sophisticated discretization of the field-strength tensor is given by the so-called clover definition

$$F_{\mu\nu}^{\text{clov}}(x) = \frac{1}{2a^2}\left[\left(W_{\mu\nu}^{(1,1)}(x) - W_{\mu\nu}^{(1,1)\dagger}(x)\right) - \frac{1}{3}\,\text{tr}\left(W_{\mu\nu}^{(1,1)}(x) - W_{\mu\nu}^{(1,1)\dagger}(x)\right)\mathbb{1}\right] + \mathcal{O}\left(a^2\right), \tag{3.21}$$

where we introduced the so-called *clover term*[6]

$$W_{\mu\nu}^{(1,1)}(x) = \frac{1}{4}\left(\square_{\mu\nu}(x) + \square_{\nu-\mu}(x) + \square_{-\mu-\nu}(x) + \square_{-\nu\mu}(x)\right) \equiv \frac{1}{4}$$

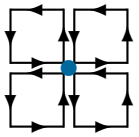

. (3.22)

The advantage of the clover discretization compared to to the simple discretization (3.20) is that as a four-plaquette average it is centered at the lattice site x and therefore the field-strength tensor also obeys the hypercubic symmetries. The corresponding discretization of the topological charge thus only has errors of $\mathcal{O}\left(a^2\right)$.

3.4.2 Improved Field-Strength Tensor

The clover discretization of the field-strength tensor that we elaborated in the last section has the advantage that it obeys the hypercubic symmetries. However, it still has large discretization effects of $\mathcal{O}\left(a^2\right)$. In the following, we therefore construct an $\mathcal{O}\left(a^4\right)$ improved version of the field-strength tensor in the spirit of the Symanzik improvement program following Refs. [142, 143]. For this, we define an extension of the clover by 1×2 rectangles:

$$W_{\mu\nu}^{(1,2)}(x) \equiv \frac{1}{8}$$

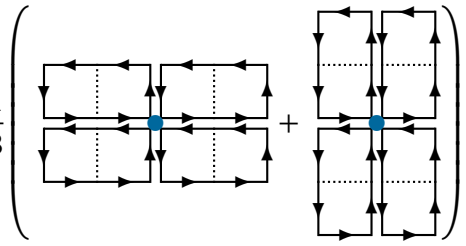

. (3.23)

We also define the combinations

$$C_{\mu\nu}^{(1,1)}(x) = \frac{1}{2a^2}\left[\left(W_{\mu\nu}^{(1,1)}(x) - W_{\mu\nu}^{(1,1)\dagger}(x)\right) - \frac{1}{3}\,\text{tr}\left(W_{\mu\nu}^{(1,1)}(x) - W_{\mu\nu}^{(1,1)\dagger}(x)\right)\mathbb{1}\right], \tag{3.24}$$

$$C_{\mu\nu}^{(1,2)}(x) = \frac{1}{2a^2}\left[\left(W_{\mu\nu}^{(1,2)}(x) - W_{\mu\nu}^{(1,2)\dagger}(x)\right) - \frac{1}{3}\,\text{tr}\left(W_{\mu\nu}^{(1,2)}(x) - W_{\mu\nu}^{(1,2)\dagger}(x)\right)\mathbb{1}\right]. \tag{3.25}$$

By expanding those expressions for small a, we obtain [143]

$$\begin{aligned} C_{\mu\nu}^{(1,1)}(x) &= F_{\mu\nu}(x) + \frac{1}{6}a^2\left(\partial_\mu^2 + \partial_\nu^2\right)F_{\mu\nu}(x) + \frac{1}{120}a^4\left(\partial_\mu^4 + \partial_\nu^4\right)F_{\mu\nu}(x) + \frac{1}{36}a^4\left(\partial_\mu^2\partial_\nu^2\right)F_{\mu\nu}(x) + \mathcal{O}\left(a^6\right), \\ C_{\mu\nu}^{(1,2)}(x) &= 2F_{\mu\nu}(x) + \frac{5}{6}a^2\left(\partial_\mu^2 + \partial_\nu^2\right)F_{\mu\nu}(x) + \frac{17}{120}a^4\left(\partial_\mu^4 + \partial_\nu^4\right)F_{\mu\nu}(x) + \frac{2}{9}a^4\left(\partial_\mu^2\partial_\nu^2\right)F_{\mu\nu}(x) + \mathcal{O}\left(a^6\right). \end{aligned} \tag{3.26}$$

[6] The name comes from the fact that the visualization of the term looks like a four-leaf clover.

Using a proper linear combination of both, we can therefore remove the $\mathcal{O}(a^2)$ corrections:

$$F_{\mu\nu}^{\text{imp}}(x) = k_1 C_{\mu\nu}^{(1,1)}(x) + k_2 C_{\mu\nu}^{(1,2)}(x), \tag{3.27}$$

where the coefficients k_1 and k_2 need to fulfill the conditions

$$k_1 + 2k_2 = 1, \tag{3.28}$$

$$\frac{1}{6}k_1 + \frac{5}{6}k_2 = 0 \tag{3.29}$$

that ensure that the terms of $\mathcal{O}(a^2)$ are removed while the terms proportional to $F_{\mu\nu}(x)$ add up to the correct weight. Solving the system, we finally obtain the improved field-strength tensor

$$F_{\mu\nu}^{\text{imp}}(x) = \frac{5}{3}C_{\mu\nu}^{(1,1)}(x) - \frac{1}{3}C_{\mu\nu}^{(1,2)}(x) = F_{\mu\nu}(x) - \frac{1}{30}a^4\left(\partial_\mu^4 + \partial_\nu^4\right)F_{\mu\nu}(x) - \frac{1}{36}a^4\left(\partial_\mu^2\partial_\nu^2\right)F_{\mu\nu}(x) + \mathcal{O}(a^6). \tag{3.30}$$

In principle, clover terms of more complex building blocks like parallelograms or larger rectangles could be used to remove even higher errors. However, as can be seen from Eq. (3.30), to remove the errors of $\mathcal{O}(a^4)$ we already need two new clover terms.

3.4.3 The Topological Charge

We now present the lattice discretization of the central quantity in a lattice determination of the topological susceptibility, namely the topological charge. On the lattice, the topological charge can be defined in various ways. For a comparison of different definitions, see, e.g., Ref. [144]. On the one hand, the index theorem (2.32) can be used to define the topological charge as the difference of the number of left- and right-handed zero modes of the Dirac operator. The advantage of this fermionic definition is that the lattice topological charge is per definition an integer, as it has to be in the continuum. However, it requires the precise determination of chiral zero modes of the Dirac operator which is a highly non-trivial task since not all lattice discretizations of the Dirac operator obey chiral symmetry, and using, e.g., the chirally symmetric overlap discretization is quite expensive [145–147]. For a review on chiral fermions on the lattice, we refer to Ref. [148].

On the other hand, the lattice topological charge is in the field theoretic or gluonic definition given as the sum over the topological charge density

$$Q = a^4 \sum_x q(x), \tag{3.31}$$

where

$$q(x) = -\frac{1}{32\pi^2}\epsilon_{\mu\nu\rho\sigma}\,\text{tr}\left(\hat{F}_{\mu\nu}(x)\hat{F}_{\rho\sigma}(x)\right) = \frac{1}{8\pi^2}\left(\hat{F}_{01}^a(x)\hat{F}_{23}^a(x) + \hat{F}_{02}^a(x)\hat{F}_{31}^a(x) + \hat{F}_{03}^a(x)\hat{F}_{12}^a(x)\right) \tag{3.32}$$

with $\hat{F}_{\mu\nu}$ being a discretization of the field-strength tensor. We therefore have three different lattice versions of the topological charge that we shall use throughout this work:

$$Q_{\text{lat}} = Q + \mathcal{O}(a), \tag{3.33a}$$

$$Q_{\text{clov}} = Q + \mathcal{O}(a^2), \tag{3.33b}$$

$$Q_{\text{imp}} = Q + \mathcal{O}(a^4). \tag{3.33c}$$

However, a naïve computation of the topological charge as defined in Eqs. (3.31) and (3.32) leads to severe problems. On the one hand, due to discretization effects, the lattice topological charge in general does not give an integer. We have, however, already mildened this problem by improving the lattice discretization of the field strength tensor.[7] The improved version of the topological charge gives values that are much closer to integers as we shall see in detail in Chap. 4 in the context of the lattice discretization of instantons and calorons. While in the continuum the different topological sectors are truly disparate and are only connected via configurations with infinite action, on the lattice there are still finite-action configurations that connect the sectors. These are referred to as *dislocations* and their existence is of great importance for our reweighting technique described in Chap. 5 since they allow for a smooth "tunneling" between topological sectors. On the other hand, the lattice topological charge is badly contaminated by UV fluctuations. This is especially problematic for the topological charge since one is in general not only interested in the expectation value, where the UV fluctuations should average out with a large enough number of configurations, but also wants to decide whether a given configuration is an instanton or not. However, the UV fluctuations can lead to completely wrong results for the topological charge. To avoid this issue, we need to remove those fluctuations and "smoothen" our lattice configurations. This is done with the aid of gradient flow as discussed in the next section.

3.5 Gradient Flow

In this work, we use the *Yang-Mills gradient flow* that was developed in the last decade as a very useful tool to study non-perturbative effects of strongly-coupled gauge theories [149–155]. It is a smoothing technique that systematically removes ultraviolet fluctuations by driving the system towards the minimum of the (flow-)action. This technique has its roots in older studies employing *cooling* [156–159], with gradient flow representing a better-controlled and better-understood form of gauge-link cooling. With gradient flow, a well-defined parameter $t \geq 0$, the so-called *flow time*,[8] controls the extent of smearing applied. In the continuum, this is achieved by evolving the system with the flow equation

$$\partial_t B_\mu(x,t) = D_\nu G_{\nu\mu}(x,t), \qquad B_\mu(x,0) = A_\mu(x), \tag{3.34}$$

where $B_\mu(x,t)$ is the gauge field flowed by t, and

$$G_{\mu\nu} = \partial_\mu B_\nu - \partial_\nu B_\mu + \left[B_\mu, B_\nu\right] \tag{3.35}$$

and $D_\mu = \partial_\mu + \left[B_\mu, \cdot\right]$ are the flowed field-strength tensor and covariant derivative, respectively. The smoothing property can be explicitly seen by expressing the flowed gauge field to leading order in the coupling in terms of the initial gauge field [151]

$$B_\mu(x,t) \simeq \int \mathrm{d}^4 y \, K_t(x-y) A_\mu(y) \tag{3.36}$$

with the Gaußian kernel

$$K_t(z) = \frac{\mathrm{e}^{-z^2/4t}}{(4\pi t)^2}\,. \tag{3.37}$$

[7] Note, however, that our results are only free of $\mathcal{O}(a^2)$ errors if both all observables and the action that is used for the update of the configurations are $\mathcal{O}(a^2)$ improved, cf. Sec. 3.7.

[8] In order to avoid confusion, we denote the flow time with t while the (imaginary) time is denoted with τ or x_0.

This expression explicitly shows that – to leading order – applying gradient flow corresponds to averaging the gauge field over a spacetime sphere with radius $2\sigma = \sqrt{8t}$, where $\sigma = \sqrt{2t}$ is the standard deviation of the Gaußian kernel. Note that on the lattice the full flow equation is solved non-perturbatively and hence higher-order effects appear that spoil this simple interpretation.

The simplest lattice discretization of the flow equation was found by Lüscher [150, 151] and uses the simplest Yang-Mills lattice action, namely the Wilson action (3.11). The so-called *Wilson flow equation* reads

$$a^2\big(\partial_t V_\mu(x,t)\big)V_\mu^\dagger(x,t) = -g_s^2\partial_{x,\mu}S_{\mathrm{W}}[V_\mu], \qquad V_\mu(x,0) = U_\mu(x), \tag{3.38}$$

where $V_\mu(x,t)$ denotes the flowed link variables and $\partial_{x,\mu}f(U) = T^a\partial^a_{x,\mu}f(U)$ is the Lie-algebra valued derivative of a function $f(U)$ with respect to the link variable $U_\mu(x)$. We define the Lie derivative in the direction of the generator T^a via

$$\partial^a_{x,\mu}f(U_\nu(y)) = \frac{\mathrm{d}}{\mathrm{d}\epsilon}f\big(U^\epsilon_\nu(y)\big)\bigg|_{\epsilon=0}, \qquad U^\epsilon_\nu(y) = \begin{cases} \mathrm{e}^{\epsilon T^a}U_\mu(x), & (\nu,y) = (\mu,x) \\ U_\nu(y), & \text{otherwise} \end{cases}. \tag{3.39}$$

One problem with the Wilson flow as described above is that it has large cutoff effects that are of $\mathcal{O}(a^2)$. Recently, the Symanzik improvement program was applied and all cutoff effects of $\mathcal{O}(a^2)$ were removed at tree level, leading to the so-called *Zeuthen flow* [160]

$$a^2\big(\partial_t V_\mu(x,t)\big)V_\mu^\dagger(x,t) = -g_s^2\left(1 + \frac{a^2}{12}\nabla^*_\mu\nabla_\mu\right)\partial_{x,\mu}S_{\mathrm{imp}}[V], \tag{3.40}$$

where S_{imp} is the tree-level improved Lüscher-Weisz action as defined in Eq. (3.14) and

$$a\nabla_\mu f(x) = U_\mu(x)f(x+\hat{\mu})U_\mu^\dagger(x) - f(x), \tag{3.41}$$

$$a\nabla^*_\mu f(x) = f(x) - U_\mu^\dagger(x-\hat{\mu})f(x-\hat{\mu})U_\mu(x-\hat{\mu}) \tag{3.42}$$

are the discretized adjoint covariant forward and backward derivatives, respectively. The unexpected additional factor $\left(1 + a^2\nabla^*_\mu\nabla_\mu/12\right)$ can be understood as follows. We know that improvement requires replacing square plaquettes with a linear combination of squares and rectangles. The Symanzik action does this in the four spacetime directions; the added term does it in the flow-time direction.

Additionally, we use an overimproved gradient flow

$$a^2\big(\partial_t V_\mu(x,t)\big)V_\mu^\dagger(x,t) = -g_s^2\partial_{x,\mu}S_{\mathrm{OI}}[V_\mu] \tag{3.43}$$

that uses the overimproved action defined in Sec. 3.3 and allows for stable topological solutions under flow, cf. Chap. 4.

In the remainder of this section, we explicitly calculate the Lie derivatives in the Wilson and Zeuthen flow equations to obtain an explicit expression that can be coded on the lattice. In practice, these flow equations are then integrated using Euler or Runge-Kutta integrators as already implemented in openQCD. For a comprehensive overview of those numerical methods, we refer to Ref. [161].

3.5.1 Wilson Flow

We now explicitly calculate the "Wilson gauge force"

$$\mathcal{F}^{\mathrm{W}}_\mu(x) \equiv -g_s^2T^a\partial^a_{x,\mu}S_{\mathrm{W}}[U] \tag{3.44}$$

that is part of the Wilson flow equation (3.38). Using the definition of the Lie derivative (3.39), the Wilson action (3.11), and the chain rule, we obtain

$$\begin{aligned}
\partial^a_{x,\mu} S_{\mathrm{W}} &= \frac{\mathrm{d}}{\mathrm{d}\epsilon} S_{\mathrm{W}}[U^\epsilon] \\
&= -\frac{2}{g_{\mathrm{s}}^2} \sum_n \sum_{\sigma<\nu} \mathrm{Re}\,\mathrm{tr}\Big\{ \frac{\mathrm{d}}{\mathrm{d}\epsilon} \big[U^\epsilon_\sigma(n) U^\epsilon_\nu(n+\hat{\sigma}) U^{\epsilon\dagger}_\sigma(n+\hat{\nu}) U^{\epsilon\dagger}_\nu(n) \big] \Big\}_{\epsilon=0} \\
&= -\frac{2}{g_{\mathrm{s}}^2} \mathrm{Re}\,\mathrm{tr}\Bigg\{ T^a \Bigg[\sum_{\mu<\nu} \Big(U_\mu(x) U_\nu(x+\hat{\mu}) U^\dagger_\mu(x+\hat{\nu}) U^\dagger_\nu(x) + U_\mu(x) U^\dagger_\nu(x-\hat{\nu}+\hat{\mu}) U^\dagger_\mu(x-\hat{\nu}) U_\nu(x-\hat{\nu}) \Big) \\
&\qquad + \sum_{\nu<\mu} \Big(U_\mu(x) U^\dagger_\nu(x-\hat{\nu}+\hat{\mu}) U^\dagger_\mu(x-\hat{\nu}) U_\nu(x-\hat{\nu}) + U_\mu(x) U_\nu(x+\hat{\mu}) U^\dagger_\mu(x+\hat{\nu}) U^\dagger_\nu(x) \Big) \Bigg] \Bigg\} \\
&= -\frac{2}{g_{\mathrm{s}}^2} \mathrm{Re}\,\mathrm{tr}\Bigg\{ T^a \sum_{\nu\neq\mu} \big(\square_{\mu\nu}(x) + \square_{\mu-\nu}(x) \big) \Bigg\} \equiv -\frac{2}{g_{\mathrm{s}}^2} \mathrm{Re}\,\mathrm{tr}\big\{ T^a \Omega_\mu(x) \big\} ,
\end{aligned} \tag{3.45}$$

where we defined

$$\Omega_\mu(x) \equiv \sum_{\nu\neq\mu} \big(\square_{\mu\nu}(x) + \square_{\mu-\nu}(x) \big) \equiv \sum_{\nu\neq\mu} \Bigg(\quad + \quad \Bigg) . \tag{3.46}$$

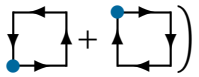

The real part is eliminated via

$$\mathrm{Re}\,\mathrm{tr}\big\{ T^a \Omega_\mu \big\} = \frac{1}{2} \Big(\mathrm{tr}\big\{ T^a \Omega_\mu \big\} + \mathrm{tr}\big\{ T^a \Omega_\mu \big\}^\dagger \Big) = \frac{1}{2} \Big(\mathrm{tr}\big\{ T^a \Omega_\mu \big\} + \mathrm{tr}\big\{ \Omega^\dagger_\mu T^{a\dagger} \big\} \Big) = \frac{1}{2} \mathrm{tr}\Big\{ T^a \Big(\Omega_\mu - \Omega^\dagger_\mu \Big) \Big\} , \tag{3.47}$$

where we used that the generators are antihermitian. Contracting with the generators, we therefore find

$$\mathcal{F}^{\mathrm{W}}_\mu(x) = -g_{\mathrm{s}}^2 T^a \partial^a_{x,\mu} S_{\mathrm{W}} = T^a \,\mathrm{tr}\Big\{ T^a \Big(\Omega_\mu(x) - \Omega^\dagger_\mu(x) \Big) \Big\} . \tag{3.48}$$

We finally contract the generators using the identity[9] $A \equiv \frac{1}{3}\mathrm{tr}(A)\mathbb{1} - 2T^a \,\mathrm{tr}(T^a A)$ that holds for any $A \in \mathbb{C}^{3\times 3}$ and obtain

$$\mathcal{F}^{\mathrm{W}}_\mu(x) = \frac{1}{2} \Big(\Omega_\mu(x) - \Omega^\dagger_\mu(x) \Big) - \frac{1}{6} \mathrm{tr}\Big(\Omega_\mu(x) - \Omega^\dagger_\mu(x) \Big) \mathbb{1} . \tag{3.49}$$

3.5.2 Zeuthen Flow

In this section we explicitly calculate the gauge force of the Lüscher-Weisz action of the form

$$S_{\mathrm{imp}} = \frac{2}{g_{\mathrm{s}}^2} \sum_x \sum_{\mu<\nu} \Big\{ c_0 \,\mathrm{Re}\,\mathrm{tr}\big(\mathbb{1} - \square_{\mu\nu}(x) \big) + c_1 \,\mathrm{Re}\,\mathrm{tr}\Big[2\cdot\mathbb{1} - \Big(P^{(1\times 2)}_{\mu\nu} + P^{(2\times 1)}_{\mu\nu} \Big) \Big] \Big\} \equiv c_0 S_{\mathrm{W}} + c_1 S_{\mathrm{rect}} , \tag{3.50}$$

[9] Note that the set $\{\mathbb{1}, T^a\}$ builds a basis of $\mathbb{C}^{3\times 3}$.

where $c_0 = 5/3$ and $c_1 = -1/12$ corresponds to the Symanzik action and $c_0 = 7/3$ and $c_1 = -1/6$ corresponds to the overimproved action. After a lengthy but straightforward calculation, the Lie derivative of the rectangle part of the Symanzik action reads

$$\begin{aligned}\partial^a_{x,\mu} S_{\text{rect}} &= -\frac{2}{g_s^2}\,\text{Re}\,\text{tr}\left\{ T^a \sum_{\nu\neq\mu}\Big(P^{(1\times 2)}_{\mu\nu}(x) + P^{(2\times 1)}_{\mu\nu}(x) + P^{(1\times 2)}_{\mu-\nu}(x) + P^{(2\times 1)}_{\mu-\nu}(x) + Q_{\mu\nu}(x) + Q_{\mu-\nu}(x)\Big)\right\} \\ &\equiv \text{Re}\,\text{tr}\big\{T^a \Xi_\mu(x)\big\}\,, \end{aligned} \tag{3.51}$$

where

$$\Xi_\mu(x) \equiv \sum_{\nu\neq\mu}\Big(P^{(1\times 2)}_{\mu\nu}(x) + P^{(2\times 1)}_{\mu\nu}(x) + P^{(1\times 2)}_{\mu-\nu}(x) + P^{(2\times 1)}_{\mu-\nu}(x) + Q_{\mu\nu}(x) + Q_{\mu-\nu}(x)\Big) \tag{3.52}$$

$$\equiv$$ 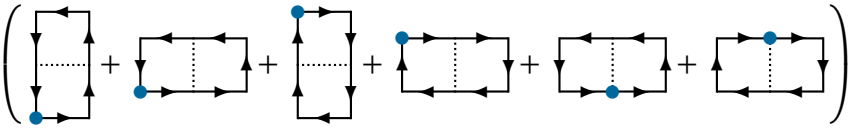 (3.53)

with the additional rectangle

$$Q_{\mu\nu}(x) = U_\mu(x) U_\nu(x+\hat\mu) U^\dagger_\mu(x+\hat\nu) U^\dagger_\mu(x+\hat\nu-\hat\mu) U^\dagger_\nu(x-\hat\mu) U_\mu(x-\hat\mu) \equiv$$ 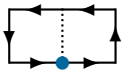 . (3.54)

The rectangle part of the gauge force then reads

$$\mathcal{F}^{\text{rect}}_\mu(x) = \frac{1}{2}\Big(\Xi_\mu(x) - \Xi^\dagger_\mu(x)\Big) - \frac{1}{6}\,\text{tr}\Big(\Xi_\mu(x) - \Xi^\dagger_\mu(x)\Big)\mathbb{1} \tag{3.55}$$

and the complete gauge force of the Lüscher-Weisz action eventually reads

$$\mathcal{F}^{\text{LW}}_\mu(x) = \frac{1}{2}\Big[c_0\Big(\Omega_\mu(x) - \Omega^\dagger_\mu(x)\Big) + c_1\Big(\Xi_\mu(x) - \Xi^\dagger_\mu(x)\Big)\Big] - \frac{\mathbb{1}}{6}\,\text{tr}\Big[c_0\Big(\Omega_\mu(x) - \Omega^\dagger_\mu(x)\Big) + c_1\Big(\Xi_\mu(x) - \Xi^\dagger_\mu(x)\Big)\Big]. \tag{3.56}$$

For the right-hand side of the Zeuthen flow equation (3.40) we also need to apply the lattice derivatives to the force:

$$\tilde{\mathcal{F}}^{\text{LW}}_\mu(x) = \left(1 + \frac{a^2}{12}\nabla^*_\mu\nabla_\mu\right)\mathcal{F}^{\text{LW}}_\mu(x)\,. \tag{3.57}$$

We therefore calculate

$$a\nabla_\mu \mathcal{F}^{\text{LW}}_\mu(x) = U_\mu(x)\mathcal{F}^{\text{LW}}_\mu(x+\hat\mu)U^\dagger_\mu(x) - \mathcal{F}^{\text{LW}}_\mu(x)\,, \tag{3.58}$$

$$a^2\nabla^*_\mu\nabla_\mu \mathcal{F}^{\text{LW}}_\mu(x) = U_\mu(x)\mathcal{F}^{\text{LW}}_\mu(x+\hat\mu)U^\dagger_\mu(x) - 2\mathcal{F}^{\text{LW}}_\mu(x) + U^\dagger_\mu(x-\hat\mu)\mathcal{F}^{\text{LW}}_\mu(x-\hat\mu)U_\mu(x-\hat\mu) \tag{3.59}$$

and find our final result

$$\tilde{\mathcal{F}}^{\text{LW}}_\mu(x) = \frac{5}{6}\mathcal{F}^{\text{LW}}_\mu(x) + \frac{1}{12}\Big[U_\mu(x)\mathcal{F}^{\text{LW}}_\mu(x+\hat\mu)U^\dagger_\mu(x) + U^\dagger_\mu(x-\hat\mu)\mathcal{F}^{\text{LW}}_\mu(x-\hat\mu)U_\mu(x-\hat\mu)\Big]. \tag{3.60}$$

Geometrically, the force link variable is replaced by $5/6$ of itself plus $1/12$ of the parallel-transported in positive and negative μ direction neighboring force links.

3.6 Scale Setting

In order to extract physics information from a lattice calculation, first the scale has to be set, i.e., we need to determine the size of the lattice spacing a. This can be done by measuring a quantity in lattice units that is already known in physical units. A common choice is the so-called *Sommer parameter* r_0 [162] which is connected to the static quark potential $V(r)$. Its physical value is given as $r_0 = 0.49(2)\,\mathrm{fm}$ [163]. On the lattice, the static quark potential is connected to the Wilson loop [128]

$$\langle W_{\mathcal{C}} \rangle \propto \exp(-\tau V(r)), \tag{3.61}$$

where the contour $\mathcal{C}$ is a $\tau \times r$ Wilson loop, i.e., an $aN_\tau \times aN_\mathrm{L}$ rectangle on the lattice. Taking the spatial derivative of the potential, we arrive at the force between two static quarks

$$F(r) = \frac{\mathrm{d}V(r)}{\mathrm{d}r}. \tag{3.62}$$

The Sommer parameter on the lattice is now defined via

$$F(r_0) r_0^2 = 1.65 \tag{3.63}$$

in accordance with experimental data. In Ref. [164], Necco and Sommer found a parametrization of the Sommer parameter valid in the range $5.7 \leq \beta_\mathrm{lat} \leq 6.92$

$$\log(a/r_0) = c_0 + c_1(\beta_\mathrm{lat} - 6) + c_2(\beta_\mathrm{lat} - 6)^2 + c_3(\beta_\mathrm{lat} - 6)^3, \tag{3.64}$$

where $c_0 = -1.6804$, $c_1 = -1.7331$, $c_2 = 0.7849$, and $c_3 = -0.4428$. In Ref. [165], an improvement of this parametrization was presented that is also consistent with perturbation theory

$$\log(r_0/a) = \left[\frac{\beta_\mathrm{lat}}{12b_0} + \frac{b_1}{2b_0^2}\log\left(\frac{6b_0}{\beta_\mathrm{lat}}\right)\right]\frac{1 + c_1/\beta_\mathrm{lat} + c_2/\beta_\mathrm{lat}^2}{1 + c_3/\beta_\mathrm{lat} + c_4/\beta_\mathrm{lat}^2}, \tag{3.65}$$

where $b_0 = 11/(4\pi)^2$ and $b_1 = 102/(4\pi)^4$. In Ref. [166], the parameters c_i were updated to be $c_1 = -8.9664$, $c_2 = 19.21$, $c_3 = -5.25217$, and $c_4 = 0.606828$.

Eq. (3.65) defines the coupling $\beta_\mathrm{lat}(a)$ as a function of lattice spacing. Using $T = (aN_\tau)^{-1}$, we can therefore relate the coupling to temperature: $\beta_\mathrm{lat}(T, N_\tau)$. Fig. 3.1 shows the temperature in units of the transition temperature T_c as a function of the coupling for different temporal lattice extents. The coupling constant β_lat for the lattices and temperatures used in this work are collected in Tab. 3.1.

Following Eq. (6) from Ref. [165], the confinement-deconfinement crossover transition temperature in SU(3) pure Yang-Mills theory is given as $T_\mathrm{c} = 287.4(70)\,\mathrm{MeV}$. Note that this temperature differs from the transition temperature of full QCD.

Table 3.1.: Coupling constant β_lat for the lattices and temperatures used in this work.

		N_τ				
		6	8	10	12	14
T/T_c	2.5	6.50094	6.72273	6.90097	7.04966	7.17706
	4.1	6.88794	7.12324	7.30916	7.46275	7.59354
	7.0	7.32939	7.57254	7.76294	7.91939	8.05216

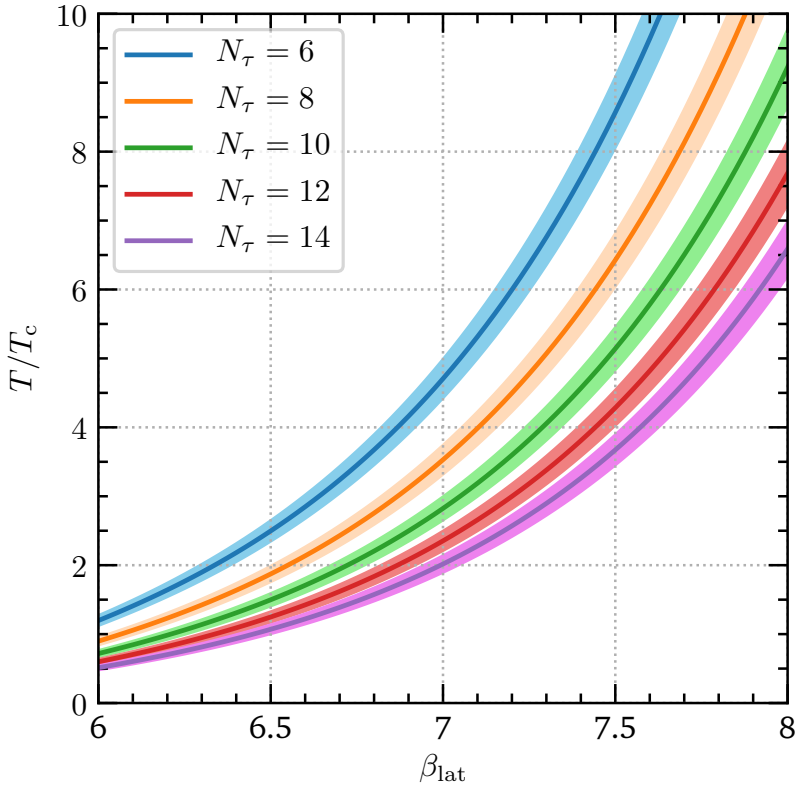

Figure 3.1.: Temperature in units of the critical temperature as a function of the coupling β_{lat} in pure SU(3) Yang-Mills theory.

3.7 Monte Carlo Simulations

We now discuss how the lattice discretization of QCD as discussed above is used to determine actual expectation values of observables. In the continuum, the expectation value of an observable O is given in the path-integral formulation as

$$\langle O \rangle = \frac{1}{\mathcal{Z}} \int \mathcal{D}U \, \mathrm{e}^{-S[U]} O[U], \tag{3.66}$$

where

$$\mathcal{Z} = \int \mathcal{D}U \, \mathrm{e}^{-S[U]} \tag{3.67}$$

is the partition function and

$$\mathcal{D}U = \prod_{x \in \Lambda} \prod_{\mu=0}^{3} \mathrm{d}U_\mu(x) \tag{3.68}$$

denotes the integral over all link variables via the so-called *Haar measure* $\mathrm{d}U_\mu(x)$ that allows for integrations over compact groups [167]. The defining properties of the Haar measure of a group G are

$$\mathrm{d}U = \mathrm{d}(UV) = \mathrm{d}(VU) \qquad \forall V \in G \qquad \text{and} \qquad \int \mathrm{d}U\, 1 = 1\,. \tag{3.69}$$

However, even though on the lattice the path integral is reduced to a finite number of group integrals, the number of degrees of freedom is in general still too large to allow for an explicit computation. For instance, even a rather small lattice with 12^4 sites requires more than 600,000 integrations.[10] The path integral is therefore approximated by a Monte Carlo sample. From the definition of the expectation value in Eq. (3.66), we observe that each gauge configuration is weighted by the Boltzmann weight $\exp(-S)$. Consequently, most of the configurations are exponentially suppressed and only configurations close to the classical configuration of minimum action contribute significantly. Instead of approximating the path integral by a set of randomly chosen gauge configurations, we therefore create configurations via *importance sampling* according to the probability distribution

$$\mathrm{d}P(U) = \frac{\mathrm{e}^{-S[U]}\mathcal{D}U}{\int \mathcal{D}U\, \mathrm{e}^{-S[U]}}\,. \tag{3.70}$$

After creating N configurations in this way, the expectation value is approximated by a simple mean of all the individual measurements:

$$\langle O \rangle = \frac{1}{N}\sum_{i=1}^{N} O_i + \mathcal{O}\left(\frac{1}{\sqrt{N}}\right). \tag{3.71}$$

The crucial and expensive part in a lattice simulation is generating the lattice configurations according to the probability distribution (3.70). This is done by starting with an arbitrary configuration U_0 and then subsequently generating configurations in a so-called *Markov chain*

$$U_0 \to U_1 \to U_2 \to \ldots \tag{3.72}$$

that eventually follows the equilibrium distribution $P(U)$. The step of replacing the configuration U_n with U_{n+1} is a so-called *update*. A Markov chain is characterized by the transition probability to end up at U' if starting at U,

$$T\big(U', U\big), \qquad 0 \le T\big(U', U\big) \le 1\,, \qquad \sum_{U'} T\big(U', U\big) = 1\,. \tag{3.73}$$

Let us discuss some important constraints on the transition probability. First, it must be possible to reach all configurations in configuration space in a finite number of updates. This property is called *ergodicity* and requires that the transition probability is strictly positive, $T(U', U) > 0\,\forall(U, U')$. Second, in equilibrium the probability of ending at the configuration U' at one update has to be the same as leaving this configuration at the same update, i.e.,

$$\sum_{U} T\big(U', U\big)\, P(U) \stackrel{!}{=} \sum_{U} T\big(U, U'\big)\, P(U') = P(U')\,. \tag{3.74}$$

[10] Each site has four link variables, and every SU(3) matrix is defined by eight real parameters. This gives $4{\cdot}8{\cdot}12^4 = 663{,}552$ degrees of freedom.

This balance equation therefore ensures that the probability distribution P is a fixed point of the Fokker-Planck equation describing the probability distribution generated by the Markov chain and the system stays there once the equilibrium is obtained. In practice, most of the update algorithms obey a special case of the equilibrium equation (3.74), where the equation is fulfilled term-by-term, i.e.,

$$T\big(U',U\big)P(U) = T\big(U,U'\big)P(U')\,. \tag{3.75}$$

This condition is called *detailed balance* and means that it cannot be distinguished if the system evolves forwards or backwards in time.

Before one can really use the Markov chain to approximate the path integral via importance sampling, it is necessary to bring the system to the equilibrium distribution P. It can be shown that, starting from an arbitrary configuration U_0 with distribution $P^{(0)}(U) = \delta(U-U_0)$, subsequent updates bring the system to the equilibrium distribution, i.e.,

$$P^{(0)} \to P^{(1)} \to P^{(2)} \to \ldots \to P\,. \tag{3.76}$$

At the beginning of a lattice simulation, it is therefore mandatory to start with a number of equilibrating updates that bring the system to the equilibrium distribution. Those updates need to be thrown away and cannot be used for actual measurements. For a more detailed discussion of Markov chains and detailed balance, we refer to the literature [128].

The most elementary algorithm that obeys detailed balance is the so-called *Metropolis algorithm* that was developed in Ref. [168]. It describes the update from a gauge configuration U_{n-1} to U_n and contains the following steps:

0. Initialize the global gauge field to the gauge configuration U_0, i.e., set up the $4\cdot N_\tau\cdot N_\mathrm{L}^3$ link variables as SU(3) matrices. Two common choices are the *cold start*, where all link variables are initialized at unity, and the *hot start*, where all link variables are initialized as random SU(3) matrices.

1. Being at the configuration U_{n-1}, propose a candidate configuration U'.

2. Accept the candidate configuration with probability

$$P = \min\big(1,\, \mathrm{e}^{-\Delta S}\big), \tag{3.77}$$

   where $\Delta S = S[U'] - S[U_{n-1}]$ is the change of the action. If the candidate configuration is accepted, then $U_n = U'$, otherwise we go back to the initial configuration, i.e., $U_n = U_{n-1}$. In practice, a random number $r \in [0,1)$ is computed and the new configuration is accepted if $r \leq \mathrm{e}^{-\Delta S}$ and rejected otherwise. This accept/reject step is called a *Metropolis step*. The consequence is that if the action decreases, the new configuration is always accepted; the fact that configurations with larger action are also accepted from time to time creates "quantum fluctuations" and thereby prevents the system to minimize the action and just move to the classical solution.

3. Repeat the preceding steps from 1.

The Metropolis algorithm is very simple and easy to implement; however, it is usually inefficient and hence more sophisticated algorithms are commonly used. We discuss one of the standard algorithms for simulating lattice QCD next.

3.7.1 Hybrid Monte Carlo Algorithm

The standard update algorithms for pure Yang-Mills theory on the lattice are the *heat bath* [169,170] and *overrelaxation* [171] algorithms. The great advantage of these algorithms is that they are local, i.e., when

updating one link, the change of the action depends only on a few links surrounding the changed link. When fermions are included, however, the action also contains the determinant of the Dirac operator which depends on the whole gauge field and is therefore non-local. In this work, we consider only pure SU(3) Yang-Mills theory and it would hence be sufficient and efficient to only consider, e.g., the heat bath and overrelaxation algorithms. However, the ultimate goal is to consider full QCD, which requires non-local update algorithms. In order that the method that we develop in this work for studying topology at high temperatures can be extended to full QCD without conceptual problems, we therefore work with the hybrid Monte Carlo (HMC) algorithm that we shall discuss in this section. This is nowadays a standard update algorithm that is used in many lattice simulations.

The basic idea of the HMC algorithm is to consider a non-relativistic molecular-dynamics Hamiltonian of the general form

$$H[P,Q] \equiv \frac{1}{2}P^2 + S[Q] \tag{3.78}$$

and evolve the system in the so-called *computer time* τ by solving the Hamiltonian equations of motion

$$\partial_\tau P = -\frac{\partial H}{\partial Q} = -\frac{\partial S}{\partial Q}\,, \qquad \partial_\tau Q = \frac{\partial H}{\partial P} = P\,. \tag{3.79}$$

Here Q are generalized coordinates and P are the corresponding conjugate momenta. In this work, we only study pure SU(3) Yang-Mills theory, where the action is simply given by the (Wilson or some kind of improved) gauge action, but in general the action is the sum of the gauge action and a pseudo-fermion action. In the case of SU(3) Yang-Mills theory, we identify the generalized coordinates with the link variables, i.e., $Q \equiv U_\mu(x)$, and the conjugate momenta with Lie-algebra valued momentum fields

$$P \equiv \Pi_\mu(x) = \Pi_\mu^a(x) T^a \in \mathfrak{su}(3)\,. \tag{3.80}$$

The Hamiltonian and the corresponding equations of motion then read

$$\begin{aligned} H[\Pi,U] &\equiv \frac{1}{2}\sum_{x\in\Lambda}\sum_{\mu=0}^{3}\Pi_\mu^a(x)\Pi_\mu^a(x) + S[U]\,,\\ \partial_\tau \Pi_\mu(x) &= -T^a \partial^a_{x,\mu} S[U]\,,\\ \partial_\tau U_\mu(x) &= \Pi_\mu(x)\,, \end{aligned} \tag{3.81}$$

where $\partial^a_{x,\mu}$ is the Lie derivative (3.39) that we already defined in the context of the discretization of the gradient flow equation. The HMC algorithm therefore requires the same gauge force that we also need for the gradient flow.

In an exact integration of the Hamiltonian equations of motion, the Hamiltonian is a constant of motion. Consequently, the phase space is sampled according to the canonical partition function, if the conjugate momenta are chosen randomly according to a Gaußian probability distribution $\exp\left(-\frac{1}{2}\Pi_\mu^a\Pi_\mu^a\right)$ at each trajectory. This combination of a molecular dynamics evolution with randomly generated Gaußian distributed conjugate momenta is called *hybrid algorithm* [172, 173].

In practice, the equations of motion are solved numerically; openQCD provides for this purpose a leapfrog and a fourth-order Omelyan-Mryglod-Folk (OMF) [174] integrator. This requires a discrete step size $\epsilon \equiv \Delta\tau$ and numerical errors are unavoidable. The simple leapfrog algorithm has errors of $\mathcal{O}\left(\epsilon^2\right)$, the fourth-order OMF integrator has errors of $\mathcal{O}\left(\epsilon^4\right)$. Since the integration is not exact, the sample

also does not follow the correct distribution. However, the integration can be made exact by adding a Metropolis step and accepting the new configuration only with probability

$$P = \min\left(1,\, \mathrm{e}^{-\Delta H}\right), \tag{3.82}$$

where $\Delta H = H_{\text{final}} - H_{\text{initial}}$ is the change of the Hamiltonian. If the integration of the equations of motion were exact, then $\Delta H \equiv 0$ and the new configuration is always accepted. This combination of a hybrid algorithm with an additional Metropolis accept/reject step is called *hybrid Monte Carlo algorithm* and was first described in Ref. [175].

3.8 Autocorrelation and Error Analysis

In a Monte Carlo simulation, a set of configurations is generated via importance sampling, and the desired observable is measured on each configuration. To obtain the expectation value of the observable with errors, the data needs to be analyzed statistically. In this section, we address how to obtain those final numbers from a Monte Carlo simulation. In this discussion we follow Ref. [128]; for a more detailed depiction we refer to Ref. [176].

If we assume that all our N measurements of an observable O are completely independent and uncorrelated, the final result is given by

$$\langle O \rangle = \hat{O} \pm \frac{\hat{\sigma}_O}{\sqrt{N}}, \tag{3.83}$$

where

$$\hat{O} = \frac{1}{N}\sum_{i=1}^{N} O_i \qquad \text{and} \qquad \hat{\sigma}_O^2 = \frac{1}{N-1}\sum_{i=1}^{N}\left(O_i - \hat{O}\right)^2 \tag{3.84}$$

denote the simple mean and variance, respectively. In practice, however, subsequently generated configurations in a Monte Carlo sample are correlated, leading to a non-vanishing autocorrelation function

$$\Gamma(\tau) = \frac{1}{N-\tau}\sum_{i=1}^{N-\tau}\left(O_i - \hat{O}\right)\left(O_{i+\tau} - \hat{O}\right), \tag{3.85}$$

where τ is the computer time. Usually the normalized autocorrelation function

$$\rho(\tau) \equiv \frac{\Gamma(\tau)}{\Gamma(0)}, \qquad \Delta\rho(\tau) = \sqrt{\frac{1}{N}\sum_{k=1}^{t+\Lambda}\Big(\rho(k+t) + \rho(|k-t|) - 2\rho(k)\rho(t)\Big)^2} \tag{3.86}$$

is used, where the expression for the error of this function is given in Appendix E of Ref. [177]. Here, Λ is a cutoff whose exact choice is irrelevant; $\Lambda \gtrsim 100$ gives consistent results. For large computer times, the autocorrelation function has an exponential decay

$$\rho(\tau) \propto \exp\left(-\frac{\tau}{\tau_{\text{cor}}}\right), \tag{3.87}$$

where τ_{cor} is the so-called *autocorrelation time*. If two subsequent configurations are separated by the computer time τ, autocorrelation induces systematic errors of $\mathcal{O}(\exp[-\tau/\tau_{\text{cor}}])$. To minimize those sys-

tematic errors it is therefore necessary that two subsequent configurations are separated by a computer time of at least several autocorrelation times.

3.8.1 Binning and Jackknife

In practice, it is often expensive and inconvenient to determine the autocorrelation time of all desired observables. There are, however, other ways to estimate and reduce the correlation of a given set of data by using *binning* or *data blocking*. We divide the original data $(O_1, O_2, \ldots, O_N)$ into bins of length B and use the average of those bins as the new data $\left(O_1^{\mathrm{b}}, O_2^{\mathrm{b}}, \ldots, O_{N_{\mathrm{b}}}^{\mathrm{b}}\right)$, where

$$O_i^{\mathrm{b}} = \frac{1}{B} \sum_{n=1+(i-1)B}^{iB} O_n \,, \qquad N_{\mathrm{b}} = {}^{N}\!/_{B} \,. \tag{3.88}$$

Using these new data, we can now determine the error. Note that binning does not change the mean of the data. However, after binning the number of data points is usually too small to determine the variance reliably via Eq. (3.84).

The *jackknife method* [178, 179] allows for a reliable estimation of the error of also a small set of uncorrelated data. It is based on the generation of N_{b} so-called *jackknife replicas*

$$O_i^{\mathrm{J}} = \frac{1}{N_{\mathrm{b}} - 1} \sum_{j \neq i} O_j^{\mathrm{b}} \,, \tag{3.89}$$

where the ith replica is the average of the binned data with the ith data point removed. The statistical error is then simply calculated via

$$\Delta O = \sqrt{\frac{N_{\mathrm{b}} - 1}{N_{\mathrm{b}}} \sum_{i=1}^{N_{\mathrm{b}}} \left(O_i^{\mathrm{J}} - \hat{O}\right)^2} \,. \tag{3.90}$$

At this point, we want to make a couple of remarks. First, the determination of the error via Eq. (3.90) can easily be extended to functions f of the observable by just replacing each O with $f(O)$. In this way, the propagation of errors that is not obvious in the "traditional" approach can be easily taken care of. Next, a natural question is how to choose the binsize B. In general, larger binsizes lead to less correlated data, but if we bin too much, the resulting set of data may be too small and the error of the error becomes too large. In practice, we calculate the jackknife error for larger and larger values of B. As soon as the data is uncorrelated, we expect the error to reach a plateau. One then uses the smallest possible binsize such that the error has reached the plateau. Finally, the method for generating the jackknife replicas as presented here is not unique. For instance, one could also create the jackknife replicas by omitting two ore more data points. In fact, the error could also be determined in different ways by generating different jackknife replica. By using the jackknife method on this set of errors, one could then determine the statistical error of the error and so on.

3.8.2 Example of a Statistical Analysis

To give an example of the statistical analysis of a lattice simulation, we present the "brute-force" determination of the topological susceptibility at two temperatures, namely $1.2\,T_{\mathrm{c}}$ and $2.0\,T_{\mathrm{c}}$ in pure SU(3) Yang-Mills theory with the HMC algorithm on a 10×32^3 lattice. The respective coupling constants $\beta_{\mathrm{lat}}(1.2\,T_{\mathrm{c}}) = 6.33718$ and $\beta_{\mathrm{lat}}(2.0\,T_{\mathrm{c}}) = 6.72273$ are chosen according to the scale setting described in Sec. 3.6. One update consists of an HMC trajectory of 16 steps of length $0.1875\,a$. The analysis is sum-

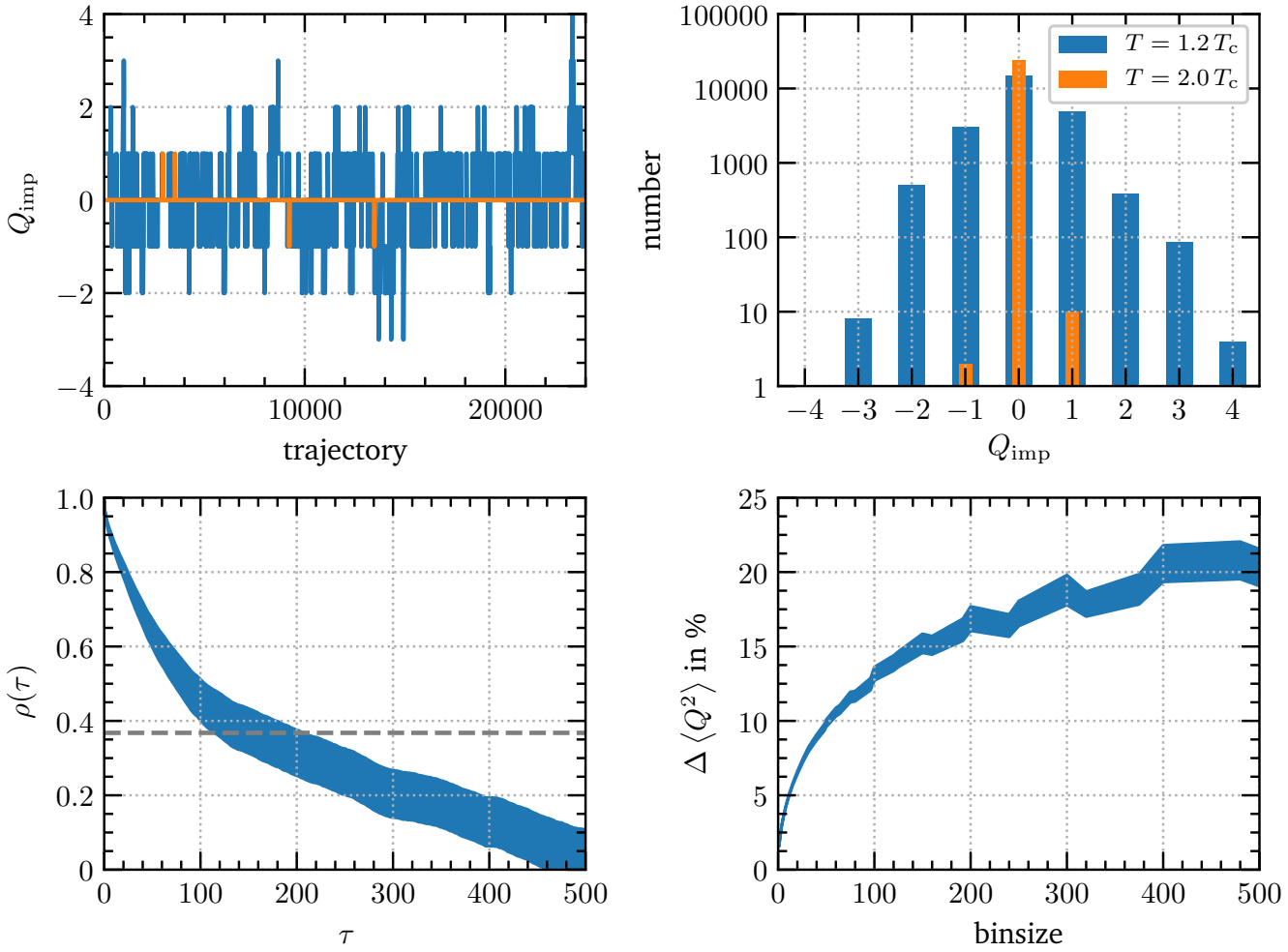

Figure 3.2.: Lattice measurement of the topological susceptibility at $T = 1.2\,T_c$ and $T = 2.0\,T_c$ in pure SU(3) Yang-Mills theory. Upper left: Monte Carlo history of the improved topological charge. Upper right: Number of measurements in different topological sectors. Lower left: Autocorrelation function of the $T = 1.2\,T_c$ measurement. The dashed line shows the value $\rho(\tau_{\mathrm{cor}}) \equiv \mathrm{e}^{-1}$. Lower right: Statistical error of the squared topological charge of the $T = 1.2\,T_c$ measurement as a function of binsize.

marized in Fig. 3.2. The upper left panel shows the history of the topological charge that is evaluated after $t = 1.0\,a^2$ of gradient flow and rounded to the nearest integer at each trajectory (after thermalization) for both temperatures. The upper right panel shows the appearance of the different topological sectors. The figure clearly shows that higher topological sectors are strongly suppressed already at $2\,T_c$ making a "brute-force" determination very inefficient. At $1.2\,T_c$, on the other hand, the algorithm rather easily moves between different topological sectors up to $|Q| = 4$. The lower left panel shows the autocorrelation function for $1.2\,T_c$. It shows the expected exponential fall, with the autocorrelation time being rather large, $\tau_{\mathrm{cor}} \approx 150$. This shows that subsequent measurements of the topological charge are highly correlated which makes studying topology on the lattice computationally expensive. The lower right panel of Fig. 3.2 shows the statistical jackknife error as a function of the binsize. In accordance with the large autocorrelation time, a lot of binning is required before the error reaches a plateau. The final result of this simulation is then

$$\chi_{\mathrm{top}}(1.2\,T_c) = 0.0327(67)\,T_c^4\,, \tag{3.91}$$

where we used a binsize of 400 to estimate the error. The literature does not provide a direct value that we could compare our result with, but in Ref. [58], the susceptibility was determined at $1.2\,T_c$ using a lattice with $N_\tau = 6$ that is compatible with our result, and the continuum extrapolated result of Ref. [62] also agrees with our result.

A determination of the topological charge at $T = 2.0\,T_c$ from the given data lacks statistical power and therefore suffers from large errors; less than 0.05% of the measurements are topological. A plethora of measurements is hence required for a precise determination of χ_{top} at high temperatures. This study also explicitly shows that higher topological sectors are strongly suppressed at high temperatures, which is expected from the dilute instanton gas approximation, cf. Sec. 2.4.4. While at $T = 1.2\,T_c$ the $|Q| = 1$ sector is only suppressed by a factor of roughly 2 compared to the $Q = 0$ sector, at $T = 2.0\,T_c$, the $|Q| = 1$ sector is already suppressed by a factor of roughly 2000 compared to the $Q = 0$ sector, and higher sectors are suppressed even more strongly. This means that it is sufficient to only consider the $|Q| = 1$ sector for temperatures above $2\,T_c$ as higher sectors contribute only extremely little to the topological charge. We shall utilize this constraint throughout this work and explicitly test this assumption in the context of reweighting in Chap. 5.

Chapter 4

Topological Configurations on the Lattice

A modern tool for studying topology on the lattice is the integration of a lattice discretized version of the topological charge Q after the lattice fields have been subjected to gradient flow (cf. Sec. 3.5). Gradient flow tends to eliminate dislocations [180], but since there is no clean distinction between dislocations and small-but-physical instantons, it may also destroy the smallest instantons that are physically relevant. This issue is addressed phenomenologically in most lattice studies that attempt a calculation of the topological susceptibility, but we are surprised by the absence of a more systematic study, which might help in understanding how wide the flow time window actually is, and how large we should expect the lattice artifacts in the topological susceptibility to be. In other words, it would be useful to get a better analytical understanding of how lattice spacing and flow-depth effects may influence the determined topological susceptibility.

In this chapter, we shall explore this issue by studying exactly how much gradient flow destroys exactly what size of Harrington-Shepard calorons (cf. Sec. 2.4.1). This requires a lattice implementation of instantons and calorons, which we supply. The goal is then to study the effect of the different "types" of gradient flow, namely Wilson (3.38), Zeuthen (3.40), and overimproved flow (3.43), on our constructed clean topological configurations to learn about how their topological properties are changed. This can represent interesting information to better control systematic errors when performing lattice calculations of topological observables with the help of flow. We are hardly the first to implement discretized topological configurations on the lattice [181–183] or to consider topology after cooling [157–159,184,185]. But our emphasis is a little different; we aim to understand and control what size of dislocation/caloron survives what amount of flow, and what impact this may have on the determination of the topological susceptibility at finite lattice spacing and on the corresponding extrapolation to the continuum limit.

A natural objection to our study is that, in the temperature range of relevance, the coupling is still quite large. Therefore, the actual topological objects from the lattice will not be clean calorons, but will have large fluctuations. Nonetheless, gradient flow will drive any topological object towards a caloron solution in a much smaller amount of flow time than it takes for the object to disappear since the caloron is a stationary point of the action up to a^2 corrections. The actual topological objects' flow trajectories should therefore be very similar to those for calorons. (In fact, in the continuum, we could even define the size of a topological object to be the size of the caloron it approaches under gradient flow.) Therefore, our study can still shed light on how much flow removes what size of topological objects. Combining this with an estimate for the size distribution of calorons based on Gross, Pisarski, and Yaffe's work [124] can illuminate what flow depths affect the topological objects we want to keep and what lattice spacings may be too coarse to distinguish between dislocations and physically relevant topological objects.

This chapter is based on work published in The European Physical Journal C [64]. In order to respect the formulation of the precise arguments and their interpretation originally made, most parts of this chapter are adopted from the original publication. The author of this thesis was involved in all steps of this project. It is structured as follows: In Sec. 4.1, we present the lattice discretization of the topological configurations. Sec. 4.2 then contains the discussion of some properties of the lattice instantons and calorons. In particular, we compute $\rho_{\text{crit}}(t)$ which indicates the value of the radius of a caloron that barely survived the amount of flow time t. These curves are further used in Sec. 4.3 to estimate how lattice spacing systematics interfere with flow effects in the approach to the continuum. An example study at $T = 4\,T_c$ is used. Our conclusions can then be found in Sec. 4.4.

4.1 Instanton and Caloron Discretization

In this section, we present the lattice discretization of the continuum BPST instanton

$$A_\mu^{\text{BPST}}(x) = \bar{\eta}_{a\mu\nu}\frac{\rho^2(x-z)_\nu\tau_a}{(x-z)^2\big((x-z)^2+\rho^2\big)} \tag{4.1}$$

and the continuum HS caloron

$$A_\mu^{\text{HS}}(x) = -\frac{1}{2}\bar{\eta}_{a\mu\nu}\partial_\nu \ln\phi_{\text{HS}}(x)\tau_a\,, \qquad \phi_{\text{HS}}(x) = 1+\frac{\pi\rho^2\sinh\frac{2\pi|\vec{x}-\vec{z}|}{\beta}}{\beta|\vec{x}-\vec{z}|\Big(\cosh\frac{2\pi|\vec{x}-\vec{z}|}{\beta}-\cos\frac{2\pi(x_0-z_0)}{\beta}\Big)} \tag{4.2}$$

with τ_a being the antihermitian Pauli matrices (cf. App. A for the conventions used in this work and Sec. 2.4.1 for a detailed discussion of instantons and calorons). Note that these gauge fields are given in the singular gauge, meaning that they have a singularity at the center of the object, i.e., at $x = z$. On the lattice, we avoid these singularities by placing the topological objects in between lattice points. Unless stated otherwise, the topological objects are always placed at the center of the lattice, i.e., at

$$z = (z_0\,, z_i) = \left(\frac{N_\tau-1}{2}, \frac{N_{\text{L}}-1}{2}\right). \tag{4.3}$$

As elaborated in Sec. 3.2, the lattice discretization of a continuum gauge field is given by the path-ordered exponential

$$U_\mu(x) = \mathcal{P}\exp\left(a\int_0^1 \mathrm{d}\lambda A_\mu\big(\Gamma_\mu(x,\lambda)\big)\right), \tag{4.4}$$

where $\Gamma_\mu(x,\lambda) = x+\lambda\hat{\mu}$ is an appropriate parameterization for the corresponding path connecting the two neighboring lattice sites x and $x+\hat{\mu}$ with $\lambda\in[0,1]$ (no summation over μ is implied in Eq. (4.4)). In the case of the BPST instanton, the gauge fields commute everywhere along the link, i.e., $\big[A_\mu(\Gamma_\mu(x,\lambda)), A_\mu(\Gamma_\mu(x,\lambda'))\big] = 0$. Therefore, the path-ordered exponential can be done exactly by simply performing the integral analytically and exponentiating the result. This is explicitly done in App. B.

In the case of the HS caloron, however, the gauge fields do not commute with each other along a link anymore and the path ordering becomes crucial. Consequently, the integral cannot be performed exactly. In order to compute the links, we rewrite Eq. (4.4) as a product of n shorter links,

$$U_\mu(x) = \lim_{n\to\infty}\mathcal{P}\prod_{k=1}^{n}\exp\left[\frac{a}{n}A_\mu\left(\Gamma_\mu\left(x,\frac{2k-1}{2n}\right)\right)\right], \tag{4.5}$$

where in practice we use $n\sim 40$ rather than taking the strict $n\to\infty$ limit.

Finally the embedding into an SU(3) background is trivial since a particular lattice gauge exists in which the links take the following form:

$$U_\mu^{\text{SU(3)}} = \left(\begin{array}{cc|c} & & 0\\ & U_\mu^{\text{SU(2)}} & 0\\ \hline 0 & 0 & 1\end{array}\right). \tag{4.6}$$

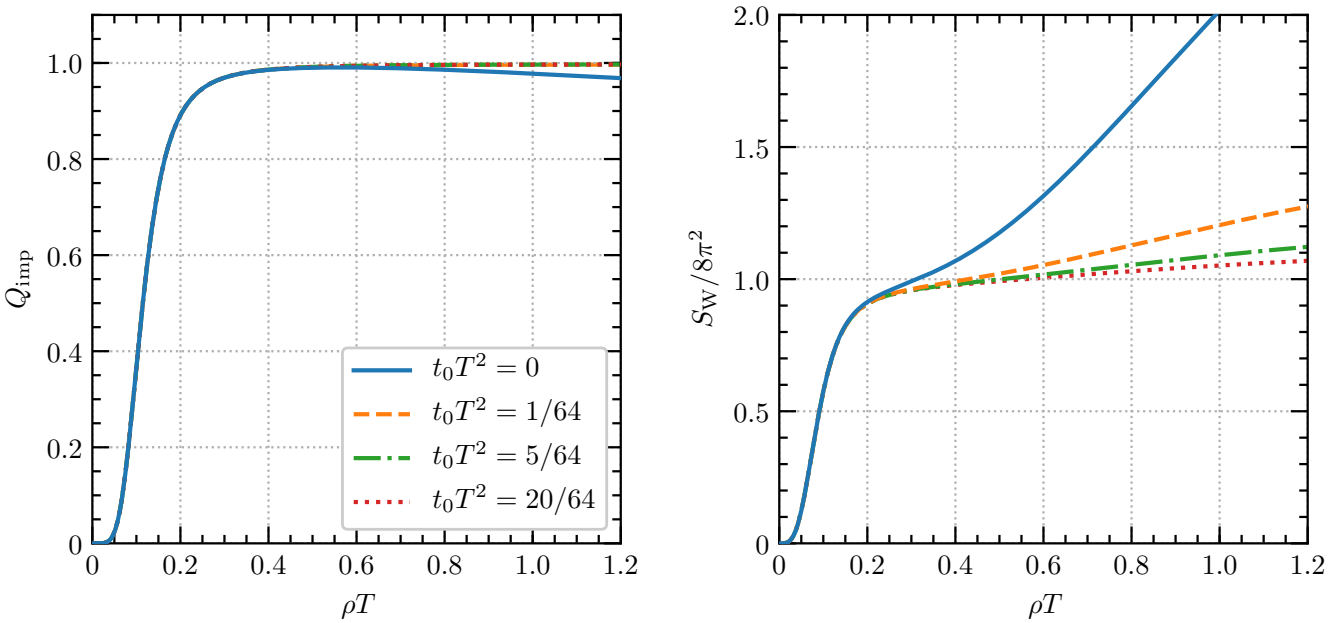

Figure 4.1.: Caloron topological charge (left) and Wilson action (right) for different values of t_0T^2 as defined in Eq. (4.8) on an 8×48^3 lattice. A similar figure is published in our paper [64].

Note that this corresponds to the continuum embedding (2.63). Therefore, we *effectively* consider SU(2) configurations. This makes our study less general than Ref. [182], who also consider calorons in the background of nontrivial holonomy. Note, however, that if we are primarily interested in *high* temperatures, nontrivial holonomy is not likely to be relevant, since fluctuations create an effective potential for the Polyakov loop which favors trivial holonomy [124].

Periodicity is imposed in all four dimensions, and while boundary effects are absent for the calorons in the time direction, our lattice field will have a discontinuity at the spatial edges of the box (instantons also at the temporal edges). To reduce this effect as much as possible, we "flow the boundaries away." What this means is that we perform a spacetime dependent flow where the core of the configuration (where most of the topological charge is localized) is unaffected while boundary effects are smoothed out. A similar idea was used in Ref. [158], where a discretized version of $D_\mu F_{\mu\nu}(x)$ was measured on every spacetime point and an improved form of cooling was performed on those lattice points that satisfied the bound $D_\mu F_{\mu\nu}(x) > \epsilon$.

In this work, we apply gradient flow using a flow time that depends on the relative distance

$$d = \sqrt{(x-z)^2} \tag{4.7}$$

of the base point of the link $U_\mu(x)$ and the center of the topological object. The flow time gets modified as

$$t(d) = \begin{cases} 0\,, & d < \frac{L}{4} \\ \frac{t_0}{2}\left(1 + \sin\left[\frac{4\pi}{L}\left(d - \frac{3}{8}L\right)\right]\right), & \frac{L}{4} \le d \le \frac{L}{2} \\ t_0\,, & d > \frac{L}{2} \end{cases} = \tag{4.8}$$

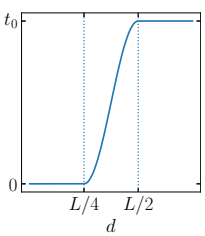

where t_0 is the "normal" flow time. This is nothing but a smooth interpolation between zero flow (close to the center of the caloron) and full flow (close to the boundary). With this procedure, we

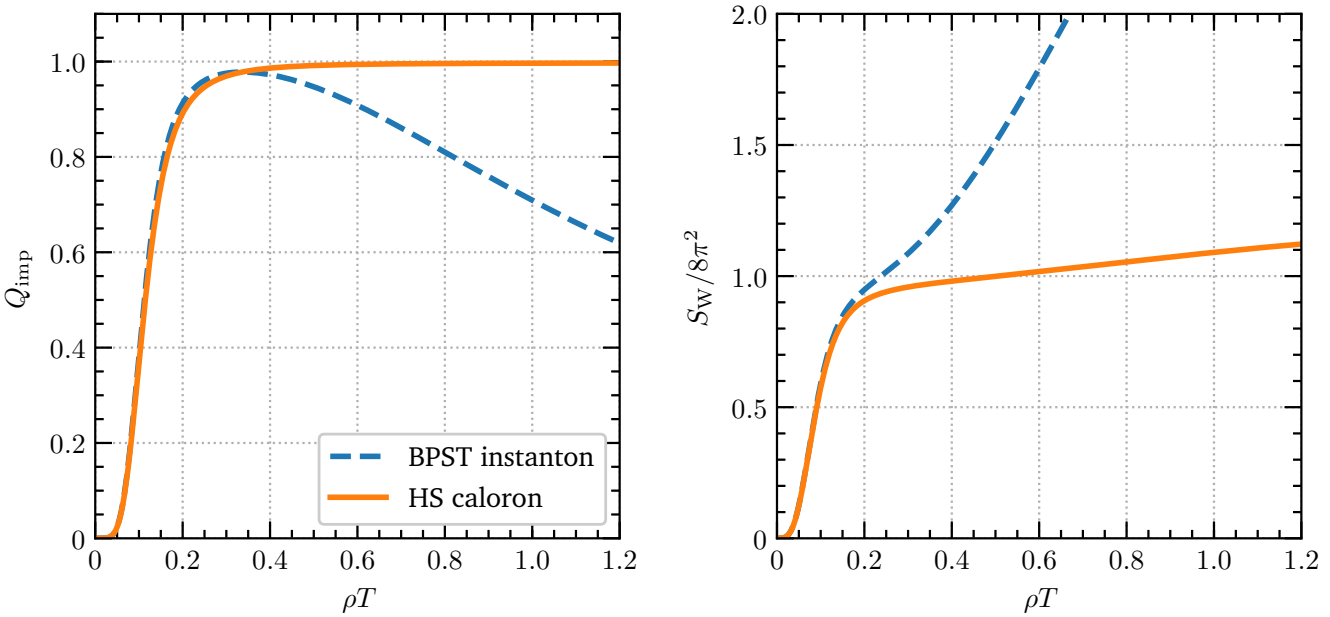

Figure 4.2.: Left: Topological charge for caloron and instanton as a function of their size ρ. Right: Caloron and instanton Wilson actions normalized by the continuum value $8\pi^2$. Both instanton and caloron are placed at the center of an 8×32^3 lattice.

reduce boundary effects while the core of the caloron remains unaffected. In Fig. 4.1, we show both the topological charge and the Wilson action of the caloron for different values of t_0. We observe that the Wilson action suffers significantly more from boundary effects than the topological charge. Applying this modified version of Wilson flow indeed reduces boundary effects. We find that a flow time of $t_0 T^2 = 5/N_\tau^2$ is sufficient to satisfactorily reduce most of the boundary effects. From now on, when setting up a topological configuration, we always implicitly apply this procedure. Note that the gradient flow used to reduce the boundary effects should not be confused with the usual gradient flow that we apply for some calculations in the remainder of this work.

4.2 Lattice Instanton and Caloron Properties

In this section, we study the properties of the lattice discretizations of the instanton and caloron under gradient flow. Mainly we will focus on the measurement of the topological charge Q and the action S which in the continuum take the values $Q = 1$ and $S = 8\pi^2$, respectively. Deviations from these numbers occur on a finite lattice due to cutoff and boundary effects. We will try to disentangle those to more deeply understand the effect of flow.

4.2.1 Caloron vs. Instanton

First of all, it is interesting to check whether the caloron and instanton implementations work as expected. In Fig. 4.2, we show how temperature effects are fully taken into account in the case of the caloron while instantons suffer from temperature corrections as soon as $\rho T \gtrsim 0.25$. The right panel shows that the Wilson action starts small for small values of the radius and is suppressed until about $\rho T = 0.2$. Therefore this is about the scale where we should switch from considering the configurations as dislocations to thinking of them as small instantons. Above this size, the Wilson action of the caloron approaches the continuum value $8\pi^2$ while the instanton rapidly exceeds this value due to boundary effects; the topological charge for the caloron plateaus to the expected value of 1 while the instanton rapidly drops due to boundary effects in the temporal direction.

4.2.2 Actions

We consider Lüscher-Weisz actions of the form (cf. Eq. (3.15))

$$S(c_0,c_1)=\frac{\beta_{\text{lat}}}{3}\sum_x\sum_{\mu<\nu}\Big\{c_0\,\text{Re}\,\text{tr}\big(\mathbb{1}-\square_{\mu\nu}(x)\big)+c_1\Big[\text{Re}\,\text{tr}\Big(\mathbb{1}-P^{(1\times2)}_{\mu\nu}(x)\Big)+\text{Re}\,\text{tr}\Big(\mathbb{1}-P^{(2\times1)}_{\mu\nu}(x)\Big)\Big]\Big\}\,, \quad (4.9)$$

which contains plaquettes and 2×1 (and 1×2) rectangles, where both loop orientations are taken into account by the Re tr operation. A correct normalization requires $c_0+8c_1=1$. In particular, we consider the three actions

$$S_{\text{W}}=S(1,0) \qquad \text{(Wilson)}\,, \quad (4.10a)$$
$$S_{\text{Sym}}=S(5/3,-1/12) \qquad \text{(Symanzik)}\,, \quad (4.10b)$$
$$S_{\text{OI}}=S(7/3,-1/6) \qquad \text{(Overimproved)}\,. \quad (4.10c)$$

Fig. 4.3 explores how each action varies as a function of the caloron size ρT, on a lattice with $N_\tau=8$ and an aspect ratio of 6. We find that all actions start small and are suppressed until about $\rho=1.6\,a$, which is $\rho T=0.2$ for this N_τ value. A rapid rise towards the expected value of $8\pi^2$ is then observed, followed eventually by a rise above $8\pi^2$. These two features – the rapid rise from zero towards $8\pi^2$, and the eventual rise above this value – arise from different artifacts. The former is a lattice spacing artifact, which we now explore. We overlay each curve with an estimate based on a small-a expansion, taken to first nontrivial subleading order. Specifically, the expansion of the Wilson action in operator dimension takes the form

$$S_{\text{W}}=-\frac{1}{2}\,\text{tr}\{F_{\mu\nu}F_{\mu\nu}\}+\frac{a^2}{12}\,\text{tr}\{D_\mu F_{\mu\nu}D_\mu F_{\mu\nu}\}+\mathcal{O}\big(a^4\big)\,, \quad (4.11)$$

where each index is summed once. This leads to a^2 corrections to the caloron action. Inserting the caloron field from Eq. (4.2), a corresponding finite temperature integration $\int_0^{1/T}\text{d}\tau\int\text{d}^3x$ yields

$$S_{\text{W}}=8\pi^2\left[1+\mathcal{F}(\rho T)\left(\frac{a}{\rho}\right)^2+\mathcal{O}\left(\frac{a}{\rho}\right)^4\right]. \quad (4.12)$$

We have evaluated $\mathcal{F}(\rho T)$ numerically and find that it is very well fit by

$$\mathcal{F}(\rho T)=-\frac{1}{5}+b(\rho T)^2+\mathcal{O}(\rho T)^4 \quad (4.13)$$

with $-1/5$ the zero-temperature (instanton) value and $b=-0.758$. The first (vacuum) effect is $\mathcal{O}(a^2/\rho^2)$; because of it, the action is significantly smaller for $\rho<1.6\,a$, and we should consider such objects as "dislocations" rather than true continuum-like calorons. The second term gives rise to an $\mathcal{O}(a^2T^2=1/N_\tau^2)$ correction, which is present at all caloron sizes, and represents a size-independent mis-estimate of the caloron action due to the lattice spacing. For the overimproved case, the a^2 correction is the same but with opposite sign. For the Symanzik case, we have not evaluated the full temperature-dependent $\mathcal{O}(a^4)$ correction, but instead use the $\mathcal{O}(a^4)$ correction to the instanton action found by Ref. [186]. This is adequate because the correction is small for $\rho T\sim1$ where thermal effects are expected.

The overimproved action possesses positive a^2 corrections and therefore develops a maximum. This will be of importance when flowing with this action as it will stabilize calorons larger than the size where S is maximum, preventing them from shrinking, "falling through the lattice," and being lost. As we will

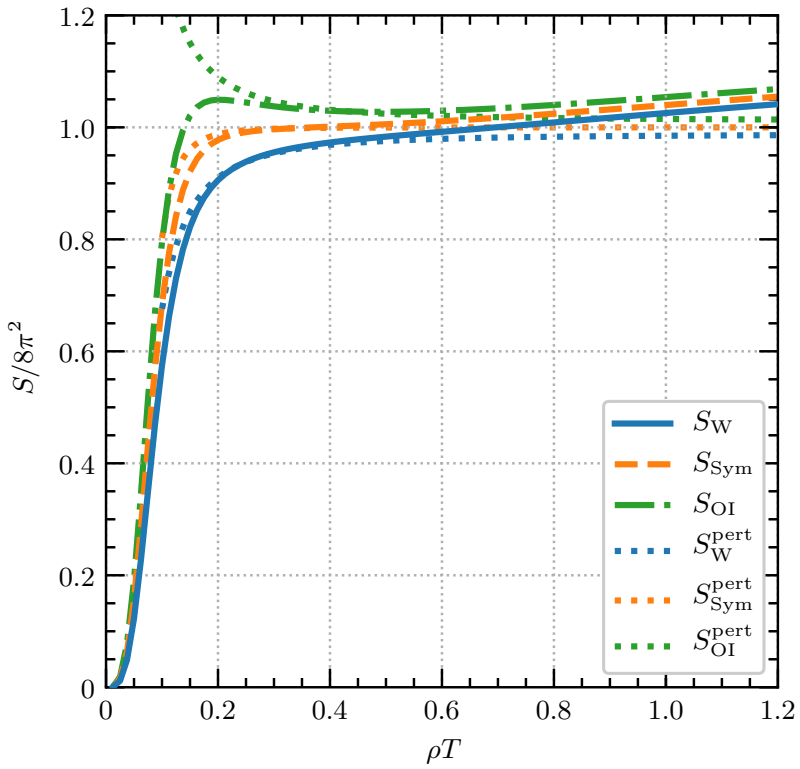

Figure 4.3.: Different actions together with the perturbative predictions as a function of the caloron size. The caloron is placed at the center of an 8×48^3 lattice. In this plot, we used $t_0 T^2 = 20/64$ for reducing the boundary effects (cf. Sec. 4.1). Dotted lines indicate a small-a expansion up to the first nontrivial correction. A similar figure is published in our paper [64].

see, although promising, this approach does not substantially help in the calculation of the topological susceptibility.

The figure also features a rise in the action above $8\pi^2$ at large caloron sizes; for the lattice considered in the figure, this effect becomes larger than the a^2 effects above about $\rho T = 0.7$. This is a finite-volume effect that is ameliorated by going to a larger aspect ratio. It is also partly an artifact of the way we construct the caloron solution since we take properly into account the temporal periodicity but not the space periodicity. In order to reduce this effect as much as possible, we "flow the boundaries away" as described in Sec. 4.1.

4.2.3 Topological Charges

The field-strength tensor $F_{\mu\nu}(x)$ is the main building block for constructing gauge operators like the topological charge. Apart from the popular geometrical clover definition (4-plaquette average), we considered an improved version thereof. To this end, we implement an improved field-strength tensor $\hat{F}^{\mathrm{imp}}_{\mu\nu}$ free of $\mathcal{O}(a^2)$ errors by considering weighted averages of 1×1 plaquettes and 2×1 rectangles [142, 143], cf. also Sec. 3.4 for more details.

We then study the two definitions

$$Q_{\mathrm{clov/imp}} = -\frac{1}{32\pi^2} \epsilon_{\mu\nu\rho\sigma} \sum_x \mathrm{tr}\big(\hat{F}_{\mu\nu}(x) \hat{F}_{\rho\sigma}(x)\big), \tag{4.14}$$

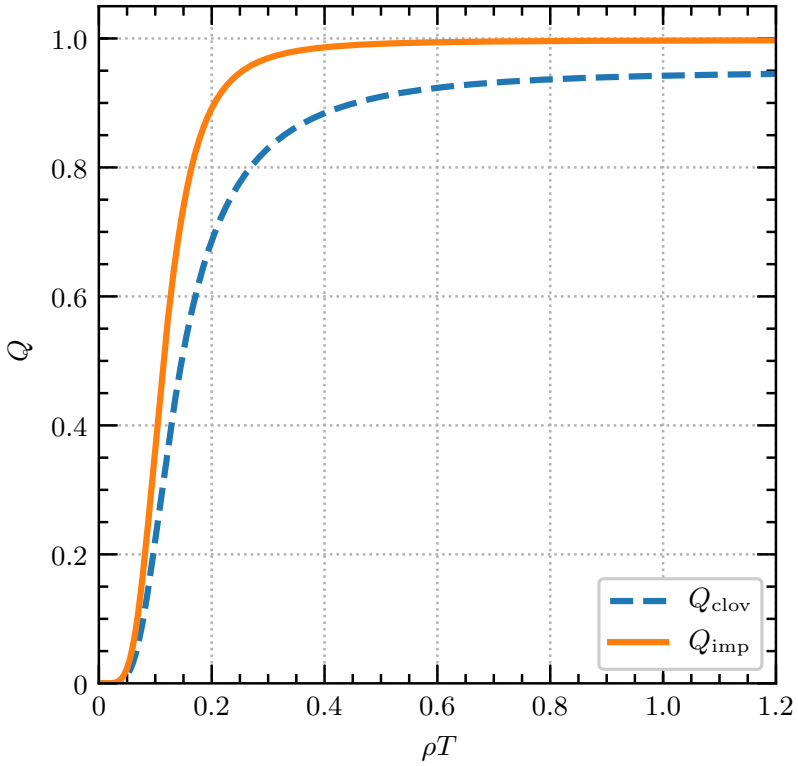

Figure 4.4.: Two different discretizations of the topological charge operator as a function of the caloron size on an 8×32^3 lattice. A similar figure is published in our paper [64].

where in each case

$$\begin{aligned} \hat{F}^{\mathrm{clov}}_{\mu\nu}(x) &= F_{\mu\nu}(x) + \mathcal{O}\left(a^2\right), \\ \hat{F}^{\mathrm{imp}}_{\mu\nu}(x) &= F_{\mu\nu}(x) + \mathcal{O}\left(a^4\right). \end{aligned} \tag{4.15}$$

As can be seen from Fig. 4.4, the improved topological charge operator shows a much better behavior at all investigated values of the radius. Notice that boundary effects are milder for the topological charge than for the action. We see only advantages to using the improved definition and therefore implicitly always use it in what follows.

4.2.4 Critical Radius

One of the relevant aspects we want to address in this chapter is the behavior of a discretized caloron configuration under different flow equations. We see in Fig. 4.4 that, for $N_\tau = 8$, a caloron with $\rho T \gtrsim 0.12$ will have a Q value larger than $1/2$ if the measurement is made before any flow is applied. In practice, such a measurement would be impossible since the Q of the caloron would be swamped by contributions from non-topological fluctuations. These disappear after a modest amount of gradient flow. But calorons also shrink and tend to disappear as flow is applied, precisely because of the action corrections which we explored in Fig. 4.3. We illustrate this effect in Fig. 4.5 which shows how the Q value changes under flow for a "large" caloron with $\rho T = 0.5$ on an $N_\tau = 8$ lattice. We see that, after some amount of flow time, the measured topological charge abruptly collapses. This occurs because flow causes the caloron to shrink, eventually abruptly shrinking away and disappearing between lattice sites. At least for Wilson and Zeuthen flow, any caloron will eventually disappear in this way.

The collapse is slower for Zeuthen flow because of the absence of a^2 lattice-spacing corrections to the action, but the a^4 and finite-volume effects nevertheless eventually lead to a collapse. The overimproved

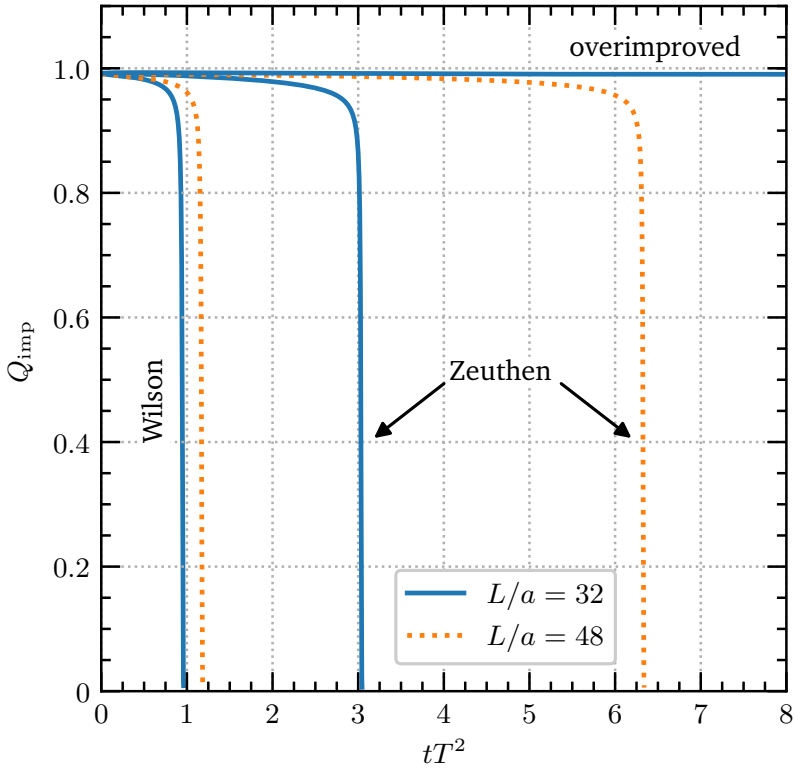

Figure 4.5.: Topological charge Q_{imp} as a function of flow time for a caloron with $\rho T = 0.5$, for three flow definitions and two box sizes ($N_\tau = 8$ is fixed). Calorons live much longer under Zeuthen flow, and forever under overimproved flow. A similar figure is published in our paper [64].

action has – in contrast to the other considered actions – a maximum which prevents flow from ever destroying the caloron.

It would be very useful to know more precisely how much flow destroys what size of calorons. To investigate this, we first establish a definition of when we consider a caloron to really exist: when the topological charge Q exceeds some threshold which we choose to be 0.5.[1] This corresponds well to the typical procedure one will use in determining the topological susceptibility in a simulation: a configuration is generated, Q is measured, and then its value is thresholded to an integer. The choice 0.5 corresponds to thresholding to the nearest integer. We therefore define the critical radius ρ_{crit} of a caloron where it becomes topological as

$$Q_{\mathrm{imp}}(\rho_{\mathrm{crit}}) \equiv 0.5\,. \tag{4.16}$$

We can then study how flow causes lattice calorons to shrink and disappear by investigating ρ_{crit} as a function of flow time, that is, what initial caloron radii ρ still have $Q_{\mathrm{imp}} > 0.5$ after some flow depth t. This is shown in Fig. 4.6 which can be used to look up how much flow is needed to collapse calorons of a given size. We see in the figure that ρ_{crit} grows almost linearly with $t^{1/4}$ which is easily explained analytically. An ordinary perturbative fluctuation of momentum p decays as $\exp\left(-p^2 t\right)$ (this is a leading result coming from the gradient flow equation (3.34)), and so doubling the size requires four times the flow time, or $t \propto \rho^2$. However, calorons are nearly extrema of the action, up to a^2/ρ^2 corrections in the Wilson action, so we expect $t \propto \rho_{\mathrm{crit}}^4$. Therefore Fig. 4.6 plots ρ_{crit} against $t^{1/4}$ (Wilson case) which would be a straight line for $1/N_\tau \ll \rho T \ll 1$. The figure shows that calorons also collapse under Zeuthen flow, though more slowly (as the energy depends on scale only at $\mathcal{O}\left(a^4\right)$, we therefore expect $t \propto \rho_{\mathrm{crit}}^6$)

[1] We see in Fig. 4.5 that the exact choice is almost immaterial.

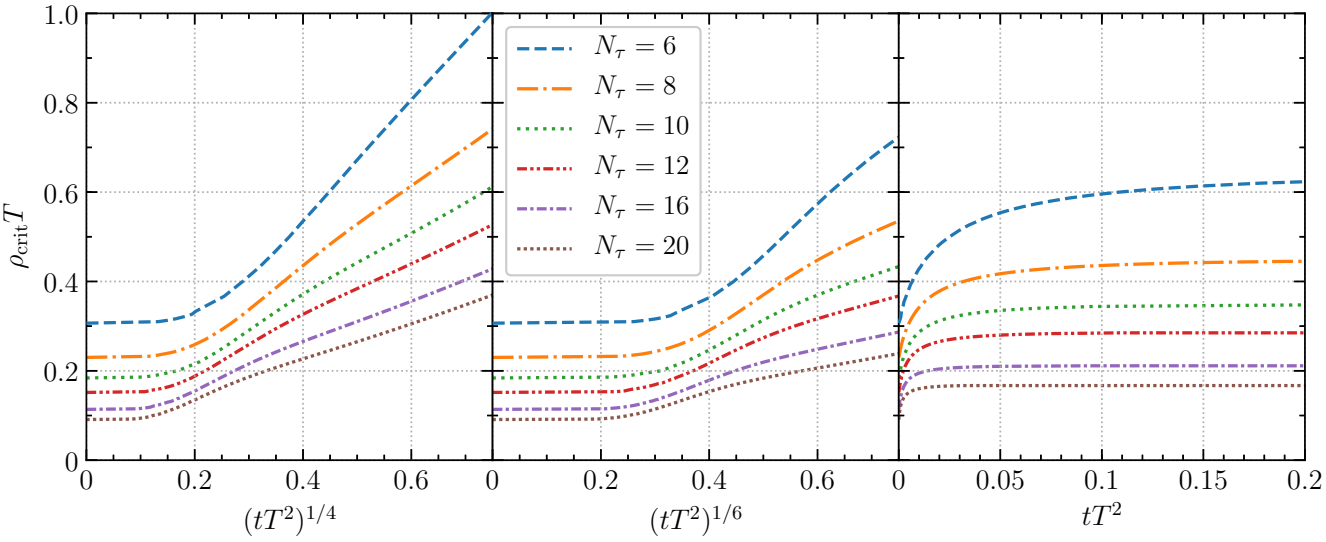

Figure 4.6.: Critical caloron radius (separating calorons which survive from those which collapse) as a function of flow depth for three types of flow and several different temporal lattice extents. Left: Wilson flow. Middle: Zeuthen flow. Right: Overimproved flow. A similar figure is published in our paper [64].

and, in fact, the curves show a linear trend. Under overimproved flow, calorons are preserved above some critical size which was the original motivation for considering it [186].

4.3 Estimated a^2 Errors in the Topological Susceptibility

We want to apply our results to get a semi-analytical understanding of how both flow depth and a^2 errors may influence lattice determinations of the topological susceptibility at high temperatures. Our goal is *not* to calculate the topological susceptibility *per se,* but to see how flow and lattice spacing may influence its determination at finite lattice spacing.

We will do so by approximating the distribution of topological objects using the DIGA as introduced in Sec. 2.4.4. In the continuum, the topological susceptibility is given by

$$\chi_{\mathrm{top}}(T/T_{\mathrm{c}}) \simeq 2 \int_0^{1/\Lambda_{\overline{\mathrm{MS}}}^{N_{\mathrm{f}}=0}} \mathrm{d}\rho \, D(\rho) G(\pi\rho T) \tag{4.17}$$

with

$$D(\rho) = \frac{d_{\overline{\mathrm{MS}}}}{\rho^5} \left(\frac{8\pi^2}{g_{\mathrm{s}}^2(\mu_{\mathrm{r}} = \rho^{-1})} \right)^6 \exp\left(-\frac{8\pi^2}{g_{\mathrm{s}}^2(\mu_{\mathrm{r}} = \rho^{-1})} \right) \tag{4.18}$$

the vacuum density of instantons with size ρ, and

$$G(\lambda) = \exp\left(-2\lambda^2 - 18A(\lambda)\right), \tag{4.19}$$

$$A(\lambda) = -\frac{1}{12} \ln\left(1 + \frac{\lambda^2}{3}\right) + \alpha\left(1 + \gamma\lambda^{-3/2}\right)^{-8} \tag{4.20}$$

the thermal corrections, first computed by Gross, Pisarski, and Yaffe [124]. The parameter values in these expressions are $\alpha = 0.0128974$, $\gamma = 0.15858$, and $d_{\overline{\mathrm{MS}}} = \frac{\mathrm{e}^{5/6}}{\pi^2} \mathrm{e}^{-4.534122}$. The running of the coupling

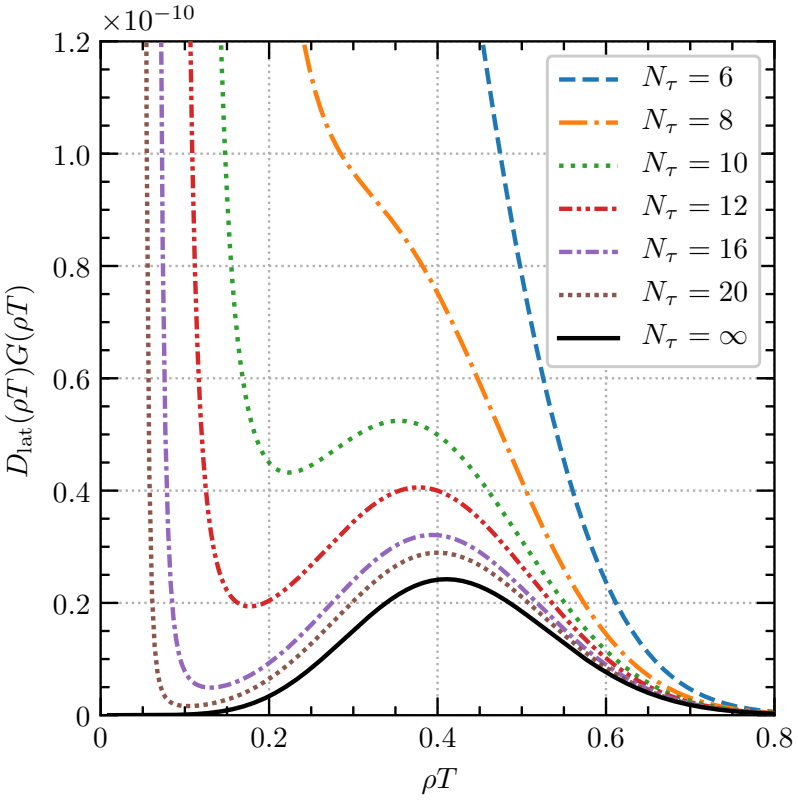

Figure 4.7.: Integrand of Eq. (4.22) at $T = 4\,T_c$ for different numbers of temporal lattice points N_τ. The black solid curve represents the continuum case and corresponds to the integrand of Eq. (4.17). A similar figure is published in our paper [64].

$g_s^2\left(\rho^{-1}\right)$ is given in Eq. (2.111) and $T_c/\Lambda_{\overline{\rm MS}}^{N_f=0} = 1.26$ is taken from Ref. [187]. The product of $D(\rho)$ and of $G(\pi\rho T)$ in Eq. (4.17) leads to an integrand with a broad peak near $\rho T \simeq 0.4$ (solid black curve in Fig. 4.7), which is then the typical size for the calorons which dominate the topological susceptibility.

In performing a lattice Monte Carlo study, the practitioner chooses an action for sampling configurations. The choice is logically independent of the choice of the action used in gradient flow, but it can be equally impactful. In particular, if the lattice study is based on sampling with the Wilson action, something we assume throughout this section, then the continuum action $8\pi^2$ in Eq. (4.18) should be replaced by the lattice Wilson action of a caloron from Eq. (4.12), leading to an a^2 correction to $D(\rho)$:

$$D_{\rm lat}(\rho, T/T_c, N_\tau) = D(\rho)\exp\left[-\frac{8\pi^2}{g_s^2(\mu_r = \rho^{-1})}\left(\frac{1}{\rho T N_\tau}\right)^2 \mathcal{F}(\rho T)\right]. \tag{4.21}$$

This rests on an assumption that the coefficient in front of the dimension-six a^2-suppressed operator $(DFDF)$ takes its tree-level value. Realistically, we expect corrections from, e.g., the renormalization of the a^2 action correction and from higher-order effects in $G(\pi\rho T)$, so our results here should be viewed only as estimates, based on the best tools we have available, for how a^2 effects will affect the caloron density on the lattice.

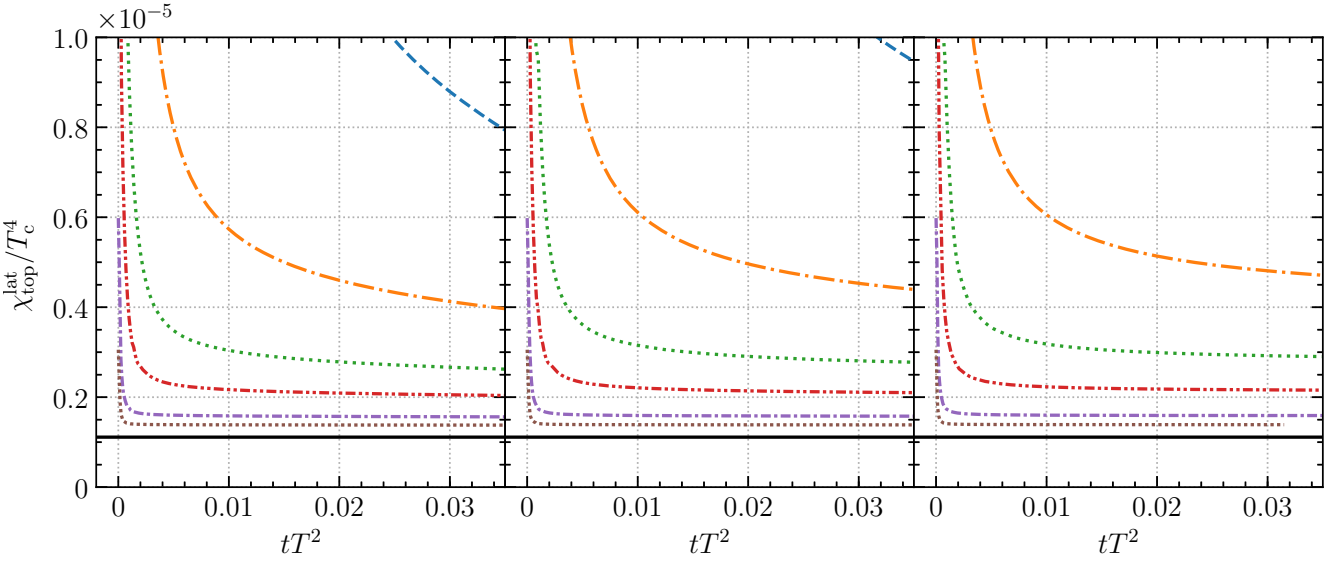

Figure 4.8.: Estimated effect of lattice artifacts on the topological susceptibility at $T = 4\,T_c$ for different numbers of temporal lattice points N_τ as a function of the flow depth tT^2. Left: Wilson flow. Middle: Zeuthen flow. Right: Overimproved flow. The solid line denotes the continuum limit and the legend is the same as in Figs. 4.6 and 4.7. A similar figure is published in our paper [64].

To estimate the topological susceptibility as measured on the lattice, we integrate this modified caloron density over those caloron sizes which are not destroyed by gradient flow – which is precisely all $\rho > \rho_{\text{crit}}$ as determined in Fig. 4.6. We therefore write

$$\chi^{\text{lat}}_{\text{top}}(T/T_c, N_\tau, tT^2) = 2\int_{\rho_{\text{crit}}(tT^2,N_\tau)}^{1/\Lambda_{\overline{\text{MS}}}^{N_f=0}} \mathrm{d}\rho\, D_{\text{lat}}\big(\mu_r = \rho^{-1}, T/T_c\big) G(\pi\rho T)\,. \tag{4.22}$$

We illustrate the integrand for several N_τ values in Fig. 4.7.

Fig. 4.8 shows the resulting estimate of the topological susceptibility which we would obtain by working at a given N_τ and applying a given amount of gradient flow. The lattice corrections to the action raise the contributions in the peak of Eq. (4.17) near $\rho T \simeq 0.4$. But lattice artifacts also dramatically increase the number of dislocations with $\rho \sim a$, as we see from the integrand in Fig. 4.7. If these two scales, a and $0.4/T$, are well separated, then gradient flow can erase the dislocations with little impact on the typical calorons. That is, there will be a minimum in the integrand of Fig. 4.7 and we can use Fig. 4.6 to choose a flow depth which will erase calorons below this minimum. This leads to a plateau in the susceptibility over a range of flow depths as seen in Fig. 4.8. For coarser lattices such as $N_\tau = 6, 8$, examining Fig. 4.7, it is not clear where to cut to separate calorons from dislocations, and there is no associated plateau in Fig. 4.8. Therefore $N_\tau = 6, 8$ will likely not be sufficient to give results which are stable against the amount of flow, but larger N_τ will, especially if we use Zeuthen flow. Overimproved flow is good for completely "cleaning" a configuration of perturbative fluctuations, but in terms of eliminating small instantons it is effectively equivalent to using a specific fixed depth of Wilson flow. Therefore it is not preferred if we want *flexibility* in choosing the size of calorons/dislocations which we eliminate.

Finally, we consider the extrapolation to zero lattice spacing in Fig. 4.9. The lattice-spacing corrections are very large even for $N_\tau = 10$ and a simple extrapolation in χ_{top} can easily lead to a negative result. But that is because the a^2 errors are best viewed as a correction to the *logarithm* of χ_{top}, as we see in Eq. (4.21). If we extrapolate in terms of $\ln(\chi_{\text{top}})$, the procedure works much better.

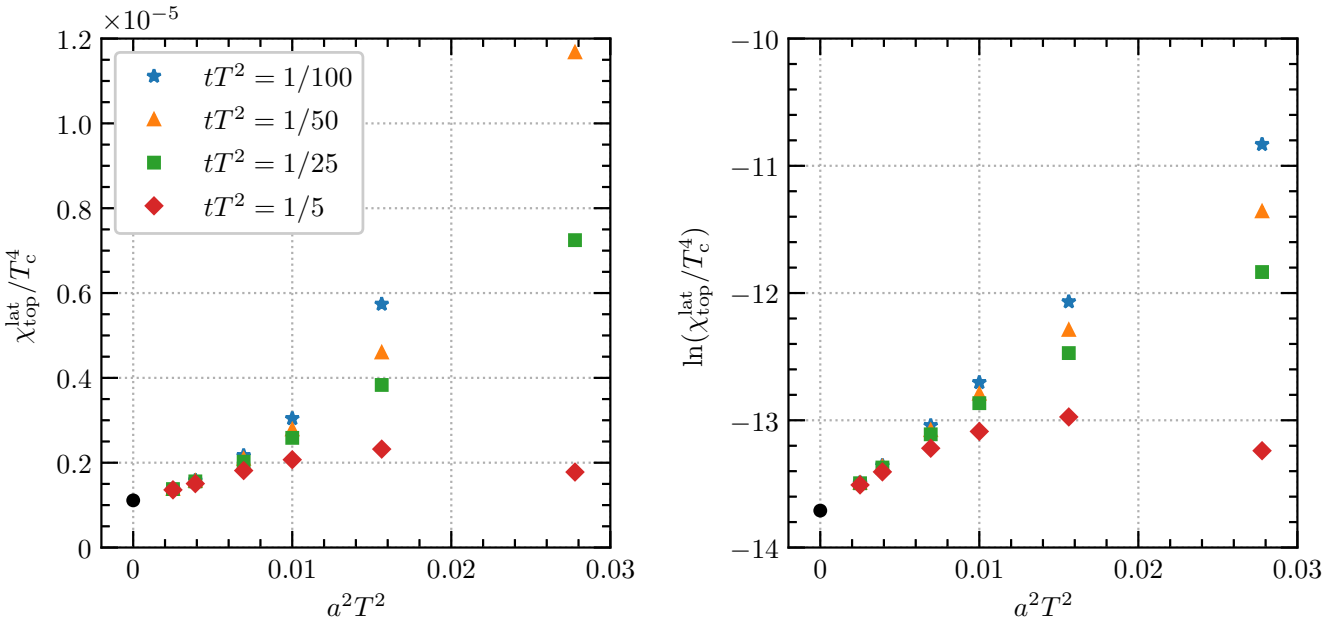

Figure 4.9.: Left: Continuum extrapolation of Eq. (4.22) at $T = 4\,T_c$ at fixed (Wilson) flow time. Right: Logarithm of left plot. The black point represents the continuum value. A similar figure is published in our paper [64].

4.4 Conclusions

We have constructed calorons on the lattice. We find that they possess most of the action and topological charge if $\rho T \gtrsim 1/N_\tau$, and nearly all of the charge and action if $\rho T \gtrsim 2/N_\tau$. Wilson flow destroys small calorons, with progressively more flow destroying larger calorons, as expected. Our work quantitatively expresses this in Fig. 4.6.

Also, if a lattice study were to flow each topologically nontrivial configuration until it loses topological character ($Q_{\mathrm{imp}} < 0.5$), and keep track of the distribution of flow depths needed, then a plot as the one in Fig. 4.5 could be used to turn this result into a size distribution of the topological objects observed on the lattice.

Using our results to estimate the a^2 errors that arise when computing the topological susceptibility $\chi_{\mathrm{top}}(T)$ on the lattice, we find that $N_\tau = 6$ is insufficient to be in the scaling regime (probably $N_\tau = 8$ as well), and lattice spacing errors are expected to lead to a severe overestimate of $\chi_{\mathrm{top}}(T)$ at finite a which may lead to negative values if we extrapolate $\chi_{\mathrm{top}}(T)$ against a^2. It is more natural to extrapolate $\ln\big(\chi_{\mathrm{top}}(T)\big)$ against a^2 because this corresponds better to the way in which a^2 errors enter in the susceptibility.

Note that the inclusion of light quarks in Eq. (4.19) would change the factor $-2\lambda^2$ to $-(2 + N_{\mathrm{f}}/3)\lambda^2$ which makes the dominant size of calorons smaller. Therefore, since $\rho T N_\tau$ becomes smaller, the corrections in Eq. (4.21) become larger (since $\mathcal{F}$ is negative), and the value of N_τ needed to reach scaling will be still larger.

Chapter 5

The Topological Susceptibility via Reweighting

As already elaborated in Chaps. 1 and 2, the properties of the QCD axion are sensitive to the topological susceptibility of QCD $\chi_{\text{top}}(T)$, defined as (cf. Sec. 2.4.3)

$$\chi_{\text{top}}(T) = \int \mathrm{d}^4x \, \langle q(x)q(0)\rangle_\beta = \frac{1}{\beta V}\langle Q^2\rangle, \tag{5.1}$$

with $q(x)$ the topological charge density and $Q = \int \mathrm{d}^4x \, q(x)$ the topological charge. While the topological susceptibility at low temperatures is well established [53, 54], calculations become much more challenging at high temperatures, and axion cosmology requires knowledge of $\chi_{\text{top}}(T)$ at temperatures up to about $7\,T_{\text{c}}$ [51, 55]. Recently, there has been a burst of progress in determining $\chi_{\text{top}}(T)$ at high temperatures [56–62]. However, we feel that it would still be valuable to make an independent study of the topological susceptibility that reaches up to $7\,T_{\text{c}}$.

At high temperatures, topology is expected to be dominated by rare single caloron configurations with a typical size $\rho \sim 0.4/T$ [124], cf. also Fig. 4.7. These configurations become more suppressed as one considers higher temperatures, by $\chi_{\text{top}}(T) \propto T^{-7-N_{\text{f}}/3}$ (at lowest perturbative order within the DIGA, cf. Sec. 2.4.4). This makes studying topology by lattice Monte Carlo simulations challenging; in an ensemble of high-temperature gauge theory configurations, virtually none of the configurations will possess topology, leading to severely limited statistics. This was already seen in our exemplary "brute-force" determination of the topological susceptibility in Sec. 3.8.2. For instance, if we keep the number of temporal points across the lattice fixed, the instanton density in terms of lattice sites vanishes as T^{-11}. Furthermore, the efficiency with which a Markov chain algorithm samples these topological configurations will be additionally suppressed because the chain must pass through "small" instantons (or dislocations) to move between distinct topological sectors, and these dislocations get rarer with decreasing lattice spacing as a^{-11}.

One way around this problem is to measure topology at a low temperature where instantons are not rare and to work up to high temperatures [56, 57]. But we feel it is important as a cross-check to be able to perform a direct study of topology at high temperatures. This will require a reweighting procedure to overcome the sampling challenges. Our goal in this chapter is to present such a reweighting approach. Since this work is exploratory, we will content ourselves with a study of the quenched (or pure-glue) theory, i.e., of pure SU(3) Yang-Mills theory. Once the technique is well established, we see no obstacles in adapting it to the unquenched case (though there will be the usual increase in numerical cost associated with going from pure glue to unquenched).

This chapter is based on work published in Physical Review D [65] and Proceedings of Science [66]. In order to respect the formulation of the precise arguments and their interpretation originally made, most parts of this chapter are adopted from the original publications. The author of this thesis was involved in all steps of this project. It is structured as follows: In Sec. 5.1, we discuss in detail the method that we use to enhance the number of instantons in the lattice simulations, namely a combination of gradient flow and reweighting. Results of the topological susceptibility of the quenched theory up to $4.1\,T_{\text{c}}$ obtained with this method are presented in Sec. 5.2. Conclusions and a discussion of the main results are then provided in Sec. 5.3.

5.1 The Reweighting Method

In this section, we describe the reweighting method that we use to determine the topological susceptibility. We start by describing the general idea of reweighting and then address in detail how it is used to enhance the number of caloron configurations at high temperatures. This is necessary for a statistically powerful method that allows a precise measurement of the topological susceptibility.

5.1.1 Definition of Reweighting

Our reweighting approach is an evolution of those in Refs. [188–191]. It was originally developed to overcome the problem of critical slowing down in studying phase transitions and successfully applied to the electroweak phase transition. Since the topological charge is not restricted to integer values on the lattice, rare events exist that will enable tunneling between different sectors. The goal is then to enhance those and use them to generate a sample of configurations almost homogeneously distributed across the topological sectors of interest. At the same time, it is mandatory to be able to know by how much they were enhanced so that this effect can be removed at the end without losing the statistical power. In the following, we describe one way of achieving this for the case of pure SU(3) Yang-Mills theory with periodic boundary conditions.

The nonperturbative approach of lattice gauge theory is based on a stochastic evaluation of the partition function

$$\mathcal{Z} = \int \mathcal{D}U \, \mathrm{e}^{-S_{\mathrm{W}}[U]}, \tag{5.2}$$

cf. Sec. 3.7. Here $S_{\mathrm{W}}[U]$ is the ordinary SU(3) plaquette Wilson action (3.11) and U are the gauge link variables. The algorithmic challenge consists in obtaining a sample of configurations which is precisely distributed according to the probability distribution

$$\mathrm{d}P(U) = \frac{1}{\mathcal{Z}} \mathrm{e}^{-S_{\mathrm{W}}[U]} \mathcal{D}U \, . \tag{5.3}$$

In this way, importance sampling enables the calculation of expectation values of gauge-invariant operators via the simple mean

$$\langle O \rangle = \frac{1}{N} \sum_{i=1}^{N} O_i \, . \tag{5.4}$$

At high temperatures well above T_{c}, the ordinary approach just described will yield an ensemble with very little topological information, cf. our exemplary "brute-force" approach in Sec. 3.8.2. Reweighting works by rewriting Eq. (5.2) as

$$\mathcal{Z} = \int \mathcal{D}U \, \mathrm{e}^{-S_{\mathrm{W}}[U]+W(\xi)} \, \mathrm{e}^{-W(\xi)}, \tag{5.5}$$

and therefore Eq. (5.4) turns into

$$\langle O \rangle = \frac{\sum_i^N O_i \mathrm{e}^{-W(\xi_i)}}{\sum_i^N \mathrm{e}^{-W(\xi_i)}} \tag{5.6}$$

if the ensemble is distributed according to the modified probability distribution

$$\mathrm{d}P_{\mathrm{rew}}(U) = \frac{\mathrm{e}^{-S_{\mathrm{W}}[U]+W(\xi)}\mathcal{D}U}{\int \mathcal{D}U\,\mathrm{e}^{-S_{\mathrm{W}}[U]+W(\xi)}}\,. \tag{5.7}$$

Notice that it is guaranteed that Eqs. (5.4) and (5.6) yield identical results for any choice of the *reweighting function* W as long as our algorithm converges to Eq. (5.7) and $N \to \infty$. The argument ξ is an arbitrary set of *reweighting variables* which need to be measured on each produced configuration.

5.1.2 Choice of Reweighting Variable

If chosen correctly, reweighting variables can account for a clear distinction between different phases and therefore favor or suppress certain sectors in Monte Carlo space. A natural choice is then the topological charge itself because this is the quantity that distinguishes the different topological sectors:

$$Q = \sum_x q(x) = \frac{1}{64\pi^2}\epsilon_{\mu\nu\rho\sigma}\sum_x \hat{F}^a_{\mu\nu}(x)\hat{F}^a_{\rho\sigma}(x)\,. \tag{5.8}$$

Here $\hat{F}_{\mu\nu}(x)$ is a lattice-discretized form of the field-strength tensor as elaborated in Sec. 3.4. We use the $\mathcal{O}\big(a^2\big)$-improved field-strength tensor (3.30) throughout.

However, using Q directly on the original configuration actually fails, because the topological density contains high-dimension operator corrections which are not topological and which receive large random additive contributions. The solution is well-known; we should apply some amount of gradient flow (cf. Sec. 3.5) to remove the UV fluctuations responsible for this problem. We therefore define our single reweighting variable ξ as

$$\xi \equiv Q' \equiv \frac{1}{64\pi^2}\epsilon_{\mu\nu\rho\sigma}\sum_x \Big(\hat{F}^a_{\mu\nu}(x)\hat{F}^a_{\rho\sigma}(x)\Big)_{t'} \tag{5.9}$$

where t' denotes a relatively small amount of Wilson flow. Specifically, we choose t' to be enough Wilson flow that topology-1 configurations are clearly distinguished from random fluctuations, *but not enough* to remove "dislocations," small concentrations of topological charge which are the intermediate steps between the $Q = 0$ and $Q = 1$ sectors. Therefore, Q' is able to distinguish between fluctuations about the $Q = 0$ sector, dislocations which lie between topological sectors, and genuine $Q = 1$ configurations. The true topological charge of the configuration is denoted by Q and is measured after a larger amount of flow. We shall come back to this distinction in Sec. 5.1.5.

5.1.3 Updating with an Arbitrary Weight Function

Next, we describe the Markov chain algorithm whose equilibrium probability distribution is

$$\mathrm{d}P_{\mathrm{rew}}(U) = \frac{\mathrm{e}^{-S_{\mathrm{W}}[U]+W(Q')}\,\mathrm{d}U}{\int \mathcal{D}U\,\mathrm{e}^{-S_{\mathrm{W}}[U]+W(Q')}} \tag{5.10}$$

assuming that the function $W(Q')$ is already known. Although it is common practice to use the heat-bath/overrelaxation algorithm in the context of pure gauge theories, the hybrid Monte Carlo (HMC) algorithm (cf. Sec. 3.7.1) supports a conceptually simple fermionic extension, so we will use it instead.

One of the simplest ways of producing a sample according to a given probability distribution is to use a Metropolis-inspired algorithm. This algorithm fulfills detailed balance and therefore the Markov chain has an equilibrium distribution to which the system converges if enough updates are done. After

having evolved the Hamilton equations as part of the standard molecular dynamics evolution, an accept or reject step accepts the configuration with probability

$$P_{\mathrm{HMC}} = \min\{1, \mathrm{e}^{-\Delta H}\}, \tag{5.11}$$

where $\Delta H = H_{\mathrm{f}} - H_{\mathrm{i}}$ is the energy difference (the subscripts "i" and "f" refer to "initial" and "final," respectively). It is given by $H(\pi, U) = \frac{1}{2}\sum_x \pi(x)^2 + S_{\mathrm{W}}[U]$. This step alone is of course not sufficient for incorporating reweighting. Therefore, the configuration cannot be fully accepted yet. An additional reweighting accept or reject step in terms of Q' accepts the configuration with probability

$$P_{\mathrm{rew}} = \min\{1, \mathrm{e}^{\Delta W}\}, \tag{5.12}$$

where $\Delta W = W_{\mathrm{f}} - W_{\mathrm{i}}$ is the change in the reweighting function. In total, the transition probability $P(C_{\mathrm{i}} \to C_{\mathrm{f}})$ is given by

$$P(C_{\mathrm{i}} \to C_{\mathrm{f}}) = \int \mathrm{d}\pi_{\mathrm{i}}\, \mathrm{d}\pi_{\mathrm{f}}\, P_{\mathrm{G}}(\pi_{\mathrm{i}})\, P_{\mathrm{M}}\Big((\pi_{\mathrm{i}}, U_{\mathrm{i}}) \to (\pi_{\mathrm{f}}, U_{\mathrm{f}})\Big) \times P_{\mathrm{HMC}}(\Delta H)\, P_{\mathrm{rew}}(\Delta W)\,.$$

The probability $P_{\mathrm{G}}(\pi_{\mathrm{i}}) \sim \exp\big(-\frac{1}{2}\pi_{\mathrm{i}}^2\big)$ with which the conjugate momenta are chosen is drawn Gaußian as usual. The probability P_{M} refers to the molecular dynamics evolution which is a deterministic process. Therefore, P_{M} can be seen as a δ-function that evolves the fields from $(\pi_{\mathrm{i}}, U_{\mathrm{i}}) \to (\pi_{\mathrm{f}}, U_{\mathrm{f}})$ with a unit probability. Our procedure can be summarized as follows:

1. Generate a candidate configuration by evolving the Hamilton equations.
2. Perform a Metropolis step in terms of $\Delta H(\pi, U)$.
   2.1 If accepted, store the candidate configuration.
   2.2 If rejected, return to the initial current configuration (go to step 1).
3. If 2.1 is true, integrate the flow equation (3.38) up to flow time t' and perform a Metropolis step in terms of $\Delta W(Q')$.
   3.1 If accepted, return to the unflowed candidate configuration and fully accept it.
   3.2 If rejected, return to the initial current configuration (go to step 1).

We have described the algorithm assuming a known reweighting function $W(Q')$. In the next section, we shall address the question of how to choose $W(Q')$ such that the final sample is, in the best-case scenario, homogeneously distributed across topological sectors.

5.1.4 Building the Reweighting Function

As explained in the previous section, the *a priori* knowledge of the reweighting function W is mandatory to implement reweighting. We now describe how to find an optimal choice in a completely automated way. Our approach is similar to Refs. [190, 191].

We perform two HMC Markov chains; one to determine W and one to apply the (now fixed) W function to perform our actual Monte Carlo study. Here we describe the preparatory Markov chain which determines W. This preparatory run consists of reweighting updates as described in Sec. 5.1.3 with the only difference that the function W is updated after each trajectory. In this way, we are able to force the system to visit certain sectors in Monte Carlo space that are rare and, at the same time, avoid those that already were visited quite often.

First, we need to define a *reweighting domain* Ω_{rew}. This is the interval in Q' where W will account for reweighting. A natural choice is $(-Q'_{\mathrm{max}}, Q'_{\mathrm{max}})$, where Q'_{max} is the integer value corresponding to the

highest topological sector that we want to include in the reweighting sample. Since we are ultimately interested in $\langle Q^2 \rangle$, we can make use of the symmetry $Q' \mapsto -Q'$ and redefine $Q'_{\text{new}} \equiv |Q'|$. For convenience, we drop the subscript "new" in what follows. In this way, our reweighting domain is

$$\Omega_{\text{rew}} = \left[0, Q'_{\text{max}}\right]. \tag{5.13}$$

We divide this domain into N_{int} intervals, $0 < Q'_1 < Q'_2 < \ldots < Q'_{N_{\text{int}}} \equiv Q'_{\text{max}}$, and name with ω_i the interval between Q'_i and Q'_{i+1}. The reweighting function $W(Q')$ is then defined by giving it definite values at each Q'_i and interpolating linearly between these values; that is, $W(Q')$ is taken as piecewise linear. The last interval $\omega_{N_{\text{int}}}$ is all points with $Q' > Q'_{\text{max}}$; we choose $W\left(Q' > Q'_{\text{max}}\right) \equiv W(Q'_{\text{max}})$ in this (semi-infinite) interval. In other words, values above the top edge of our reweighting domain are not rejected; they are just not reweighted any higher than the boundary value of the domain. To summarize,

$$W(Q') = \begin{cases} (1-x)W_i + xW_{i+1}\,, & Q' \in \omega_i \\ W_{N_{\text{int}}}\,, & Q' > Q'_{\text{max}} \end{cases} \tag{5.14}$$

with

$$x = \frac{Q' - Q'_i}{Q'_{i+1} - Q'_i}\,. \tag{5.15}$$

Having defined our reweighting function in the domain of interest, we can start making reweighting updates. After letting the system thermalize with ordinary HMC updates, we begin building the reweighting function with reweighting updates. We start with a constant function $W(Q') \equiv 1$.[1] Our philosophy is that, whatever value of Q' we currently have, this value is presumably oversampled and should be made less common by reducing $W(Q')$ at the current value. Because W is piecewise linear, the most local change we can make is to change the values at the two edges of the current interval. If $Q' \in \omega_i$ with $i \neq 0$, only the corresponding values W_i and W_{i+1} are changed according to

$$W_i \to W_i - s(1-x)\,, \tag{5.16}$$

$$W_{i+1} \to W_{i+1} - sx\,, \tag{5.17}$$

while the rest of the function remains unaffected. This procedure is illustrated in Fig. 5.1.

The first interval, $Q' \in \omega_0$, is a special case. We need to remember that Q' is per definition strictly positive and therefore W_0 will get updated less than the rest of the points because W_0 is the edge of only one interval and not of two as the other W_i. We correct for this via

$$W_0 \to W_0 - 2s(1-x)\,, \tag{5.18}$$

$$W_1 \to W_1 - sx\,. \tag{5.19}$$

The value of s controls by how much W changes each update. As soon as the gross features of W arise, we decrease its value to slowly reach convergence. In order to do so, it is instructive to introduce the notion of *complete sweep*. We refer to a complete sweep when the reweighting variable Q' ranges from ω_0 to $\omega_{N_{\text{int}}-1}$ *and* back to ω_0. We count the number of updates needed to accomplish this and name it M. There is no need that it visits all intervals. The combination $\delta W = sM/N_{\text{int}}$ tells us how much on

[1] Notice that overall additive constants are irrelevant.

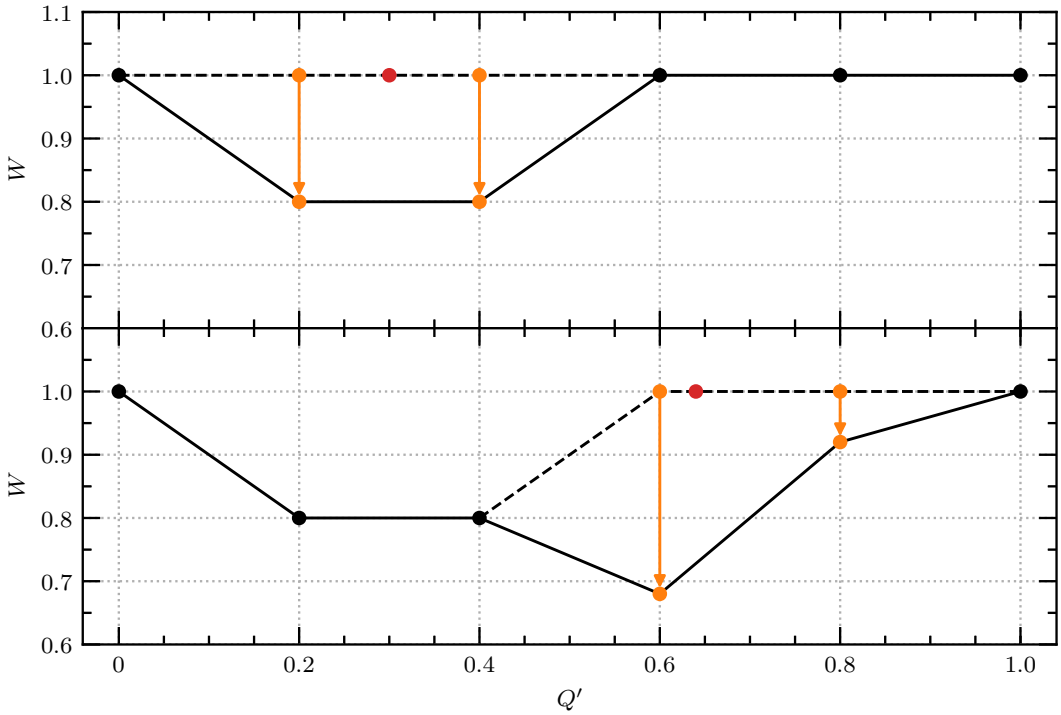

Figure 5.1.: Schematic depiction of how W is built with $N_{\text{int}} = 5$ and $s = 0.4$. The red dot indicates the measured Q', while the orange points and arrows show the change in the W function. The solid black line shows the updated W function, the dashed line is the updated part of W before the update. Top: $Q' = 0.3$. Bottom: $Q' = 0.64$. A similar figure is published in our paper [65].

average one point of W has been changed during the completion of the last sweep. After each complete sweep, we compute δW and reduce s to

$$s \to \max\left\{\frac{s}{2}, s\left(1 - \frac{\delta W}{1.5 \times 2}\right)\right\}. \tag{5.20}$$

Therefore, a sweep that changes a point in W by of average more than 1.5 will lead to s being cut in half, while a sweep that changes a point in W by a smaller average amount will result in reducing s less. After the value of s has been updated, one resets the counter of M back to zero waiting for the next completed sweep to appear and repeats the process.

Eventually, after several sweeps, once the gross features of W have arisen, δW will get small since s is being consistently lowered, and the value of M also should get smaller since fewer trajectories are needed for a completed sweep to appear (that is the whole idea of this update). We consider the procedure to be complete and $W(Q')$ to be ready for use in a Monte Carlo study when $\delta W < 0.1$. An animated GIF of how $W(Q')$ evolves in this process is included in the Supplemental Material of our paper [65].

Our approach bears some similarities to the "metadynamics" approach [192–194] which has also been considered for this problem. One difference is in the way the $W(\xi)$ function is found. Some metadynamics implementations vary $W(\xi)$ throughout the course of the evolution, while others guess an initial value and keep it fixed. We advocate a hybrid approach where $W(\xi)$ is varied at first to optimize its form, and then frozen to produce a truly detailed-balance respecting evolution. We also propose a specific, we believe quite efficient, choice for the $W(\xi)$ function and its update. The other difference is that, in metadynamics, the $W(\xi)$ function is included as part of a "force" term in an HMC evolution, whereas we implement it purely through a Metropolis accept-reject step. The force-term approach is more efficient since HMC trajectories can be longer and because the acceptance rate is higher.

But it requires evaluating the field-derivative of ξ, which may not always be possible or practical. For instance, because we implement gradient flow through stout smearing [195], our Q' is a differentiable function of the link variables. But because we use many stout-smearing steps, the differential expression is extremely unwieldy; within a quenched simulation, our Metropolis implementation is much more efficient. But because the fermionic force term is also very expensive, the price may be worth paying in the unquenched case; indeed, after the first draft of our paper [65] appeared but before its final publication, Bonati *et al.* [63] succeeded in applying such a metadynamics method to the unquenched case.

Other approaches may also be available. Recently, Bonati *et al.* [196] presented several algorithms to solve the problem of topological freezing in the context of a simple quantum mechanical system that shares basic similarities with the problem at hand. In particular, Sec. IVF of this reference contains very similar concepts as the ones used in this paper. However, it is not clear how the most effective algorithms they found could be generalized to the topology problem in QCD.

5.1.5 Parameters to Tune

The procedure described in the last section allows for the automated determination of $W(Q')$, allowing for an efficient reweighting. But several parameters are still to be determined, and we found in practice that a certain amount of hand-tuning was needed to select them.

First, there is the depth of gradient flow to use in establishing Q'. (In practice, we actually used stout smearing [195] with step-size 0.06 as our gradient flow algorithm. This would be totally inadequate if our goal were a precision study of flowed operator expectation values, but here it is only important to suppress UV fluctuations, so a more efficient if less careful implementation of flow should be adequate.) We found that $t' = 0.24\,a^2$ is insufficient to separate configurations of different topology, while $t' = 0.42\,a^2$ is enough; larger amounts of gradient flow start to destroy the dislocations, which makes it more difficult to find the configurations intermediate between topological sectors. Optimally, one should perform several beginning-to-end determinations of χ_{top}, each on the same lattice and temperature, but each time using different t' values, to do a systematic study of which choice leads to the highest statistics for a fixed computational effort; but we have not done a detailed study in this work.

Second, there is the choice of the number and location of intervals. We found 20 intervals to be adequate *except* that there were two "corners" in the $W(Q')$ function where its slope rather abruptly changes, see Fig. 5.3. These appear to be the points where the dominant type of configuration changes (regular thermal configuration to dislocation, dislocation to full-sized caloron), and the Monte Carlo simulation tends to get stuck at these points. We partly cured this by using more, narrower intervals at these points, which handles finer structure in the reweighting function and also leads to the algorithm spending more time near these points. So far we have done this by hand-tuning, though presumably an automated method of interval adjustment could be developed, based for instance on the curvature of the determined reweighting function.

Next, there are the details of the parameter s which controls how fast we adjust the $W(Q')$ function. We tried variations on the procedure described above and found little change to the efficiency with which a good $W(Q')$ is generated. In any case, if high statistics are desired, the Monte Carlo with fixed reweighting function takes most of the computational effort.

Next, there is the length of molecular-dynamics time used in the HMC algorithm updates. A larger HMC step leads to a larger change in the configuration, which is good because it more efficiently explores the phase space. But it leads to larger changes in Q' value and therefore to a higher rejection rate. So the HMC trajectory length needs to be tuned to provide about 50% acceptance rate in the $e^{\Delta W}$ acceptance step. A more careful analysis would compare the total achieved statistics at fixed numerical effort as a function of the HMC trajectory length. To date, we have not carried out such a study, and have instead used the 50% rule of thumb. Our results in what follow used HMC trajectory lengths of 0.2–0.25 a. We are well aware that such a small trajectory length will result in big autocorrelation effects between

Table 5.1.: The lattices used in this chapter. Those labeled with "A" correspond to $2.5\,T_c$ while the lattices labeled with "B" are simulations at $4.1\,T_c$. The gauge couplings β_{lat} are taken from the given references. Moreover, we give the number of measurements as well as the number of complete sweeps obtained from the individual simulations. Subsequent measurements are separated by 100 HMC trajectories.

Lat	T/T_c	N_τ	N_L	β_{lat}	#Measurements	#Complete sweeps
A_1	2.5	6	16	6.507 [197]	61,759	591
A_2	2.5	8	16	6.722 [197]	96,068	263
A_3	2.5	10	24	6.903 [197]	66,840	195
B_1	4.1	6	16	6.883 [198]	70,699	313
B_{2a}	4.1	8	8	7.135 [198]	50,992	94
B_{2b}	4.1	8	12	7.135 [198]	50,390	82
B_{2c}	4.1	8	16	7.135 [198]	52,900	145
B_{2d}	4.1	8	24	7.135 [198]	74,900	168
B_{2e}	4.1	8	32	7.135 [198]	72,800	151
B_3	4.1	10	24	7.325 [198]	82,663	104

configurations. We have taken special care in providing a reliable error estimate by making a careful error analysis based on binning and jackknife, cf. Sec. 3.8.

Finally, there is the choice of the final observable used to determine $\chi_{\text{top}}(T)$. Every 100 HMC trajectories, we make a measurement of Q which we use in our statistical analysis of the susceptibility. We use Q after some amount t of gradient flow and set its value to 1 if $Q \geq Q_{\text{thresh}}$ and to 0 if $Q < Q_{\text{thresh}}$.[2] (Configurations with $Q > 1$ are very rare at the temperatures and for the volumes of interest, as we will establish in the next section, cf. also Sec. 3.8.2.) This leaves open the exact choice of t, of Q_{thresh}, and of the gradient flow procedure (Wilson versus Zeuthen). All choices should lead to the same continuum limit and it is not expensive to sample using various choices and compare. This is what we will do; any difference between $\chi_{\text{top}}(T)$ values due to different threshold or flow depth will indicate deficiencies in our lattice spacing and must be seen to vanish when we take the continuum limit.

5.2 Results

Our goal in this chapter is to demonstrate our method and show that it can obtain statistically powerful results at high temperatures in a range of lattice spacings and volumes. With this in mind, we study ten different lattices, as listed in Tab. 5.1. We use the Wilson gauge action at two temperatures corresponding to $2.5\,T_c$ and $4.1\,T_c$; the values of the coupling β_{lat} are taken from Refs. [197, 198]. Note that we did not use the scale setting as described in Sec. 3.6 in this project as we only considered it after this project was already finished. However, the difference in the resulting temperatures from both scale settings is only around 1%. At the higher temperature, we consider aspect ratios between 1:1 and 4:1 with $N_\tau = 8$ and at both temperatures we consider lattice spacings with $N_\tau = 6$, 8, 10 with an aspect ratio of about 2.5:1. This allows one study of the volume scaling and lets us take the continuum limit, but it is not sufficient to consider both limits simultaneously. All calculations were carried out over a six month period on one eight-core desktop machine and one server node with two Xeon-Phi (KNL) CPUs. By modern standards, this is an extremely modest computational budget.

[2] Note that, as for the reweighting function Q', we implicitly mean $Q \equiv |Q|$ making use of the symmetry $Q \to -Q$ of $\langle Q^2 \rangle$.

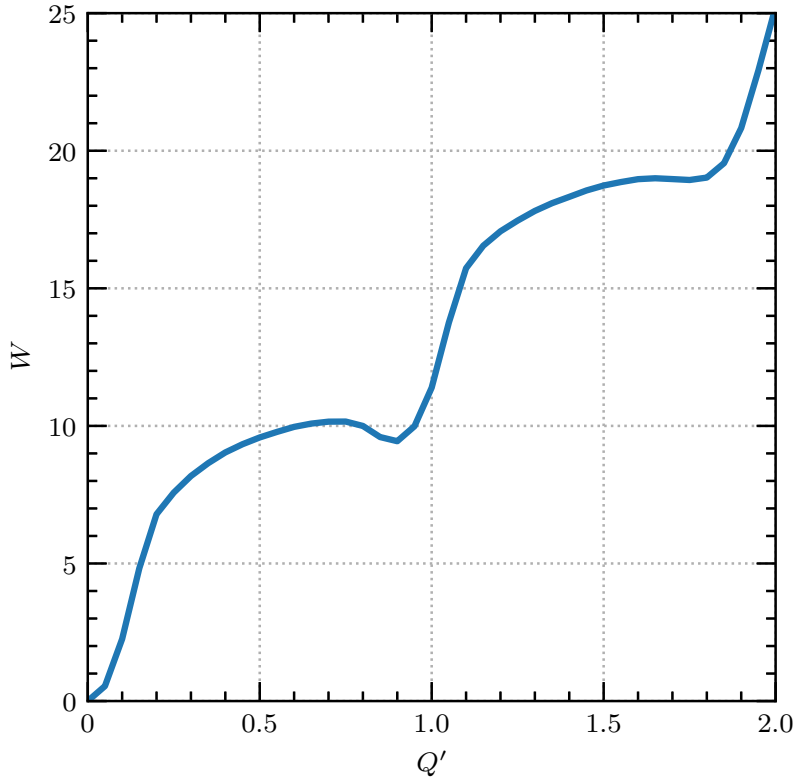

Figure 5.2.: Reweighting function W of a 6×16^3 lattice at $2.5\,T_c$ (Lattice A_1). A similar figure is published in our paper [65].

The first question is whether it is sufficient so sample only $Q=0$ and $Q=1$ sectors, or if larger values of Q are also important in establishing the topological susceptibility. To study this, first look at Eq. (5.6) and consider what happens when we use Q with a threshold as the observable:

$$\langle Q^2\rangle = \frac{\sum_i^N Q_i^2\, e^{-W(Q_i')}}{\sum_i^N e^{-W(Q_i')}} \simeq \frac{\sum_{i:\,Q=1} e^{-W(Q_i')} + \sum_{i:\,Q=2} 4\, e^{-W(Q_i')} + \dots}{\sum_{i:\,Q=0} e^{-W(Q_i')}}, \tag{5.21}$$

where in the numerator we only have to sum over $Q=1$ and higher configurations since $Q=0$ does not contribute, while in the denominator we only sum over $Q=0$ because they completely dominate the ensemble. Clearly, we need both $Q=0$ and $Q=1$ configurations to perform the calculation; but if our accuracy goal is 10%, then we only need $Q=2$ and higher if the total probability to be in one of these states is at least 2.5% of that for $Q=1$ states. Therefore we carried out the construction of $W(Q')$ in the domain $0\le Q'\le 2$, shown in Fig. 5.2, for the lower temperature we study and a 6×16^3 lattice (Lattice A_1). We see immediately from the figure that $Q'>1.5$ configurations require a reweighting of e^{-18} to occur, while $Q'>0.75$ configurations occur already with an e^{-9} reweighting. For our t' values, the $Q=1$ values all have $Q'>0.7$ and $Q=2$ values all have $Q'>1.5$, so this means that $Q=2$ configurations are suppressed relative to $Q=1$ configurations by about e^{-9}. Therefore, $Q=2$ plays a tiny role in Eq. (5.21) and can be safely ignored. In a larger volume, an instanton gas estimate says that the $Q=1$ configurations should get more common with the spacetime volume βV and the $Q=2$ configurations should get more common with $(\beta V)^2$. So $Q=2$ would start to become relevant in a box with an aspect ratio of about 15. Such enormous lattices are not needed to study $\chi_{\rm top}(T=2.5\,T_c)$, and so we do not need to consider $Q\ge2$. This conclusion only strengthens for a larger T where the susceptibility is still smaller. Obviously, at some lower temperature it will break down and we will need many topological sectors; so every time we go to lower temperatures we must revisit this issue.

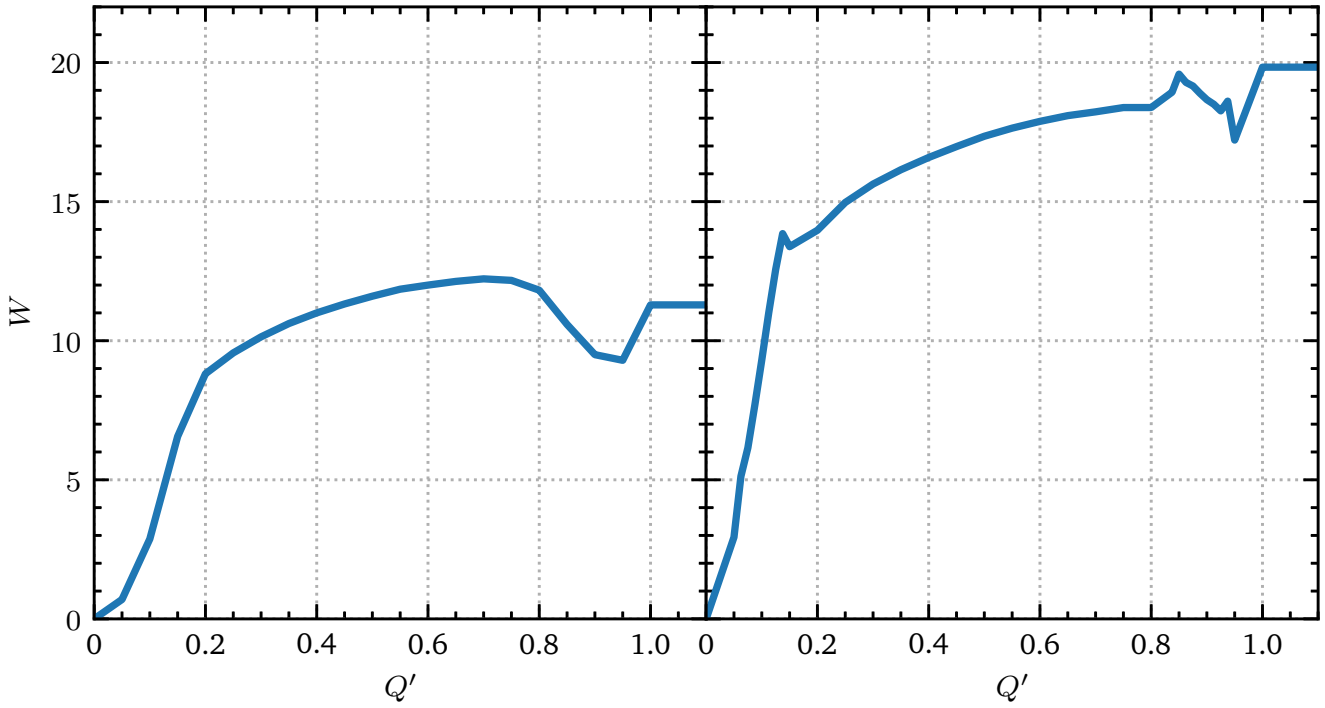

Figure 5.3.: Reweighting functions of 8×16^3 lattice. Left: $2.5\,T_c$ (Lattice A_2). Right: $4.1\,T_c$ (Lattice B_{2c}). A similar figure is published in our paper [65].

We proceed to compute the reweighting function $W(Q')$ using $Q'_{\text{max}} = 1$. Two examples are shown in Fig. 5.3. In each case there is a deep minimum at $Q' = 0$ corresponding to ordinary $Q = 0$ configurations and a much shallower minimum near $Q' = 1$, corresponding to $Q = 1$ configurations, i.e., calorons. The broad plateau in between can be understood as configurations containing a dislocation. The sharp features in the $4.1\,T_c$ plot are caused by our abruptly adjusting the width of our intervals. At finer lattices (larger N_τ), the $Q = 1$ minimum becomes deeper (or more accurately, the barrier gets higher), as the size of physical calorons becomes more different from the lattice spacing.

With the $W(Q')$ reweighting functions in hand, we proceed to evaluate the topological susceptibility via Eq. (5.21). For completeness, we present all of our results in Tab. 5.2. The errors in the table always represent our statistical uncertainty for the given lattice spacing, temperature, volume, and Q definition. Systematic errors, particularly those associated with the continuum and large-volume limits, must be determined by comparing results from different lattices. First, consider the large-volume limit, by analyzing χ_{top} as a function of aspect ratio, shown in Fig. 5.4. The figure evaluates Q after $t = 2.4\,a^2$ of improved (Zeuthen) gradient flow, and considers three different values for the threshold to distinguish between $Q = 1$ and $Q = 0$: $Q_{\text{thresh}} = 0.5, 0.7, 0.9$. The figure shows that, as expected, aspect ratios smaller than 2 are badly discrepant; but the difference between an aspect ratio of 2 and 4 is of an order of tens of a percent, and is not statistically significant. It appears that large-volume behavior sets in at a modest aspect ratio between 2 and 3 (at this temperature). Therefore, in this exploratory study, we will only consider the continuum limit for an aspect ratio of about 2.5. The figure also shows that although the value of Q_{thresh} introduces a systematic effect (the lower the threshold, the higher the determined χ_{top} value), this effect is statistically irrelevant already at $LT < 1.5$ and becomes even smaller for larger volumes (and finer lattices, see Tab. 5.2); in what follows we shall use $Q_{\text{thresh}} = 0.7$.

Finally, we consider the continuum extrapolation, using three lattice spacings with $N_\tau = 6$, 8, and 10. We show this for $T = 2.5\,T_c$ in Fig. 5.5 and $T = 4.1\,T_c$ in Fig. 5.6 (note that the $N_\tau = 8$ lattice has a slightly different aspect ratio than the $N_\tau = 6, 10$ lattices; smaller for $2.5\,T_c$ and larger for $4.1\,T_c$). At the higher temperature, we show results for two flow depths ($t = 1.2\,a^2$ and $t = 2.4\,a^2$) and two choices of flow action (Wilson and Zeuthen). The different Q definitions differ significantly for $N_\tau = 6$ (note that

Table 5.2.: This table shows $\ln\left(\chi_{\text{top}}/T_{\text{c}}^4\right)$ for all points plotted in Figs. 5.4–5.6. Errors are statistical only.

Flow:	Wilson	Wilson	Zeuthen	Zeuthen	Zeuthen	Zeuthen
t/a^2:	1.2	2.4	1.2	2.4	2.4	2.4
Q_{thresh}:	0.7	0.7	0.7	0.5	0.7	0.9
Lat.	$\ln\left(\chi_{\text{top}}/T_{\text{c}}^4\right)$	$\ln\left(\chi_{\text{top}}/T_{\text{c}}^4\right)$	$\ln\left(\chi_{\text{top}}/T_{\text{c}}^4\right)$	$\ln\left(\chi_{\text{top}}/T_{\text{c}}^4\right)$	$\ln\left(\chi_{\text{top}}/T_{\text{c}}^4\right)$	$\ln\left(\chi_{\text{top}}/T_{\text{c}}^4\right)$
A_1	−7.37(07)	−7.52(07)	−7.24(07)	−7.31(07)	−7.35(07)	−7.53(07)
A_2	−7.79(10)	−7.85(10)	−7.74(10)	−7.76(10)	−7.78(10)	−7.85(10)
A_3	−8.09(16)	−8.11(16)	−8.07(16)	−8.08(16)	−8.08(16)	−8.11(16)
B_1	−10.21(07)	−10.41(07)	−10.04(07)	−10.14(07)	−10.19(07)	−10.43(07)
B_{2a}	−12.74(09)	−13.11(10)	−12.47(10)	−12.65(09)	−12.75(10)	−13.17(10)
B_{2b}	−11.90(10)	−12.08(11)	−11.74(10)	−11.84(10)	−11.89(11)	−12.10(11)
B_{2c}	−11.36(11)	−11.46(12)	−11.26(11)	−11.31(11)	−11.34(11)	−11.46(12)
B_{2d}	−11.10(13)	−11.18(13)	−11.03(13)	−11.07(13)	−11.09(13)	−11.18(13)
B_{2e}	−11.16(14)	−11.24(14)	−11.07(13)	−11.12(14)	−11.15(14)	−11.24(14)
B_3	−11.76(17)	−11.80(17)	−11.72(17)	−11.74(17)	−11.76(17)	−11.80(17)

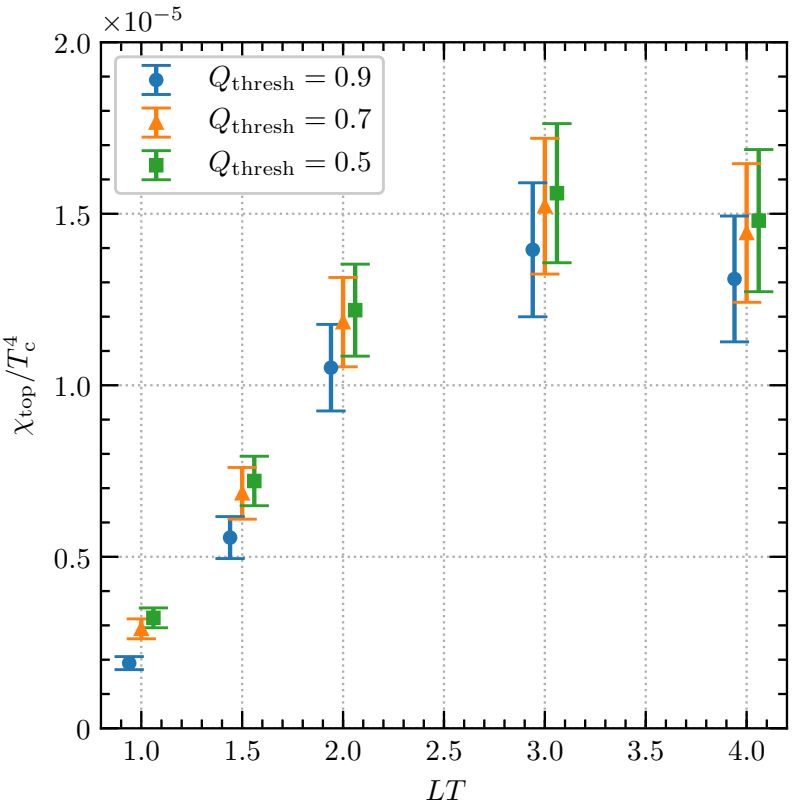

Figure 5.4.: Finite volume dependence of the susceptibility at $N_\tau = 8$ and $T = 4.1\,T_{\text{c}}$ (Lattices B_{2a} through B_{2e}), using Zeuthen flow with $t = 2.4\,a^2$ and three different values of Q_{thresh} (points have been displaced for reasons of visibility). A similar figure is published in our paper [65].

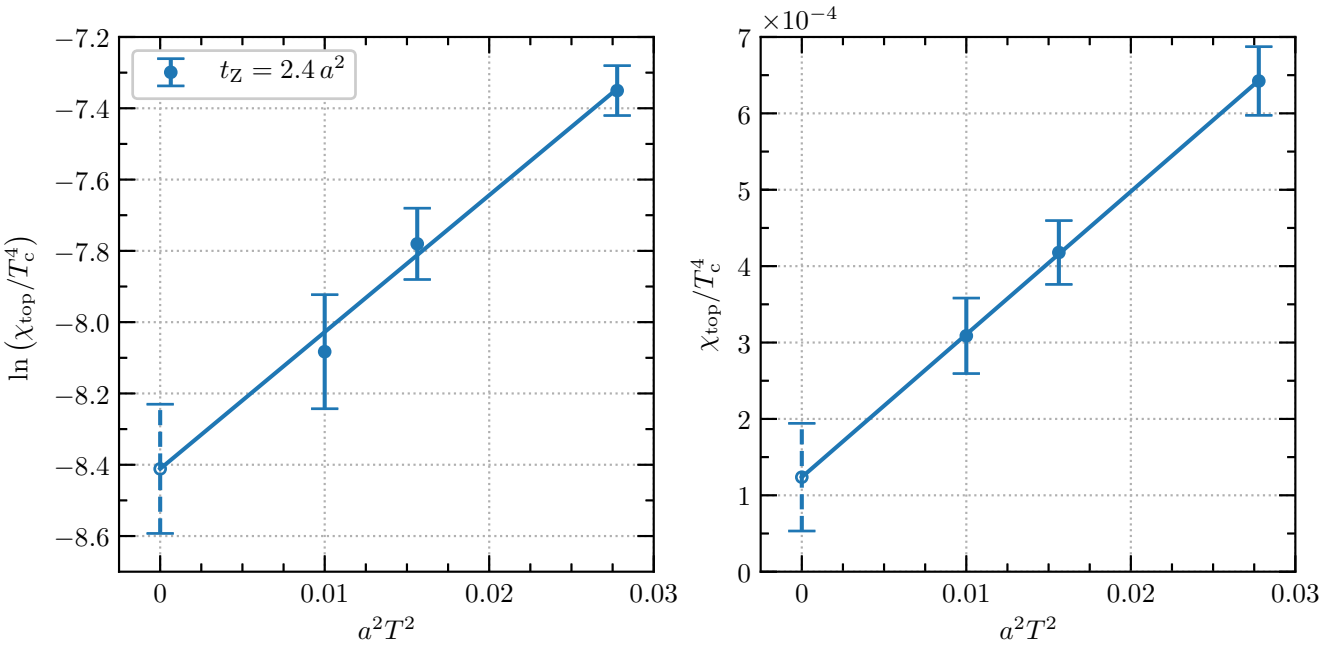

Figure 5.5.: Continuum extrapolation at $T = 2.5\,T_c$ based on lattices A_1, A_2, A_3 (cf. Tab. 5.1), carried out in terms of $\chi_{top}(T)$ directly (right) and $\ln\big(\chi_{top}(T)\big)$ (left) using Zeuthen flow with $t = 2.4\,a^2$ and $Q_{thresh} = 0.7$. The points with dashed errorbars correspond to the continuum-extrapolated results. A similar figure is published in our paper [65].

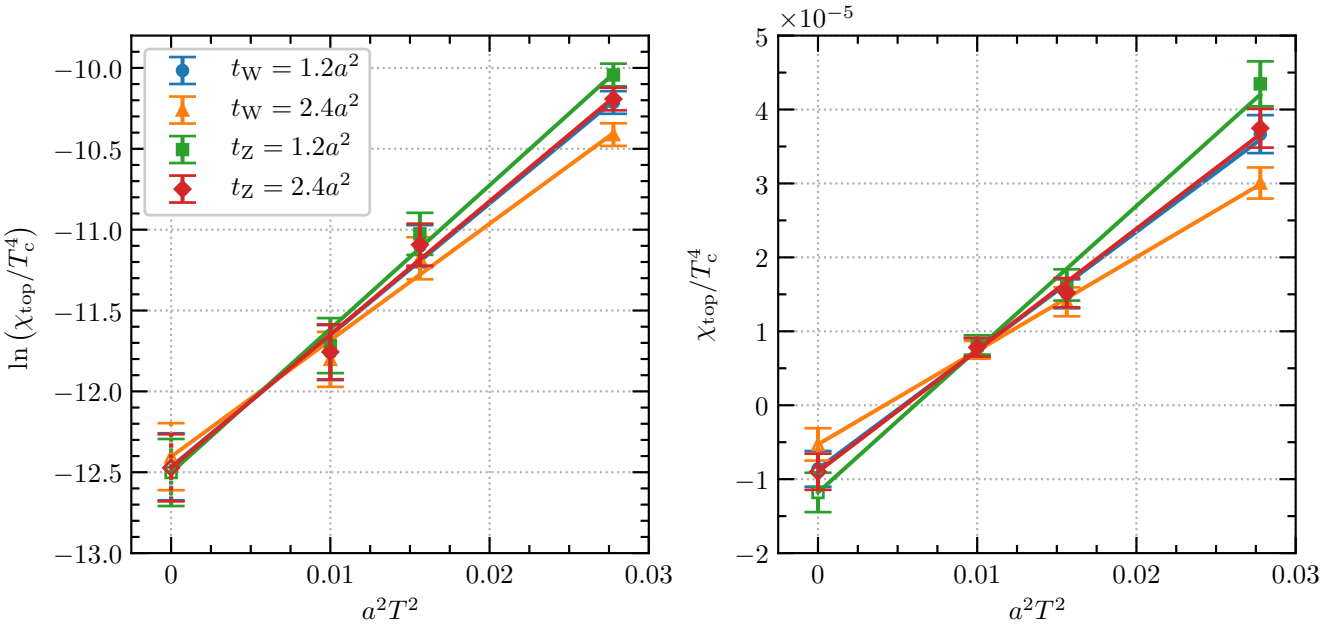

Figure 5.6.: Same as Fig. 5.5 except for $T = 4.1\,T_c$, using lattices B_1, B_{2d}, B_3 (cf. Tab. 5.1). In addition, we have shown separately the measured values for two amounts of flow $t = 1.2\,a^2$ and $t = 2.4\,a^2$ and for two flow actions (Wilson and Zeuthen). Note that the linear-extrapolated continuum limit is *negative* for all choices while the logarithm-extrapolated continuum limit gives consistent results for all choices. A similar figure is published in our paper [65].

the determinations use the same Markov chain, so the errors are highly correlated and the difference is statistically very significant) but are nearly indistinguishable for $N_\tau = 10$; so issues of topology definition are seen to become small on fine lattices. The choice of topology definition is irrelevant in the continuum limit *if* we extrapolate in terms of $\ln(\chi_{\text{top}})$.

However, if we attempt to extrapolate $\chi_{\text{top}}(T, a^2)$ linearly against a^2, we get very poor behavior. At $T = 2.5\,T_c$, the two continuum limits, based on extrapolating $\ln(\chi_{\text{top}})$ and extrapolating χ_{top} directly, differ by more than their error bars. And at $T = 4.1\,T_c$, the linear extrapolations of $\chi_{\text{top}}(T)$ using different definitions of topology are incompatible, and each definition leads to a negative extrapolated value, which is clearly unphysical. On the other hand, if we perform a linear extrapolation of $\ln(\chi_{\text{top}})$ against a^2, the different definitions of topology produce compatible results, which are finite and physical. The reason that one should extrapolate in $\ln(\chi_{\text{top}})$ and not in χ_{top} directly, as we understand it (cf. Chap. 4), is that the topological susceptibility is controlled by the exponential suppression of the caloron action $\exp(-S_{\text{caloron}}) = \exp(-8\pi^2/g_s^2(\mu \sim T))$. This action receives multiplicative $\mathcal{O}(a^2)$ lattice corrections: $\chi_{\text{top}} \propto \exp(-S) \to \exp(-[1-\mathcal{O}(a^2T^2)]S)$. That is, the a^2 corrections are best viewed as a shift in the caloron action and therefore in the logarithm of the susceptibility. An extrapolation of $\ln(\chi_{\text{top}}(T))$ in terms of a^2 is therefore better justified, and better behaved. Indeed, Fig. 5.3 shows that S_{caloron} is about twice as large at $T = 4.1\,T_c$ than at $T = 2.5\,T_c$; so the slope of the extrapolation should be twice as large in the left panel of Fig. 5.6 as in Fig. 5.5, which it is. Therefore this picture of the nature of a^2 errors is consistent with our findings, and an extrapolation of $\ln(\chi_{\text{top}})$ against a^2 is the theoretically best-motivated way to extrapolate to the continuum.

5.3 Discussion

We have presented a methodology for applying reweighting [188] to the measurement of topology in high-temperature pure-glue SU(3) QCD. Our approach involves reweighting in terms of a "poor man's" topological measurement Q' (Q measured after a small amount of flow $t' = 0.42\,a^2$ and using an $\mathcal{O}(a^2)$-improved topological density operator). There is then a two-stage simulation; first, we simulate while dynamically changing our reweight function to determine its form. Then we fix the reweight function and perform a Monte Carlo simulation to determine the topological susceptibility.

The method is effective; with modest numerical resources, we are able to treat $T = 4.1\,T_c$ up to an aspect ratio of 4 and up to a lattice spacing with $N_\tau = 10$, obtaining good statistics. Making a full continuum extrapolation but at a modest aspect ratio of 2.5 (extrapolating the $t = 2.4\,a^2$, Zeuthen flow results), we find

$$\begin{aligned} \chi_{\text{top}}(T = 2.5\,T_c) &= 2.22 \times 10^{-4}\, e^{\pm 0.18}\, T_c^4\,, \\ \chi_{\text{top}}(T = 4.1\,T_c) &= 3.83 \times 10^{-6}\, e^{\pm 0.21}\, T_c^4\,. \end{aligned} \tag{5.22}$$

Our results at individual N_τ values are consistent with previous studies; our A_1 lattice gives the same susceptibility as found by Berkowitz *et al.* [58], and our results at $4.1\,T_c$ and $N_\tau = 6, 8$ (lattices B_1 and B_{2e}) appear compatible with those at $4.0\,T_c$ from Borsanyi *et al.* [62], who have significantly larger statistical errors despite applying much more numerical effort. Those authors also provide a continuum-extrapolated functional fit for $\chi_{\text{top}}(T)$, which is in reasonable agreement with our results; applying their fit form to the temperatures we studied, we obtain $\chi_{\text{top}}(2.5\,T_c) = 1.9 \times 10^{-4}\,T_c^4$ and $\chi_{\text{top}}(4.1\,T_c) = 5.6 \times 10^{-6}\,T_c^4$.

Our results teach a few other lessons. On a lattice with $N_\tau = 6$, χ_{top} is sensitive to the exact definition of topology (depth of flow, flow action, threshold). This dependence is nearly gone by $N_\tau = 10$ and seems not to affect the continuum extrapolation. The continuum extrapolation should be performed in terms of $\ln(\chi_{\text{top}})$, not in terms of χ_{top} itself. The continuum extrapolation corrections to $\ln(\chi_{\text{top}})$ can be large and are larger at higher temperatures. In due regard to Chap. 4, none of these lessons are surprising.

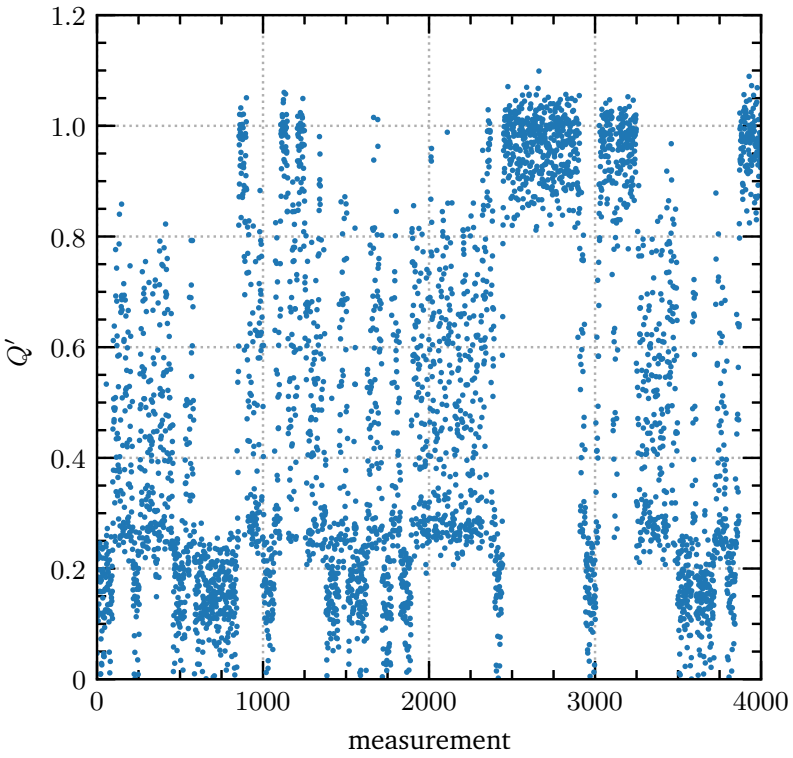

Figure 5.7.: Piece of a Markov-chain history of Q' against measurement number for lattice B_{2d}. The reweighting allows efficient sampling in three regions, $0 < Q' < 0.27$, $0.20 < Q' < 0.85$, and $0.8 < Q' < 1.05$, but has difficulty moving between these regions. A similar figure is published in our paper [65].

We should not claim that our technique solves all problems, however. Looking at the Q' value as a function of measurement number for a short portion of a Markov chain evolution, shown in Fig. 5.7, we see that despite our reweighting function, there are a few points where the simulation gets "stuck."[3] It moves easily in the range $0 < Q' < 0.27$ and similarly moves easily across $0.2 < Q' < 0.85$; but it has difficulty moving from one of these ranges to the other. There is a similar "barrier" around $Q' = 0.8$. These problems become more severe as we move to larger N_τ. We believe that this occurs because Q' is an incomplete descriptor which is missing some other information that distinguishes between these regions. We partly overcame this problem by making more, narrower reweighting bins in these overlap regions; our reweighting procedure causes the Markov chain to spend approximately equal time in each bin, so narrower bins cause more time to be spent in these regions, which helps the Markov chain to find the way between the different regions. (This is the reason for the cuspy discontinuities in Fig. 5.3.) However, while this helps, it hardly solves the problem, as Fig. 5.7 attests. We are searching for one or more additional observables to serve as further reweighting variables in the hopes of improving this sampling. This issue is discussed in detail in Chap. 6, where we present an improvement of the reweighting method. Another inefficiency is that the number of updates needed to move between topological sectors does not improve as we increase the volume. Therefore, to achieve a given level of statistics, the numerical effort must grow linearly with the volume. We do not foresee any solution to this problem.

Conceptually there are no obstacles to applying our technique to the unquenched case (at high temperatures where only one or a few topological sectors are relevant). However, we expect doing so to be numerically more difficult. First, the HMC algorithm requires far more computer power with fermions. Second, the $Q = 1$ sector has near-zero eigenvalues, while the $Q = 0$ sector should have the smallest eigenvalue close to πT. The chiral limit should be severe. Third, the characteristic size of a caloron is

[3] Of course, without reweighting, not a single point in the plot would get above $Q' = 0.15$.

smaller with light quarks than without [124], and therefore the lattice spacing should need to be smaller (N_τ values larger) than what we need in pure glue. But we view these added numerical challenges as reasons that such studies should use reweighting. The temperature range where topology is relevant for axions is $3\,T_c$ to $7\,T_c$ [51], where topology is quite suppressed and only the $Q = 1$ sector should contribute. To overcome the challenges just mentioned in this temperature range, we absolutely need the improvement in the statistical sampling of $Q = 1$ from reweighting if any statistical power is to be achieved.

It is less clear that our approach has applications at lower temperatures where multiple topological sectors are relevant. We might hope that a similar reweighting method might help with the topological-sector sampling problem, which afflicts fine lattices. However, it is not clear to us that Q' will be an effective reweighting variable in this case. We leave the study of this problem for future work.

Chapter 6

Improvement of the Reweighting Method: χ_{top} up to 2 GeV

Using the reweighting approach as developed and established in Chap. 5, we observed that there are three regions where reweighting allows for efficient sampling, while it has problems moving between those regions, as indicated in Fig. 5.7. The problem of those two "barriers" gets severe when we go to higher temperatures or finer lattices. Solving those problems would therefore give significantly better efficiency, especially in view of the inclusion of fermions. The reason for the occurrence of the barriers is that reweighting only in terms of the topological charge is incomplete and missing some information that distinguishes between the different regions. In this chapter, we address how to overcome both barriers. This leads to improved efficiency of the reweighting method and allows for a measurement of the topological susceptibility up to very high temperatures.

This chapter is based on not yet published work [67]. In order to respect the formulation of the precise arguments and their interpretation originally made, most parts of this chapter are adopted from this publication. The author of this thesis was involved in all steps of this project. It is structured as follows: In Sec. 6.1, we discuss in detail the modification of the original reweighting approach that significantly improves the efficiency of the method. Sec. 6.2 contains the lattice determination of the topological susceptibility at $T = 2.5\,T_c$ and $4.1\,T_c$ with the new method which serves as a crosscheck for the original reweighting approach. Moreover, we present a lattice determination of the topological susceptibility at $T = 7.0\,T_c$ which constitutes the first direct measurement of χ_{top} at such a high temperature. A discussion of our results can then be found in Sec. 6.3.

6.1 The Method

In this section, we discuss the improvement of the reweighting method that overcomes both "barriers." We shall refer to those barriers as the *low barrier*, i.e., the barrier at around $Q' \simeq 0.25$ in Fig. 5.7, and the *high barrier*, i.e., the barrier at around $Q' \simeq 0.8$ in Fig. 5.7. This section starts by addressing the origin of both problems and how to improve tunneling through the corresponding barriers. We shall find that both problems need to be solved differently and we hence have to split up the whole lattice setup into multiple distinct Monte Carlo samples. This section is concluded by a discussion of how the different Monte Carlo samples can be combined to a measurement of the topological susceptibility.

6.1.1 The Low Barrier

The low barrier occurs because the algorithm has problems to move between configurations with trivial topology and dislocations, i.e., small concentrations of topological charge that are the intermediate steps between the $Q = 0$ and $Q = 1$ sectors. For an additional reweighting, we therefore need a quantity that distinguishes both types of configurations. Since for dislocations the topological charge is spatially very concentrated, we expect that also the action is concentrated while the action of a topologically trivial configuration is more homogeneously distributed across the lattice. We therefore consider the peak action density

$$G \equiv \max_{\tilde{x}} \left\{ S(\tilde{x}) \right\}, \tag{6.1}$$

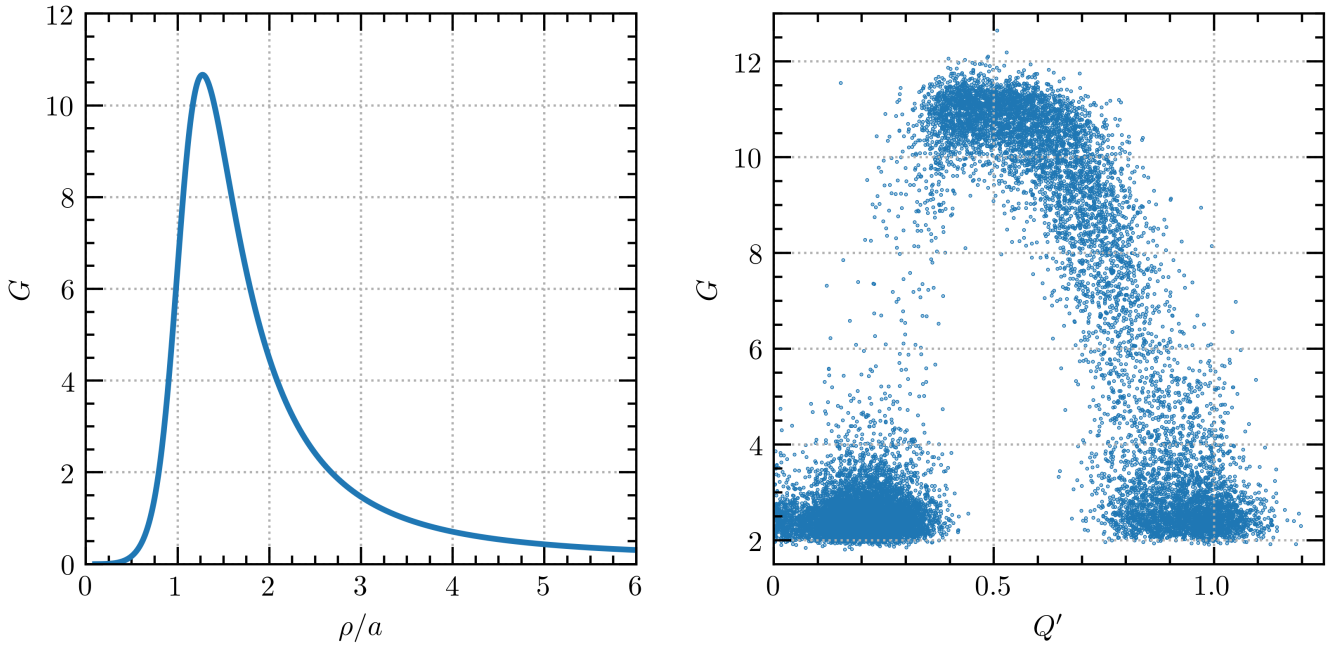

Figure 6.1.: Left: Peak action density G as a function of the caloron size in lattice units on a 10×32^3 lattice. We used a discretization of the Harrington-Shepard caloron as described in Sec. 4.1. For calorons that are one or two lattice spacings across, i.e., for dislocations, G is peaked, while for very small calorons and genuine calorons G is small. Right: Peak action density G as a function of the reweighting variable in the original reweighting approach (cf. Chap. 5) on an 8×32^3 lattice at $4.1\,T_c$. As expected, G is small at small and large Q', indicating trivial topology and genuine calorons, respectively. At intermediate Q', G is large; these are the dislocations. The "gap" between trivial topology and dislocations is precisely the low barrier.

where $\tilde{x}$ denotes a point in the dual lattice and

$$S(\tilde{x}) = \sum_{P(\tilde{x})} \mathrm{Re}\,\mathrm{tr}(1 - P(\tilde{x})) \tag{6.2}$$

with $P(\tilde{x})$ being the 24 plaquettes that are the two-dimensional boundary of the primitive cell with center $\tilde{x}$, as a quantity that distinguishes between topologically trivial configurations and dislocations.[1] Note that, by definition,

$$\sum_{\tilde{x}} S(\tilde{x}) = 2 \cdot S_{\mathrm{W}}\,, \tag{6.3}$$

where S_{W} is the Wilson gauge action (3.11).

The left panel of Fig. 6.1 shows the peak action density as the function of the radius of a discretized Harrington-Shepard caloron (cf. Sec. 4.1). As expected, G is peaked at around one or two lattice spacings, i.e., for dislocations. In the right panel of Fig. 6.1, we plot G against the reweighting variable Q' in the original approach. It clearly shows that G is small for trivial topology at small Q' and large for dislocations, i.e., around $Q' = 0.5$. It is also apparent that the algorithm has problems to sample between both types of configurations because there is a "gap" with only a few points in between.

[1] We name the peak action density G for "globbiness" because this quantity determines how "globby" in the sense of spatially concentrated a configuration is.

To enforce transitions between both types of configurations, instead of reweighting solely in terms of Q', we perform an additional reweighting in terms of G. The effective reweighting function is then the sum of two individual reweighting functions:

$$W_{\text{low}}(Q'_{\text{L}}, G) = W_Q(Q'_{\text{L}}) + W_G(G)\,. \tag{6.4}$$

Note that G is also evaluated after some amount of gradient flow t'_G that in principle does not have to equal the flow time t'_{L} after which Q'_{L} is evaluated. Hand-tuning showed that the amount of gradient flow that gives the best performance depends on the size of the lattice; larger lattices need more flow. The specific choices of these parameters for our lattices are listed in Tab. 6.1. We also saw that HMC trajectories with one step of length $0.2\,a$ give the best performance in this region. Both reweighting functions are built simultaneously in the same way as described in detail in Sec. 5.1.4.

As it is not *a priori* clear that the same method helps to overcome the high barrier, we first constrain this method around the low barrier. We refer to this region as the *low region* (L). It is constrained by $Q^{\text{L}}_{\text{min}} \equiv 0$ and $Q^{\text{L}}_{\text{max}} \equiv 1.15 \times Q'_{\text{L}}(\text{dislocation})$, where we define the dislocation as the HS caloron with maximum G. The factor of 1.15 will become clear below in the discussion of the middle region, cf. Sec. 6.1.3. Configurations with $Q'_{\text{L}} > Q^{\text{L}}_{\text{max}}$ are strictly rejected, everything below this value is allowed and reweighted according to the reweighting function W_{low}. The interval of G that is reweighted is $[G_{\text{min}}, G_{\text{max}}]$. Here, $G_{\text{max}} \equiv G(\text{dislocation})$ is obtained as the peak action density of a dislocation and $G_{\text{min}} \equiv \left\langle G(Q'_{\text{L}} = 0)\right\rangle$ is the peak action density of a non-topological thermal configuration. This is obtained by a short non-reweighted Monte Carlo sample starting from a thermal configuration. Note that configurations that are outside this G-interval are not rejected; they are just not reweighted, i.e., we use $W_G(G > G_{\text{max}}) \equiv W_G(G_{\text{max}})$ and $W_G(G < G_{\text{min}}) \equiv W_G(G_{\text{min}})$.

6.1.2 The High Barrier

The high barrier occurs because the algorithm has problems to move between dislocations and genuine $Q = 1$ calorons. However, the quantity G that we introduced for the low barrier is unfortunately not able to distinguish between dislocations and calorons because both have a peaked action density and there is no real "gap" in Fig. 6.1. Until now we were not able to find a similar variable for the high barrier. However, using larger HMC trajectories (10 steps of $0.25\,a$) significantly improves the performance in this region and partly overcomes the problem of the barrier. This is because longer HMC trajectories lead to larger changes in the configurations which leads to a more efficient sampling of the configuration space. In the low region, this yields very small acceptance rates because we need smooth transitions between topologically trivial configurations and small dislocations which cannot be afforded by too large changes in the configurations. This can also be seen by the fact that a large amount of reweighting is required to move between trivial topology and dislocations, cf. the reweighting functions in the lower panels of Fig. 6.3. Around the high barrier, however, the configurations contain genuine calorons which are large and robust objects. In this region, we need smooth transitions between calorons of different sizes and the corresponding configurations are therefore rather similar. Longer HMC trajectories thus improve the efficient sampling of this region. This can also be seen by the fact that moving between genuine calorons and large dislocations requires a rather small amount of reweighting, cf. the reweighting function in the upper left panel of Fig. 6.3. In fact, hand-tuning showed that for coarser lattices ($N_\tau = 10$ and $N_\tau = 12$), no reweighting is needed at all in this region, i.e., we set $W_{\text{high}}(Q'_{\text{H}}) \equiv 1$. At finer lattices ($N_\tau \geq 14$), however, reweighting becomes mandatory again. But, because, on finer lattices, calorons are more and more lattice spacings across, we also need more flow to remove fluctuations and clearly distinguish calorons of different sizes. We found that $t'_{\text{H}} = 1.32\,a^2$ gives the best efficiency at $N_\tau = 14$.

As this procedure only works well around the high barrier, we constrain this method around the high barrier. We refer to this region as the *high region* (H) constrained by $Q^{\text{H}}_{\text{min}} \equiv 0.7$ and $Q^{\text{H}}_{\text{max}}$. We define the upper limit as the Q'_{H} value of a discretized HS caloron with radius $\rho_{\text{max}} = N_\tau/2$, i.e., the largest

caloron that entirely fits into the lattice. Configurations with $Q'_{\mathrm{H}} < Q^{\mathrm{H}}_{\mathrm{min}}$ are strictly rejected, everything above this value is allowed and reweighted according to the reweighting function $W_{\mathrm{high}}(Q'_{\mathrm{H}})$. Note that values $Q'_{\mathrm{H}} > Q^{\mathrm{H}}_{\mathrm{max}}$ are allowed, but not reweighted, i.e., we set $W_{\mathrm{high}}\big(Q'_{\mathrm{H}} > Q^{\mathrm{H}}_{\mathrm{max}}\big) \equiv W_{\mathrm{high}}\big(Q^{\mathrm{H}}_{\mathrm{max}}\big)$. The reweighting function is built in exactly the same way that was discussed in detail in Sec. 5.1.4. However, we do not use equidistant intervals in Q'_{H} but rather equidistant steps in the caloron size because we actually want to sample different caloron sizes. In practice, we create $N_{\mathrm{int}} = 40$ discretized values of Q'_{H} by setting up $N_{\mathrm{int}} + 1$ calorons with sizes $\rho_i = \rho_{\mathrm{min}} + i \cdot \frac{\rho_{\mathrm{max}} - \rho_{\mathrm{min}}}{N_{\mathrm{int}}}$ $(i = 0, 1, \ldots, N_{\mathrm{int}})$, where ρ_{min} is the size of the HS caloron that has $Q'_{\mathrm{H}} = 0.7$.

Since we now use different flow depths for the lower and upper regions, this causes the necessity of an additional region that smoothly connects both flow depths.

6.1.3 The Middle Region

The *middle region* (M) is chosen such that it has an overlap with both the high and the low region while those regions are disjoint. In this region, we measure the topological charge after both flow times, i.e., the low-region and high-region reweighting variables Q'_{L} and Q'_{H}. Both quantities are highly correlated but still different, and the middle region aims to smoothly transition from one to the other. This then corresponds to smoothly connecting the low and high regions. The middle region is constrained by $Q^{\mathrm{M}}_{\mathrm{min}} \equiv Q'_{\mathrm{L}}(\text{dislocation})$ and $Q^{\mathrm{M}}_{\mathrm{max}} \equiv 1.15 \times Q^{\mathrm{H}}_{\mathrm{min}}$, meaning that the overlap with both the high and low regions is 15%. Configurations with $Q'_{\mathrm{L}} < Q^{\mathrm{M}}_{\mathrm{min}} \vee Q'_{\mathrm{H}} > Q^{\mathrm{M}}_{\mathrm{max}}$ are strictly rejected, everything with values in between is allowed and reweighted according to the reweighting function $W_{\mathrm{mid}}(\theta)$, where the reweighting variable θ is the angle

$$\theta = \arctan\left(\frac{Q'_{\mathrm{L}} - Q^{\mathrm{M}}_{\mathrm{min}}}{Q^{\mathrm{M}}_{\mathrm{max}} - Q'_{\mathrm{H}}}\right) \in [0,\, \pi/2]\,. \tag{6.5}$$

$\theta = 0$ then corresponds to $Q'_{\mathrm{L}} = Q^{\mathrm{M}}_{\mathrm{min}}$ which connects the middle region with the low region, and $\theta = \pi/2$ corresponds to $Q'_{\mathrm{H}} = Q^{\mathrm{M}}_{\mathrm{max}}$ which connects the middle region with the high region. The overlap regions are then defined as

$$\mathrm{O}_1 \equiv \left\{Q'_{\mathrm{L}} \colon Q^{\mathrm{M}}_{\mathrm{min}} \leq Q'_{\mathrm{L}} \leq Q^{\mathrm{L}}_{\mathrm{max}}\right\}, \tag{6.6}$$

$$\mathrm{O}_2 \equiv \left\{Q'_{\mathrm{H}} \colon Q^{\mathrm{H}}_{\mathrm{min}} \leq Q'_{\mathrm{H}} \leq Q^{\mathrm{M}}_{\mathrm{max}}\right\}. \tag{6.7}$$

The different regions are visualized in Fig. 6.2. In the middle region, using an HMC trajectory of four steps of length $0.25\,a$ turned out to give the best performance.

6.1.4 Reweighting with Multiple Regions

We now address the question of how to measure the topological susceptibility using the reweighting approach with three different regions as described above. Each Monte Carlo simulation builds a sample of configurations in its respective region and each configuration has a W reweight value and a known value of Q. To determine the topological susceptibility, we need as an ingredient the fraction of configurations which are $Q = 1$. In a single-region Monte Carlo simulation, we would determine that via

$$\left\langle Q^2 \right\rangle \equiv \frac{\int \mathcal{D}U\, \mathrm{e}^{-\beta S[U]}\, \Theta(Q - Q_{\mathrm{thresh}})}{\int \mathcal{D}U\, \mathrm{e}^{-\beta S[U]}} \simeq \frac{\sum_i \mathrm{e}^{-W[Q'_i]}\, \Theta(Q_i - Q_{\mathrm{thresh}})}{\sum_i \mathrm{e}^{-W[Q'_i]}}\,, \tag{6.8}$$

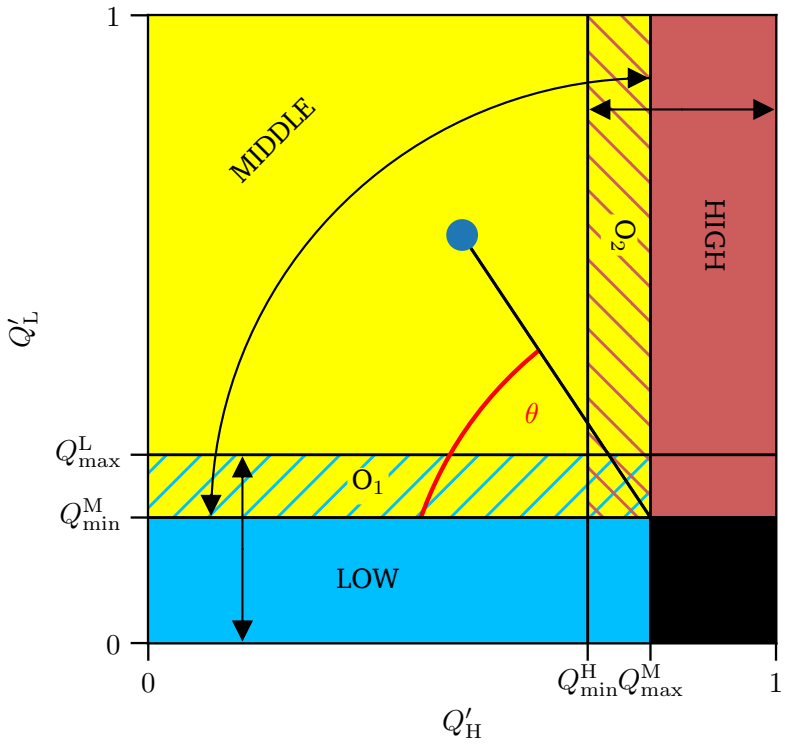

Figure 6.2.: Visualization of the different regions: Low (blue), Middle (yellow), High (red), overlap O_1 (blue hatched), and overlap O_2 (red hatched). A generic configuration in the middle region is depicted by a blue point. The arrows indicate the "transitions" that should be enhanced by reweighting in the respective regions. The black region is the region where the system is simultaneously both in the high and the low region. This region is forbidden and those configurations are strictly rejected.

where Q'_i is the determined Q' value for the i configuration in the sample. The topological susceptibility is then given as

$$\chi_{\text{top}} = \frac{\langle Q^2 \rangle}{\beta V} . \tag{6.9}$$

This approach now has to be extended for multiple regions with their own Monte Carlo samples. The key is the correct use of the overlap regions. We introduce the shorthand notation P_R for the fraction of the total probability over all configurations, which lies in region R. That is,

$$P_R = \frac{\int \mathcal{D}U \, \mathrm{e}^{-\beta S[U]} \, \Theta[Q' \in R]}{\int \mathcal{D}U \, \mathrm{e}^{-\beta S[U]}} , \tag{6.10}$$

where $\Theta[Q' \in R]$ means that we include only those configurations which satisfy the condition to be in region R. Similarly, we introduce $P_{R,Q}$ to mean the same but with the additional requirement that $Q = 1$:

$$P_{R,Q} = \frac{\int \mathcal{D}U \, \mathrm{e}^{-\beta S[U]} \, \Theta[Q' \in R] \, \Theta(Q - Q_{\text{thresh}})}{\int \mathcal{D}U \, \mathrm{e}^{-\beta S[U]}} . \tag{6.11}$$

Defining A ("All") to be the region containing the whole reweighting domain, we need to determine

$$\langle Q^2 \rangle = \frac{P_{\mathrm{A},Q}}{P_{\mathrm{A}}} = \frac{P_{\mathrm{L},Q} + P_{\mathrm{M}-\mathrm{O}_1-\mathrm{O}_2,Q} + P_{\mathrm{H},Q}}{P_{\mathrm{L}} + P_{\mathrm{M}-\mathrm{O}_1-\mathrm{O}_2} + P_{\mathrm{H}}}, \tag{6.12}$$

where we used that $\mathrm{A} = \mathrm{L} \cup (\mathrm{M} - \mathrm{O}_1 - \mathrm{O}_2) \cup \mathrm{H}$ and by $\tilde{M} \equiv \mathrm{M} - \mathrm{O}_1 - \mathrm{O}_2$ we mean all points in the middle region with both overlap regions removed. Note that this corresponds to removing the region $\mathrm{O}_1 \cap \mathrm{O}_2$ twice, i.e., $\tilde{M}$ contains all points in the middle region that are in neither of the two overlap regions with weight $+1$, the disjoint parts of the two overlap regions with weight 0, and the common part of the overlap regions, i.e., $\mathrm{O}_1 \cap \mathrm{O}_2$, with weight -1. Eq. (6.12) can be rewritten as

$$\langle Q^2 \rangle = \frac{P_{\mathrm{H},Q}}{P_{\mathrm{L}}} \times \left(\frac{P_{\mathrm{L},Q} + P_{\mathrm{M}-\mathrm{O}_1-\mathrm{O}_2,Q} + P_{\mathrm{H},Q}}{P_{\mathrm{H},Q}} \right) \times \left(\frac{P_{\mathrm{L}} + P_{\mathrm{M}-\mathrm{O}_1-\mathrm{O}_2} + P_{\mathrm{H}}}{P_{\mathrm{L}}} \right)^{-1} \equiv \Xi_0 \cdot \Xi_1 \cdot \Xi_2^{-1}. \tag{6.13}$$

Using the overlap regions, each of those terms can be rewritten as

$$\Xi_0 \equiv \frac{P_{\mathrm{H},Q}}{P_{\mathrm{L}}} = \frac{P_{\mathrm{H},Q}}{P_{\mathrm{O}_2}} \times \frac{P_{\mathrm{O}_2}}{P_{\mathrm{O}_1}} \times \frac{P_{\mathrm{O}_1}}{P_{\mathrm{L}}}, \tag{6.14a}$$

$$\Xi_1 \equiv \frac{P_{\mathrm{L},Q} + P_{\mathrm{M}-\mathrm{O}_1-\mathrm{O}_2,Q} + P_{\mathrm{H},Q}}{P_{\mathrm{H},Q}} = 1 + \left(\frac{P_{\mathrm{M}-\mathrm{O}_1-\mathrm{O}_2,Q}}{P_{\mathrm{O}_2}} \times \frac{P_{\mathrm{O}_2}}{P_{\mathrm{H},Q}} \right) + \left(\frac{P_{\mathrm{L},Q}}{P_{\mathrm{O}_1}} \times \frac{P_{\mathrm{O}_1}}{P_{\mathrm{O}_2}} \times \frac{P_{\mathrm{O}_2}}{P_{\mathrm{H},Q}} \right), \tag{6.14b}$$

$$\Xi_2 \equiv \frac{P_{\mathrm{L}} + P_{\mathrm{M}-\mathrm{O}_1-\mathrm{O}_2} + P_{\mathrm{H}}}{P_{\mathrm{L}}} = 1 + \left(\frac{P_{\mathrm{M}-\mathrm{O}_1-\mathrm{O}_2}}{P_{\mathrm{O}_1}} \times \frac{P_{\mathrm{O}_1}}{P_{\mathrm{L}}} \right) + \left(\frac{P_{\mathrm{H}}}{P_{\mathrm{O}_2}} \times \frac{P_{\mathrm{O}_2}}{P_{\mathrm{O}_1}} \times \frac{P_{\mathrm{O}_1}}{P_{\mathrm{L}}} \right), \tag{6.14c}$$

where now each ratio is determined by a single Monte Carlo simulation in the high region (red), middle region (green), or low region (blue).

We expect that almost all of the total weight of configurations is in the low region, while almost all of the total weight of $Q = 1$ configurations lies in the high region. Consequently, we presume that $\Xi_1 \approx 1 \approx \Xi_2$ such that we obtain the easier expression

$$\langle Q^2 \rangle \approx \Xi_0 = \frac{P_{\mathrm{H},Q}}{P_{\mathrm{O}_2}} \times \frac{P_{\mathrm{O}_2}}{P_{\mathrm{O}_1}} \times \frac{P_{\mathrm{O}_1}}{P_{\mathrm{L}}}. \tag{6.15}$$

Under this approximation, we end up with a product of three ratios, each of which can be determined using a single one of our Monte Carlo samples:

$$\frac{P_{\mathrm{H},Q}}{P_{\mathrm{O}_2}} = \frac{\sum_{i \in \mathrm{H}} \mathrm{e}^{-W_{\mathrm{high}}[Q'_{\mathrm{H}}]}\, \Theta(Q - Q_{\mathrm{thresh}})}{\sum_{i \in \mathrm{H}} \mathrm{e}^{-W_{\mathrm{high}}[Q'_{\mathrm{H}}]}\, \Theta\big(Q'_{\mathrm{H}} \in \mathrm{O}_2\big)}, \tag{6.16}$$

$$\frac{P_{\mathrm{O}_2}}{P_{\mathrm{O}_1}} = \frac{\sum_{i \in \mathrm{M}} \mathrm{e}^{-W_{\mathrm{mid}}[\theta]}\, \Theta\big(Q'_{\mathrm{H}} \in \mathrm{O}_2\big)}{\sum_{i \in \mathrm{M}} \mathrm{e}^{-W_{\mathrm{mid}}[\theta]}\, \Theta\big(Q'_{\mathrm{L}} \in \mathrm{O}_1\big)}, \tag{6.17}$$

$$\frac{P_{\mathrm{O}_1}}{P_{\mathrm{L}}} = \frac{\sum_{i \in \mathrm{L}} \mathrm{e}^{-W_{\mathrm{low}}[Q'_{\mathrm{L}}, G]}\, \Theta(Q'_1 \in \mathrm{O}_1)}{\sum_{i \in \mathrm{L}} \mathrm{e}^{-W_{\mathrm{low}}[Q'_{\mathrm{L}}, G]}}. \tag{6.18}$$

Therefore, within our approximations, we can easily determine all three ratios. And we need all three Monte Carlos, because each determines one of these three ratios.

6.1.5 Parameters to Tune

As in the original reweighting approach, we still find that a certain amount of hand-tuning is required to achieve the best efficiency of our method. First, there are the depths of gradient flow to use in establishing the reweighting variables Q'_{L}, G, and Q'_{H}. We find that in the high region a rather large amount of gradient flow is required to carefully distinguish calorons of different sizes. In the low region, we need to tune both t'_{L} and t'_G, and it is not clear that both flow depths should be the same. In particular, t'_G needs to be enough flow that fluctuations are removed, but too much flow shrinks the dislocations and the peak action density cannot distinguish between trivial topology and dislocations any more. Similar arguments hold for t'_{L}. We find that t'_{L} slightly larger than t'_G improves the efficiency, but a more careful analysis would be desirable, especially in view of the inclusion of fermions. This could be done by carefully comparing the peak action density of discretized calorons and thermal configurations after different amounts of gradient flow.

Second, there is the position of the lower bound of the high region. We chose $Q_{\mathrm{H}}^{\mathrm{min}} = 0.7$ throughout because this choice definitely includes the high barrier for all used lattices. However, the middle region is sampled more efficiently and it would hence be valuable to place the border as high as possible, such that still the high barrier and all of topology are included in the high region. Then the middle region is as large as possible and the sampling becomes more efficient.

Next, there is the length of the HMC trajectories used in the respective regions. We chose the lengths such the the acceptance rate of the reweighting Metropolis step is about 50%; this leads to small trajectories in the low region, large trajectories in the high region, and to intermediate-sized trajectories in the middle region. Again, a more careful analysis could still improve the efficiency of the algorithm by comparing the achieved statistics at fixed numerical effort as a function of the HMC trajectory lengths in the respective regions.

Finally, there is the definition of the topological charge as the observable for determining the topological susceptibility. Since we saw in Chap. 5 that the continuum extrapolated results are insensitive to the exact choices of both the flow depth and the threshold, we use $t = 2.4\,a^2$ of Wilson flow and $Q_{\mathrm{thresh}} = 0.7$ for deciding whether a configuration is topological or not throughout this chapter, in accordance with the choices in Chap. 5. This allows us to directly compare our results to the ones obtained with the original reweighting approach.

6.2 Results

Our goal is to demonstrate that the improved reweighting method as described above yields statistically powerful results in a range of lattice spacings and volumes and allows for the determination of the topological susceptibility up to $7.0\,T_{\mathrm{c}}$ in the quenched approximation, where the original reweighting approach from Chap. 5 is limited due to the barriers described above. To crosscheck our results, we also determine the susceptibility again at $2.5\,T_{\mathrm{c}}$ and $4.1\,T_{\mathrm{c}}$. In Chap. 5, we already saw that at such high temperatures it is sufficient to only take into account the $Q = 1$ sector because the higher topological sectors are too suppressed to significantly contribute to the topological susceptibility. We therefore only reweight the $Q = 1$ sector as discussed in the previous section. As in the original reweighting approach, we use the standard Wilson gauge action and the HMC algorithm to sample the three regions at each temperature. At the highest temperature, we consider aspect ratios between 1.2:1 and 4:1 at $N_\tau = 10$ and at all three temperatures we consider lattice spacings with $N_\tau = 10$, 12, 14 with an aspect ratio of about 3:1. This again allows for a study of the volume scaling and the continuum limit can be taken. In total, we study 13 different lattice setups as listed in Tab. 6.1. All calculations were conducted over a three month period on the Lichtenberg high performance computer of the TU Darmstadt and on one server node with four 16-core Xeon Gold CPUs.

The first task is to build the four reweighting functions that are needed to completely sample one of the lattices. In total, we therefore have 52 different reweighting functions. One example of these functions

Table 6.1.: The lattices used in this chapter. The lattices labeled with "A" correspond to simulations at $2.5\,T_c$, the lattices labeled with "B" correspond to $4.1\,T_c$, and the lattices labeled with "C" are simulations at $7\,T_c$. The gauge couplings β_{lat} are obtained using the scale setting discussed in Sec. 3.6, cf. Tab. 3.1. Moreover, we give the amount of gradient flow that was used in the definition of the reweighting functions in the respective regions.

Lat	T/T_c	N_τ	V/a^3	β_{lat}	t'_L/a^2	t'_G/a^2	t'_H/a^2
A_1	2.5	10	36×32^2	6.90097	0.48	0.42	0.96
A_2	2.5	12	40×36^2	7.04966	0.48	0.48	0.96
A_3	2.5	14	48^3	7.17706	0.54	0.48	1.32
B_1	4.1	10	36×32^2	7.30916	0.42	0.42	0.96
B_2	4.1	12	40×36^2	7.46275	0.48	0.48	0.96
B_3	4.1	14	48^3	7.59354	0.48	0.48	1.32
C_{1a}	7.0	10	12^3	7.76294	0.36	0.36	0.96
C_{1b}	7.0	10	16^3	7.76294	0.36	0.36	0.96
C_{1c}	7.0	10	24^3	7.76294	0.42	0.42	0.96
C_{1d}	7.0	10	32^3	7.76294	0.42	0.42	0.96
C_{1e}	7.0	10	40^3	7.76294	0.48	0.48	0.96
C_2	7.0	12	40×36^2	7.91939	0.48	0.48	0.96
C_3	7.0	14	48^3	8.05216	0.48	0.48	1.32

for a 14×48^3 lattice at $7\,T_c$ is shown in Fig. 6.3. The reweighting function W_{high} looks, as expected, like the high-Q' part of the reweighting function in the original reweighting approach, cf. Fig. 5.3. It shows a very narrow minimum around $Q'_H = 1$, corresponding to genuine $Q = 1$ calorons. At smaller Q'_H, the reweighting function shows a plateau corresponding to dislocations. Moving from a genuine caloron to a dislocation requires a reweighting of only about e^{-3} which is the reason that at lower temperatures and coarser lattices, where the barrier gets even smaller, no reweighting is needed at all to efficiently sample the high region. The reweighting function W_{mid} samples between dislocations of different sizes and the function shows a monotonically increasing trend. The "spikes" result from the fact that we discretized the θ domain with 50 intervals; a smaller number would have been sufficient. However, the reweighting needed to sample this region is only e^{-4} and due to the "simple" monotonically increasing form of the reweighting function the middle region is sampled very efficiently. The low region is sampled with the sum of the two reweighting functions W_Q and W_G. The topological-charge reweighting function W_Q has a deep minimum at $Q'_L = 0$, corresponding to ordinary, topologically trivial $Q = 0$ configurations. The function then increases until a maximum is reached that corresponds to dislocations. Note that reaching the dislocations requires a large amount of reweighting of roughly e^{-18}. The peak action-density reweighting function W_G shows a large maximum at intermediate G which corresponds to the "gap" in the right panel of Fig. 6.1. Moving through this gap therefore requires a large amount of reweighting of roughly e^{-15}.

With these reweighting functions at hand, we proceed to determine the topological susceptibility via Eqs. (6.9) and (6.15). Since we saw in the original reweighting approach that it does not affect the results if we use Wilson or Zeuthen flow, we only use the computationally slightly cheaper Wilson flow here. For deciding whether a configuration is topological or not, we measure the topological charge after $t = 2.4\,a^2$ Wilson flow, thresholded with $Q_{\text{thresh}} = 0.7$ throughout this chapter, in accordance with the choices in Chap. 5.

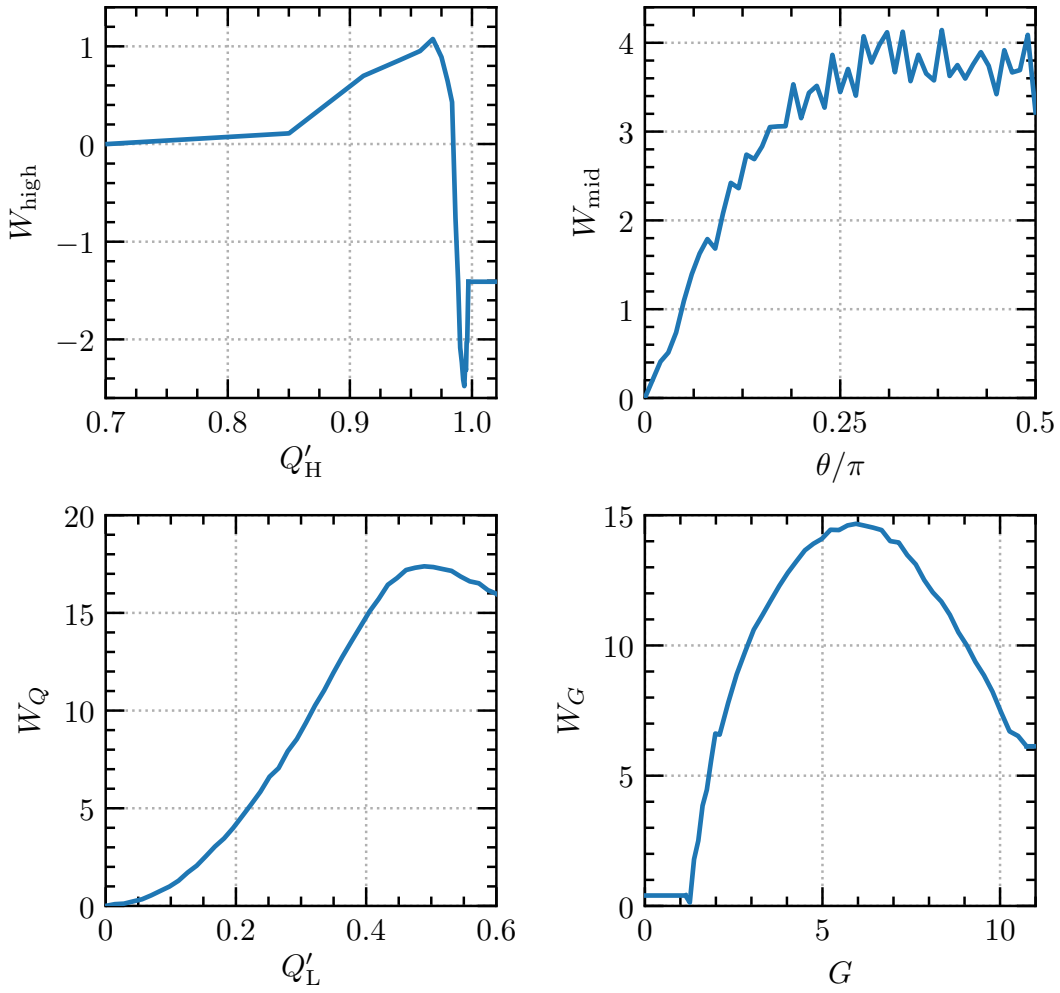

Figure 6.3.: Reweighting functions of a 14×48^3 lattice at $7\,T_c$ (Lattice C_3). The reweighting function in the low region is the sum of the two reweighting functions in the low panels, i.e., $W_{\mathrm{low}}(Q'_{\mathrm{L}}, G) = W_Q(Q'_{\mathrm{L}}) + W_G(G)$.

The first question is whether the approximations used in Eq. (6.15) are justified. For this, we tested the validity of our approximations by explicitly measuring Ξ_1 and Ξ_2 on lattices A_1 and C_2. The result is

$$\left|1-\Xi_1^{A_1}\right| \equiv 0 \equiv \left|1-\Xi_1^{C_2}\right| \tag{6.19}$$

meaning that there is not a single caloron in the middle and low regions. Also the second approximation is fulfilled very precisely:

$$\left|1-\left(\Xi_2^{A_1}\right)^{-1}\right| \approx 3.2 \times 10^{-4}\,, \qquad \left|1-\left(\Xi_2^{C_2}\right)^{-1}\right| \approx 3.6 \times 10^{-9}\,. \tag{6.20}$$

We therefore proceed using Eq. (6.15) for determining the topological susceptibility. For completeness, we present all our results in Tab. 6.2.

We now consider the large-volume limit by studying χ_{top} as a function of the aspect ratio at $7\,T_c$ with $N_\tau = 10$, using lattices C_{1a} through C_{1e}. This is presented in Fig. 6.4. In accordance with the corresponding result in the original reweighting approach, cf. Fig. 5.4, aspect ratios smaller than 2 are badly discrepant, while aspect ratios larger than about 2.5 give consistent results and the large-volume

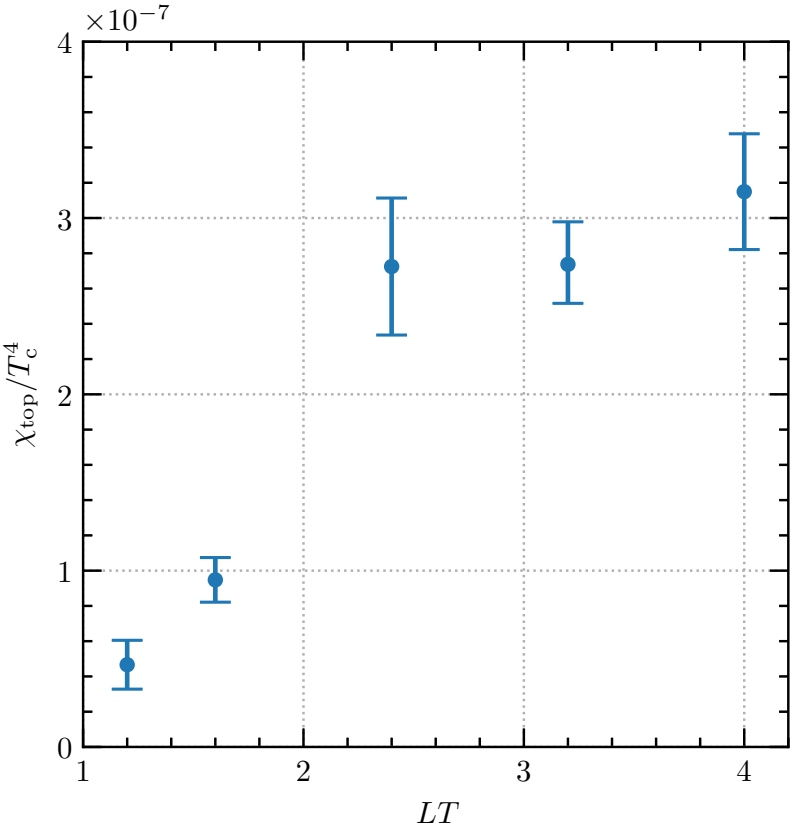

Figure 6.4.: Finite volume dependence of the topological susceptibility χ_{top} at $N_\tau = 10$ and $T = 7.0\,T_c$ (Lattices C_{1a} through C_{1e}), using Wilson flow with $t = 2.4\,a^2$.

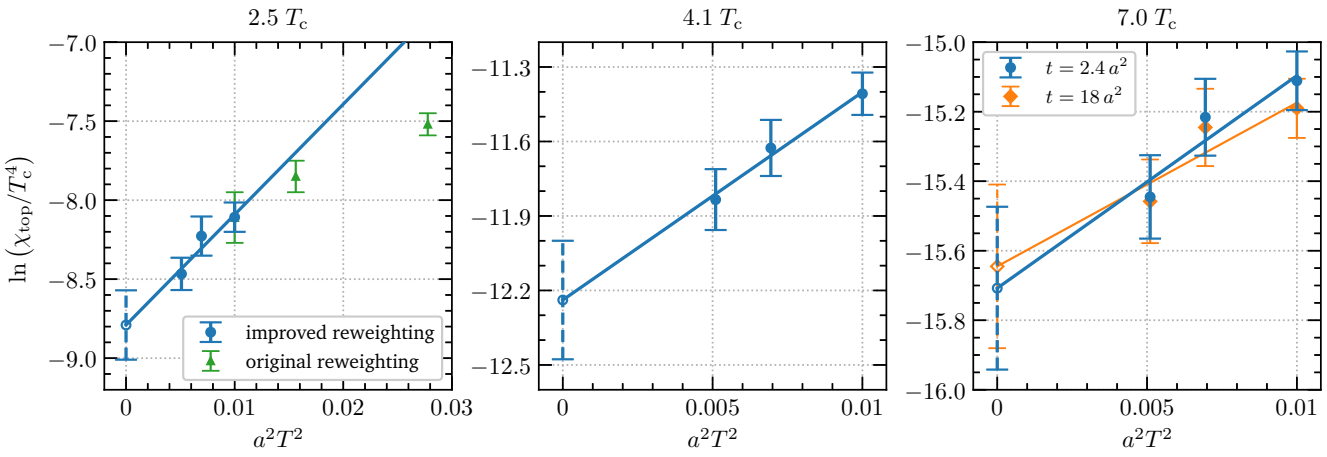

Figure 6.5.: Continuum extrapolation in terms of the logarithm of the topological susceptibility χ_{top} for the three temperatures. Left: $2.5\,T_c$. We additionally show the results from the original reweighting approach in Chap. 5. Middle: $4.1\,T_c$. Right: $7\,T_c$, using the lattices C_{1d}, C_2, and C_3. We additionally show the results with flow time $t = 18\,a^2$. The points with dashed errorbars are the continuum-extrapolated results.

Table 6.2.: This table shows all results that were obtained using the improved reweighting method. It shows for all used lattices and regions the number of measurements and the number of complete sweeps. Two subsequent measurements are separated by 10 updates. Moreover, we list $\ln\left(\chi_{\text{top}}/T_{\text{c}}^4\right)$ for all lattices.

Lat	#Measurements			#Complete sweeps			$\ln\left(\chi_{\text{top}}/T_{\text{c}}^4\right)$
	L	M	H	L	M	H	
A_1	175,560	40,680	53,820	536	861	805	−8.11(09)
A_2	139,690	16,670	62,980	464	491	554	−8.23(12)
A_3	182,460	24,790	56,760	665	626	592	−8.47(10)
B_1	237,960	32,440	61,120	768	593	970	−11.41(09)
B_2	337,540	16,940	71,530	479	453	625	−11.63(11)
B_3	167,990	21,410	59,030	490	549	526	−11.83(12)
C_{1a}	100,000	100,000	66,400	83	2,215	1,915	−16.88(30)
C_{1b}	100,000	100,000	74,200	105	2,450	1,822	−16.17(13)
C_{1c}	321,700	26,300	24,200	269	454	385	−15.12(14)
C_{1d}	368,420	21,630	84,800	483	655	1,353	−15.11(08)
C_{1e}	307,300	15,800	41,700	422	382	636	−14.97(10)
C_2	487,240	32,080	54,420	490	931	496	−15.22(11)
C_3	268,220	20,360	60,920	462	475	531	−15.45(12)

behavior is reached. For determining the continuum extrapolation of the topological susceptibility, we therefore use aspect ratios between 3 and 3.5.

Finally, we address the continuum extrapolation of the topological susceptibility at three temperatures $2.5\,T_{\text{c}}$, $4.1\,T_{\text{c}}$, and $7.0\,T_{\text{c}}$, using three lattice spacings for each temperature with $N_\tau = 10, 12, 14$. As already elaborated in the discussion of the continuum extrapolation of the original reweighting approach, the continuum extrapolation is conducted in terms of the logarithm of the susceptibility, i.e., we linearly extrapolate $\ln\left(\chi_{\text{top}}\right)$ against a^2. The continuum extrapolations of the three different temperatures are presented in Fig. 6.5. At $T = 2.5\,T_{\text{c}}$ (left panel of Fig. 6.5), we additionally show the results with $t = 2.4\,a^2$ Wilson flow from the original reweighting approach, cf. Tab. 5.2. This clearly shows that lattices with $N_\tau = 6$ are too coarse to be in the scaling region, while the finer lattices with $N_\tau = 8$ and $N_\tau = 10$ are consistent with the continuum extrapolation. To explicitly check that the continuum extrapolated results do not depend on the depth of gradient flow used for determining the topological charge, we additional show the results for $t = 18\,a^2$ in the $T = 7.0\,T_{\text{c}}$ continuum extrapolation (right panel of Fig. 6.5). In accordance with our findings in Chap. 5, the different Q definitions are nearly indistinguishable at finer lattices ($N_\tau = 12, 14$), while the difference becomes larger at coarser lattices ($N_\tau = 10$). However, the continuum extrapolated results differ only by about 6%, despite the very different flow times.

6.3 Discussion

We presented an extension of the reweighting technique developed in Chap. 5 that improves the efficiency in determining the topological susceptibility in pure SU(3) Yang-Mills theory. The method is based on the individual treatment of the topologically trivial sector $Q = 0$ ("low region"), the topological $Q = 1$ sector ("high region"), and the intermediate dislocations with fractional $0 < Q < 1$ ("middle region"). In the low region, a combined reweighting in terms of the topological charge and the peak action density, both evaluated at a small amount of gradient flow, allows to efficiently sample between topologically trivial configurations and dislocations. Since this requires a large amount of reweighting

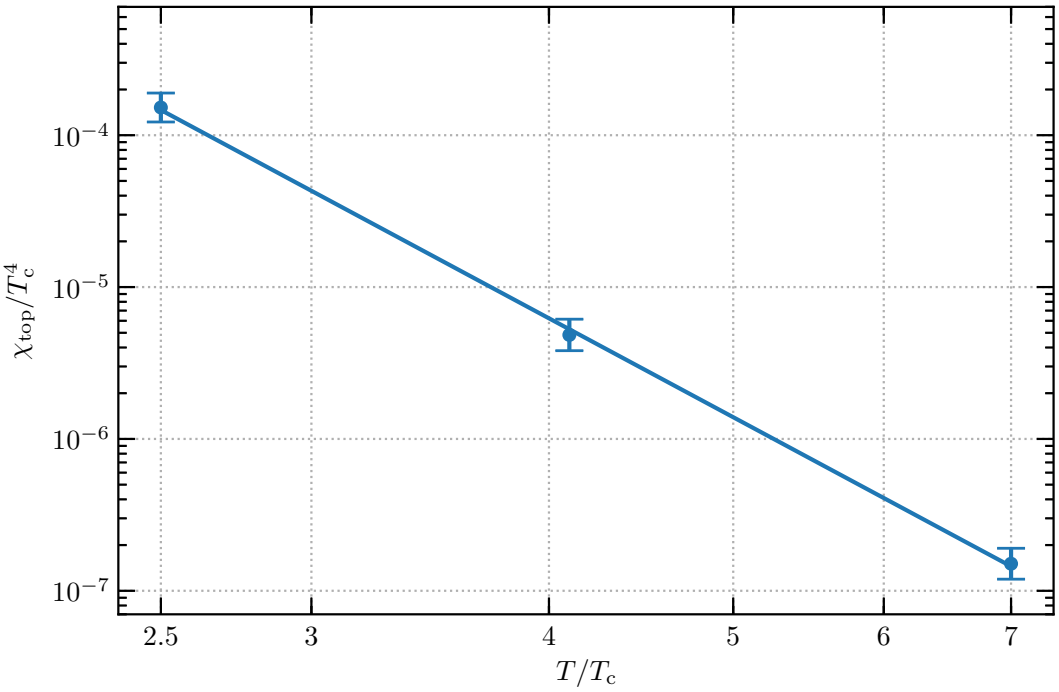

Figure 6.6.: Continuum extrapolated results of the topological susceptibility as a function of temperature in a double-logarithmic plot. We also show the simple power-law fit Eqs. (6.22) and (6.23).

and the involved topological objects are small and fragile, only very small HMC trajectories (one step of $0.2\,a$) can be used; otherwise the acceptance rate in the reweighting step becomes very small. In the high region, sampling between genuine calorons and dislocations requires only a small amount of reweighting. Since also the involved topological objects are large and robust, large HMC trajectories (eight steps of $0.25\,a$) allow for an efficient sampling. At coarser lattices ($N_\tau = 10, 12$), no reweighting is necessary at all in this region; at finer lattices ($N_\tau = 14$), a large amount $t'_{\mathrm{H}} = 1.32\,a^2$ of Wilson flow allows for a careful distinction of calorons of different sizes. In the middle region, sampling between dislocations with different sizes requires only a small amount of reweighting and using intermediate-size HMC trajectories (four steps of $0.25\,a$) allows for a very efficient sampling.

This method is very effective and allows for a continuum-extrapolated determination of the topological susceptibility up to the very high temperature $T = 7.0\,T_{\mathrm{c}}$ and up to an aspect ratio of 4 and fine lattice spacings with $N_\tau = 14$; this determination constitutes the first direct measurement of the susceptibility at such a high temperature. Our final results are

$$\begin{aligned} \chi_{\mathrm{top}}(T = 2.5\,T_{\mathrm{c}}) &= 1.52 \times 10^{-4}\ \mathrm{e}^{\pm 0.22}\ T_{\mathrm{c}}^4\,, \\ \chi_{\mathrm{top}}(T = 4.1\,T_{\mathrm{c}}) &= 4.84 \times 10^{-6}\ \mathrm{e}^{\pm 0.24}\ T_{\mathrm{c}}^4\,, \\ \chi_{\mathrm{top}}(T = 7.0\,T_{\mathrm{c}}) &= 1.51 \times 10^{-7}\ \mathrm{e}^{\pm 0.23}\ T_{\mathrm{c}}^4\,. \end{aligned} \tag{6.21}$$

The continuum-extrapolated results for $2.5\,T_{\mathrm{c}}$ and $4.1\,T_{\mathrm{c}}$ are within errors consistent with the corresponding results from the old reweighting approach (5.22) and hence also with the literature [58, 62]. Applying the grand continuum fit of Ref. [62], also the continuum extrapolated result at $7\,T_{\mathrm{c}}$ agrees well with their findings.

The continuum-extrapolated results are plotted against temperature in a double-logarithmic plot in Fig. 6.6. The DIGA prediction of the temperature dependence of the topological susceptibility at high temperatures (cf. Sec. 2.4.4) suggests that the continuum extrapolated data may be fitted in the form

$$\frac{\chi_{\text{top}}}{T_c^4} = \frac{\chi_{\text{top}}^0}{T_c^4}\left(\frac{T}{T_c}\right)^b \tag{6.22}$$

which has a linear behavior in a double logarithmic plot. The best fit parameters of our continuum extrapolated results are

$$\ln\left(\frac{\chi_{\text{top}}^0}{T_c^4}\right) = -2.67(46)\,, \qquad b = -6.72(31)\,, \tag{6.23}$$

where the uncertainties are statistical only. In pure SU(3) Yang-Mills theory, the DIGA predicts the exponent $b = -7$ which is consistent with our result. In a recent study, Borsanyi *et al.* also determined this exponent in a conventional heat-bath/overrelaxation setup [62]. Despite applying much more numerical effort, they have significantly larger statistical errors and only reach $4\,T_c$; but their result $b = -7.1(4)$ is consistent with ours. In their determination, Berkowitz *et al.* found the result $b = -5.64(4)$ [58] which differs significantly from our result. However, they only reached $2.5\,T_c$ which seems to be too low a temperature for the DIGA to be applicable.

Chapter 7

Conclusions and Outlook

The topological susceptibility of QCD is a very interesting quantity and relevant for, e.g., axion dark matter and the chiral anomaly. It results from the complex vacuum structure of QCD; the QCD vacuum comprises infinitely many topologically distinct classical vacua. The true quantum vacuum is then lifted due to tunneling between the vacua, described by instantons. The topological susceptibility is now, loosely speaking, a measure for the number of instantons/calorons that appear at a given temperature. At zero temperature, this quantity is known very precisely within the framework of chiral perturbation theory. But at very high temperatures – particularly relevant for axion cosmology – the situation is less clear. Ordinary perturbation theory predicts within the dilute instanton gas model at extremely high temperatures a falling of the susceptibility with $\sim T^{-7-N_f/3}$. This strong suppression of topological effects at high temperatures is also the reason why a standard lattice determination of the topological susceptibility is not feasible since extremely rare events have to be sampled. In recent years there was a lot of progress in the lattice determination of the topological susceptibility, but most of the studies are in the quenched approximation and do not reach high enough temperatures. The only study that determines the full QCD susceptibility up to sufficiently high temperatures [56] does not provide a direct determination of the susceptibility at fixed temperatures but only determines its global temperature dependence.

In this work, we presented a step towards the direct lattice determination of the QCD topological susceptibility up to very high temperatures. We developed and established a reweighting method that allows for an efficient sampling of the very rare topologically non-trivial configurations.

We started in Chap. 4 with developing a lattice discretization of both the BPST instanton and the HS caloron. These "clean" topological configurations were then used to combine the dilute instanton gas framework with lattice discretization effects. This allowed a study of the role of gradient flow and the continuum limit in a lattice determination of the topological susceptibility. In particular, we investigated the size of calorons that get destroyed by a given amount of gradient flow. This knowledge was then used to determine the topological susceptibility at different lattice spacings within the (modified) dilute instanton gas framework. The main results of this study were that a lattice with $N_\tau = 6$ is too coarse to be in the scaling regime and lattice spacing errors largely overestimate the topological susceptibility. This leads to the problem that a naïve linear continuum extrapolation of the susceptibility against a^2 may lead to negative results, which is clearly unphysical. However, we argued that a linear continuum extrapolation of the *logarithm* of the susceptibility against a^2 is both more natural and more stable.

In Chap. 5, we then developed the main method for determining the topological susceptibility at high temperatures. Our aim was rather to develop and establish the method instead of giving a final answer of the susceptibility in full QCD. We therefore contented ourselves with working in pure SU(3) Yang-Mills theory which is numerically much cheaper. The basic idea of our approach was to modify the weight with which the configurations are sampled by introducing a reweighting function. This function is chosen such that topologically non-trivial configurations, i.e, calorons, get a larger weight and hence are sampled more efficiently. This builds a statistically powerful method that allows for a precise determination of the topological susceptibility. We presented an automated way to build the reweighting function and then measured the continuum-extrapolated topological susceptibility at $2.5\,T_c$ and $4.1\,T_c$ with roughly 20% errors. Our results are in good agreement with the existing literature [58, 62].

However, this reweighting approach is still limited because it has problems to move between topologically trivial configurations and dislocations, i.e., the intermediate configurations between trivial topology

and calorons, and between dislocations and genuine calorons. This problem gets more severe at finer lattices or higher temperatures. In Chap. 6, we therefore presented an improvement of the reweighting technique. The basic idea here was, instead of sampling between trivial topology and calorons at once, to split up the reweighting domain into three sub-domains, namely trivial topology and small dislocations ("low region"), medium-size dislocations ("middle region"), and large dislocations and genuine calorons ("high region"). This allows for separately solving both problems. In the low region, we found that an additional reweighting is required that clearly distinguishes trivial topology and dislocations. In the high region, using larger HMC trajectories makes the sampling more efficient as we have robust and large topological objects and sampling with too small HMC trajectories requires a lot of (computer) time to "destroy" them.

Using this improved method, we were able to directly determine the continuum-extrapolated topological susceptibility up to $7\,T_c$ which is by far the highest temperature that was ever reached. As a crosscheck, we also determined the susceptibility again at $2.5\,T_c$ and $4.1\,T_c$ which gave results consistent with our original reweighting approach in Chap. 5. We also fitted our continuum extrapolated data in the form $\chi_{\text{top}} = \chi_0 T^b$ which is motivated by the high-temperature prediction of the dilute instanton gas model. Our result $b = -6.72(31)$ is consistent with the prediction $b = -7$ in the quenched approximation. It also agrees well with the result $b = -7.1(4)$ of Ref. [62] who, however, only measured the susceptibility up to $4\,T_c$. The result $b = -5.64(4)$ of Ref. [58] is inconsistent with our result; however, they only reached $2.5\,T_c$ with their approach what indicates that perturbation theory does not yet work at such low temperatures.

In conclusion, we presented a statistically powerful method that allows for a precise lattice determination of the topological susceptibility at high temperatures in pure SU(3) Yang-Mills theory. In our study, we measured the susceptibility up to $7\,T_c$ which is by far the highest temperature that was ever reached in a lattice study.

Based on these results, the next step will be to determine the topological susceptibility of full QCD. This requires transferring our method to a full QCD setup including fermions. We expect, however, that the method as described above can be applied in this case without conceptual issues. This is also the reason why we worked with the HMC algorithm and not with the heatbath/overrelaxation algorithms which are more efficient in the pure glue case. However, the HMC algorithm is numerically significantly more expensive with fermions as it needs the determinant of the Dirac operator and hence has to invert a huge matrix for every update. A second problem is that the "typical" caloron size (in the sense of Fig. 4.7) gets smaller in the presence of fermions [124]. This implies that finer lattices are needed for simulating full QCD than in the quenched case. Moreover, due to the index theorem, the Dirac operator of a caloron configuration has zero modes, while the smallest eigenvalues of topologically trivial configurations should be around πT. The full-QCD algorithm therefore requires a precise determination of the zero modes of the Dirac operator which may be very challenging. However, despite the mentioned difficulties in including fermions, a reweighting study of the topological susceptibility of full QCD at high temperatures is very promising and seems to be the only feasible way to directly determine the susceptibility at a fixed high temperature.

Another extension of this method would be to combine it with a so-called *multicanonical reweighting* approach. The idea of the present approach is to work at a fixed temperature and reweight in terms of the topological charge to induce transitions between different topological sectors. The idea of the multicanonical reweighting approach is, on the other hand, to work in fixed topological sectors and reweight in terms of the action which induces transitions between different temperatures. In this way, one can directly determine the temperature dependence of the topological susceptibility. However, this method needs as an input parameter the topological susceptibility at the "starting temperature." This can then be provided by the improved reweighting technique that we developed in this work.

Appendix A

Units and Conventions

Throughout this work we use *natural units*, where $\hbar = c = k_B \equiv 1$. This implies that the units of energy, momentum, mass, temperature, and length are all defined by the energy unit, usually taken to be MeV. To convert results in natural units to SI units, one can use the identity $\hbar c = 197.3269804\,\text{MeV fm}$ [199].

When working in four-dimensional Minkowski spacetime, we use the metric convention $(-,+,+,+)$. In four-dimensional Euclidean spacetime, the metric is given by the identity $(+,+,+,+)$. For convenience, we use an index notation, where we use Latin indices for spatial components ($i, j, k = 1, 2, 3$) and Greek indices for spacetime components ($\mu, \nu, \rho, \sigma = 0, 1, 2, 3$). We also use Einstein's summation convention: We sum over free indices that appear twice in a term. For the totally antisymmetric Levi-Civita symbol we use the convention $\epsilon_{123} = +1 = \epsilon_{0123}$.

A.1 The Lie Groups SU(N)

The special unitary group SU(N) is the group of all complex unitary $N \times N$ matrices with unit determinant. In general, a complex $N \times N$ matrix is determined by $2N^2$ real independent parameters. The properties of unit determinant and unitarity decrease the number of real parameters to $N^2 - 1$. The group is closed under Matrix multiplication; this operation is, however, not commutative, making SU(N) a *non-abelian group*.

A general element of the group is represented in the form

$$A = \exp\left(\sum_{a=1}^{N^2-1} \alpha_a T^a\right) \equiv \exp(\alpha_a T^a), \tag{A.1}$$

where the T^a are the so-called *generators* of the group and the α_a are real parameters. In general, there are many different choices of the generators that lead to different *representations* of the group. In the *fundamental representation*, the T^a are chosen as complex traceless and antihermitian[1] $N \times N$ matrices that are normalized via

$$\text{tr}\left[T^a T^b\right] = -\frac{1}{2}\delta_{ab} \tag{A.2}$$

and fulfill the commutation relation

$$\left[T^a, T^b\right] = f_{abc} T^c \tag{A.3}$$

with the so-called *structure constants* f_{abc} that are real and completely antisymmetric. The linear combinations $\alpha_a T^a$ together with the commutation relations (A.2) build the so-called *Lie algebra* $\mathfrak{su}(N)$.

[1] Note that following the conventions of Ref. [150], we use antihermitian generators, while in the physics literature often hermitian generators are used. This leads to additional factors of i.

Another important representation is the *adjoint representation*, where the generators are given by the structure constants, i.e.,

$$(T^a)_{bc} = f_{abc}\,. \tag{A.4}$$

In this representation, both the generators and group elements are given by $\left(N^2-1\right)\times\left(N^2-1\right)$ matrices.

In this work, the groups SU(2) and SU(3) play an important role since SU(3) is the gauge group of QCD and the instanton and caloron solutions are obtained for SU(2).

A.1.1 SU(2)

The fundamental representation of SU(2) is given by

$$T^a = -\frac{\mathrm{i}}{2}\sigma^a, \qquad a = 1, 2, 3 \tag{A.5}$$

with the *Pauli matrices*

$$\sigma^1 = \begin{pmatrix} 0 & 1 \\ 1 & 0 \end{pmatrix}, \qquad \sigma^2 = \begin{pmatrix} 0 & -\mathrm{i} \\ \mathrm{i} & 0 \end{pmatrix}, \qquad \sigma^3 = \begin{pmatrix} 1 & 0 \\ 0 & -1 \end{pmatrix}. \tag{A.6}$$

The structure constants then read $f_{abc} = \epsilon_{abc}$.

A.1.2 SU(3)

The fundamental representation of SU(3) is given by

$$T_a = -\frac{\mathrm{i}}{2}\lambda_a \tag{A.7}$$

with the *Gell-Mann matrices*

$$\lambda^1 = \begin{pmatrix} 0 & 1 & 0 \\ 1 & 0 & 0 \\ 0 & 0 & 0 \end{pmatrix}, \qquad \lambda^2 = \begin{pmatrix} 0 & -\mathrm{i} & 0 \\ \mathrm{i} & 0 & 0 \\ 0 & 0 & 0 \end{pmatrix}, \qquad \lambda^3 = \begin{pmatrix} 1 & 0 & 0 \\ 0 & -1 & 0 \\ 0 & 0 & 0 \end{pmatrix},$$
$$\lambda^4 = \begin{pmatrix} 0 & 0 & 1 \\ 0 & 0 & 0 \\ 1 & 0 & 0 \end{pmatrix}, \qquad \lambda^5 = \begin{pmatrix} 0 & 0 & -\mathrm{i} \\ 0 & 0 & 0 \\ \mathrm{i} & 0 & 0 \end{pmatrix}, \qquad \lambda^6 = \begin{pmatrix} 0 & 0 & 0 \\ 0 & 0 & 1 \\ 0 & 1 & 0 \end{pmatrix},$$
$$\lambda^7 = \begin{pmatrix} 0 & 0 & 0 \\ 0 & 0 & -\mathrm{i} \\ 0 & \mathrm{i} & 0 \end{pmatrix}, \qquad \lambda^8 = \frac{1}{\sqrt{3}}\begin{pmatrix} 1 & 0 & 0 \\ 0 & 1 & 0 \\ 0 & 0 & -2 \end{pmatrix}.$$

The non-vanishing structure constants of SU(3) are given as

abc	123	147	156	246	257	345	367	458	678
f_{abc}	1	$1/2$	$-1/2$	$1/2$	$1/2$	$1/2$	$-1/2$	$\sqrt{3}/2$	$\sqrt{3}/2$

Note that the set $\left\{T^1, T^2, T^3\right\}$ of SU(3) generators generates an SU(2) subalgebra of SU(3), i.e.,

$$\left[T^a, T^b\right] = \epsilon_{abc}T^c \qquad \text{for} \qquad a, b, c = 1, 2, 3\,. \tag{A.8}$$

A.2 γ Matrices and Clifford Algebra

Minkowski Spacetime

In describing spin $s = 1/2$ fermions, we use the γ matrices γ_μ that are fully determined by the *Clifford algebra*

$$\{\gamma_\mu, \gamma_\nu\} = \gamma_\mu\gamma_\nu + \gamma_\nu\gamma_\mu = -2g_{\mu\nu}\mathbb{1}_{4\times4}\,. \tag{A.9}$$

It is also convenient to define a fifth γ matrix via

$$\gamma_5 = -\mathrm{i}\gamma_0\gamma_1\gamma_2\gamma_3\,. \tag{A.10}$$

An explicit representation of those matrices is given by

$$\gamma_\mu = \begin{pmatrix} 0 & -\mathrm{i}\sigma_\mu \\ \mathrm{i}\bar{\sigma}_\mu & 0 \end{pmatrix}, \qquad \gamma_5 = \begin{pmatrix} \mathbb{1} & 0 \\ 0 & -\mathbb{1} \end{pmatrix}, \tag{A.11}$$

where

$$\sigma_\mu = (\mathrm{i}\,\mathbb{1}_{2\times2}, \vec{\sigma}) \qquad \text{and} \qquad \bar{\sigma}_\mu = (-\mathrm{i}\,\mathbb{1}_{2\times2}, \vec{\sigma})\,. \tag{A.12}$$

The γ matrices are therefore traceless and have the properties

$$\gamma_0^2 = \mathbb{1}_{4\times4}\,, \qquad \gamma_i^2 = -\mathbb{1}_{4\times4}\,, \qquad \gamma_5^2 = \mathbb{1}_{4\times4}\,, \qquad \gamma_0^\dagger = \gamma_0\,, \qquad \gamma_i^\dagger = -\gamma_i\,, \qquad \gamma_5^\dagger = \gamma_5 \tag{A.13}$$

and the matrix γ_5 anticommutes with all other γ matrices:

$$\{\gamma_5, \gamma_\mu\} = 0\,. \tag{A.14}$$

Euclidean Spacetime

In Euclidean spacetime, the γ matrices are determined by the slightly modified Clifford algebra

$$\{\gamma_\mu, \gamma_\nu\} = \gamma_\mu\gamma_\nu + \gamma_\nu\gamma_\mu = 2\delta_{\mu\nu}\mathbb{1}_{4\times4}\,. \tag{A.15}$$

The fifth γ matrix is then defined as

$$\gamma_5 = -\gamma_0\gamma_1\gamma_2\gamma_3\,. \tag{A.16}$$

An explicit representation of those matrices is

$$\gamma_0^{\mathrm{E}} = \gamma_0^{\mathrm{M}}\,, \qquad \gamma_i^{\mathrm{E}} = \mathrm{i}\gamma_i^{\mathrm{M}}\,, \qquad \gamma_5^{\mathrm{E}} = \gamma_5^{\mathrm{M}}\,, \tag{A.17}$$

where the superscripts "E" and "M" denote "Euclidean" and "Minkowski", respectively. The γ matrices in Euclidean and Minkowski spacetime therefore only differ in a factor of i in the three "spatial" matrices. The Euclidean γ matrices are therefore traceless and have the properties

$$\gamma_\mu^2 = \mathbb{1}_{4\times4}\,, \qquad \gamma_5^2 = \mathbb{1}_{4\times4}\,, \qquad \gamma_\mu^\dagger = \gamma_\mu\,, \qquad \gamma_5^\dagger = \gamma_5 \tag{A.18}$$

and the matrix γ_5 anticommutes with all other γ matrices:

$$\{\gamma_5, \gamma_\mu\} = 0\,. \tag{A.19}$$

As it should be usually clear from the context if we are working in Euclidean or Minkowski spacetime, we do not specify which of the matrices we are currently using.

A.3 The 't Hooft Symbol

For the description of instantons and calorons, the 't Hooft symbol $\eta_{a\mu\nu}$ and the anti-'t Hooft symbol $\bar{\eta}_{a\mu\nu}$ [118, 122] are very convenient. We therefore collect important definitions and relations of these objects in this appendix. For a more thorough summary of the properties of the 't Hooft symbol we refer to the appendix of Ref. [106].

The 't Hooft symbols are defined as

$$\begin{aligned} \eta_{a\mu\nu} &\equiv \epsilon_{0a\mu\nu} + \delta_{a\mu}\delta_{\nu 0} - \delta_{a\nu}\delta_{\mu 0}\,, \\ \bar{\eta}_{a\mu\nu} &\equiv \epsilon_{0a\mu\nu} - \delta_{a\mu}\delta_{\nu 0} + \delta_{a\nu}\delta_{\mu 0}\,, \end{aligned} \tag{A.20}$$

where $a = 1,2,3$ is a color index and $\mu, \nu = 0,1,2,3$ are Lorentz indices. They form a basis of the antisymmetric 4×4 matrices and are (anti-)self-dual in the Lorentz indices:

$$\begin{aligned} \eta_{a\mu\nu} &= \frac{1}{2}\epsilon_{\mu\nu\alpha\beta}\eta_{a\alpha\beta}\,, \\ \bar{\eta}_{a\mu\nu} &= -\frac{1}{2}\epsilon_{\mu\nu\alpha\beta}\bar{\eta}_{a\alpha\beta}\,. \end{aligned} \tag{A.21}$$

The following contractions of the 't Hooft symbols with themselves and with the Levi-Civita tensor hold for both the 't Hooft symbol and the anti-'t Hooft symbol:

$$\eta_{a\mu\nu}\eta_{b\mu\nu} = 4\delta_{ab}\,, \tag{A.22}$$

$$\eta_{a\mu\nu}\eta_{a\mu\sigma} = 3\delta_{\nu\sigma}\,, \tag{A.23}$$

$$\eta_{a\mu\nu}\eta_{a\mu\nu} = 12\,, \tag{A.24}$$

$$\epsilon_{abc}\eta_{b\mu\nu}\eta_{c\rho\sigma} = \delta_{\mu\rho}\eta_{a\nu\sigma} - \delta_{\mu\sigma}\eta_{a\nu\rho} - \delta_{\nu\rho}\eta_{a\mu\sigma} + \delta_{\nu\sigma}\eta_{a\mu\rho}\,. \tag{A.25}$$

Other important contractions that differ for the 't Hooft symbol and the anti-'t Hooft symbol are

$$\eta_{a\mu\nu}\eta_{a\rho\sigma} = \delta_{\mu\rho}\delta_{\nu\sigma} - \delta_{\mu\sigma}\delta_{\nu\rho} + \epsilon_{\mu\nu\rho\sigma}\,, \tag{A.26}$$

$$\bar{\eta}_{a\mu\nu}\bar{\eta}_{a\rho\sigma} = \delta_{\mu\rho}\delta_{\nu\sigma} - \delta_{\mu\sigma}\delta_{\nu\rho} - \epsilon_{\mu\nu\rho\sigma}\,, \tag{A.27}$$

$$\epsilon_{\mu\nu\rho\lambda}\eta_{a\sigma\lambda} = \delta_{\sigma\mu}\eta_{a\nu\rho} + \delta_{\sigma\rho}\eta_{a\mu\nu} - \delta_{\sigma\nu}\eta_{a\mu\rho}\,, \tag{A.28}$$

$$\epsilon_{\mu\nu\rho\lambda}\bar{\eta}_{a\sigma\lambda} = -\delta_{\sigma\mu}\bar{\eta}_{a\nu\rho} - \delta_{\sigma\rho}\bar{\eta}_{a\mu\nu} + \delta_{\sigma\nu}\bar{\eta}_{a\mu\rho}\,. \tag{A.29}$$

Appendix B

Lattice Discretization of the BPST Instanton

In this appendix, we explicitly derive the lattice discretized version of the BPST instanton in the singular gauge

$$A_\mu^{\mathrm{BPST}}(x) = \bar{\eta}_{a\mu\nu}\frac{\rho^2(x-z)_\nu\tau_a}{(x-z)^2\big((x-z)^2+\rho^2\big)} \tag{B.1}$$

from Sec. 4.1. For this, we need to calculate the exponential

$$U_\mu(x) = \exp\left(a\int_0^1 \mathrm{d}\lambda A_\mu\big(\Gamma_\mu(x,\lambda)\big)\right), \tag{B.2}$$

where $\Gamma_\mu(x,\lambda) = x + \lambda\hat{\mu}$ is an appropriate parameterization for the corresponding path connecting the two neighboring lattice sites x and $x+\hat{\mu}$ with $\lambda\in[0,1]$ (no summation over μ is implied). The integral explicitly reads

$$\begin{aligned}
\int_0^1 \mathrm{d}\lambda A_\mu\big(\Gamma_\mu(x,\lambda)\big) &= \int_0^1 \mathrm{d}\lambda\,\frac{\bar{\eta}_{a\mu\nu}\rho^2(x_\nu-z_\nu)\tau_a}{\big[\lambda^2-2\lambda\big(x_\mu-z_\mu\big)+(x-z)^2\big]\big[\lambda^2-2\lambda\big(x_\mu-z_\mu\big)+(x-z)^2+\rho^2\big]} \\
&= \Big[\bar{\eta}_{a\mu\nu}\rho^2(x_\nu-z_\nu)\tau_a\Big]\times \\
&\quad\times\left[\frac{\arctan\left(\frac{x_\mu-z_\mu+\lambda}{\sqrt{(x-z)^2-\left(x_\mu-z_\mu\right)^2}}\right)}{\rho^2\sqrt{(x-z)^2-\left(x_\mu-z_\mu\right)^2}}\right|_0^1 - \left.\frac{\arctan\left(\frac{x_\mu-z_\mu+\lambda}{\sqrt{(x-z)^2-\left(x_\mu-z_\mu\right)^2+\rho^2}}\right)}{\rho^2\sqrt{(x-z)^2-\left(x_\mu-z_\mu\right)^2+\rho^2}}\right|_0^1\Bigg] \\
&= \Big[\bar{\eta}_{a\mu\nu}(x_\nu-z_\nu)\tau_a\Big]\times\Bigg[\frac{\arctan\left(\frac{x_\mu-z_\mu+1}{\sqrt{(x-z)^2-\left(x_\mu-z_\mu\right)^2}}\right)-\arctan\left(\frac{x_\mu-z_\mu}{\sqrt{(x-z)^2-\left(x_\mu-z_\mu\right)^2}}\right)}{\sqrt{(x-z)^2-\left(x_\mu-z_\mu\right)^2}} \\
&\qquad - \frac{\arctan\left(\frac{x_\mu-z_\mu+1}{\sqrt{(x-z)^2-\left(x_\mu-z_\mu\right)^2+\rho^2}}\right)-\arctan\left(\frac{x_\mu-z_\mu}{\sqrt{(x-z)^2-\left(x_\mu-z_\mu\right)^2+\rho^2}}\right)}{\sqrt{(x-z)^2-\left(x_\mu-z_\mu\right)^2+\rho^2}}\Bigg].
\end{aligned}$$

The next step is exponentiating the result. For this we utilize the relation

$$\exp[\mathrm{i}\lambda\hat{n}\cdot\vec{\sigma}] = \cos\lambda\cdot\mathbb{1} + \mathrm{i}\sin\lambda\cdot(\hat{n}\cdot\vec{\sigma}) \tag{B.3}$$

for any $\lambda \in \mathbb{C}$, a unit vector $\hat{n}$, and the standard (hermitian) Pauli matrices $\vec{\sigma}$. Note that in our conventions $\vec{\tau} = -\mathrm{i}\vec{\sigma}$. In the present case we identify the (not yet normalized) vector $\vec{n}_\mu$ with

$$n_\mu^a \equiv \overline{\eta}_{a\mu\nu}(x_\nu - z_\nu)\,. \tag{B.4}$$

The norm of this vector reads[1]

$$\begin{aligned}\left|\vec{n}_\mu\right| &= \sqrt{n_\mu^a n_\mu^a} = \sqrt{\overline{\eta}_{a\mu\nu}\overline{\eta}_{a\mu\sigma}(x_\nu - z_\nu)(x_\sigma - z_\sigma)} \\ &= \sqrt{\left(\delta_{\mu\mu}\delta_{\nu\sigma} - \delta_{\mu\sigma}\delta_{\mu\nu} + \epsilon_{\mu\nu\mu\sigma}\right)(x_\nu - z_\nu)(x_\sigma - z_\sigma)} \\ &= \sqrt{(x-z)^2 - \left(x_\mu - z_\mu\right)^2}\,.\end{aligned} \tag{B.5}$$

The scalar quantity λ is finally identified with

$$\begin{aligned}\lambda_\mu(x,z,\rho) \equiv &-\arctan\left(\frac{x_\mu - z_\mu + 1}{\sqrt{(x-z)^2 - \left(x_\mu - z_\mu\right)^2}}\right) + \arctan\left(\frac{x_\mu - z_\mu}{\sqrt{(x-z)^2 - \left(x_\mu - z_\mu\right)^2}}\right) \\ &+ \frac{\sqrt{(x-z)^2 - \left(x_\mu - z_\mu\right)^2}}{\sqrt{(x-z)^2 - \left(x_\mu - z_\mu\right)^2 + \rho^2}} \times \left[\arctan\left(\frac{x_\mu - z_\mu + 1}{\sqrt{(x-z)^2 - \left(x_\mu - z_\mu\right)^2 + \rho^2}}\right)\right. \\ &\left. - \arctan\left(\frac{x_\mu - z_\mu}{\sqrt{(x-z)^2 - \left(x_\mu - z_\mu\right)^2 + \rho^2}}\right)\right].\end{aligned} \tag{B.6}$$

Altogether, the discretized BPST instanton reads

$$U_\mu(x,z,\rho) = \cos\lambda_\mu(x,z,\rho)\cdot\mathbb{1} + \mathrm{i}\cdot\sigma_a \cdot \frac{\overline{\eta}_{a\mu\nu}(x_\nu - z_\nu)\sin\lambda_\mu(x,z,\rho)}{\sqrt{(x-z)^2 - \left(x_\mu - z_\mu\right)^2}}\,. \tag{B.7}$$

[1] We again want to stress that μ is fixed and hence no summation over μ is implied.

Bibliography

[1] D. Huterer and M. S. Turner, *Prospects for probing the dark energy via supernova distance measurements*, Phys. Rev. D **60**, 081301 (1999).

[2] S. Perlmutter, M. S. Turner, and M. J. White, *Constraining Dark Energy with Ia Supernovae and Large-Scale Structure*, Phys. Rev. Lett. **83**, 670 (1999).

[3] V. C. Rubin, *The rotation of spiral galaxies*, Science **220**, 1339 (1983).

[4] D. Clowe *et al.*, *A direct empirical proof of the existence of dark matter*, The Astrophysical Journal **648**, L109 (2006).

[5] A. G. Bergmann, V. Petrosian, and R. Lynds, *Gravitational Lens Models of Arcs in Clusters*, The Astrophysical Journal **350**, 23 (1990).

[6] COBE collaboration, G. F. Smoot *et al.*, *Structure in the COBE differential microwave radiometer first year maps*, The Astrophysical Journal **396**, L1 (1992).

[7] G. R. Blumenthal, S. M. Faber, J. R. Primack, and M. J. Rees, *Formation of Galaxies and Large Scale Structure with Cold Dark Matter*, Nature **311**, 517 (1984).

[8] Planck collaboration, Y. Akrami *et al.*, *Planck 2018 results. I. Overview and the cosmological legacy of Planck*, arXiv:1807.06205 (2018).

[9] Planck collaboration, N. Aghanim *et al.*, *Planck 2018 results. VI. Cosmological parameters*, arXiv:1807.06209 (2018).

[10] Particle Data Group collaboration, M. Tanabashi *et al.*, *Review of Particle Physics*, Phys. Rev. D **98**, 030001 (2018).

[11] ATLAS collaboration, G. Aad *et al.*, *Observation of a new particle in the search for the Standard Model Higgs boson with the ATLAS detector at the LHC*, Phys. Lett. B **716**, 1 (2012).

[12] CMS collaboration, S. Chatrchyan *et al.*, *Observation of a New Boson at a Mass of 125 GeV with the CMS Experiment at the LHC*, Phys. Lett. B **716**, 30 (2012).

[13] F. Englert and R. Brout, *Broken Symmetry and the Mass of Gauge Vector Mesons*, Phys. Rev. Lett. **13**, 321 (1964).

[14] P. W. Higgs, *Broken Symmetries and the Masses of Gauge Bosons*, Phys. Rev. Lett. **13**, 508 (1964).

[15] G. S. Guralnik, C. R. Hagen, and T. W. B. Kibble, *Global Conservation Laws and Massless Particles*, Phys. Rev. Lett. **13**, 585 (1964).

[16] B. C. Odom, D. Hanneke, B. D'Urso, and G. Gabrielse, *New Measurement of the Electron Magnetic Moment Using a One-Electron Quantum Cyclotron*, Phys. Rev. Lett. **97**, 030801 (2006), [Erratum: Phys. Rev. Lett. **99**, 039902 (2007)].

[17] C. P. Burgess and G. D. Moore, *The standard model: A primer*. Cambridge University Press, Cambridge, UK (2007).

[18] A. Einstein, *Die Grundlage der allgemeinen Relativitätstheorie*, Annalen der Physik **49**, 769 (1916).

[19] LIGO Scientific, Virgo collaboration, B. P. Abbott *et al.*, *Observation of Gravitational Waves from a Binary Black Hole Merger*, Phys. Rev. Lett. **116**, 061102 (2016).

[20] L. R. Weih, E. R. Most, and L. Rezzolla, *Optimal neutron-star mass ranges to constrain the equation of state of nuclear matter with electromagnetic and gravitational-wave observations*, The Astrophysical Journal **881**, 73 (2019).

[21] G. Bertone, D. Hooper, and J. Silk, *Particle dark matter: Evidence, candidates and constraints*, Phys. Rept. **405**, 279 (2005).

[22] S. Weinberg, *Gravitation and Cosmology: Principles and Applications of the General Theory of Relativity*. John Wiley and Sons, New York, USA (1972).

[23] C. W. Misner, K. S. Thorne, and J. A. Wheeler, *Gravitation*. W. H. Freeman, San Francisco, USA (1973).

[24] S. Weinberg, *Cosmology*. Oxford University Press, Oxford, UK (2008).

[25] M. Bauer and T. Plehn, *Yet Another Introduction to Dark Matter*, Lect. Notes Phys. **959**, 1 (2019).

[26] L. E. Strigari, *Galactic Searches for Dark Matter*, Phys. Rept. **531**, 1 (2013).

[27] T. D. Brandt, *Constraints on MACHO Dark Matter from Compact Stellar Systems in Ultra-Faint Dwarf Galaxies*, The Astrophysical Journal **824**, L31 (2016).

[28] G. Jungman, M. Kamionkowski, and K. Griest, *Supersymmetric dark matter*, Phys. Rept. **267**, 195 (1996).

[29] J. Dragos, T. Luu, A. Shindler, J. de Vries, and A. Yousif, *Confirming the Existence of the strong CP Problem in Lattice QCD with the Gradient Flow*, arXiv:1902.03254 (2019).

[30] C. A. Baker *et al.*, *An Improved experimental limit on the electric dipole moment of the neutron*, Phys. Rev. Lett. **97**, 131801 (2006).

[31] J. M. Pendlebury *et al.*, *Revised experimental upper limit on the electric dipole moment of the neutron*, Phys. Rev. D **92**, 092003 (2015).

[32] A. Grinbaum, *Which fine-tuning arguments are fine?*, Found. Phys. **42**, 615 (2012).

[33] R. D. Peccei and H. R. Quinn, *CP Conservation in the Presence of Instantons*, Phys. Rev. Lett. **38**, 1440 (1977).

[34] R. D. Peccei and H. R. Quinn, *Constraints Imposed by CP Conservation in the Presence of Instantons*, Phys. Rev. D **16**, 1791 (1977).

[35] F. Wilczek, *The Birth of Axions*, Current Contents **16**, 8 (1991).

[36] S. Weinberg, *A New Light Boson?*, Phys. Rev. Lett. **40**, 223 (1978).

[37] F. Wilczek, *Problem of Strong P and T Invariance in the Presence of Instantons*, Phys. Rev. Lett. **40**, 279 (1978).

[38] J. Preskill, M. B. Wise, and F. Wilczek, *Cosmology of the Invisible Axion*, Phys. Lett. B **120**, 127 (1983).

[39] L. F. Abbott and P. Sikivie, *A Cosmological Bound on the Invisible Axion*, Phys. Lett. B **120**, 133 (1983).

[40] M. Dine and W. Fischler, *The Not So Harmless Axion*, Phys. Lett. B **120**, 137 (1983).

[41] M. Kuster, G. Raffelt, and B. Beltrán, *Axions: Theory, cosmology, and experimental searches*, Lect. Notes Phys. **741**, 1 (2008).

[42] D. J. E. Marsh, *Axion Cosmology*, Phys. Rept. **643**, 1 (2016).

[43] M. Kawasaki and K. Nakayama, *Axions: Theory and Cosmological Role*, Ann. Rev. Nucl. Part. Sci. **63**, 69 (2013).

[44] O. Wantz and E. P. S. Shellard, *Axion Cosmology Revisited*, Phys. Rev. D **82**, 123508 (2010).

[45] J. E. Kim, *Light Pseudoscalars, Particle Physics and Cosmology*, Phys. Rept. **150**, 1 (1987).

[46] I. G. Irastorza and J. Redondo, *New experimental approaches in the search for axion-like particles*, Prog. Part. Nucl. Phys. **102**, 89 (2018).

[47] Y. Nambu, *Quasiparticles and Gauge Invariance in the Theory of Superconductivity*, Phys. Rev. **117**, 648 (1960).

[48] J. Goldstone, *Field Theories with Superconductor Solutions*, Nuovo Cim. **19**, 154 (1961).

[49] J. Goldstone, A. Salam, and S. Weinberg, *Broken Symmetries*, Phys. Rev. **127**, 965 (1962).

[50] ALPHA collaboration, M. Bruno *et al.*, *QCD Coupling from a Nonperturbative Determination of the Three-Flavor Λ Parameter*, Phys. Rev. Lett. **119**, 102001 (2017).

[51] G. D. Moore, *Axion dark matter and the Lattice*, EPJ Web Conf. **175**, 01009 (2018).

[52] HotQCD collaboration, A. Bazavov *et al.*, *Chiral crossover in QCD at zero and non-zero chemical potentials*, Phys. Lett. B **795**, 15 (2019).

[53] G. Grilli di Cortona, E. Hardy, J. Pardo Vega, and G. Villadoro, *The QCD axion, precisely*, JHEP **01**, 034 (2016).

[54] M. Gorghetto and G. Villadoro, *Topological Susceptibility and QCD Axion Mass: QED and NNLO corrections*, JHEP **03**, 033 (2019).

[55] V. B. Klaer and G. D. Moore, *The dark-matter axion mass*, JCAP **1711**, 049 (2017).

[56] S. Borsanyi *et al.*, *Calculation of the axion mass based on high-temperature lattice quantum chromodynamics*, Nature **539**, 69 (2016).

[57] J. Frison, R. Kitano, H. Matsufuru, S. Mori, and N. Yamada, *Topological susceptibility at high temperature on the lattice*, JHEP **09**, 021 (2016).

[58] E. Berkowitz, M. I. Buchoff, and E. Rinaldi, *Lattice QCD input for axion cosmology*, Phys. Rev. D **92**, 034507 (2015).

[59] Y. Taniguchi, K. Kanaya, H. Suzuki, and T. Umeda, *Topological susceptibility in finite temperature (2+1)-flavor QCD using gradient flow*, Phys. Rev. D **95**, 054502 (2017).

[60] C. Bonati *et al.*, *Axion phenomenology and θ-dependence from $N_f = 2+1$ lattice QCD*, JHEP **03**, 155 (2016).

[61] P. Petreczky, H.-P. Schadler, and S. Sharma, *The topological susceptibility in finite temperature QCD and axion cosmology*, Phys. Lett. B **762**, 498 (2016).

[62] S. Borsanyi *et al.*, *Axion cosmology, lattice QCD and the dilute instanton gas*, Phys. Lett. B **752**, 175 (2016).

[63] C. Bonati *et al.*, *Topology in full QCD at high temperature: a multicanonical approach*, JHEP **11**, 170 (2018).

[64] P. T. Jahn, G. D. Moore, and D. Robaina, *Estimating χ_{top} lattice artifacts from flowed SU(2) calorons*, Eur. Phys. J. C **79**, 510 (2019).

[65] P. T. Jahn, G. D. Moore, and D. Robaina, *$\chi_{\text{top}}(T \gg T_c)$ in pure-glue QCD through reweighting*, Phys. Rev. D **98**, 054512 (2018).

[66] P. T. Jahn, G. D. Moore, and D. Robaina, *Topological Susceptibility to High Temperatures via Reweighting*, PoS **LATTICE2018**, 155 (2018).

[67] P. T. Jahn, G. D. Moore, and D. Robaina, *in preparation*.

[68] S. Weinberg, *The quantum theory of fields. Vol. 2: Modern applications*. Cambridge University Press, Cambridge, UK (1996).

[69] M. E. Peskin and D. V. Schroeder, *An Introduction to quantum field theory*. Addison-Wesley, Reading, USA (1995).

[70] D. J. Gross and F. Wilczek, *Ultraviolet Behavior of Nonabelian Gauge Theories*, Phys. Rev. Lett. **30**, 1343 (1973).

[71] H. D. Politzer, *Reliable Perturbative Results for Strong Interactions?*, Phys. Rev. Lett. **30**, 1346 (1973).

[72] R. Alkofer and J. Greensite, *Quark Confinement: The Hard Problem of Hadron Physics*, J. Phys. G **34**, S3 (2007).

[73] E. Epelbaum, H.-W. Hammer, and U.-G. Meissner, *Modern Theory of Nuclear Forces*, Rev. Mod. Phys. **81**, 1773 (2009).

[74] R. Machleidt and D. R. Entem, *Chiral effective field theory and nuclear forces*, Phys. Rept. **503**, 1 (2011).

[75] J. M. Maldacena, *The Large N limit of superconformal field theories and supergravity*, Int. J. Theor. Phys. **38**, 1113 (1999).

[76] G. Policastro, D. T. Son, and A. O. Starinets, *The Shear viscosity of strongly coupled N=4 supersymmetric Yang-Mills plasma*, Phys. Rev. Lett. **87**, 081601 (2001).

[77] A. Buchel and J. T. Liu, *Universality of the shear viscosity in supergravity*, Phys. Rev. Lett. **93**, 090602 (2004).

[78] M. Laine and A. Vuorinen, *Basics of Thermal Field Theory*, Lect. Notes Phys. **925**, 1 (2016).

[79] M. L. Bellac, *Thermal Field Theory*. Cambridge Monographs on Mathematical Physics. Cambridge University Press, Cambridge, UK (2011).

[80] J. I. Kapusta and C. Gale, *Finite-temperature field theory: Principles and applications*. Cambridge Monographs on Mathematical Physics. Cambridge University Press, Cambridge, UK (2011).

[81] M. Srednicki, *Quantum Field Theory*. Cambridge University Press, Cambridge, UK (2007).

[82] P. de Forcrand, *Simulating QCD at finite density*, PoS **LAT2009**, 010 (2009).

[83] P. Bicudo, N. Cardoso, and M. Cardoso, *The Chiral crossover, static-light and light-light meson spectra, and the deconfinement crossover*, PoS **BORMIO2011**, 062 (2011).

[84] Y. Aoki, G. Endrodi, Z. Fodor, S. D. Katz, and K. K. Szabo, *The Order of the quantum chromodynamics transition predicted by the standard model of particle physics*, Nature **443**, 675 (2006).

[85] Wuppertal-Budapest collaboration, S. Borsanyi *et al.*, *Is there still any T_c mystery in lattice QCD? Results with physical masses in the continuum limit III*, JHEP **09**, 073 (2010).

[86] P. Braun-Munzinger and J. Wambach, *The Phase Diagram of Strongly-Interacting Matter*, Rev. Mod. Phys. **81**, 1031 (2009).

[87] K. Fukushima and T. Hatsuda, *The phase diagram of dense QCD*, Rept. Prog. Phys. **74**, 014001 (2011).

[88] B. Friman *et al.*, *The CBM physics book: Compressed baryonic matter in laboratory experiments*, Lect. Notes Phys. **814**, 1 (2011).

[89] S. Sharma, *Recent Progress on the QCD Phase Diagram*, PoS **LATTICE2018**, 009 (2019).

[90] S. Weinberg, *The U(1) Problem*, Phys. Rev. D **11**, 3583 (1975).

[91] E. Noether, *Invariante Variationsprobleme*, Nachrichten von der Gesellschaft der Wissenschaften zu Göttingen, Mathematisch-Physikalische Klasse **1918**, 235 (1918).

[92] S. L. Adler, *Axial vector vertex in spinor electrodynamics*, Phys. Rev. **177**, 2426 (1969).

[93] J. S. Bell and R. Jackiw, *A PCAC puzzle: $\pi^0 \to \gamma\gamma$ in the σ model*, Nuovo Cim. A **60**, 47 (1969).

[94] H. Forkel, *A Primer on instantons in QCD*, arXiv:hep-ph/0009136 (2000).

[95] M. F. Atiyah and I. M. Singer, *The Index of elliptic operators. 1*, Annals Math. **87**, 484 (1968).

[96] M. F. Atiyah and I. M. Singer, *The index of elliptic operators on compact manifolds*, Bull. Am. Math. Soc. **69**, 422 (1969).

[97] M. Nakahara, *Geometry, Topology and Physics*. Institute of Physics Publishing, Bristol, UK, second ed. (2003).

[98] R. Bott, *An application of the Morse theory to the topology of Lie-groups*, Bulletin de la Société Mathématique de France **84**, 251 (1956).

[99] R. Jackiw and C. Rebbi, *Vacuum Periodicity in a Yang-Mills Quantum Theory*, Phys. Rev. Lett. **37**, 172 (1976).

[100] S. Coleman, *Aspects of Symmetry: Selected Erice Lectures*. Cambridge University Press, Cambridge, UK (1985).

[101] E. J. Weinberg, *Classical solutions in quantum field theory: Solitons and Instantons in High Energy Physics*. Cambridge University Press, Cambridge, UK (2012).

[102] R. Rajaraman, *Solitons and Instantons: An Introduction to Solitons and Instantons in Quantum Field Theory*. North-Holland, Amsterdam, Netherlands (1982).

[103] A. I. Vaĭnshteĭn, V. I. Zakharov, V. A. Novikov, and M. A. Shifman, *ABC's of Instantons*, Sov. Phys. Usp. **25**, 195 (1982).

[104] M. A. Shifman, ed., *Instantons in gauge theories*. World Scientific, Singapore (1994).

[105] T. Schäfer and E. V. Shuryak, *Instantons in QCD*, Rev. Mod. Phys. **70**, 323 (1998).

[106] A. V. Belitsky, S. Vandoren, and P. van Nieuwenhuizen, *Yang-Mills and D instantons*, Class. Quant. Grav. **17**, 3521 (2000).

[107] D. Diakonov, *Instantons at work*, Prog. Part. Nucl. Phys. **51**, 173 (2003).

[108] S. Vandoren and P. van Nieuwenhuizen, *Lectures on instantons*, arXiv:0802.1862 (2008).

[109] A. M. Polyakov, *Compact Gauge Fields and the Infrared Catastrophe*, Phys. Lett. B **59**, 82 (1975).

[110] A. A. Belavin, A. M. Polyakov, A. S. Schwartz, and Yu. S. Tyupkin, *Pseudoparticle Solutions of the Yang-Mills Equations*, Phys. Lett. B **59**, 85 (1975).

[111] C. G. Callan, Jr., R. F. Dashen, and D. J. Gross, *The Structure of the Gauge Theory Vacuum*, Phys. Lett. B **63**, 334 (1976).

[112] A. M. Polyakov, *Quark Confinement and Topology of Gauge Groups*, Nucl. Phys. B **120**, 429 (1977).

[113] K. M. Bitar and S.-J. Chang, *Vacuum Tunneling of Gauge Theory in Minkowski Space*, Phys. Rev. D **17**, 486 (1978).

[114] E. B. Bogomolny, *Stability of Classical Solutions*, Sov. J. Nucl. Phys. **24**, 449 (1976).

[115] E. Corrigan and D. B. Fairlie, *Scalar Field Theory and Exact Solutions to a Classical SU(2) Gauge Theory*, Phys. Lett. B **67**, 69 (1977).

[116] R. Jackiw, C. Nohl, and C. Rebbi, *Conformal Properties of Pseudoparticle Configurations*, Phys. Rev. D **15**, 1642 (1977).

[117] B. J. Harrington and H. K. Shepard, *Periodic Euclidean Solutions and the Finite Temperature Yang-Mills Gas*, Phys. Rev. D **17**, 2122 (1978).

[118] G. 't Hooft, *Symmetry Breaking Through Bell-Jackiw Anomalies*, Phys. Rev. Lett. **37**, 8 (1976).

[119] C. G. Callan, Jr., R. F. Dashen, and D. J. Gross, *Toward a Theory of the Strong Interactions*, Phys. Rev. D **17**, 2717 (1978).

[120] E. Witten, *Current Algebra Theorems for the U(1) Goldstone Boson*, Nucl. Phys. B **156**, 269 (1979).

[121] G. Veneziano, *U(1) Without Instantons*, Nucl. Phys. B **159**, 213 (1979).

[122] G. 't Hooft, *Computation of the Quantum Effects Due to a Four-Dimensional Pseudoparticle*, Phys. Rev. D **14**, 3432 (1976), [Erratum: Phys. Rev. D **18**, 2199 (1978)].

[123] C. G. Callan, Jr., R. F. Dashen, and D. J. Gross, *A Theory of Hadronic Structure*, Phys. Rev. D **19**, 1826 (1979).

[124] D. J. Gross, R. D. Pisarski, and L. G. Yaffe, *QCD and Instantons at Finite Temperature*, Rev. Mod. Phys. **53**, 43 (1981).

[125] R. D. Pisarski and L. G. Yaffe, *The density of instantons at finite temperature*, Phys. Lett. B **97**, 110 (1980).

[126] A. Ringwald and F. Schrempp, *Confronting instanton perturbation theory with QCD lattice results*, Phys. Lett. B **459**, 249 (1999).

[127] K. G. Wilson, *Confinement of Quarks*, Phys. Rev. D **10**, 2445 (1974).

[128] C. Gattringer and C. B. Lang, *Quantum chromodynamics on the lattice*, Lect. Notes Phys. **788**, 1 (2010).

[129] H. J. Rothe, *Lattice Gauge Theories – An Introduction*. World Scientific, Singapore, fourth ed. (2012).

[130] M. Creutz, *Quarks, gluons and lattices*. Cambridge Monographs on Mathematical Physics. Cambridge University Press, Cambridge, UK (1985).

[131] T. DeGrand and C. E. Detar, *Lattice methods for quantum chromodynamics*. World Scientific, New Jersey, USA (2006).

[132] `http://luscher.web.cern.ch/luscher/openQCD/index.html`.

[133] P. Hasenfratz and F. Karsch, *Chemical Potential on the Lattice*, Phys. Lett. B **125**, 308 (1983).

[134] K. Symanzik, *Continuum Limit and Improved Action in Lattice Theories. 1. Principles and phi**4 Theory*, Nucl. Phys. B **226**, 187 (1983).

[135] K. Symanzik, *Continuum Limit and Improved Action in Lattice Theories. 2. O(N) Nonlinear Sigma Model in Perturbation Theory*, Nucl. Phys. B **226**, 205 (1983).

[136] P. Weisz, *Continuum Limit Improved Lattice Action for Pure Yang-Mills Theory. 1.*, Nucl. Phys. B **212**, 1 (1983).

[137] P. Weisz and R. Wohlert, *Continuum Limit Improved Lattice Action for Pure Yang-Mills Theory. 2.*, Nucl. Phys. B **236**, 397 (1984), [Erratum: Nucl. Phys. B **247**, 544 (1984)].

[138] M. Lüscher and P. Weisz, *On-Shell Improved Lattice Gauge Theories*, Commun. Math. Phys. **97**, 59 (1985), [Erratum: Commun. Math. Phys. **98**, 433 (1985)].

[139] G. Curci, P. Menotti, and G. Paffuti, *Symanzik's Improved Lagrangian for Lattice Gauge Theory*, Phys. Lett. B **130**, 205 (1983), [Erratum: Phys. Lett. B **135**, 516 (1984)].

[140] Y. Iwasaki, *Renormalization Group Analysis of Lattice Theories and Improved Lattice Action: Two-Dimensional Nonlinear O(N) Sigma Model*, Nucl. Phys. B **258**, 141 (1985).

[141] Y. Iwasaki, *Renormalization Group Analysis of Lattice Theories and Improved Lattice Action. II. Four-dimensional non-Abelian SU(N) gauge model*, `arXiv:1111.7054` (1983).

[142] G. D. Moore, *Improved Hamiltonian for Minkowski Yang-Mills theory*, Nucl. Phys. B **480**, 689 (1996).

[143] S. O. Bilson-Thompson, D. B. Leinweber, and A. G. Williams, *Highly improved lattice field strength tensor*, Annals Phys. **304**, 1 (2003).

[144] C. Alexandrou *et al.*, *Comparison of topological charge definitions in Lattice QCD*, `arXiv:1708.00696` (2017).

[145] P. H. Ginsparg and K. G. Wilson, *A Remnant of Chiral Symmetry on the Lattice*, Phys. Rev. D **25**, 2649 (1982).

[146] D. B. Kaplan, *A Method for simulating chiral fermions on the lattice*, Phys. Lett. B **288**, 342 (1992).

[147] R. Narayanan and H. Neuberger, *Chiral fermions on the lattice*, Phys. Rev. Lett. **71**, 3251 (1993).

[148] D. B. Kaplan, *Chiral Symmetry and Lattice Fermions*, arXiv:0912.2560 (2009).

[149] R. Narayanan and H. Neuberger, *Infinite N phase transitions in continuum Wilson loop operators*, JHEP **03**, 064 (2006).

[150] M. Lüscher, *Trivializing maps, the Wilson flow and the HMC algorithm*, Commun. Math. Phys. **293**, 899 (2010).

[151] M. Lüscher, *Properties and uses of the Wilson flow in lattice QCD*, JHEP **08**, 071 (2010), [Erratum: JHEP **03**, 092 (2014)].

[152] M. Lüscher, *Topology, the Wilson flow and the HMC algorithm*, PoS **LATTICE2010**, 015 (2010).

[153] M. Lüscher and P. Weisz, *Perturbative analysis of the gradient flow in non-abelian gauge theories*, JHEP **02**, 051 (2011).

[154] M. Lüscher, *Chiral symmetry and the Yang–Mills gradient flow*, JHEP **04**, 123 (2013).

[155] M. Lüscher, *Future applications of the Yang-Mills gradient flow in lattice QCD*, PoS **LATTICE2013**, 016 (2014).

[156] B. Berg, *Dislocations and Topological Background in the Lattice O(3) σ Model*, Phys. Lett. B **104**, 475 (1981).

[157] P. de Forcrand, M. Garcia Perez, and I.-O. Stamatescu, *Topology of the SU(2) vacuum: A Lattice study using improved cooling*, Nucl. Phys. B **499**, 409 (1997).

[158] M. Garcia Perez, O. Philipsen, and I.-O. Stamatescu, *Cooling, physical scales and topology*, Nucl. Phys. B **551**, 293 (1999).

[159] M. Garcia Perez, A. Gonzalez-Arroyo, A. Montero, and P. van Baal, *Calorons on the lattice: A New perspective*, JHEP **06**, 001 (1999).

[160] A. Ramos and S. Sint, *Symanzik improvement of the gradient flow in lattice gauge theories*, Eur. Phys. J. C **76**, 15 (2016).

[161] W. H. Press, S. A. Teukolsky, W. T. Vetterling, and B. P. Flannery, *Numerical Recipes: The Art of Scientific Computing*. Cambridge University Press, Cambridge, UK, third ed. (2007).

[162] R. Sommer, *A New way to set the energy scale in lattice gauge theories and its applications to the static force and α_s in SU(2) Yang-Mills theory*, Nucl. Phys. B **411**, 839 (1994).

[163] S. Durr, Z. Fodor, C. Hoelbling, and T. Kurth, *Precision study of the SU(3) topological susceptibility in the continuum*, JHEP **04**, 055 (2007).

[164] S. Necco and R. Sommer, *The N(f) = 0 heavy quark potential from short to intermediate distances*, Nucl. Phys. B **622**, 328 (2002).

[165] A. Francis, O. Kaczmarek, M. Laine, T. Neuhaus, and H. Ohno, *Critical point and scale setting in SU(3) plasma: An update*, Phys. Rev. D **91**, 096002 (2015).

[166] Y. Burnier *et al.*, *Thermal quarkonium physics in the pseudoscalar channel*, JHEP **11**, 206 (2017).

[167] A. Haar, *Der Massbegriff in der Theorie der kontinuierlichen Gruppen*, Annals of Mathematics **34**, 147 (1933).

[168] N. Metropolis, A. W. Rosenbluth, M. N. Rosenbluth, A. H. Teller, and E. Teller, *Equation of state calculations by fast computing machines*, J. Chem. Phys. **21**, 1087 (1953).

[169] M. Creutz, *Monte Carlo Study of Quantized SU(2) Gauge Theory*, Phys. Rev. D **21**, 2308 (1980).

[170] N. Cabibbo and E. Marinari, *A New Method for Updating SU(N) Matrices in Computer Simulations of Gauge Theories*, Phys. Lett. B **119**, 387 (1982).

[171] R. Petronzio and E. Vicari, *An Overrelaxed Monte Carlo algorithm for SU(3) lattice gauge theories*, Phys. Lett. B **248**, 159 (1990).

[172] S. Duane and J. B. Kogut, *Hybrid Stochastic Differential Equations Applied to Quantum Chromodynamics*, Phys. Rev. Lett. **55**, 2774 (1985).

[173] S. Duane and J. B. Kogut, *The Theory of Hybrid Stochastic Algorithms*, Nucl. Phys. B **275**, 398 (1986).

[174] I. Omelyan, I. Mryglod, and R. Folk, *New optimized algorithms for molecular dynamics simulations*, Cond. Mat. Phys. **5**, 369 (2002).

[175] S. Duane, A. D. Kennedy, B. J. Pendleton, and D. Roweth, *Hybrid Monte Carlo*, Phys. Lett. B **195**, 216 (1987).

[176] ALPHA collaboration, U. Wolff, *Monte Carlo errors with less errors*, Comput. Phys. Commun. **156**, 143 (2004), [Erratum: Comput. Phys. Commun. **176**, 383 (2007)].

[177] M. Lüscher, *Schwarz-preconditioned HMC algorithm for two-flavour lattice QCD*, Comput. Phys. Commun. **165**, 199 (2005).

[178] M. H. Quenouille, *Problems in Plane Sampling*, Ann. Math. Statist. **20**, 355 (1949).

[179] J. W. Tukey, *Bias and confidence in not quite large samples (abstract)*, Ann. Math. Statist. **29**, 614 (1958).

[180] M. Teper, *Instantons in the Quantized SU(2) Vacuum: A Lattice Monte Carlo Investigation*, Phys. Lett. B **162**, 357 (1985).

[181] D. J. R. Pugh and M. Teper, *Topological Dislocations in the Continuum Limit of SU(2) Lattice Gauge Theory*, Phys. Lett. B **224**, 159 (1989).

[182] F. Bruckmann, D. Nogradi, and P. van Baal, *Higher charge calorons with non-trivial holonomy*, Nucl. Phys. B **698**, 233 (2004).

[183] F. Bruckmann *et al.*, *Calorons with non-trivial holonomy on and off the lattice*, Nucl. Phys. Proc. Suppl. **140**, 635 (2005).

[184] P. de Forcrand, M. Garcia Perez, and I.-O. Stamatescu, *Improved cooling algorithm for gauge theories*, Nucl. Phys. Proc. Suppl. **47**, 777 (1996).

[185] P. de Forcrand and S. Kim, *Topological susceptibility and instanton size distribution from over improved cooling*, Nucl. Phys. Proc. Suppl. **47**, 278 (1996).

[186] M. Garcia Perez, A. Gonzalez-Arroyo, J. R. Snippe, and P. van Baal, *Instantons from over - improved cooling*, Nucl. Phys. B **413**, 535 (1994).

[187] S. Borsanyi, G. Endrodi, Z. Fodor, S. D. Katz, and K. K. Szabo, *Precision SU(3) lattice thermodynamics for a large temperature range*, JHEP **07**, 056 (2012).

[188] B. A. Berg and T. Neuhaus, *Multicanonical algorithms for first order phase transitions*, Phys. Lett. B **267**, 249 (1991).

[189] K. Kajantie, M. Laine, K. Rummukainen, and M. E. Shaposhnikov, *The Electroweak phase transition: A Nonperturbative analysis*, Nucl. Phys. B **466**, 189 (1996).

[190] M. Laine and K. Rummukainen, *The MSSM electroweak phase transition on the lattice*, Nucl. Phys. B **535**, 423 (1998).

[191] F. Wang and D. P. Landau, *Efficient, Multiple-Range Random Walk Algorithm to Calculate the Density of States*, Phys. Rev. Lett. **86**, 2050 (2001).

[192] A. Barducci, G. Bussi, and M. Parrinello, *Well-Tempered Metadynamics: A Smoothly Converging and Tunable Free-Energy Method*, Phys. Rev. Lett. **100**, 020603 (2008).

[193] A. Laio, G. Martinelli, and F. Sanfilippo, *Metadynamics surfing on topology barriers: the CP^{N-1} case*, JHEP **07**, 089 (2016).

[194] F. Sanfilippo, A. Laio, and G. Martinelli, *Metadynamics Remedies for Topological Freezing*, PoS **LATTICE2016**, 274 (2017).

[195] C. Morningstar and M. J. Peardon, *Analytic smearing of SU(3) link variables in lattice QCD*, Phys. Rev. D **69**, 054501 (2004).

[196] C. Bonati and M. D'Elia, *Topological critical slowing down: variations on a toy model*, Phys. Rev. E **98**, 013308 (2018).

[197] M. Caselle, A. Nada, and M. Panero, *QCD thermodynamics from lattice calculations with nonequilibrium methods: The SU(3) equation of state*, Phys. Rev. D **98**, 054513 (2018).

[198] L. Giusti and H. B. Meyer, *Thermal momentum distribution from path integrals with shifted boundary conditions*, Phys. Rev. Lett. **106**, 131601 (2011).

[199] CODATA Internationally recommended 2018 values of the Fundamental Physical Constants.

Thank You!

My time as a graduate student was definitely a life-changing period and I would doubtlessly not have finished this thesis without the help and support of many persons. I therefore feel that it is appropriate to communicate my deep gratitude at this point.

First of all, I have to express my deepest appreciation to my supervisor Guy Moore for giving me the opportunity to work on this very exciting project in his group. His physics intuition and broad (not only physics-related) knowledge impresses me time and again. His door was literally always open and whenever I was stuck, he always had very profound ideas that helped me a lot.

I am also extremely grateful to Daniel Robaina for being such a great mentor. Without him, I would probably still not know anything about lattice QCD and openQCD. The uncountable discussions with him always made things clear and helped me coding and analyzing the right things.

I also want to thank Jens Braun for being part of my Ph.D. committee, and especially for taking the time to be the second reviewer of this thesis; and Michael Vogel and Thomas Walther for being part of my examination committee.

Special thanks go to our whole (extended) group: Marwin Acker, Marc Barroso Mancha, Michael Buballa, A. Max Eller, Marco Hofmann, Parikshit Junnarkar, Vincent Klaer, Max Lenz, Deniz Nitt, Jillur Rahman, Niels Schlusser, and Martin Steil. Especially I want to thank office 306 for the nice atmosphere and for many deep and enlightening discussions, not only physics-related... In particular, Max whose broad physics interest often turned out to be useful; Vincent, my doctoral twin, for being my training partner in the mornings, for always having an open ear, for sharing his green tea with me, and for many other things; Deniz for always getting precisely the point ;-); Niels, my Mannheimer almost-neighbor, for sharing my passion for premium TV shows and for always having suitable worldly wisdom; Martin for being the perfect office mate – whenever I had some issues with Mathematica or Python, he usually had a working solution within five minutes; and Parry for many enlightening discussions.

I gratefully acknowledge the great effort of everybody who proofread parts of this manuscript: Adrian, Guy, Max, Niels, Parry, and Svenja. Your helpful advice and practical suggestions cannot be overestimated, although they now and then engulfed me in little crises.

This work was supported by the DFG-funded collaborative research center transregio 211 (CRC-TR 211). The regular meetings were always interesting and I met many very nice people. I especially want to thank Olaf Kaczmarek and Lukas Mazur for the nice collaboration in project A05, and Adrian Koenigstein for sharing his expertise on (not only) topology with me.

I acknowledge funding by the GSI Helmholtzzentrum für Schwerionenforschung through a Ph.D. recruitment stipend at the beginning of my time as a graduate student. I am also indebted to my graduate school HGS-HIRe for organizing workshops and lecture weeks. In particular, the soft-skill seminars were extremely interesting and helpful for getting along not only in the scientific world. I also acknowledge financial support through travel money. Together with the CRC-TR 211, this allowed me to attend very interesting international conferences and workshops in Spain, the US, China, and Japan.

Gratitude should also go to Martin Lüscher for providing the open-source lattice code *openQCD*. Thanks to this very well written and documented code, my first steps on the lattice were not completely frustrating. Parts of the simulations were conducted on the Lichtenberg high performance computer of the TU Darmstadt (HHLR). I especially want to thank the HHLR team for being a great support whenever I had some trouble with the machine.

My appreciation goes to all friends that (not only) share my passion for SV Darmstadt 98, for very nice days at the Böllenfalltor and at away matches: Sascha, Sven, Andrea, Laura, Lukas, and Ubbi.

I am deeply thankful to my dear parents for financial support during my studies, for always supporting my way and for ... yeah for everything! Without you, I would have never made it so far.

Last but not least, my heartfelt thanks go to Svenja for always being there for me. You, Niccy, Klary, Kaya, and Baghira make my life so much richer.

Curriculum Vitae

Personal Information

Name:	Peter Thomas Jahn
Date of Birth:	August 21, 1990
Place of Birth:	Gelnhausen, Germany

Education & Employment

since 02/2019	**Research associate** **Technische Universität Darmstadt**
since 10/2016	**Doctoral studies in Physics** **Technische Universität Darmstadt**
01/2014 – 08/2016	**Master of Science in Physics (grade 1.37 – very good)** **Technische Universität Darmstadt** Master's thesis (supervised by Prof. Dr. Bengt Friman): *"Renormalization Group Study of Scaling Near the Tricritical Point of Strongly Interacting Matter"* Minor subject: Mathematics
04/2011 – 01/2014	**Bachelor of Science in Physics (grade 1.46 – very good)** **Technische Universität Darmstadt** Bachelor's thesis (supervised by Prof. Dr. Jens Braun): *"Phases of Strongly Interacting Spin-Polarized Fermi Gases in Harmonic Traps"* Minor subject: Mathematics
07/2010 – 12/2010	**Basic Military Service** 7./ Logistikbataillon 472, Kümmersbruck and 4./ Feldjägerbataillon 451, Amberg
2001 – 06/2010	**Abitur (grade 1.7)** **Grimmelshausen Gymnasium Gelnhausen** Advanced courses: Mathematics and Physics

Miscellaneous

since 2017	Member of the *equal opportunities team* of the *DFG – CRC-TR 211*
since 2011	Member of the *Deutsche Physikalische Gesellschaft*